eman ta zabal zazu
Universidad del País Vasco
Euskal Herriko Unibertsitatea
Kimika Fisikoa Saila
Departamento de Química Física

NEW PHOTOACTIVE DYE-DOPED ZEOTYPIC MATERIALS: TOWARDS OPTICAL APPLICATIONS

PhD Thesis by:

AINHOA OLIDEN SÁNCHEZ

Supervisors:
Virginia Martínez Martínez
Rebeca Sola Llano

Degree in Chemistry
Molecular Spectroscopy Group
Department of Physical Chemistry
Faculty of Science and Technology
University of the Basque Country UPV-EHU

Bilbao, May 2022

Supervisors:
Virginia Martínez Martínez
Rebeca Sola Llano

Location:
Bilbao

Time Frame:
May 2022

Familiari

Maite dudana maite dut hainbeste,
jasotzen dudalako ematen dudan beste,
hainbeste.

— Izaro (Hainbeste)

Yo quiero, yo puedo, yo voy.

— Tony Meléndez

ABSTRACT

The present thesis deals with the development and study of photoactive zeotypic hybrid materials in order to obtain multifunctional solid-state systems with interesting optical properties suitable for applications in the field of photonics. For this purpose, organic dyes are trapped into constrained nanocavities of metal-doped inorganic aluminophosphate frameworks (with Si or Mg, obtaining SAPO and MgAPO-type structures, respectively) to promote new and/or improved photophysical processes in the materials by synergistic effect, compared to isolated fluorophores.

A large number of dye-AlPO materials are prepared, combining various structures of different pore/channel shapes and sizes, in the range of molecular dimensions, with a wide range of organic dyes, mainly from the styryl and three-ring fused aromatic families. The inclusion of fluorophores into the cavities of AlPOs performed "in situ" by the *crystallization inclusion* method allows the direct development of fluorescent hybrid materials with outstanding and specific optical functionalities in a single step and in short periods of time, thus describing a cost-effective and efficient synthesis for advanced systems.

On the one hand, as a result of the synergism between push-pull photoactive molecules with 1D-channeled aluminophosphate hosts (AFI, ATS, and AEL) and a 3D-like cage structure (CHA), optically dense solid systems are obtained with enhanced fluorescence capability and highly anisotropic response to linearly polarized light. Through this strategy, the founded applications are diverse, ranging from NIR emitters to second-harmonic generators and solid-state lasers at the single-particle level.

On the other hand, the simultaneous occlusion of different photoactive species on aluminophosphates (IFO and AEL) promotes the probability of cascade FRET processes

between organic molecules occluded in the restricted space of the zeotypic channels. The co-encapsulation of suitable and rationally elected species (FRET-pairs) in the right proportion leads to new artificial antenna systems, with properties such as tunable emission and white light emission.

The syntheses of the dye-doped hybrid materials are optimized (varying gel composition, temperature, and heating time and method), and the morphology and crystallization of all the phases herein presented are checked by SEM and powder X-ray diffraction techniques. The photophysical properties of the hybrid materials and photoactive dyes are analyzed in-depth by means of steady-state and time-correlated techniques (absorption and emission spectroscopies) as well as fluorescence microscopy, which allows the analysis at single-particle level. In addition, the final applicabilities of the materials are demonstrated by sophisticated techniques such as the detection of second-harmonic generation signal and microlaser action response.

LABURPENA

Tesi honetan material zeotipiko fotoaktiboak garatu eta aztertzen dira, propietate optiko interesgarriak dituzten eta egoera solidoan dauden sistema multifuntzionalak lortzeko, hain zuzen ere fotonikaren alorrean erabiltzeko aproposak direnak. Horretarako, metalekin dopatutako aluminofosfato euskarri ez-organikoen nanobarrunbe estuetan (Si-arekin edo Mg-arekin, hurrenez hurren, SAPO eta MgAPO motako egiturak lortzen dira) koloratzaile organikoak txertatu dira, efektu sinergikoen bidez propietate fotofisiko berriak eta/edo hobetuak sustatzeko fluoroforo isolatuekin alderatuta.

Koloratzaile-AlPO material ugari prestatu dira, molekulen dimentsio antzekoak dituzten poro/kanal tamaina desberdineko hainbat egitura konbinatuz, koloratzaile organikoen sorta zabal batekin, batez ere estiriloekin eta hiru eraztun aromatiko fusionatuta dituzten koloratzaile familiekin. *Kristalizazio-inklusio* metodoaren bidez AlPOen barrunbeetan "in situ" fluoroforoak barneratuz gero, funtzio optiko bereziak dituzten material hibrido fluoreszenteak zuzenean gara daitezke, urrats bakar batean eta denbora-tarte laburrean. Hala, sistema aurreratuak lortzeko sintesi errentagarria eta eraginkorra deskribatzen da.

Alde batetik, optikoki dentsoak diren sistema solidoak lortzen dira, bultza-tira molekula fotoaktiboen eta aluminofosfato harrera konposatuen arteko sinergiaren ondorioz; zehazki, 1D kanalak (AFI, ATS eta AEL) eta 3D-gelaxkak (CHA) dituzten egiturekin. Horrela, fluoreszentzia-ahalmen handiagoko sistemak eta argi polarizatuarekiko erantzun anisotropikoa duten materialak lortu dira. Estrategia horren bidez, hainbat aplikazio erdietsi dira: NIR igorgailuak, bigarren harmonikoaren sorgailuak eta partikula mailako laser solidoak.

Bestalde, aluminofosfatoen (IFO eta AEL) barnean zenbait espezie fotoaktibo aldi berean buxatzean, molekula organikoen arteko FRET kate prozesuak gertatzeko probabilitatea sustatzen da kanal zeotipikoen espazio murriztuan. Arrazionalki aukeratutako espezie aproposak (FRET pareak) proportzio egokietan barneratzean, hainbat propietate dituzten antena artifizial sistema berriak sortzen dira, hala nola, igorpen sintonizagarria edota argi zuriaren igorpena.

Lan honetan zehar, koloratzailez dopaturiko material hibridoen sintesia optimizatu egin da (gel-konposizioa, tenperatura, berotze denbora eta metodoa aldatuz), eta faseen morfologia eta kristalizazioa MEB eta X-izpien hautsaren difrakzio tekniken bidez egiaztatu dira. Material hibridoen eta koloratzaile fotoaktiboen propietate fotofisikoak sakon aztertu dira, egoera estazionario eta denbora-korrelazio espektroskopia (xurgapen eta igorpen espektroskopia) tekniken bidez, bai eta fluoreszentzia-mikroskopiaren bidez ere, partikula-mailan analizatzea xede. Horrez gain, materialaren erabilgarritasuna frogatzeko aparatu sofistikatuak erabili dira, hala nola, bigarren harmonikoaren seinalearen detekzioa eta mikrolaser ekintzaren erantzuna.

RESUMEN

En esta tesis se desarrollan y estudian materiales híbridos zeotípicos fotoactivos para la obtención de sistemas multifuncionales en estado sólido con interesantes propiedades ópticas aptas para aplicaciones en el campo de la fotónica. Para ello, se atrapan colorantes orgánicos en nanocavidades restringidas de estructuras inorgánicas de aluminofosfato dopadas con metales (con Si o Mg, obteniendo estructuras tipo SAPO y MgAPO, respectivamente) para promover procesos fotofísicos nuevos y/o mejorados en los materiales por efecto sinérgico, en comparación con los fluoróforos aislados.

En este trabajo se preparan un gran número de materiales de colorante-AlPO, combinando varias estructuras con diferentes formas y tamaños de poros/canales en el rango de dimensiones moleculares, con una amplia gama de colorantes orgánicos, principalmente de las familias de estirilos y aromáticos fusionados de tres anillos. La inclusión de fluoróforos en las cavidades de los AlPOs realizada "in situ" por el método de *inclusión por cristalización* permite el desarrollo directo de materiales híbridos fluorescentes con funcionalidades ópticas destacadas y específicas en un solo paso y en cortos periodos de tiempo, describiendo así una síntesis rentable y eficiente para sistemas avanzados.

Por un lado, como resultado de la sinergia entre moléculas fotoactivas push-pull con anfitriones de aluminofosfato canalizados en 1D (AFI, ATS y AEL) y una estructura de tipo jaula-3D (CHA), se obtienen sistemas sólidos ópticamente densos con capacidad de fluorescencia mejorada y respuesta altamente anisotrópica a la luz linealmente polarizada. A través de esta estrategia las aplicaciones logradas son diversas, desde emisores NIR hasta generadores de segundo armónico y láseres en estado sólido a nivel de partícula.

Por otro lado, la oclusión simultánea de diferentes especies fotoactivas en los aluminofosfatos (IFO y AEL) promueve la probabilidad de procesos de FRET en cascada entre moléculas orgánicas ocluidas en el espacio restringido de los canales zeotípicos. La coencapsulación de especies adecuadas y racionalmente seleccionadas (pares FRET) proporciones idóneas conduce a nuevos sistemas de antenas artificiales, con propiedades como la emisión sintonizable y la emisión de luz blanca.

A lo largo de este trabajo, las síntesis de los materiales híbridos dopados con colorantes se optimizan (variando la composición del gel, la temperatura y el tiempo y método de calentamiento) y la morfología y cristalización de todas las fases presentadas se comprueban mediante técnicas de SEM y difracción de rayos-X en polvo. Las propiedades fotofísicas de los materiales híbridos y de los colorantes fotoactivos se analizan en profundidad mediante técnicas de estado estacionario y resueltas en el tiempo (espectroscopias de absorción y emisión), así como mediante microscopía de fluorescencia, que permite el análisis a nivel de partícula. Además, se demuestra la aplicabilidad final de los materiales mediante técnicas sofisticadas como la detección de señales de generación de segundo armónico y la respuesta de acción del microláser.

PUBLICATIONS

THESIS-RELATED PUBLICATIONS

- **International publications**

  (1) Sola-Llano, R.; Oliden-Sánchez, A.; Alfayate, A.; Gómez-Hortigüela, L.; Pérez-Pariente, J.; Arbeloa, T.; Hofkens, J.; Fron, E.; Martínez-Martínez, V. White Light Emission by Simultaneous One Pot Encapsulation of Dyes into One-Dimensional Channelled Aluminophosphate. *Nanomaterials* **2020**, *10*, 1173.

  (2) Sola-Llano, R.; Gartzia-Rivero, L.; Oliden-Sánchez, A.; Bañuelos, J.; Arbeloa, I. L.; Martínez-Martínez, V., Dye Encapsulation Into One-Dimensional Zeolitic Materials for Optical Applications In *Chemistry of Silica and Zeolite-Based Materials*; Elsevier: 2019, pp 229–248.

  (3) Oliden-Sánchez, A.; Sola-Llano, R.; López-Arbeloa, I.; Martínez-Martínez, V. Enhancement of NIR emission by a tight confinement of a hemicyanine dye within zeolitic MgAPO-5 nanochannels. *Photochemical & Photobiological Sciences* **2018**, *17*, 917–922.

- **Publications in basque**

  (4) Sánchez, A. O.; Llano, R. S. Mikrouhinen bidezko beroketaren onurak koloratzailez dopaturiko material hibridoen sintesian. *Ekaia, Zientzia eta Teknologia Aldizkaria* **2020**, *37*, 117–128.

(5) Oliden-Sánchez, A.; Sola-Llano, R.; Martínez-Martínez, V.; Arbeloa, I. L., NIR propietate fotofisikoen hobekuntza LDS730 hemizianina koloratzailea 1D-$AlPO_4$-5 nanokaleetan barneratzearen ondorioz In *Materialen Zientzia eta Teknologia IV. Kongresua, Lanen Bilduma*; CEIT-IK4 eta Tecnun - Universidad de Navarra: 2018, pp 351–357.

- **In preparation**

  i) Microlaser and SHG response in a single crystal: DMASBT styryl dye within AEL channels.

  ii) Exploiting the photophysical features of DMAN template in ITQ-51.

OTHER PUBLICATIONS

- **International publications**

  (7) Jiménez, J.; Prieto-Montero, R.; Maroto, B. L.; Moreno, F.; Ortiz, M. J.; Oliden-Sánchez, A.; López-Arbeloa, I.; Martínez-Martínez, V.; de la Moya, S. Manipulating Charge-Transfer States in BODIPYs: A Model Strategy to Rapidly Develop Photodynamic Theragnostic Agents. *Chemistry–A European Journal* **2020**, *26*, 601–605.

  (8) Oliden-Sánchez, A.; Sola-Llano, R.; Bañuelos, J.; García-Moreno, I.; Uriel, C.; López, J. C.; Gómez, A. M. Tuning the photonic behavior of symmetrical bis-BODIPY architectures: the key role of the spacer moiety. *Frontiers in chemistry* **2019**, *7*, 801.

  (9) Cristóbal López, J; del Rio, M.; Oliden, A.; Bañuelos, J.; López-Arbeloa, I.; García-Moreno, I.; Gómez, A. M. Solvent-Sensitive Emitting Urea-Bridged bis-BODIPYs: Ready Access by a One-Pot Tandem Staudinger/Aza-Wittig Ureation. *Chemistry–A European Journal* **2017**, *23*, 17511–17520.

(10) Del Río, M.; Lobo, F.; Loípez, J. C.; Oliden, A.; Banuelos, J.; Loípez-Arbeloa, I.; Garcia-Moreno, I.; Goímez, A. M. One-pot synthesis of rotationally restricted, conjugatable, BODIPY derivatives from phthalides. *The Journal of organic chemistry* **2017**, *82*, 1240–1247.

- **Publications in basque**

(11) Zaballa, E. A.; Sánchez, A. O.; Llano, R. S.; Rivero, L. G.; Prieto, J. B. Balizko molekula fotoaktibo multifuntzionala biomedikuntzarako. *Ekaia, Zientzia eta Teknologia Aldizkaria* **2021**, *41*, 207–224.

- **Patents**

(12) Chiara Romero, J. L.; Blázquez Moraleja, A.; Mann Morales, E. A.; Maierhofer, L.; Prieto Montero, R.; Oliden Sánchez, A.; Martínez Martínez, V.; Chiara Romero, M. D.; Celada Crespo, L. (CSIC; UPV-EHU; FINBA). Compuestos para etiquetado fluorescente pat., 2021.

I am incapable of conceiving infinity,
and yet I do not accept finity.
I want this adventure that is the context of my life
to go on without end.

Simone de Beauvoir, La Vieillesse

ACKNOWLEDGMENTS

First and foremost, I would like to express my sincere gratitude to my supervisors, Dr. Virginia Martínez Martínez and Dr. Rebeca Sola Llano, for their continuous support during my PhD study and research, and for sharing with me such knowledge throughout these four years. They have provided me invaluable guidance, giving me freedom and autonomy whenever necessary. This has allowed me to evolve as a scientist, which has always been my desire. Apart from research, we have overcome many challenges that have made it possible to be who and where I am now, with this precious thesis in my hands. For that and many other reasons, I will always be grateful to them.

In addition to my supervisors, I would like to thank to all the scientists that have worked in collaboration with this research project. First of all, to the colleagues from the *Institute of Catalysis and Petrochemistry (CSIC)*, Luis Gómez Hortigüela and Joaquín Perez Pariente, for guiding me in the inorganic synthesis of zeolites and for their immense knowledge. Even if the stays in Madrid were quite short, they welcomed me with open arms and made my stays awesome. Especially, I will like to thank all my labmates there, Ramón, Ricardo, Fernando, Isabel, Asun...

Besides, I have to also thank Shuhei Furukawa for accepting me in his incredible scientific group at the *Institute for Integrated Cell-Material Sciences* in Kyoto. Although this stay was shorter than expected, I have to say that it was the most intense period of my thesis, due to the difficulties caused by the pandemic. Thanks to their hospitality I always felt at home

and learned a lof from their expertise and valuable knowledge in the fabrication of novel materials. I am also very grateful to Melanie Lebental and Clement Lafargue for the stay in Paris at LuMIn (*Laboratory of Light, Matter and Interfaces*) group. I must admit that chemists have so much to learn from physicis. The synergy between researchers from different fields makes research enriching and fruitful, and this stay was a clear example of that. I will always be grateful for everything that I learned in the field of optics.

On the other hand, I would like to thank Jorge Bañuelos, one of the best professors of my Chemistry degree, but above all, the one who has been my mentor since the beginning of my research career. He has always given me very good advice and has helped me whenever I needed it throughout these years. He also gave me the opportunity to work in the *Molecular Spectroscopy Group*, which is how I ended up doing my PhD. In addition, this doctoral thesis would not have been possible without the grant awarded by the *University of the Basque Country (UPV-EHU)*, to which I am deeply grateful.

Furthermore, I could not fail to mention each and every member of our laboratory for always wanting to lend me a hand. It has been a pleasure to work with you all. Eskerrik asko, Leire, Rebeca, Edu, Ruth, Edurne, Carolina, Enrique, Virginia, Teresa, Iñigo eta Hegoi, lanegunetan emandako momentu zoragarriengatik, eta nola ez, irakatsitako guztiagatik. Zalantzarik gabe, lagun oso onak egin ditudalako.

Azkenik, ez dut sarreratxo hau amaitu nahi eskerrak eman gabe bidai luze honetan lagundu didaten lagun guztiei; eta bihotz-bihotzez eskerrik asko beti ondoan izan zaretenoi: atta, ama, ahizpatxo, amama eta Gontzal, nik bezainbeste sufritu eta gozatu duzuelako. Mila esker egunero emandako animo, babes, laguntza eta mimoengatik. Egun txarrak ohartezin eta onak ahaztezin bihurtu dituzuelako, hurrengo lerroak eskaintzen dizkizuet. Maite zaituztet.

This challenging project is a result of a lot of things that I wouldn't be able to express in just one page, because as most of the thesis projects, this has been a real roller coaster. I am not the one that I used to be, and I am very proud of it.

Hope you enjoy the reading. Gozatu irakurketaz!

CONTENTS

LIST OF FIGURES

LIST OF TABLES

ACRONYMS

4-DASPI	Trans-4-[4-(dimethylamino)-styryl]-1-methylpyridinium iodide
AC	Acridine, 9-Azaanthracene
ACO	Acridine orange, N,N,N′,N′-tetramethylacridine-3,6-diamine
ACY	Acridine yellow, 3,6-diamino-2,7-dimethylacridine monohydrochloride
AlPO	Aluminophosphate
B3LYP	Becke, 3-parameter, Lee–Yang–Parr
BBO	Barium borate
BBU	Basic building units
BDP	Bodipy, 4,4-difluoro-4-difluoro-4-bora-3a,4a-diaza-s-indacene
CH	Conventional heating
CT	Charge-transfer
D6R	Double six-membered rings
DABCO	1,4-diazabicyclo[2.2.2]octane
DC	Dication
DFT	Density functional theory
DMA	Dimethylamine
DMAN	1,8-bis(dimethylamino)naphthalene
DMASBT	Trans-2-[4-[(dimethylamino)styryl]benzothiazol
DPA	Dipropylamine
DRA	Diffuse reflectance accessory

EBA	N-Ethylbutylamine
EET	Excitation energy transfer
FAST	Fluorescence analysis software
FRET	Förster resonance energy transfer
FWHM	Full width at half maximun
HOMO	Highest occupied molecular orbital
IC	Internal conversion
ICT	Intramolecular charge-transfer
interCT	Intermolecular charge-transfer
intraCT	Intramolecular charge-transfer
IRF	Instrument response function
ISC	Intersystem crossing
IZA	International Zeolite Association
KDP	Monopotassium phosphate
KTP	Potassium titanyl phosphate
LDS 722	Pyridine 2, 4-[4-[4-(dimethylamino)phenyl]-1,3-butadienyl]-1-ethyl-pyridinium perchlorate
LDS 730	2-[4-[4-(dimethylamino)phenyl]-1,3-butadienyl]-1,3,3-trimethyl-3H-indolium perchlorate
LDS 751	6-(Dimethylamino)-2-[4-[4-(dimethylamino)phenyl]-1,3-butadienyl]-1-ethyl-quinolinium Perchlorate
LE	Locally excited state
LUMO	Lowest unoccupied molecular orbital
MAOPTMS	3-(Trimethoxysilyl)propyl methacrylate
MAPO	Metalloaluminophosphates
MAPSO	Metalloaluminosilicophosphates
MC	Monocation
MCP PMT	Microchannel plate photomultiplier

MEP	Molecular electrostatic potential
MgAPO	Magnesium-doped aluminophosphate
MR	Member ring
MW	Microwave heating
NB	Nile blue
Nd:YAG	Neodymium-doped yttrium aluminium garnet
NIR	Near infrared
NLO	Nonlinear optics
OLED	Organic light-emitting diode
OPO	Optical parametric oscillator
OSDA	Organic structure-directing agents
PICT	Planar intramolecular charge-transfer
PMT	Photomultichannel
PTFE	Polytetrafluoroethylene
PXRD	Powder x-ray diffraction
PY	Pyronine Y, 3,6-Bis(dimethylamino)xanthylium chloride
R123	Rhodamine 123, 3,6-Diamino-9-(2-(methoxycarbonyl)phenyl)xanthylium chloride
RGB	Red green blue
RISC	Reverse intersystem crossing
SAPO	Silicoaluminophosphates
SBU	Secondary building units
SDA	Structure-directing agent
SEM	Scanning electron microscopy
SHG	Second-harmonic generation
SSL	Solid-state lighting

TADF	Thermally activated delayed fluorescence
TCSPC	Time correlated single photon counting
TEA	Triethylamine
TEOS	Tetraethylorthosilicate
TGA	Thermogravimetric analysis
TICT	Twisted intramolecular charge-transfer
TMHD	N,N,N′,N′-tetramethyl-1,6-hexanediamine
TPA	Tripropylamine
UMS	Universal measurement spectrophotometer
UV	Ultraviolet
Vis	Visible
VTES	Triethoxyvinylsilane
wB97XDA	Becke's 97 functional with additional dispersion correction
XRD	X-ray diffraction

1

INTRODUCTION

Light is essential for life. It is recognized as a mixture of colors in the electromagnetic spectrum visible to the human eye. However, light is more than just color and is anything but ordinary. It is energy, traveling at incredible speeds through the universe. Since prehistoric times, humans became aware of its unique properties through fire, and over the centuries the discoveries and breakthroughs in the fields of optics, physics, and chemistry have been numerous (Figure 1.1).[1–9] For example, the discovery of fluorescence in 1845,[10] which led to the development of the first spectrofluorimeter, and the revolutionary invention of the laser in 1960,[11] that opened the door to many practical applications in industry, are two of the most remarkable ones.[12–16]

The discoveries driven by light have been numerous since prehistoric times.

In recent years, the desire for new sophisticated optical properties has generated a growing demand for novel materials capable of fulfilling multiple functions. As a result, new areas of research have emerged, such as the design and development of organic-inorganic hybrid systems, which have greatly expanded the field of materials chemistry.[17–20] These composite materials consist on the combination of organic and inorganic components at the nanometer scale. One of the examples is host-guest hybrid materials, where the characteristics of the hosted molecule are complemented with those of the host material, the matrix, exhibiting superior properties compared to the pure counterparts.[21,22]

Development in organic-inorganic hybrid systems, such as host-guest materials.

In this context, by incorporating molecules of interest into nanostructured matrices, it is possible to develop mul-

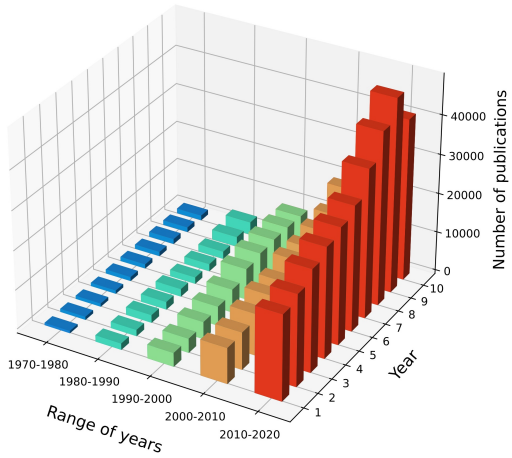

Figure 1.1: The number of publications in the field of optical applications from 1970 to 2020. Source taken from WOS database.

tifunctional solid-state materials with a great variety and versatility in physical and chemical properties.[23,24] In particular, the encapsulation of photoactive species, such as organic dyes, into inorganic porous frameworks of different types and shapes has attracted considerable interest in the design of materials for optical applications, due to the great advantages offered by the combination of both components:[25]

Advantages of the encapsulation of photoactive dyes into inorganic porous frameworks.

i) An enhanced thermal, chemical and mechanical stability is provided to the guest molecules by the protection of rigid inorganic matrices, reinforcing the properties of the chromophores.[23,26] Since the hybrid materials are chemically produced, the photoactive organic dyes are easily entrapped into the forming porous matrix and preserved inside without being destroyed or damaged.[27]

ii) The photoactive guest molecules are accommodated in a constrained and nanoporous environment that allows to modify/control the photophysical properties towards a particular interest, developing materials with very specific and customizable

functionalities.[28,29] It is possible to tightly encapsulate large amounts of emitting molecules while keeping them isolated from each other, decreasing non-radiative pathways and/or quenching phenomena, boosting the photophysical features.[30,31]

Improved properties as a result of the synergism between both components.

In this way, the hybrid material can exhibit new or improved properties as a result of the synergism between the organic and inorganic moieties; where the optical, spectroscopic, and chemical characteristics of the guest molecule are complemented with the structural, mechanical, and thermal properties of the host material. There are a large number of existing host-guest combinations for a wide range of applications of technological interest such as optics and photonics. Some of these applications based on the incorporation of photoactive molecules into solid matrices, pursued in this thesis, are described below:

Aplications of interest in this thesis.

- *Solid-state lasers*

  Dye lasers are based on fluorescent organic compounds usually dissolved in a liquid medium. They exhibit a broad gain bandwidth, offering the possibility to modulate the gain region over a wide range, which makes them highly regarded for industrial applications.[32] The liquid medium is necessary to avoid degradation of the dyes caused by local heat generated during excitation (pumping). In this way, excess heat is removed by flow systems and the lifetime of the organic dyes prolonged. However, this entails a large use and disposal of large volumes of organic solutions, most of them flammable and toxic, as well as great complexity in the assembly and difficult handling of the flow systems.[33–35]

  Drawbacks of liquid dye lasers and solid-state lasers as an alternative.

  Interestingly, solid-state dye lasers offer a promising alternative for the development of compact, inexpensive, versatile, manageable, efficient, and tunable laser sources.[36] Their design is based on the encapsulation of laser dyes into rigid matrices that are transparent

to radiation, homogeneous, and thermally and chemically stable. Their high photostability guarantees a long lifetime of the active laser media with high output powers and low scattering losses. Furthermore, in situations involving large microcrystals with a regular shape, the particles themselves can act as a laser resonator resembling the Fabry-Perot type cavity, providing selective feedback of light to the gain medium and offering a straightforward and simple approach to fabricating a microlaser.[37,38]

NIR systems are very interesting for biomedical imaging.

- *Red and near-infrared (NIR) emissive systems*

  Today, the expansion of lasers, apart from having high output power and conversion efficiency, requires the wavelength range to be tunable. Organic dyes emitting in the 700-1000 nm range of the electromagnetic spectrum allow broadening the tuning range of solid-state dye lasers.[39] Besides, they are very interesting for biomedical imaging due to their ability to minimize background interference from organisms and tissues and improve penetration depth, offering high contrast and high sensitivity in noninvasive fluorescence imaging.[40–42]

Porous inorganic systems can provide rigidity to the organic molecules and boost the fluorescence.

  However, fluorophores that can emit from this low-energy region are often deactivated by other non-radiative deactivation pathways (*e.g.* internal conversion) and suffer from photobleaching and small Stokes shifts.[43,44] Interestingly, the excellent stability of porous inorganic systems can be exploited to provide rigidity to emissive compounds by occluding them within these porous systems. In this way, a restricted environment is generated where the motions of organic molecules are hindered, leading to an increase in fluorescence efficiency in the optical window of interest.

- *Nonlinear optic devices*

  Another efficient way to achieve tunability in solid-state lasers is through systems with nonlinear op-

tical (NLO) response.[45] Indeed, many applications in optics and photonics involving light detection and modulation are based on this phenomenon. Systems with NLO properties are those whose response does not vary linearly with intensity, producing radiation with a different wavelength or phase to the incident beam. These effects are generally limited to high incident power lasers, processes with high-intensity fields involving two or more photons.[46] One of the best-known examples are frequency doubling crystals, which generate the second harmonic (SHG) of the incident radiation, that is, radiation with half the wavelength of the initial one.

How to favor SHG properties and the importance of organic-inorganic systems in this field.

To favor this phenomenon, the structure of the material must be non-centrosymmetric, since systems with randomly distributed molecules and isotropic behavior do not exhibit second NLO properties.[47,48] Furthermore, the constituent molecules of the material must have high hyperpolarizability values, that is, intrinsic nonlinear optical properties from the outset, as is the case, for example, for asymmetric molecules.[49,50] For this reason, in recent years, macroscopic crystals with a specific orientation of molecules with high intrinsic hyperpolarizability within a non-centrosymmetric structure have proven to be perfect candidates to obtain materials with second NLO effects.[51] These materials with high ordering and orientation of molecules can be rationally and easily synthesized by introducing them directly into porous inorganic structures that fit well with the dimensions of the dye.[52]

- *Artificial light-harvesting systems*

  Mimicking the natural process of photosynthesis: capturing light and transferring it to another site.

  Artificial light-harvesting systems that mimic the natural process of photosynthesis through energy transfer processes (typically Förster resonance energy transfer, FRET) provide another feasible approach to tune the emission of a given organic dye.[53] They capture light through absorption of an organic donor

molecule and transfer this energy to an acceptor molecule exciting it indirectly and resulting in a change in the emission wavelength.[54,55] Their main advantage to harvest light, together with the ability to modulate the wavelength of the final emission signal over a wide spectral range, makes them useful for a wide range of applications, such as solar cells, photonic antennas, light modulators, and light-emitting devices.[56–60]

White light emitting devices are very interesting. They are the result of blue, green and red emissions.

Among the light-emitting devices, those with white light emission are very interesting. In these systems, the emission of the entire region of the visible spectrum is collected by recording the simultaneous emission of the blue, green, and red regions of the electromagnetic spectrum (RGB region).[61,62] The strategy for white light generation is based on mixed multicomponent systems that emit in different regions by a partial energy transfer process between donor and acceptor molecules.[63–65] However, the materials must be optically dense for optical applications and organic molecules tend to self-associate under high concentrations, negatively affecting the final fluorescent efficiency.

The co-encapsulation of several organic dyes within inorganic structures promotes FRET processes.

In this context, in the development of artificial light-harvesting systems, co-encapsulation of several chromophores within inorganic structures provides suitable hybrid materials with high dye loadings and thus molecules are close enough to give rise to FRET processes while preventing or even modulating aggregation.[66]

To build up these host-guest optical materials, there are currently a wide variety of inorganic structures available that can provide a suitable environment for the accommodated organic dyes. Nevertheless, it is very important to ensure that they meet the following requirements:[21]

- Good chemical, mechanical, photo, and thermal stability.

- Must be highly transparent throughout the visible range.
- Should not have close interactions with trapped active chromophores.
- Should not interfere (non-radiative pathways) in the photophysical processes of the chromophores.

Requirements to build up host-guest optical materials.

Among all types of inorganic matrices, zeolites (aluminosilicates) are excellent molecular containers for this purpose, which are characterized by their high absorption and ion exchange capacity. The structure of a zeolite is built by three-dimensionally arranged tetrahedrons joined by tetrahedral corners that generate cavities or channels of molecular dimensions. The high thermal stability of these solids together with their open and ordered frameworks and high surface areas make them ideal as molecular sieves.

Zeotypes have been selected, in particular, aluminophosphates, due to their cavities and high stability.

For this reason, in the search for multifunctional materials, this thesis has focused on zeolite-type inorganic frameworks with the main objective of developing dye-loaded materials subjected to photophysical changes. Among them, there are a multitude of zeolites with different pore sizes, shapes, and topologies. In particular, in this work, zeotypes (tetrahedral elements are different from Si and Al) have been selected as hosts, specifically aluminophosphates (AlPO) doped with metals such as magnesium (MgAPO) or silicon (SAPO) because they originate acid centers, and consequently promote the incorporation of cationic dye molecules (illustrative example shown in Figure 1.2).

What it is sought with dye encapsulation.

With the encapsulation of dyes, what is sought, on the one hand, is the protection of guests, reducing their photo- and thermal degradation; and on the other hand, the development of new and/or improved properties from the synergistic combination of both. In this way, the photophysical properties of the dye can be modulated by playing with the size and shape of the pores of the structures.[18,21,67] In addition, most of the structures selected in this thesis have 1D channels, in order to provide a regular and in-line distribu-

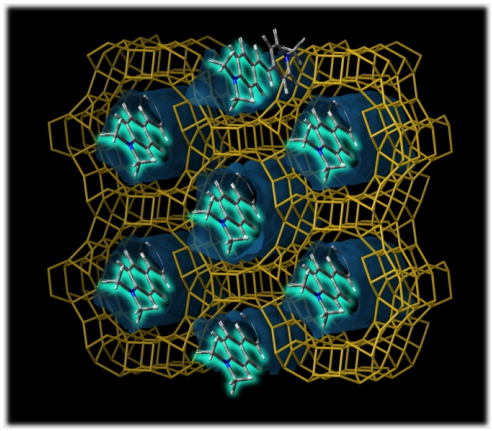

Figure 1.2: An illustrative example of the encapsulation of a chromophore within one-dimensional aluminophosphate channels (IFO).

tion of the dyes along the channels and achieve a hybrid system with important implications in nonlinear optics.[68]

The inclusion of dye molecules is accomplished "in situ" by the crystallization inclusion method.

In this work, the inclusion of the dye molecules in the AlPO cavities is accomplished "in situ" by the *crystallization inclusion* method without applying any post-synthetic diffusional process, allowing a high constraint even in cases where the host framework has a pore size very close to the dimensions of the molecular structure, which it is impossible otherwise. This method avoids traffic jams at the pore entrances, obtaining more homogeneous dye loadings even in large crystals, and avoids subsequent leakage, since the molecules remain hermetically trapped. In addition, it is a one-step process, fast and energetically inexpensive.

Several structures have been combined with a lot of organic dyes.

All in all, several structures with different pore/channel sizes in the range of molecular dimensions have been combined with a wide range of organic dyes, mainly from the styryl and three fused aromatic ring families. The results have been divided into two main chapters in the results part (Part III) of the book:

- Chapter 7 deals mainly with one-dimensional nanochanneled AlPOs (AFI, AEL, ATS type frameworks), which are ideal for providing a preferential

alignment of photoactive guest molecules and controlling their aggregation state. In this way, highly fluorescent and ordered solid systems ideal for new optical devices have been achieved such as near-infrared (NIR) emitters,[28] frequency doublers (SHG), or big crystals with the so-called microlaser action. In addition, a structure with 3D cavities (CHA) is also tested to confer distinct optical properties as a result of a more restricted environment.

The division of the results presented throughout this thesis and the main objectives.

- Chapter 8 also covers unidirectional channeled aluminophosphates (novel extra-large pore IFO and AEL) but with the particular difference of containing several dyes simultaneously occluded into the inorganic matrices. The main goal has been to achieve novel artificial antenna systems involving energy transfer processes (FRET) between the different organic units, with properties such as tunable emission and white light emission.

Throughout this book, the influence of the synthesis parameters on the incorporation of the encapsulated dye molecules within the zeolitic host will be discussed, as well as the effects on the final photophysical properties of the resulting materials. This information will be of great value for producing brand new and advanced materials that expand the range of optical applications.

BIBLIOGRAPHY

(1) Sayili, A. M. The Aristotelian explanation of the rainbow. *Isis* **1939**, *30*, 65–83.

(2) Newton, I., *Opticks*; Prabhat Prakashan: 2021.

(3) Newton, I., *The Optical Papers of Isaac Newton: Volume 1, The Optical Lectures 1670-1672*; Cambridge University Press: 1984; Vol. 1.

(4) Kirchhoff, G In *Annales scientifiques de l'École Normale Supérieure*, 1886; Vol. 3, pp 303–342.

(5) Einstein, A. Über das relativitätsprinzip und die aus demselben gezogene Folgerungen (1907). *The Collected Papers of Albert Einstein: The Swiss Years: Writings* **1900**, *1909*, 252–311.

(6) Einstein, A. On the electrodynamics of moving bodies. *Annalen der physik* **1905**, *17*, 891–921.

(7) Einstein, A. Über einem die Erzeugung und Verwandlung des Lichtes betreffenden heuristischen Gesichtspunkt. *Annalen der physik* **1905**, *4*, 132–148.

(8) Maxwell, J. C. VIII. A dynamical theory of the electromagnetic field. *Philosophical transactions of the Royal Society of London* **1865**, 459–512.

(9) Strehler, B. L.; Arnold, W. Light production by green plants. *The Journal of General Physiology* **1951**, *34*, 809–820.

(10) Herschel, J. F. W. On a case of superficial colour presented by a homogeneous liquid internally colourless. *Philosophical Transactions of the Royal Society of London* **1845**, 143–145.

(11) Maiman, T. H. Stimulated optical radiation in ruby. *Nature* **1960**, 493–494.

(12) Waynant, R. W.; Ilev, I. K.; Gannot, I. Mid–infrared laser applications in medicine and biology. *Philosophical Transactions of the Royal Society of London. Series A: Mathematical, Physical and Engineering Sciences* **2001**, *359*, 635–644.

(13) Partovi, A.; Peale, D.; Wuttig, M.; Murray, C. A.; Zydzik, G.; Hopkins, L.; Baldwin, K.; Hobson, W. S.; Wynn, J.; Lopata, J.; Dhar, L.; Chichester, R.; H-J Yeh, J. High-power laser light source for near-field optics and its application to high-density optical data storage. *Applied Physics Letters* **1999**, *75*, 1515–1517.

(14) Wang, X.; Pang, Y.; Ku, G.; Xie, X.; Stoica, G.; Wang, L. V. Noninvasive laser-induced photoacoustic tomography for structural and functional in vivo imaging of the brain. *Nature biotechnology* **2003**, *21*, 803–806.

(15) Vanwiggeren, G. D.; Roy, R. Communication with chaotic lasers. *Science* **1998**, *279*, 1198–1200.

(16) Strickland, D. T., *Development of an ultrabright laser and an application to multiphoton ionization*; University of Rochester: 1989.

(17) Parola, S.; Julián-López, B.; Carlos, L. D.; Sanchez, C. Optical properties of hybrid organic-inorganic materials and their applications. *Advanced Functional Materials* **2016**, *26*, 6506–6544.

(18) Lebeau, B.; Innocenzi, P. Hybrid materials for optics and photonics. *Chemical Society Reviews* **2011**, *40*, 886–906.

(19) Sanchez, C.; Shea, K.; Kitagawa, S Hybrid materials. *Chem. Soc. Rev* **2011**, *40*, 453–1152.

(20) Férey, G. Hybrid porous solids: past, present, future. *Chemical Society Reviews* **2008**, *37*, 191–214.

(21) Kickelbick, G. In *Hybrid materials: Synthesis, Characterization, and Applications*, Wiley Online Library: 2007; Vol. 1, pp 1–48.

(22) Yang, Q.; Xu, Q.; Jiang, H.-L. Metal–organic frameworks meet metal nanoparticles: synergistic effect for enhanced catalysis. *Chemical Society Reviews* **2017**, *46*, 4774–4808.

(23) Davis, M. E. Ordered porous materials for emerging applications. *Nature,* **2002**, *417*, 813–821.

(24) Calvo, M. E.; Colodrero, S.; Hidalgo, N.; Lozano, G.; López-López, C.; Sanchez-Sobrado, O.; Miguez, H. Porous one dimensional photonic crystals: novel multifunctional materials for environmental and energy applications. *Energy & Environmental Science* **2011**, *4*, 4800–4812.

(25) Martínez, V. M., *Intercalación de rodamina 6G en películas ordenadas de arcilla*; Universidad del País Vasco: 2005.

(26) Brühwiler, D.; Calzaferri, G. Molecular sieves as host materials for supramolecular organization. *Microporous and Mesoporous Materials* **2004**, *72*, 1–23.

(27) Dias Carlos, L. A.; Sá Ferreira, R.; de Zea Bermudez, V. In *Hybrid Materials: Synthesis, Characterization, and Applications*, Wiley Online Library: 2006, pp 337–400.

(28) Oliden-Sánchez, A.; Sola-Llano, R.; López-Arbeloa, I.; Martínez-Martínez, V. Enhancement of NIR emission by a tight confinement of a hemicyanine dye within zeolitic MgAPO-5 nanochannels. *Photochemical & Photobiological Sciences* **2018**, *17*, 917–922.

(29) Martinez-Martinez, V.; Garcia, R.; Gómez-Hortigüela, L.; Sola Llano, R.; Perez-Pariente, J.; Lopez-Arbeloa, I. Highly luminescent and optically switchable hybrid material by one-pot encapsulation of dyes into MgAPO-11 unidirectional nanopores. *ACS Photonics* **2014**, *1*, 205–211.

(30) Li, H.; Zhang, L.; He, H.; Yang, Y.; Cui, Y.; Qian, G. Tunable nonlinear optical responses based on host-guest MOF hybrid materials. *Science China Materials* **2021**, *64*, 698–705.

(31) Alarcos, N.; Cohen, B.; Ziółek, M.; Douhal, A. Photochemistry and photophysics in silica-based materials: ultrafast and single molecule spectroscopy observation. *Chemical reviews,* **2017**, *117*, 13639–13720.

(32) Wei, Y.; Dong, H.; Wei, C.; Zhang, W.; Yan, Y.; Zhao, Y. S. Wavelength-Tunable Microlasers Based on the Encapsulation of Organic Dye in Metal–Organic Frameworks. *Advanced Materials* **2016**, *28*, 7424–7429.

(33) Costela, A.; Cerdán, L.; García-Moreno, I. Solid state dye lasers with scattering feedback. *Progress in Quantum Electronics* **2013**, *37*, 348–382.

(34) Li, Z.; Psaltis, D. Optofluidic dye lasers. *Microfluidics and Nanofluidics* **2008**, *4*, 145–158.

(35) Singh, S.; Kanetkar, V.; Sridhar, G; Muthuswamy, V; Raja, K Solid-state polymeric dye lasers. *Journal of Luminescence* **2003**, *101*, 285–291.

(36) Garcia-Moreno, I.; Costela, A.; Martin, V.; Pintado-Sierra, M.; Sastre, R. Materials for a Reliable Solid-State Dye Laser at the Red Spectral Edge. *Advanced Functional Materials* **2009**, *19*, 2547–2552.

(37) Xu, R.; Zhu, G.; Yin, X.; Wan, X.; Qiu, S. Epitaxial growth of highly-oriented $AlPO_4$-5 molecular sieve films for microlaser systems. *Journal of Materials Chemistry* **2006**, *16*, 2200–2204.

(38) Vietze, U; Krauss, O; Laeri, F; Ihlein, G; Schüth, F; Limburg, B; Abraham, M Zeolite-dye microlasers. *Physical review letters* **1998**, *81*, 4628–4631.

(39) Liu, J. X.; Mei, S. L.; Chen, X. H.; Yao, C. J. Recent Advances of Near-Infrared (NIR) Emissive Metal Complexes Bridged by Ligands with N-and/or O-Donor Sites. *Crystals* **2021**, *11*, 155.

(40) Pansare, V. J.; Hejazi, S.; Faenza, W. J.; Prud'homme, R. K. Review of long-wavelength optical and NIR imaging materials: contrast agents, fluorophores, and multifunctional nano carriers. *Chemistry of materials* **2012**, *24*, 812–827.

(41) Li, L.; Dong, X.; Li, J.; Wei, J. A short review on NIR-II organic small molecule dyes. *Dyes and Pigments* **2020**, *183*, 108756.

(42) Du, Y.; Liu, X.; Zhu, S. Near-infrared-II cyanine/polymethine dyes, current state and perspective. *Frontiers in Chemistry* **2021**, *9*, 718709.

(43) Escobedo, J. O.; Rusin, O.; Lim, S.; Strongin, R. M. NIR dyes for bioimaging applications. *Current opinion in chemical biology* **2010**, *14*, 64–70.

(44) Kim, K. H.; Singha, S.; Jun, Y. W.; Reo, Y. J.; Kim, H. R.; Ryu, H. G.; Bhunia, S.; Ahn, K. H. Far-red/near-infrared emitting, two-photon absorbing, and bio-stable amino-Si-pyronin dyes. *Chemical science* **2019**, *10*, 9028–9037.

(45) Yao, J.; Wang, Y., *Nonlinear optics and solid-state lasers: advanced concepts, tuning-fundamentals and applications*; Springer: 2012; Vol. 164.

(46) Franson, J.; Pittman, T. In *Summaries of Papers Presented at the International Quantum Electronics Conference*, 1998, pp 90–91.

(47) Suresh, S; Ramanand, A; Jayaraman, D; Mani, P Review on theoretical aspect of nonlinear optics. *Reviews on Advanced Materials Science*, **2012**, *30*, 175–183.

(48) Soljačić, M.; Ibanescu, M.; Johnson, S. G.; Fink, Y.; Joannopoulos, J. D. Optimal bistable switching in nonlinear photonic crystals. *Physical Review E* **2002**, *66*, 055601.

(49) He, G. S.; Tan, L. S.; Zheng, Q.; Prasad, P. N. Multiphoton absorbing materials: molecular designs, characterizations, and applications. *Chemical reviews* **2008**, *108*, 1245–1330.

(50) Lou, A. J. T.; Marks, T. J. A twist on nonlinear optics: understanding the unique response of π-twisted chromophores. *Accounts of chemical research* **2019**, *52*, 1428–1438.

(51) Shi, R.; Han, X.; Xu, J.; Bu, X. H. Crystalline Porous Materials for Nonlinear Optics. *Small* **2021**, *17*, 2006416.

(52) Sola-Llano, R.; Martínez-Martínez, V.; Fujita, Y.; Gómez-Hortigüela, L.; Alfayate, A.; Uji-i, H.; Fron, E.; Pérez-Pariente, J.; López-Arbeloa, I. Formation of a nonlinear optical host–guest hybrid material by tight confinement of LDS 722 into aluminophosphate 1D nanochannels. *Chemistry–A European Journal,* **2016**, *22*, 15700–15711.

(53) Scholes, G. D.; Fleming, G. R.; Olaya-Castro, A.; Van Grondelle, R. Lessons from nature about solar light harvesting. *Nature chemistry* **2011**, *3*, 763–774.

(54) Gust, D.; Moore, T. A.; Moore, A. L. Mimicking photosynthetic solar energy transduction. *Accounts of Chemical Research* **2001**, *34*, 40–48.

(55) El-Khouly, M. E.; El-Mohsnawy, E.; Fukuzumi, S. Solar energy conversion: From natural to artificial photosynthesis. *Journal of photochemistry and photobiology C: Photochemistry Reviews* **2017**, *31*, 36–83.

(56) Calzaferri, G.; Li, H.; Brühwiler, D. Dye-modified nanochannel materials for photoelectronic and optical devices. *Chemistry–A European Journal* **2008**, *14*, 7442–7449.

(57) Huang, Y.; Qiu, F.; Chen, R.; Yan, D.; Zhu, X. Fluorescence resonance energy transfer-based drug delivery systems for enhanced photodynamic therapy. *Journal of Materials Chemistry B* **2020**, *8*, 3772–3788.

(58) Stanisavljevic, M.; Krizkova, S.; Vaculovicova, M.; Kizek, R.; Adam, V. Quantum dots-fluorescence resonance energy transfer-based nanosensors and their application. *Biosensors and Bioelectronics* **2015**, *74*, 562–574.

(59) Anand, V.; Dhamodharan, R. White light emission from fluorene-EDOT and phenothiazine-hydroquinone based D–π–A conjugated systems in solution, gel and film forms. *New Journal of Chemistry* **2017**, *41*, 9741–9751.

(60) Calzaferri, G. Nanochannels: Hosts for the supramolecular organization of molecules and complexes. *Langmuir* **2012**, *28*, 6216–6231.

(61) Wen, Y.; Sheng, T.; Zhu, X.; Zhuo, C.; Su, S.; Li, H.; Hu, S.; Zhu, Q.-L.; Wu, X. Introduction of red-green-blue fluorescent dyes into a metal–organic framework for tunable white light emission. *Advanced Materials* **2017**, *29*, 1700778.

(62) Maiti, D. K.; Roy, S.; Baral, A.; Banerjee, A. A fluorescent gold-cluster containing a new three-component system for white light emission through a cascade of energy transfer. *Journal of Materials Chemistry C* **2014**, *2*, 6574–6581.

(63) Vijayakumar, C.; Praveen, V. K.; Ajayaghosh, A. RGB emission through controlled donor self-assembly and modulation of excitation energy transfer: A novel strategy to white-light-emitting organogels. *Advanced materials* **2009**, *21*, 2059–2063.

(64) Denißen, M.; Hannen, R.; Itskalov, D.; Biesen, L.; Nirmalananthan-Budau, N.; Hoffmann, K.; Reiss, G. J.; Resch-Genger, U.; Müller, T. J. One-pot synthesis of a white-light emissive bichromophore operated by aggregation-induced dual emission (AIDE) and partial energy transfer. *Chemical Communications* **2020**, *56*, 7407–7410.

(65) Rao, K. V.; Datta, K.; Eswaramoorthy, M.; George, S. J. Highly Pure Solid-State White-Light Emission from Solution-Processable Soft-Hybrids. *Advanced Materials* **2013**, *25*, 1713–1718.

(66) Sola-Llano, R.; Fujita, Y.; Gómez-Hortigüela, L.; Alfayate, A.; Uji-i, H.; Fron, E.; Toyouchi, S.; Pérez-Pariente, J.; López-Arbeloa, I.; Martínez-Martínez, V. One-directional antenna systems: Energy transfer from monomers to J-Aggregates within 1D nanoporous aluminophosphates. *Acs Photonics* **2017**, *5*, 151–157.

(67) Nicole, L.; Laberty-Robert, C.; Rozes, L.; Sanchez, C. Hybrid materials science: a promised land for the integrative design of multifunctional materials. *Nanoscale* **2014**, *6*, 6267–6292.

(68) García, R.; Martínez-Martínez, V.; Gómez-Hortigüela, L.; Arbeloa, Í. L.; Pérez-Pariente, J. Anisotropic fluorescence materials: Effect of the synthesis conditions over the incorporation, alignment and aggregation of Pyronine Y within MgAPO-5. *Microporous and mesoporous materials,* **2013**, *172*, 190–199.

Part I

FUNDAMENTALS

The main goal of this chapter is, on the one hand, to provide an introduction to zeotypic materials, learn about their origin and their physical and chemical characteristics; and on the other hand, to recall the basic principles of photophysics, which are fundamental to understand the analysis in Part III of the results.

First, Chapter 2 will deal with inorganic host systems. In this chapter, the history of zeolites will be presented, but special emphasis will be given to zeotypes, in particular to aluminophosphates, giving explanations on the isomorphic substitution necessary to obtain these molecular sieves. Next, some of the ways to classify these aluminophosphates will be explained and, finally, the chapter will end with the selection of the different porous materials for the incorporation of the dyes. It is important to note that the selection of the porous structures is not arbitrary and that they have been chosen after a thorough study.

After, in Chapter 3 all photophysical processes important for the comprehension of the results will be fully described, taking into account the main unimolecular and bimolecular processes that can occur in organic chromophores. Furthermore, since nonlinear optical properties (NLO) have been observed in the resulting hybrid systems and these are closely related to the anisotropy of the medium, the most important points of polarized spectroscopy will be described, as well as the main NLO phenomenon (*i.e.* second-harmonic generation) detected in our systems. On the other hand, an explanation of microlaser action will also be given, since stimulated emission processes have been observed in some of the systems operating as microcavities. Finally, the chapter will conclude with a brief review of the photophysical properties of the dyes, and will explain the pursued effects on their final optical properties through their incorporation into the inorganic host structures.

The intention has been to explain in simple terms the theoretical foundations, without going into complex equations. For a more detailed explanation, the reader is referred to more specialized books.[1–4]

2

HOST SYSTEMS

Zeolites were first discovered in 1756 by a Swedish chemist, Axel Fredrick Cronstedt, when he realized that during the heating of a new type of mineral (stilbite, Figure 2.1), moisture appeared on its surface. Besides that, he also found that the process was reversible, rendering a hydrated mineral when cooled again,[5] enabling successive hydration-dehydration cycles.[6] For that reason, etymologically, the term zeolite is derived from the Greek word *zeos*, meaning to boil, and *lithos*, meaning stone: stone that boils.

Figure 2.1: Stilbite mineral.

Today, the term zeolite is used for the entire family of minerals with properties similar to those of the stilbite. However, this is a very broad definition of zeolites and nowadays, they are defined as microporous crystalline oxides, typically composed of silicon, oxygen, and aluminum, with cavities interconnected by smaller windows. Structurally, zeolites are composed of alternating AlO_4 and SiO_4 tetrahedra, each of them linked by a corner-sharing oxygen atom (see Figure 2.2).

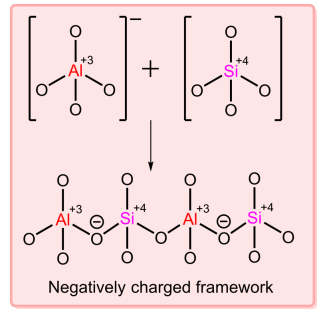

Figure 2.2: General scheme of the formation of the aluminosilicate network.

The arrangement obtained in the space by the connection of 4-corner TO_4 (being T Al or Si) gives rise to periodically arranged three-dimensional (3D) structures with pores and cavities of molecular dimensions, typically from 0.3 to 2 nm in diameter, which are usually occupied by cations and water molecules.[7] In the network, the replacement of Si (IV) by Al (III) in alternating tetrahedrons induces a negative charge. Therefore, there is a need to stabilize the structure through charge balancing using cations (inorganic/organic cations).

2.1 ZEOTYPES: ALUMINOPHOSPHATES

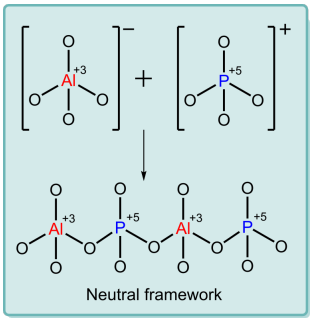

Figure 2.3: General shceme of the formation of the aluminophosphate network.

Initially, zeolites were composed exclusively of aluminosilicates, which implied, as explained above, that the tetrahedra contained only silicon or aluminum. However, in zeolitic lattices, both elements can be replaced by many others of the periodic system, which are also capable of forming tetrahedral oxide lattices. When the tetrahedral elements of the zeolitic structure are other than silicon and aluminum, the materials are called zeotypes. The incorporation of these elements allows not only the discovery of new structures but also expands their use in many fields such as catalysis, adsorption and ion exchange.[8,9]

Within the zeotypes, microporous materials based on aluminophosphates (phosphate oxides denoted as $AlPO_4$-n, where n refers to the specific crystallographic structure; see the network in Figure 2.3) are particularly relevant, both because of their abundance (wide range of pore morphology) and their broad versatility for applications.. The first aluminophosphate type material was synthesized by Wilson and co-workers in 1982 and was named $AlPO_4-5$ (for simplicity the subscript 4 is usually omitted and it is directly named AlPO-5). In these structures, the microporous network is formed by strictly alternating aluminum and phosphorus tetrahedra (Figure 2.3), according to Lowenstein's restriction rule.[10] In contrast to zeolites, the negative charge associated with the aluminum oxide tetrahedron is balanced by positively charged phosphate oxide, resulting in a final neutral lattice.

Most zeolitic structures are made of basic (BBU) and secondary (SBU) building units.

Specifically, most zeolitic structures are made of two building units: TO_4-type tetrahedra (AlO_4 and SiO_4 in zeolites; AlO_4 and PO_4 in aluminophosphates) are the basic building units (BBU) of the material, which are assembled into secondary building Units (SBU). The latter can range from single or double rings to polyhedra such as cubes or hexagonal prisms, or even more complex ones, such as cubo-octahedra.

The final structure of the material will consist of the assembly of these secondary building units, either by linking

a single SBU with other analogous SBUs or by combining different building units. Figure 2.4 shows the process of the structure formation of the Chabazite (AlPO-34), leading from the primary building units (the TO_4 tetrahedra) to the final microporous structure. In the structure drawing, note that only the positions of the T atoms are shown and the T-O-T bridges are represented by straight lines. Thus, depending on the stacking sequences that different microporous networks have in common, it is possible to establish a structural relationship between zeolites and group them into families according to their construction elements.

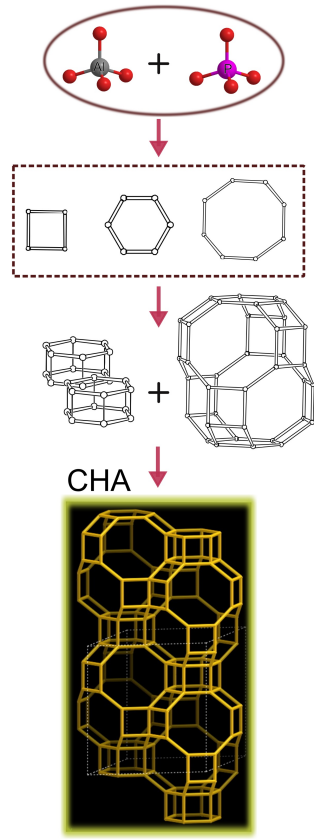

Figure 2.4: Schematic diagram of the formation of Chabazite from primary and secondary building units (BBU and SBU, respectively). Each vertex is designated to a TO_4 tetrahedron where T is Al or P and the T-O-T bridges are represented by straight lines.

2.2 ISOMORPHIC SUBSTITUTION

Two years after the first synthesis of microporous aluminophosphates, in 1984, Lok and co-workers added silicon to the $AlPO_4$ network, discovering a new family of materials called silicoaluminophosphates (SAPO).[11,12] Shortly afterward, in 1985, Messina and co-workers obtained a series of metalloaluminophosphates that they named MAPO, which besides phosphorus and aluminum, contained a third element corresponding to a metal cation M in their structure.[13] Since then, a multitude of different metallic elements have been introduced into the $AlPO_4$ networks in different proportions and combinations, such as magnesium, chromium, manganese, cobalt, and many others; and even substitutions with some metal and silicon, giving rise to new materials called MAPSO.[14]

It is now well documented that phosphate-based materials are capable of taking high concentrations of metals, which is more difficult and rarely observed in aluminosilicate networks. Theoretical calculations suggest that the bonding in aluminophosphates is ionic rather than semicovalent as observed in aluminosilicates. This ionic bonding nature is responsible for the lower stability of microporous AlPO compared to aluminosilicates; however, it allows a greater inclusion of metal ions such as magnesium by isomorphic substitution. This process consists of the re-

placement of an element in a crystal lattice by a metal heteroatom with similar cationic radius and coordination properties, in such a way that it can be incorporated in the same position of the substituted element. It is especially important in aluminophosphates, since it is the origin of the formation of the acid centers, an essential characteristic for their use in applications related to catalytic processes.

Isomorphic substitution rules and different possible mechanisms.

The isomorphic substitution is mainly governed by the oxidation state of the cations that are present in the inorganic lattice. In the case of $AlPO_4$, the presence of two substitutable cations (Al^{3+} and P^{5+}) allows a great versatility regarding isomorphic substitution, being able to incorporate di-, tri- or tetravalent cations in different positions. As a result, it is possible to introduce different metallic elements by substituting aluminum with divalent or trivalent metals, such as magnesium, chromium, manganese, cobalt, iron, nickel, etc.; or phosphorus with tetravalent ones, such as germanium, silicon, titanium, vanadium, etc.

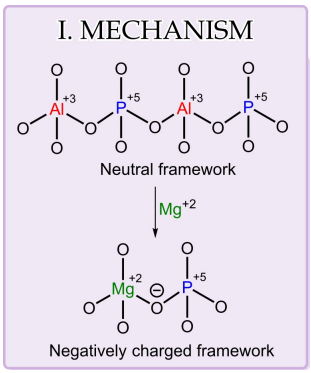

Figure 2.5: Incorporation mechanism of magnesium into $AlPO_4$ framework.

Therefore, to incorporate other elements into the $AlPO_4$ framework, either Al or P (or even both) have to undergo partial or complete substitution. The structural chemical rules that govern isomorphic substitution in $AlPO_4$ lattices were first suggested by Flanigen,[13] and shortly thereafter three isomorphic substitutions mechanisms were proposed by Martens and co-workers.[15] Since oxide networks are electronegative (capable of stabilizing negative charges, but not positive charges) and to ensure that the $AlPO_4$ network has no positive charge or, on the contrary, a high net negative charge, the mechanisms proposed were the followings:[16]

i) Al atoms can be substituted by divalent metals (such as Mg) and trivalent elements, which in turn are bonded to phosphorus through corner-sharing oxygen atoms (Figure 2.5).

ii) P atoms can be substituted by tetravalent (*e.g.* Si) and pentavalent elements (Figure 2.6).

iii) Adjacent Al (III) and P (V) can be simultaneously substituted by two silicon atoms (Figure 2.6).

In the case of the substitution of aluminum by a divalent element (I. mechanism, Figure 2.5), a negative charge is generated in the network . These materials are referred to as metal aluminophosphates (MAPO-n). Likewise, silicon atoms can be incorporated in phosphorus positions, generating also a negative charge for each silicon atom (II. mechanism, Figure 2.6).[17] However, the case of Si is somewhat peculiar since two silicon atoms can be incorporated through another mechanism by substituting a phosphorus and an aluminum atom adjacent to each other, generating a neutral lattice (see Figure 2.6). This simultaneous substitution generates what is known as a "silicon island" whose network is comprised of Si-O-Si bridges. It may also happen that some of these silicon atoms of the "silicon islands" are substituted by aluminum, generating a charge difference in the lattice.[18]

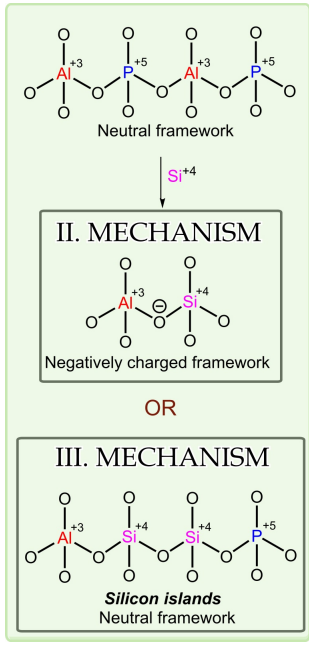

Figure 2.6: Different incorporation mechanisms of silicon.

However, in general, substitution in SAPO materials ($AlPO_4$ material substituted by silicon) occurs by a combination of both substitution mechanisms (II and III), always avoiding the formation of unstable Si-O-P bonds, and generating different types of silicon environments depending on the type of substitution and the proportion of silicon incorporated into the network (low silicon contents give rise to the II mechanism while high proportions produce the incorporation of silicon by both mechanisms, Figure 2.6).

SAPO and MgAPO structres have been chosen to promote negative charge and facilitate the incoroporation of cationic dye molecules.

In the present case, special emphasis is given to the description of SAPO and MgAPO structures since all the materials presented in this thesis belong to the aluminophosphate type doped with Mg or Si. In particular, inorganic hosts with a net negative charge have been selected to facilitate the incorporation of cationic guest dyes (selected dyes are explained in Section 3.6 and the incorporation process in Chapter 4) by electrostatic interactions. For this purpose, different inorganic precursors will be used (more details in Chapter 4) in order to promote a negative charge into the phosphate-based networks. It is important to note that although special emphasis has been given to Mg- and Si-

doped materials, all the mentioned mechanisms and rules can be applied in the same way for other substituent metals.

2.3 CLASSIFICATION OF ALUMINOPHOSPHATES

Because of the numerous possible arrangements that make up zeolitic networks and the progress made in the synthesis mechanism, more than 220 zeolitic structures have been reported so far.[19,20] Furthermore, they can exhibit a variety of compositions which expands the range of their potential applications, traditionally known in the fields of catalysis and molecular sieving, but which have also broken into the field of optics or electronics due to the interesting features that zeotypes offer as host.[21,22] To classify such a large number of existing structures, there are several approaches. Some of these possible ways of grouping them will be discussed in the following paragraphs.

Zeotypes are represented by a code of three capital letters.

Overall, the classification of zeotypes is based on the topology and symmetry of their unit cells, with each structure type symbolized by a code of three capital letters given by the *International Zeolite Association* (IZA) *Structure Commission*,[20] *e.g.* AFI for the structural type of $AlPO_5$ or CHA for chabazite. These codes do not include numbers and characters other than capital Roman letters. For example, AFI comes from **a**luminophosphate **fi**ve and CHA from the first three letters of the framework type, **Cha**bazite. A list of the currently accepted structure types with all their properties can be found in the Atlas of Zeolite Structure Types and on the web of the IZA Commission.[19,20]

Classification according the pore size and the number of tetrahedra forming the window openings.

A typical classification of zeolitic structures is based on the pore size, geometry, and connectivity between the channels of the network.[23] Four different categories can be distinguished depending on the number of tetrahedra forming the window openings to the channel system (usually depicted as the number of tetrahedra followed by MR, which means member ring):[7]

- *Small pore materials*, with 8 MR windows and a diameter from 3 to 5 Å.

- *Medium pore materials*, with 10 MR windows and a diameter from 5 to 6 Å.
- *Large pore materials*, with 12 MR windows and a diameter from 6 to 9 Å.
- *Extra-large pore frameworks*, with windows bigger than 12 MR and a diameter greater than 9 Å.

In some cases, even if the channel is delimited by the same number of tetrahedra, the shape may vary between circular channels, elliptical channels, channels with side pockets, etc. Likewise, these channels that make up the structures can be arranged in one, two or all three directions of space, giving rise to mono-, bi-, or tridirectional channel systems, respectively.[17]

They can also be classified by their density.

Another way of categorizing these microporous framework materials is by their framework density (or tetrahedral density), which can be expressed by the number of tetrahedra (TO_4) per 1000 Å. The tetrahedral density is indicative of the porosity of the structures, decreasing as the volume portion of the voids (porosity) increases.

In this memory, the most interesting ways to classify zeolites have been considered in order to study our hybrid systems. However, there are other additional ways that will not be discussed here.

2.4 SELECTED ALUMINOPHOSPHATES

The reason why aluminophosphates have been selected and the main objective of this work.

The porous materials presented in this thesis and discussed below were selected after extensive research, carried out on the basis of providing a suitable medium for the dispersion of the photoactive molecule. They must be optically inert materials, with high mechanical and thermal stability and similar to the molecular dimensions of the incorporated dyes. With this environmental rigidity, on the one hand, the aim is to induce a constrained environment for the fluorophore to limit its molecular movement, avoiding the formation of non-fluorescent aggregates (Section 3.2.1); and, in the case of unidirectional porous materials, on the

other hand, to induce a preferential orientation of the dye, giving rise to highly ordered materials.

Therefore, in this thesis different commercial dyes were tested on several aluminophosphate doped hosts with different heteroatoms (Si and Mg), to trigger enhanced photophysical properties. In this section, we will focus only on the description of the aluminophosphate hosts and the main properties related to the selected dyes will be described in the next chapter (Section 3.6), although the synthesis is performed in a single step by synthesizing the structure and at the same time encapsulating the dye inside the cavities (mechanism in Chapter 4).

The selected aluminophosphates are divided into two groups.

All the aluminophosphates employed will be described by their topology, especially by the type of polyhedra that forms their cavities. In total, five different structures were synthesized with different combinations of occluded dyes, obtaining a wide range of photoactive hybrid materials (dye guest-host aluminophosphates). In this work, we will distinguish these structures into two main blocks; on the one hand, there will be frameworks already known and previously studied in the laboratory, and on the other hand, other very interesting new structures that will bring into play different dimensionalities and pore cavities.

Summary of each aluminophoshpate host.

In the next paragraphs, a brief summary of each host aluminophosphate will be given highlighting the most important aspects of each molecular sieve. More detailed information can be found in the hosts database in Appendix A, where the data sheets of each AlPO have been included with all their structural properties (general and specific properties: name explanation, unit cell, density...) and illustrative 3D figures. Importantly, a list of all the dye-loaded aluminophosphate systems synthesized throughout this thesis is included for each particular structure.

AFI, ATS and AEL unidirectional nanochanneled structures.

To begin with, AFI, ATS, and AEL structures with unidirectional nanochannels were chosen to study the effect of channel dimensions on the photophysical properties of occluded dyes (results in Chapter 7).[24] The three structures are illustrated in Figure 2.7.

To synthesize of these host systems, generally, linear amines are used as structure-directing agents (SDA). These organic molecules assist in structure formation and act as templates; and will finally reside within the intracrystalline voids. Their role is crucial since they preferentially stabilize one phase over all possible structures that could be formed depending on the metastability of the zeolites in the reaction medium. Therefore, to obtain each of the structures detailed below (the step-by-step procedure is detailed in Chapter 4), different structure-directing agents need to be used. However, it is unusual to find a unique relationship between the SDA and the zeotype to be produced, which means that sometimes more than one SDA can be used for the formation of a specific structure, or that even a single SDA can drive the formation of more than one structure.

The AFI structure is a prime example of this. The AFI framework (Figure 2.7a) is classified as a large pore material formed by straight and cylindrical unidirectional channels of 12 MR (types of classification in Section 2.3) and whose diameter is 7.3 Å. It is a highly stable microporous structure that can be obtained with a great diversity of organic molecules as templates; there is no specific template for its preparation. In our case, despite the wide range of possibilities, only triethylamine (TEA) was used and the structure was doped with different heteroatoms to yield the SAPO-5 and MgAPO-5 structures.

In the case of the mesoporous aluminophosphate ATS structure, it was doped with magnesium (MgAPO-36). This structure is formed by unidirectional channels of 12 tetrahedra, but elliptical instead of cylindrical like those of the AFI structure, rendering a pore size of 6.5 Å x 7.5 Å (Figure 2.7b). This structure is commonly synthesized using tripropylamine (TPA) as SDA.

Regarding materials with AEL framework structure, it was demonstrated in previous work done by the group that the 1D MgAPO-11 acts as a perfect host for the incorporation of many commercial dyes due to the tight fit achieved between the dye molecular dimensions and the framework pore size. The opening windows of the channels are built

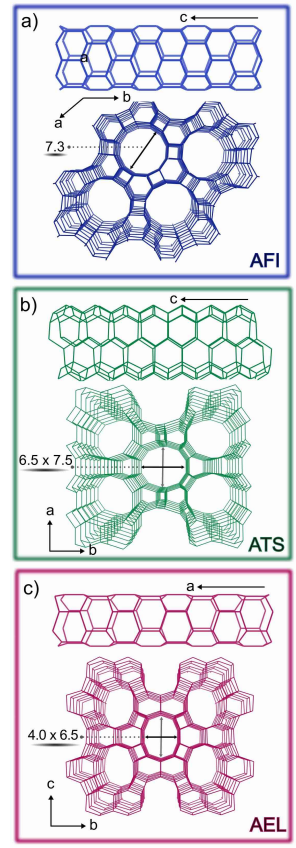

Figure 2.7: **(a)** AFI, **(b)** ATS, **(c)** AEL type structures, represented with a side view of their channels (upper part of the frame). The dimensions of the channels are given in amstrongs.

of 10 rings, in which the cavities do not intersect and have dimensions of 6.5 × 4 Å. Hence, in this thesis, other different commercial dyes were tested in the same magnesium doped aluminophosphate, and for that ethylbuthylamine (EBA) and dipropylamine (DPA) were tested as templates, with the aim of achieving a final pure phase. Overall, the three structures mentioned so far have a very similar periodic arrangement structure with channel walls covered by other fused ring channels of 4 and 6 tetrahedra (Figure 2.7) but can be easily differentiated by their different pore sizes.

CHA structure with cage pockets.

Among the new structures synthesized for the first time in our group and to be presented in this thesis are CHA with 3D-connected cage systems instead of 1D- channels, and IFO framework, with unidimensional extra-large pores of 16 MR.

The chabazite (CHA structure code) is included in the ABC-6 family of zeolites.[25–27] The periodic building unit in the ABC-6 family of framework types consists of a hexagonal array of non-connected planar double six rings, which are related by pure translations along *a* and *b* axes (Figure 2.8). Within this family, CHA is one of the most widespread natural zeolites and was one of the first zeolites to be studied (structure discovered in 1958).[28] Its lattice consists of a parallel stacking of double six-membered rings (D6R) in ABC sequence order (each letter represents a different position of the six-membered ring around the stacking direction parallel to the z-axis), which are linked by inclined 4-membered rings.

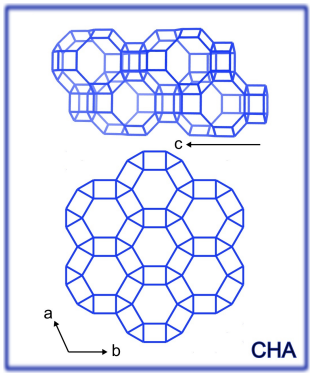

Figure 2.8: Chabazite (CHA) type structure with a view of its cages (top).

A schematic representation of the CHA structure is shown in Figure 2.8. The resulting cavity is a three-dimensional channel system, with confined cages formed by 3.8 Å x 3.8 Å double six-ring apertures (D6R), opening into large 6.7 Å x 10.0 Å ellipsoidal cavities[29] formed by 8-membered rings (small pore materials, Section 2.3) inside with a longitudinal distance of 11.7 Å. This framework was obtained doped with magnesium, denominated as MgAPO-34, and using TEA as a template.

IFO extra-large pore novel structure.

The last novel structure, called either IFO or ITQ-51 (Figure 2.9), presents extra-large 16-ring pores (approx. 9-

10 Å) in its crystalline structure. It has been discovered very recently, in 2013, and its structure is very similar to those of the AFI, AEL, and ATS. It contains one-directional nanochannels but with the difference of having very big opening windows. To obtain this extra-large pore network, bulky and rigid organic molecules as structure-directing agents (OSDA) are required. Particularly, DMAN (1,8-bis(dimethylamino) naphthalene) has been used as a template, already proven as a successful SDA for the crystallization of this structure.[30] However, due to the aromatic nature of the template it must be taken into account that it can interfere with the resulting photophysical properties, and for that reason, an exhaustive photophysical analysis is also described later in Section 8.1.1.

Since this thesis aims to study the final optical properties of the resulting hybrid systems, as well as the main photophysical properties of the invited organic chromophores, the following chapter will focus on the understanding of all these properties and processes.

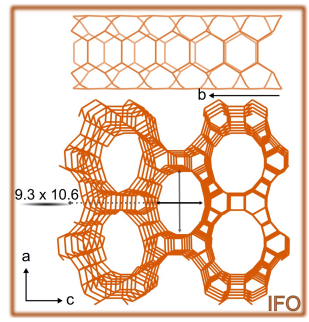

Figure 2.9: IFO type structure with a view of its channels (top). The dimensions of the nanochannels are given in amstrongs.

3

BASIC PRINCIPLES OF PHOTOPHYSICS

This chapter will lay the foundations of the main photophysical processes that can occur after the absorption of UV-Visible radiation, involving transitions between electronic states of molecules. First, the different pathways that a molecule can undergo to dissipate the excess of energy obtained by absorption will be explained. These can be classified into two main groups: unimolecular processes, in which a single molecule is involved, and bimolecular processes when there are interactions with more than one molecule in the ground or excited state.

The main unimolecular processes that will be covered in this thesis.

The main unimolecular processes that will be covered are absorption, internal conversion, fluorescence, and the intersystem crossing; and as part of the latter, phosphorescence and delayed fluorescence will be discussed. Regarding the processes involving interactions with other molecules, processes that can occur both in the ground state (molecular aggregation) and in the excited state (excimer, exciplex formation, or energy transfer processes) will be detailed.

The basics of spectroscopy with polarized light and other phenomena will be explained.

Next, in order to understand the anisotropic light response of the systems covered in this thesis, the basics of spectroscopy with polarized light will be introduced, and the specific optical phenomena obtained in our systems will be described: on the one hand, there are nonlinear phenomena such as second-harmonic generation (SHG); and on the other hand, the so-called microlaser action. At the end of this section, the description of the dye structures and their

main photophysical features, as well as the potential optical properties pursued into the hybrid systems will be detailed.

3.1 UNIMOLECULAR PROCESSES

The electronic states and transitions of a molecule are explained by the Jablonski diagram.

The electronic states of a molecule and the transitions that occur between those states are illustrated schematically with the classical Jablonski energy diagram (Figure 3.1), proposed by the Polish physicist Aleksander Jablónski, who devoted his life to the study of molecular spectroscopy and photophysics.[31]

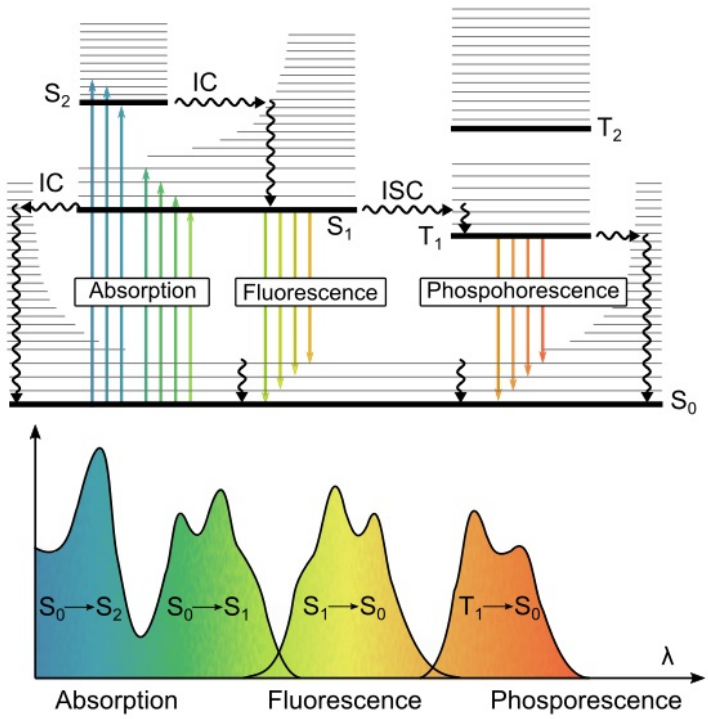

Figure 3.1: Jablonski diagram and illustration of the relative positions of absorption, fluorescence and phosphoresce as a function of wavelength or energy (the representation of the bands shows the displacement between them, but they are not real, the positions of the bands depend on the characteristic of each molecule). IC and ISC denote internal conversion and intersystem crossing, respectively. Adapted from literature.[1]

Explanation of the Jablonski diagram.

The electronic states are grouped vertically according to their relative energy and horizontally according to spin multiplicity. Bold horizontal lines represent the lower vibrational states (v = 0) of each electronic level, while the higher vibrational states (v = 1, 2, 3...) are indicated by thin lines. In general, due to the enormous number of possible vibrations in a molecule and for clarity, only some of the vibrational eigenstates are represented. Transitions are depicted by the use of straight and curved lines, indicating radiative and non-radiative transition pathways, respectively. The singlet electronic states are denoted by S_0 (fundamental electronic state), S_1, S_2, etc.; whereas the triplet states are called T_1, T_2...

3.1.1 *Excitation*

Franck-Condon principle.

When a fluorophore absorbs light, the energy of the photon is transferred to the molecule and an electron from this molecule undergoes a transition from the ground state (lowest electronic state) to a state of higher energy (S_1, S_2...). This transition is very fast (10^{-15} s, Table 3.1) and follows the Franck-Condon principle.[1] According to this principle, as the mass of the nucleus is much higher than the mass of the electron, there is no time for significant displacement of nuclei.[2] The resulting transition is vertical and that is how they are depicted in the Jablonski diagram (Figure 3.1).

Usually broad absorption and emission bands due to multiple vibrational levels.

However, it must be taken into account that most fluorescent molecules have broad absorption and emission bands, which means that each electronic state involves multiple vibrational levels as shown in Figure 3.1. It should also be noted that this diagram assumes that the excited and ground state geometries and their respective electron densities are the same, although this is not always true. Changes in geometry or charge distribution in the excited state often cause the absorption and emission spectra not to be mirror images (experimentally proven in Part III).[1]

Table 3.1: Characteristic time scales for each type of transition.[1]

Transition	Time Scale (s)	Process Type
Absorption	10^{-15}	-
Internal Conversion	10^{-11}-10^{-9}	Non-radiative
Vibrational Relaxation	10^{-12}-10^{-10}	Non-radiative
Fluorescence	10^{-10}-10^{-7}	Radiative
Intersystem Crossing	10^{-10}-10^{-8}	Non-radiative
Phosphorescence	10^{-6}-10	Radiative

Characterization of light absorption.

The characterization of the light absorption of a compound at a given wavelength (λ) is done by its absorbance A or transmittance T by the following equations:

$$A(\lambda) = \log \frac{I_\lambda^0}{I_\lambda} = -\log T(\lambda) \tag{3.1}$$

$$T(\lambda) = \frac{I_\lambda}{I_\lambda^0} \tag{3.2}$$

where $I^\lambda{}_0$ and I_λ are the light intensities when the beam enters and leaves the absorbing medium, respectively. The transmittance is defined as the ratio of intensities of transmitted to incident light.

Beer-Lambert law.

In most cases, there is a linear relationship between the concentration and the absorbance of the solution, known as the Beer-Lambert law:

$$A(\lambda) = \log \frac{I_\lambda^0}{I_\lambda} = \varepsilon(\lambda)\, lc \tag{3.3}$$

where ε is the molar absorption coefficient (expressed in $L \cdot mol^{-1} \cdot cm^{-1}$), c is the concentration ($mol \cdot L^{-1}$) of the absorbing species, and l is the optical path length (cm).[1]

However, for solid samples instead of measuring the absorption, reflectance is used. Diffuse reflectance occurs in all directions as a result of refraction, reflection, absorption, and scattering processes on rough surfaces. The reflectance of a powder sample is the ratio of intensities of reflected and incident light:

$$R_\infty = \frac{J}{I_0} \tag{3.4}$$

Where R_∞ is absolute reflectance and J is the intensity of the reflected radiation. The infinity symbol denotes that the sample is very thick. For simplicity, the measurements are carried out in relative reflectance as follows:

$$R'_\infty = \frac{R_{\infty\ sample}}{R_{\infty\ standard}} \tag{3.5}$$

For solid samples reflectance is used instead.

Note here that if the $R_{\infty standard}$ is 1, then the absolute and relative reflectances will be equal.

In order to relate Beer-Lambert's law with reflectance, the Kubelka and Munk function is used.[32] This phenomenon proposes that incident radiation on a scattering medium is attenuated by simultaneous absorption and scattering processes as the light penetrates the solid. This theory considers a layer of infinite thickness composed of particles that absorb and scatter light, which are uniformly distributed in space and whose dimensions are much smaller than the thickness of the layer.

Kubelka Mulk equation to obtain absorption-like spectra from reflectance measurements.

$$F(R_\infty) = \frac{(1-R_\infty)^2}{2R_\infty} = \frac{K}{S} = \frac{2.303\varepsilon C}{S} \tag{3.6}$$

where K is the absorption coefficient (twice the Beer-Lambert's law absorption coefficient), S is twice the scattering coefficient of the sample, ε is the absorptivity, and C is the analyte concentration.[33] Based on the above, absorption-like spectra of the species present can be derived from diffuse reflectance measurements after applying the Kubelka Mulk equation (F(R), Equation 3.6). It should be noted that it is not possible to quantify with this method.

Non-radiative processes.

3.1.2 *Vibrational relaxation and internal conversion*

Following light absorption, several pathways can take place. When a fluorophore is excited to a vibrational level higher than v = 0 of the first electronic state (S_1), usually relaxes by vibrational relaxation towards the last vibrational level

o of the electronic state S_1. In the case of being excited to an electronic state higher than S_1, internal conversion would occur first followed by vibrational relaxation.[34] Internal conversion (IC) is a non-radiative transition between electronic states of the same multiplicity (such as S_2 to S_1) that occurs within 10^{-11}-10^{-9} s (Table 3.1). Such relaxation is very fast and, therefore, is very likely to occur immediately after absorption. Note that vibrational relaxation is one or two orders of magnitude faster than internal conversion.

Internal conversion is followed by vibrational relaxation.

Specifically, internal conversion allows isoenergetic transitions from an electronic state with low vibrational energies to a lower electronic state but with higher vibrational modes. In solution, after this process, there is also a vibrational relaxation to the lowest vibrational level of the fundamental state. In general, this energy is released through collisions with the environment (*i.e.* nearby molecules, such as the solvent) triggered by molecular motion and resulting in the generation or transfer of heat energy.

There are other competitive transitions.

Even though the internal conversion from S_1 to S_0 is also possible, is less probable than that between S_2 to S_1 states due to a much larger energy gap between S_1 and S_0. This often leads to other competitive transitions, such as photon emission from the singlet state (fluorescence) or triplet state (phosphorescence) after intersystem crossing.[1]

3.1.3 *Fluorescence*

It is a radiative process and follows the Kasha's Rule.

In good fluorophores, the preferred route back to the ground state is usually by the emission of a photon from S_1 to any of the S_0 vibrational states. Fluorescence lifetimes are typically close to 10^{-8} s, so that vibrational relaxation and internal conversion are usually completed before emission (see kinetics in Table 3.1). Therefore, the fluorescence radiative deactivation does not depend on the excitation wavelength (assuming there is only one species) since it generally results from a thermally equilibrated excited state, *i.e.*, the lowest energy vibrational state (v = 0) of S_1.[1] This is known as Kasha's rule.[35,36]

Usually is the mirror image of the absorption band.

The Jablonski diagram and the spectra represented below in Figure 3.1 reveal that the fluorescence spectrum is usually the mirror image of the absorption band provided that the differences between the vibrational levels are similar in the ground and excited states and no major changes in molecular geometry occur after excitation. It appears shifted to longer wavelengths, because of the energy loss in the excited state due to vibrational relaxation and internal conversion. The energy gap between the maximum of the absorption and fluorescence bands is called the Stokes shift ($\Delta\upsilon_{St}$, expressed in wavenumbers) and the displacement can vary depending on solvent effects, excited state reactions, complex formation, and/or energy transfer.

The definition of fluorescence intensity.

The fluorescence photon emission described above is a spontaneous process. Its intensity (I_{fl}) depends on the deactivation constant (k_{fl}) and the population of molecules in the first excited state ($[S_1]$). It can be defined as follows:

$$I_{fl} = k_{fl}[S_1] \tag{3.7}$$

where [S1] is directly proportional to the number of absorbed photons of the sample in the excitation process.[24]

Quantification of fluorescence efficiency.

To quantify fluorescence efficiency, the quantum yield parameter is used. It is defined as the ratio between the number of photons emitted over the number of photons absorbed.

$$\phi_{fl} = \frac{I_{fl}}{I_a} \tag{3.8}$$

The number of photons absorbed is equal to the number of deactivation process from S_1.

Taking into account that in conventional excitations the processes are uniphotonic and that generally, all excited states reach the fluorescent state S_1 before deactivating to S_0, then under stationary excitation conditions the number of photons absorbed (I_a) is equal to the number of deactivation processes from S_1 depicted in Jablonsky diagram (Figure 3.1, fluorescence deactivation, internal conversion, and intersystem crossing):

$$I_a = k_{fl}[S_1] + k_{ic}[S_1] + k_{isc}[S_1] \tag{3.9}$$

where k_{ic} and k_{isc} are the rate constants for IC and ISC, respectively.

Combining the aforementioned three equations (Equation 3.7, 3.8 and 3.9) it becomes:

When the non-radiative decay rate is much lower than the radiative decay rate the quantum yield is close to unity.

$$\phi_{fl} = \frac{k_{fl}}{k_{fl} + k_{ic} + k_{isc}} = \frac{k_{fl}}{k_{fl} + k_{nr}} \tag{3.10}$$

Being $k_{nr} = k_{ic} + k_{isc}$ the sum of both non-radiative transitions.

Thus, the fluorescence quantum yield is given by the ratio of the fluorescence rate over the rate of all possible deactivation processes of the S_1 state, being all competitive processes. From this equation, it is concluded that when the non-radiative decay rate is much slower than the radiative decay rate ($k_{nr} < \tau$) the quantum yield can be close to unity.

Fluorescence quantum yield can be measured either in liquid or solid samples.

Fluorescence quantum yield measurements can be performed both in solution and in solid samples by different procedures. The methods and equations applied for each particular case for the determination of the ϕ_{fl} are detailed in the experimental part (Part III, Section 6.2).

Another very important feature of fluorescence is the lifetime (τ) of a fluorophore. The excited molecules remain in the S_1 state for a certain time (from 10 ps to 100 ns) before emitting a photon or being deactivated by other non-radiative processes such as internal conversion or intersystem crossing (ISC). Therefore, the lifetime (τ) of a fluorophore is defined as the average time that a photon spends in the excited state before returning to the ground state, since few molecules emit their photons precisely at $t = \tau$.[1] This lifetime is related to the constant rates of all those deactivation processes involving S_1 and it can be expressed as:

Definition of the lifetime of a fluorophore.

$$\tau_{fl} = \frac{1}{k_{fl} + k_{ic} + k_{isc}} = \frac{1}{k_{fl} + k_{nr}} \tag{3.11}$$

To experimentally determine the fluorescence lifetime, the evolution of the fluorescent emission intensity after excitation is monitored. The fluorescent intensity for a mo-

lecule showing a decay with monoexponential kinetics is defined as follows:

$$I_{fl}(t) = I_{fl,0} e^{-t/\tau_{fl}} \tag{3.12}$$

Experimental determination of the lifetime.

where $I_{fl,o}$ is the immediate intensity after the excitation pulse. A logarithmic representation of Equation 3.12 gives a straight line and from that slope, the lifetime is obtained:

$$\ln(I_{fl}(t)) = \ln(I_{fl,0}) - \frac{t}{\tau_{fl}} \tag{3.13}$$

Experimentally, this lifetime measurement (τ_{fl}) is obtained from the deconvolution of the fluorescence decay curve by time-resolved fluorescence. However, the reality is usually more complex and monoexponential lifetimes are rarely achieved when dealing with solid samples. The equations used experimentally for the determination of multiexponential lifetimes and the setup details are described in Section 6.3.

3.1.4 *Intersystem crossing and photophysical processes from triplet states*

Non-radiative transition between electronic states of different multiplicity.

The third possibility for a molecule to dissipate energy is the so-called intersystem crossing (ISC), a non-radiative transition between two isoenergetic vibrational levels belonging to electronic states of different multiplicity. The electron changes spin multiplicity from a singlet excited state to a triplet excited state (it is indicated by a horizontal curved arrow in the Jablonski diagram, Figure 3.1).

In principle, the intersystem crossing is forbidden due to the different multiplicities between states, but the spin-orbit coupling (coupling between the orbital moment and the spin moment) may be large enough to allow it. To be visible and to compete with other de-excitation pathways such as fluorescence or internal conversion, it has to be fast enough (10^{-7} - 10^{-9} s, see Table 3.1) and its probability will depend on the singlet and triplet states involved.

ISC gives rise to several interesting routes back to the ground state: phosphorescence, a radiative transition from the low lying excited triplet state to the singlet ground state; and delayed fluorescence, a process in which the first excited singlet state is re-populated by a reverse intersystem crossing from the triplet state, leading to emission from S_1 in a much longer time scale (delayed emission).

ISC leads to other processes, such as phosphorescence and delayed fluorescence.

3.1.4.1 *Phosphorescence*

Phosphorescence is another radiative deactivation process that results in the emission of light from a triplet state T_1, which is populated by intersystem crossing (ISC). Since the transitions from states of different multiplicities are forbidden due to the slow radiative rate constant k_{ph} (several orders of magnitude lower than those of fluorescence), phosphorescence lifetimes are usually on the order of microseconds to seconds (Table 3.1), sometimes even visible to the naked eye.

Very large lifetimes and it is difficult to see at room temperature.

Given the long lifetime of the triplet state (10^{-6}-10 s) compared to the average lifetime of an excited singlet state (10^{-10}-10^{-7} s) it is difficult to see the phosphorescent emission in solution at room temperature, mainly because the non-radiative de-excitation predominates over the radiative one due to the numerous collisions with the solvent. However, phosphorescence emission can be activated at low temperatures or in rigid media where collision processes are minimized.

In general, the phosphorescence spectrum shifts to longer wavelengths relative to fluorescence because the energy of the lowest vibrational level of the triplet state T_1 is lower than that of the singlet state S_1 (see Figure 3.1).

3.1.4.2 *Delayed fluorescence*

As shown in Figure 3.2 thermally activated delayed fluorescence (TADF, the only mechanism that will be discussed in this work although there are other types) involves intersystem crossing (ISC) from the singlet to the triplet excited

state ($S_1 \rightarrow T_1$) followed by a subsequent reverse intersystem crossing (RISC) from the triplet to the singlet excited state ($T_1 \rightarrow S_1$).

As a result, fluorescent emission arises from the S_1 to the S_0 state with the same spectral distribution as normal fluorescence but with a much longer decay constant. What makes this process so special is its very long emission lifetime, ranging from nanoseconds to milliseconds, and even several seconds, being visible to the naked eye even after the excitation source has been removed.[37]

TADF can occur when the energy difference between S_1 and T_1 is low and when the lifetime of T_1 is sufficiently long. Therefore, an increase in the temperature activates the intersystem crossing (necessary energy to jump back to the S_1) which leads to an enhancement of the fluorescence emission. The rate constant of thermal activation of the transition from the triplet level to the excited singlet level (k_e) will depend on both the energy gap between singlet and triplet states (ΔE_{ST}) and the temperature (T) (Figure 3.2). Through the Arrhenius equation it is defined as follows:

$$k_e = Ae^{-\frac{\Delta E_{ST}}{RT}} \tag{3.14}$$

where A is a frequency factor.

As RISC competes with other triplet deactivation processes, such as non-radiative deactivation processes and phosphorescence, it is very difficult to encounter this phenomenon at room temperature; although some exceptional cases can be found.[38]

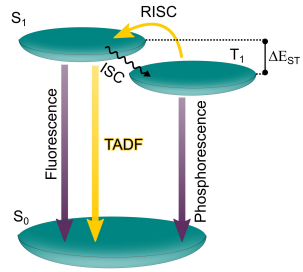

Figure 3.2: Illustration of prompt fluorescence and the possible radiative relaxations after intersystem crossing: delayed fluorescence (TADF) and phosphorescence. *(edited from Adachi 2014, Jpn. J. Appl. Phys., 53)*

3.2 BIMOLECULAR PROCESSES

Usually interactions among different molecules occur in both ground and excite states.

Although all the unimolecular processes described above can take place to a greater or lesser extent in a single molecule, in practical terms the situation is usually more complicated, leading to intermolecular interactions or bimolecular processes. Interactions among different molecules may occur in both ground and excited states and usually results

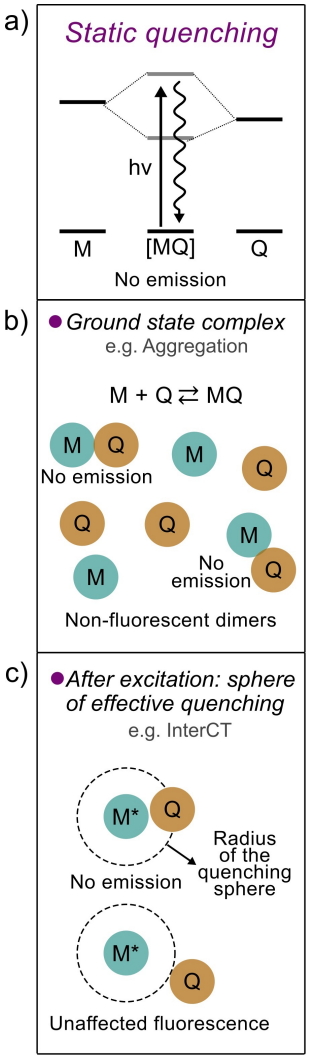

Figure 3.3: Illustration of *static quenching* **(a)** in the ground **(b)** and excited state **(c)**.

in a decrease in the fluorescence intensity. Hence, in this section, several bimolecular processes will be discussed.

Any process involving a loss in the intensity of the radiative decay of fluorophores is considered as fluorescence quenching regardless of the nature and origin of the competing intermolecular process.[1] It should be emphasized that in general quenching processes occur without any permanent change in the molecules, which implies that there is no photochemical reaction.[2]

In general, they are divided into two types of quenching mechanisms. On the one hand, there is *static quenching*, a process in which the initial formation of the emissive excited state is inhibited without any diffusion processes occurring. On the other hand, there is *dynamic quenching*, a process that interferes with the emission of the excited state of a fluorophore during its lifetime after its excitation. A distinguishing feature of *dynamic quenching* is thus a change in the observed fluorescence lifetime of the fluorophore, whereas in *static quenching* no apparent change is observed.[2,39]

As illustrated in Figure 3.3, *static quenching* arises from the formation of a nonfluorescent complex between the fluorophore and the quencher in the ground state (Figure 3.3b) or either from the presence of a sphere of effective quenching in the excited state (Figure 3.3c). It is worth stressing that the quencher could sometimes be the fluorophore itself. This topic will be covered in the following section (Section 3.2.1).

Static quenching can also occur from the excited state (Figure 3.3c), that is, when an excited molecule M* encounters a quencher Q that cannot change its relative position in space during M*'s excited state lifetime (*i.e.* in rigid matrices such as zeolites). If the quencher molecule Q is located inside a sphere that surrounds the fluorophore, called the sphere of quenching, the excitation will be followed by the complete quenching of the fluorophore. This model was proposed by Perrin and he assumed that if a quencher is outside the active sphere, it does not affect the starting molecule at all.[40]

In both situations that may involve ground and excited states, the fluorescence intensity of the solution will decrease upon the addition of the quencher Q, but the excited state lifetime of the monomer M after pulse excitation will remain unchanged. However, the opposite happens in diffusion-controlled reactions, in which the observed rate constant for quenching depends on the time.

In *dynamic quenching* (Figure 3.4), the quencher diffuses to the fluorophore during the lifetime of the excited state; thus, those excited fluorophores M* that are close to a quencher Q will react and collision at shorter times (on average) than those that are located further away. The main consequence is that after excitation, the fluorophore emission decays faster at short times.

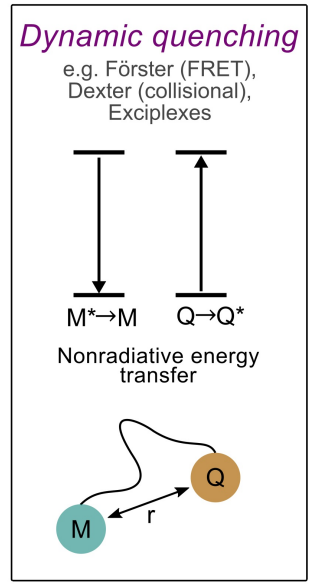

Figure 3.4: Illustrative scheme of *dynamic quenching*.

Regarding a heterogeneous emitting system with more than one fluorophore embedded in an environment, there is a high probability that some of the preceding processes may take place.[2] Hence, those cases relevant to the hybrid materials presented in this thesis will be considered, among which are molecular aggregation in the ground state and intermolecular processes in the excited state, such as the formation of excimers or exciplexes, charge-transfer (CT) complexes and energy transfer.

3.2.1 *Molecular Aggregation in the ground state*

The main objective of this thesis has been to obtain fluorescent hybrid materials to be used in optical applications. This requires a very high dye loading, and even if they are introduced into channels and cavities, the chromophores can interact if they are close enough to each other often leading to the formation of aggregates in the ground state.

In aggregates the Beer Lambert's law is no longer fulfilled.

Under these circumstances, the linear relationship between concentration and absorbance given by Beer Lambert's law is no longer fulfilled due to variations in the absorption spectra. In comparison with the monomer species, the aggregates may exhibit bathochromic or hypsochromic shifts in the absorption spectra, higher rates of intersystem

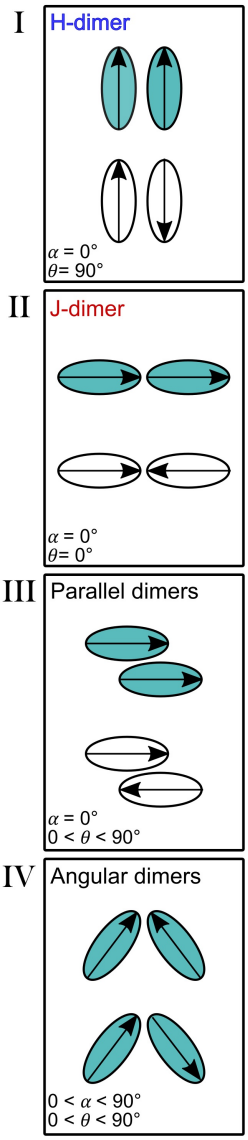

Figure 3.5: Different geometry possibilities for a dimer with their respective α and β angles. **(I)** Sandwich-like H-dimer. **(II)** Head-to-tail J-dimer. **(III)** Displaced dimer. **(IV)** Oblique dimer.

crossing, and non-radiative deactivation processes, which is usually the main cause of the quenching for certain aggregates.

The changes in photophysical and spectroscopic properties associated with aggregation can be explained by exciton theory,[41] a concept developed by Kasha.[42,43] The excitonic theory is based on the dipole-dipole interaction between the monomer units forming the aggregate and predicts the splitting of the first excited state of the monomers (E_m). It gives rise to two excited states in the dimer depending on the resulting transition moment among the molecules: E_1, with the lowest energy as a result of the electrostatic attraction between the dipoles of the molecules, which is lower than E_m; and E_2, with the highest energy due to electrostatic repulsions.

The different geometry arrangements adopted by the monomers in the dimer are depicted in Figure 3.5. The total transition moment of the aggregate is the sum of the transition dipole moments of each monomer, α is the angle between the transition moments of the monomers, and θ is the angle between the line joining the two monomer centers and the transition dipole moment of the monomer. In the figure, the two possible excited states of the dimers are represented, where the arrows represent the transition dipoles, surrounded by ovals symbolizing the molecules. This helps to explain why certain electronic transitions are allowed and others forbidden (represented in blue and white color in Figure 3.5, respectively), since on some occasions these are canceled by one another.

The diagram in Figure 3.6 shows the states corresponding to the monomer (isolated molecule) and those resulting from the dipole interaction as a function of the geometrical parameters of the aggregate. Taking into account this scheme, we will now consider the spectroscopic changes associated with dimers of different geometries:

I) **H-dimers, with parallel dipoles ($\alpha = 0^\circ$, $\theta = 90^\circ$, Figure 3.5I)**: the transition occurs to the E_2 state because the transition from the S_0 to E_1 (transition moment is

zero) state is forbidden; thus, the absorption spectrum of the dimer has a blue shift (hypsochromic shift, Figure 3.6b) compared to the spectrum of the monomer. Nevertheless, this excitation to the E_2 level is followed by rapid internal conversion to the E_1 state. Since the transition to E_1 is forbidden, no radiative processes can occur efficiently, and the deactivation continues until the ground state, or could as well be deactivated by intersystem crossing to triplet formation. As a consequence, fluorescence is not observed in this type of dimers because they drastically quench the fluorescence of the monomer (Figure 3.6b).

The absorption is blue shifted and the aggregates do not have fluorescence.

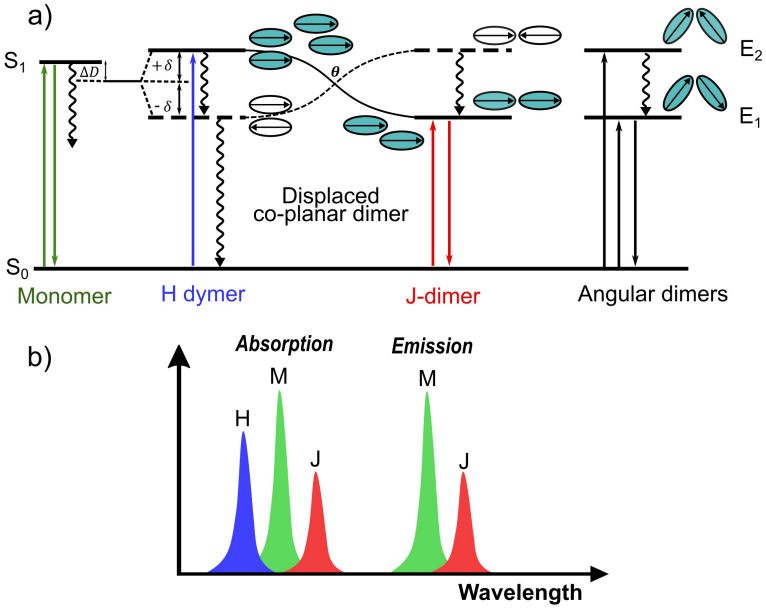

Figure 3.6: **(a)** Energy level diagrams of the monomer and the different dimers (the splittings are depicted at the same energy to facilitate compression). **(b)** Schematic representation of the spectroscopic bands (absorption and emission) of H and J dimer with respect to the monomer. Modified from literature.[44]

II) **J-dimers with collinear dipoles (α = 0° , θ = 0°, Figure 3.5II)**: in the higher energy state E_2 the dipoles are compensated with one another and, therefore, the transition to this state is forbidden. The E_1

Their absorption and fluorescence bands are red shifted.

state corresponds to a minimum energy, in-phase dipole position. Consequently, the only allowed transition is to the E_1 state, and the absorption spectra of these dimers show a red shifted absorption band (bathochromic shift) with respect to the spectrum of the isolated molecule. J-dimers can fluoresce at higher wavelengths, but given the low energy of the excited state, radiative emission competes with non-radiative de-excitation, such as internal conversion or intersystem crossing, and often their emission is low (Figure 3.6b).

Cases I and II are extreme and idealistic geometries and in general, the aggregates adopt structures with intermediate θ and α angles.

They present absorption at higher wavelengths and have the possibility to fluoresce.

III) **Dimers with parallel dipole moments** ($\alpha = 0°$, $0 < \theta < 90°$, **Figure 3.5III**): the transition dipole moments are parallel ($\alpha = 0°$) and the θ angle varies between 0 and 90°. Considering the relative position of the molecules there are two possible scenarios: first, when the θ angle is lower than the intersection point (θ = 54.7°) and the dimers are closer to the J type dimers (right side of the intersection, Figure 3.6a); and second, when the angle is higher and the dimers adopt a geometry closer to the H type sandwich dimers (left side of the intersection). Thus, in the former case, the dimers will present an absorption band at higher wavelengths with the possibility to fluoresce, and this emission will depend on the magnitude of the θ angle. For the latter, in contrast, a blue-shifted absorption and no fluorescence will be shown.[24]

The absorption band splits and two bands are observed.

IV) **Angular dimers with oblique dipoles** ($0 < \alpha < 90°$, $0 < \theta < 90°$, **Figure 3.5IV**): the resulting transition moment is not canceled in either of the positions and transitions to both excitonic states are allowed. E_1 corresponds to an in-phase arrangement of the transition dipoles, while E_2 corresponds to an out-of-phase arrangement. Consequently, a splitting of the absorp-

tion band of the monomer will be observed and the relative intensity between the two will depend on the geometry of the dimer.[45]

This excitonic theory is applied when the Born-Oppenheimer approximation is valid.

This excitonic theory is applied to cases of strong coupling where the Born-Oppenheimer (B-O) approximation is considered valid and the electronic wave functions are separated from the vibrational ones in each molecule.[46] Thus, in the absorption spectra of the dimers the splitting effects are appreciable.[47]

In this work, in order to obtain fluorescent systems, the objective has been to avoid or limit aggregation or to obtain at least fluorescent J-aggregates by occluding the chromophores in channeled aluminophosphate systems or in lattices formed by cages.

3.2.2 *Intermolecular processes in the excited state*

The majority of the de-excitation processes entail interaction with another molecule in the excited state.

The former assembly interactions arise from the ground state. Nevertheless, many other phenomena can occur at the excited state and compete with all the unimolecular de-excitation processes. Energy or electron transfer reactions between separate molecules (intermolecular) are some of the most typical photochemical primary processes. The majority of the processes responsible for de-excitation of molecules entail the interaction of an excited molecule M* with another molecule Q, among which can be found: collision with a heavy atom or a paramagnetic species, electron transfer, excimer or exciplex formation, proton transfer and energy transfer. Herein, we will focus only on the formation of excimers, exciplexes, CT complexes, and energy transfer, the most interesting features encountered in our systems so far.[1]

In the presence of Q, the fluorescence quantum yield and its lifetime of M* can be affected by intermolecular processes that compete with the intrinsic de-excitation of the M molecule, leading to a decrease in both parameters. The amount of Q plays a crucial role in the alteration of the photophysical properties, which gives rise to two scenarios:

I) The amount of Q is high and the probability of M* and Q to have a mutual approach at the moment of excitation is high since they can be at a distance in which the interactions between them are significant. In addition to *dynamic quenching*, in these environments where the Q concentration is high *static quenching* may also be present.

Two possible scenarios in the presence of Q.

II) The amount of Q is not high but there is a mutual approach between M* and Q. Despite Q not being in large excess, diffusion (*dynamic quenching*) can happen during the excited state lifetime and lead to a possible collision between the two molecules (see the introduction of Section 3.2).

If Q and M are the same molecules, the dimer is called excimer.

Both are collisional processes, but different complexes are formed depending on the nature of M and Q. If both Q and M are the same molecules, the dimeric short-lived species generated in the excited state is called excimer (MM)*, which means excited dimer and it will have different fluorescence spectrum and lifetime values in comparison to the monomer in the excited state M* (self-quenching). If Q is different than M, however, the heterodimeric species that is formed is known as exciplex (MQ)* and a new term regarding the rate constant k_{MQ} ($= 1/\tau_0'$) must be introduced for the intrinsic de-excitation process. The formation of these complexes will be explained in the next section (Section 3.2.2.1).

If Q is different than M, the dimer is called exciplex.

It should be noted that although intermolecular processes have been mainly considered so far, electron or energy transfer reactions between distinct regions within the molecule (intramolecular reactions) can also affect fluorescence features. This topic will be covered briefly in Section 3.2.2.2 and explained in more detail in Section 3.6, where the particular photophysical processes of each chromophore family used in this thesis project will be discussed.

3.2.2.1 *Formation of Excimers and Exciplexes*

The term excimer comes from "excited dimer" and is formed when an excited molecule collides with an identical molecule in the ground state to form an unstable complex.

$$M^* + M \rightleftarrows (MM)^*$$

where the symbol (MM)* indicates that the excitation energy is delocalized in the dimer. This complex exists while one of the pair components is in the excited electronic state and dissociates after photon emission.

They possess a bathochromically shifted fluorescence band.

Many aromatic hydrocarbons, such as naphthalene and pyrene, can form excimers.[48] These excimers usually possess a bathochromically shifted fluorescence band without vibrational structure (broad bands, example in Figure 3.7a). Their photophysics can be explained by the energy surfaces illustrated in Figure 3.7b. In this figure, the lower curve represents the repulsion energy between the two molecules in the ground state, and the upper curve is also related to the two molecules, but one is in the ground state whereas the other is in the excited state.

Explanation of the excimer formation and its energy diagram.

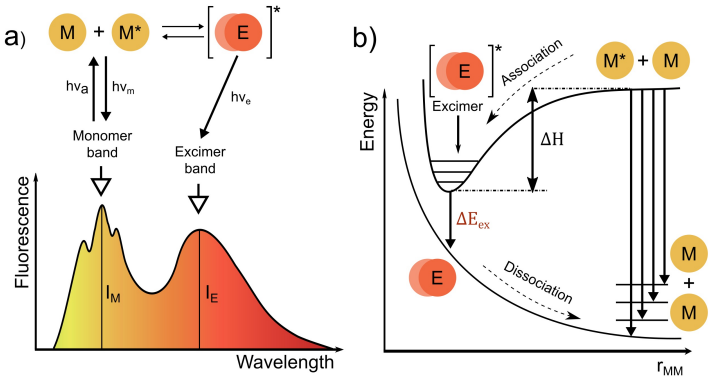

Figure 3.7: **(a)** The formation of an excimer from two monomers and their corresponding fluorescence bands. **(b)** Repulsive energy diagram between two monomers and the energy surfaces for the formation of the excimer complex. Adapted from *Molecular Fluorescence: Principles and Applications (p. 164), by B. Valeur, and M.N Berberan-Santos, 2012, Willey.*

Since the excimer is dissociate a continuous emission band is observed.

In the upper curve, there is an energy minimum corresponding to the excimer formation, where the molecules are disposed in a sandwich cofacial arrangement at a very low distance, indicating that the excimer formation is favored in this situation. Since the relaxation energy gap of an excimer to the ground state is smaller compared to that of the monomer, it emits at longer wavelengths; and since the excimer is dissociative, it finally returns to its monomeric ground state, observing a continuous emission without vibrational structure (compare fluorescence bands between monomer and excimer in Figure 3.7a).

The same energy diagram is used for excimers and exciplexes.

The generation of exciplexes in the excited state is also possible. Exciplexes are complexes formed by the interaction of an electronically excited molecular entity with a ground-state partner of a different molecular structure.

$$M^* + Q \rightleftarrows (MQ)^*$$

Their formation is based on the intermolecular interaction between the two molecules and can be explained by the same energy diagram used for excimers (see Figure 3.7b), so that their fluorescence is also observed at longer wavelengths.[49]

3.2.2.2 *Formation of CT complexes*

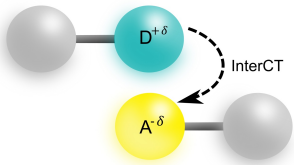

Figure 3.8: Intermolecular charge transfer process between two molecules with push-pull (donor-acceptor) character.

It may be the case where the pairs of different entities have a marked electron donor and acceptor character (Figure 3.8), involving a redistribution of charge between the molecules. In this case, the exciplex attains an ionic pair character (different from those described above) with a very large excited state dipole moment and is often referred to as a CT complex.[50]

$$D^* + A \rightleftarrows (DA)^*$$

$$A^* + D \rightleftarrows (DA)^*$$

The reaction product is usually called a charge transfer (CT) state or intermolecular charge transfer (interCT) and is favored in polar media. Anthracene and N-N-diethylaniline

are a good example of a pair that can form a CT complex in the excited state that,resulting in the transfer of an electron from an amine of the diethylaniline to the anthracene molecule.[51]

It should be noted that all these terms (exciplex and CT complex or interCT) are widely used in the literature and, although many attempts have been made to distinguish and characterize them independently in solution, the task is more than complicated. Nevertheless, certain guidelines may be useful when trying to determine which is the main process taking place.

Generally, the excited electronic states are a combination of the charge transfer states and the excitonic resonance contribution of the locally excited states. In exciplexes, their formation is governed by the geometrical arrangements between the D and A molecules and their relative orientation. Consequently, the face-to-face configurations (sandwich geometry in a π-stack) between the electron acceptor and the aromatic electron donor allow an effective overlap of orbitals. In contrast, emission in CT complexes involves a rather large D-A charge separation in solvents of intermediate and high polarity. Therefore, a slight increase in solvent polarity usually results in a reduction of pure exciplex emission due to the promotion of the interCT state. In conclusion, the CT complex or the interCT complex is more favored in polar solvents, whereas the exciplex in nonpolar solvents.

Note here that, there are molecules with intrinsic push-pull character, in which an intramolecular charge transfer (ICT) process can be promoted in the photoexcited state. Although this is not considered a bimolecular process it will be briefly explained in the following lines as it is very similar to the interCT described above.

In molecules with donor-acceptor moieties, excitation facilitates the transfer of an electron from the electron donor to the electron acceptor unit (Figure 3.9a), which makes the charge distribution in the excited state markedly different from that in the ground state. This is referred to as intramolecular charge transfer (ICT) and its emission is

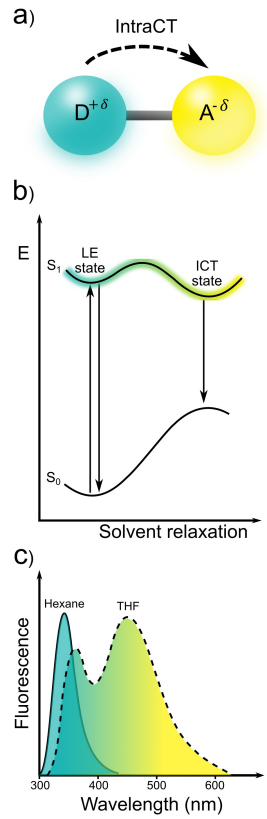

Figure 3.9: **(a)** Intramolecular charge transfer (ICT) process within a molecule with push-pull (donor-acceptor) character. **(b)** Potential energy diagram for the ICT process as a function of the solvent relaxation. **(c)** Fluorescence spectra for DMABN in different solvents (hexane and THF, continuous and dashed lines, respectively).[1]

characterized by a broad, red shifted band relative to the LE state and, as in the case of CT complexes, is generally favored in polar solvents (Figure 3.9b-c).[52,53]

Sometimes the two LE and ICT states can be reached, resulting in dual fluorescence.

In some molecules, depending on the polarity of the solvent, even the two Franck-Condon fluorescence states corresponding to the LE and ICT can be reached, resulting in a dual fluorescence (see the fluorescence spectrum of DMABN in THF, Figure 3.9c).[46] In general, the higher the polarity of the solvent, the greater the Stokes shift due to a further stabilization towards the ICT state, and the greater the quenching of LE emission (Figure 3.9b).[1,2]

As stated before, this interaction is closely linked and is very similar to the interCT process, the only difference between them is that while interCT involves interaction between two neighboring molecules (bimolecular process), intraCT occurs within the donor and acceptor of the same molecule without the formation of a CT complex. Interestingly, there are also molecular structures designed to emit from both charge-transfer states. For example, Lee et al. have developed a novel technique to obtain white light emission by a single molecule that can emit by both intramolecular and intermolecular charge transfer states at the same time.[54]

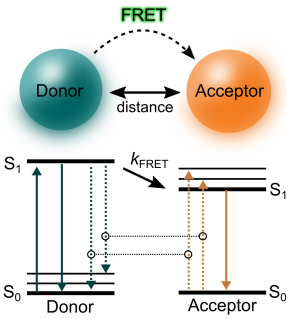

Figure 3.10: Energy level scheme of energy donor and acceptor molecules in the Förster resonance energy transfer.

3.2.2.3 *Energy transfer processes (FRET)*

Another important photophysical process that occurs in the excited state is the energy transfer from one molecule (donor) to another (acceptor).

$$D^* + A \rightarrow D + A^*$$

It is considered *a non-radiative* transfer and takes place at a long-range distance, in which no collisions are involved, and occurs in space without the need for contact between the two molecules. It consists of an energy donor chromophore, initially in its electronic excited state, which may transfer its energy to an acceptor chromophore through non-radiative dipole-dipole coupling (Figure 3.10). For this to happen, the emission spectrum of the energy

donor fluorophore must overlap with the absorption spectrum of the acceptor as represented in Figure 3.11. This type of transfer is known as Förster resonance energy transfer (FRET).

The emission band of the donor and the absorption of the acceptor must overlap.

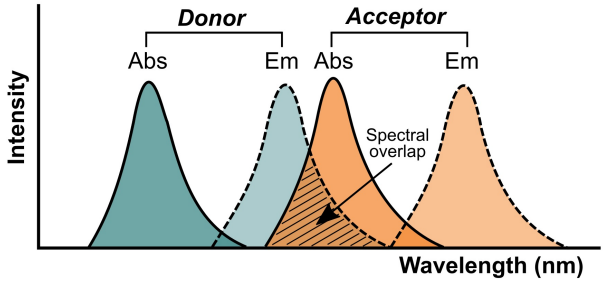

Figure 3.11: Illustration of the spectral overlap between the emission spectrum of the donor and the absorption of the acceptor in FRET.

FRET results in a decrease in the fluorescence intensity and lifetime of the donor and an increase in the fluorescence of the acceptor, in the case that the acceptor is fluorescent; if it is not, the energy is dissipated as heat. Consequently, from the point of view of the fluorescence of the donor, FRET can be considered as a quenching process. The degree of energy transfer will be influenced mainly by:[53]

- The extent of the spectral overlap.
- The quantum yield and lifetime of D.
- The relative orientation of the dipoles of D and A molecules.[24]
- The distance between the donor and acceptor molecules.

Several factors that influence the FRET process.

In fact, an important magnitude is the Förster distance (R_0), defined as the distance between donor and acceptor in which the FRET efficiency is 50%.

$$R_0^6 = 8.79 \cdot 10^{-5} (\kappa^2 \, n^{-4} \phi_D \, J(\lambda)) \tag{3.15}$$

where κ^2 is a factor to describe the relative orientation of the transition dipoles of the donor and acceptor species

(κ^2 is maximum for a head to tail disposition and minimum for a perpendicular disposition between D and A), n is the refraction index, ϕ_D the fluorescence quantum yield of the donor in absence of the acceptor and $J(\lambda)$ is the spectral overlap.

The concentration dictates the distance between molecules and consequently the FRET process.

Thus, the concentration of both molecules is a particularly important factor to take into account as it can dictate the distance between the molecules. At very low concentrations, the FRET process will be barely visible, while at high concentrations the likelihood of the process will be higher, being a strongly distance-dependent process. Indeed, the interaction is possible at relatively long distances (10-100 Å)[55] and such transfer is often used as a spectroscopic ruler to measure distances between molecules of interest.[49]

The rate of energy transfer $k_T(r)$ is denoted as:

$$k_T(r) = \frac{1}{\tau_D}\left(\frac{R_0}{r}\right)^6 \tag{3.16}$$

where r is the distance between the donor (D) and acceptor (A) and τ_D is the lifetime of the donor in the absence of energy transfer.

Determination of FRET efficiency.

It is also possible to calculate the FRET efficiency (ϕ_{FRET}) determining the lifetime of the donor in the presence (τ) and absence of the acceptor (τ_o):[49]

$$\phi_{FRET} = 1 - \frac{\tau}{\tau_0} \tag{3.17}$$

3.3 POLARIZED LIGHT SPECTROSCOPY: ANISOTROPY

Microscopy is used to quickly check the incorporation of dye molecules.

The simplest and quickest way to know if the incorporation of guest species into the zeolitic materials has been successful is by means of microscopy, as the color of the crystals is a clear indicator of this inclusion. In addition, information about the alignment of the guest molecules within the restricted geometry in one-dimensional pores of the host can be obtained using linearly polarized light.[56] For this reason, the theoretical basis of polarized light spectroscopy is now briefly described.

3.3.1 *Polarized photoselection and dye-alignment*

Light can be defined as a traveling electromagnetic wave consisting of an electric $\vec{E}$ and magnetic field $\vec{B}$ perpendicular to each other and to the direction of propagation (see Figure 3.12a). All common light sources, including the sun and artificial light, produce non-polarized light, which means that the fields do not have a preferential orientation (Figure 3.12b). However, when there is a spatial orientation and the electric field oscillates along a given direction of the xy plane, it is called linearly polarized light.[1] Consequently, if the light is linearly polarized in the x-direction, the y component of the electric field is zero and vice versa (Figure 3.12c).

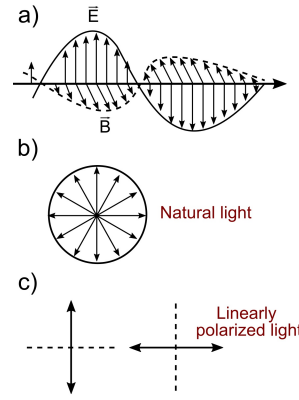

Figure 3.12: **(a)** Spatial representation of electromagnetic radiation and representation of **(b)** natural and **(c)** linearly polarized light.

Spectroscopy with linearly polarized light is applied in a wide variety of systems due to its versatility. It can be useful to obtain information about molecular structures (transition moments) and their optical properties, as well as to know the orientation of molecules within ordered structures, one of the main goals of this work.

Anisotropy measurements are based on the principle of photoselective excitation of fluorophores using polarized light. This process depends on the transition dipole moment of the fluorophore, which has a specific orientation with respect to its molecular axis. Thus, when the molecules are illuminated by polarized light, those whose transition dipole moments are oriented in a direction close to that of the electric vector of the incident beam will be preferentially excited.[1]

Explanation of photoselection rule in anisotropy measurements.

Consequently, for most chromophores, the absorption probability depends on their orientation with respect to the electric field and the electronic transition state, since each transition has a different transition moment. Nevertheless, in emission, the response to polarized light will be the same because the transition momentum is the same regardless of the excited state reached by the molecule upon excitation, due to the internal conversion to the first singlet state.

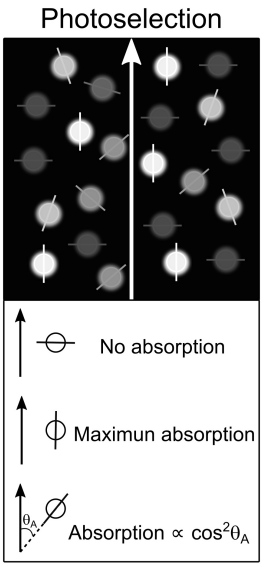

Figure 3.13: Photoselection rule: those molecules oriented within a particular range of angles to the applied polarization will be excited.

This process known as photoselection is represented in Figure 3.13. The probability for a dye molecule to absorb the light is proportional to $\cos^2(\theta_A)$, where θ_A is the angle between the light polarization direction and the absorption transition dipole $\overrightarrow{d_A}$ of the molecule. Accordingly, the emission of the molecule is assumed to be that of an emitting transition dipole $\overrightarrow{d_E}$ in the far-field. The direction of the transition dipoles $\overrightarrow{d_A}$ and $\overrightarrow{d_E}$ depends on the transitions which are involved in the absorption and emission processes.

In an isotropic system, the distribution of fluorophores is random, so that upon excitation with polarized light, only those molecules whose absorption transition dipole is parallel to the excitation vector are excited. Since the excitation is selective, the fluorescence emission is not a priori equally polarized along with the directions parallel $I_{||}$ and perpendicular $I_\perp$ to the polarization and we obtain a population of partially oriented fluorophores (photoselection).[57] Thereby, emission can only occur when the polarized light is along the dipole moment of the molecule, which is usually arranged along the major molecular axis of the fluorophore.

One of the best ways to quantify anisotropy and thus determine the preferential orientation of a molecular system is through the dichroic ratio, D. In fluorescence measurements, the dichroic ratio is defined as the ratio between the intensities recorded for orthogonal emission polarization, while keeping the excitation polarization constant:

The anisotropy is quantified through the dichroic ratio, D.

$$D = \frac{I_{||}}{I_\perp} \tag{3.18}$$

where $I_{||}$ and $I_\perp$ are the fluorescence intensities measured with the electric vector of linearly polarized light parallel and perpendicular to the sample axis, respectively (see Section 6.5 for further explanations on polarization experiments with the fluorescence microscope).

There are some phenomena that can influence the anisotropy and can result in experimental values below the expected theoretical ones by inducing a partial depolariza-

tion of fluorescence. For example, in a liquid solution, the dye molecules can rotate freely and a displacement of the transition momentum by rotational diffusion in the excited state is feasible.[2,58] Therefore, preventing such effects by occluding the dyes within the zeolitic structures and achieving a higher nonlinear response has been one of the main objectives of this work.

The anisotropy can also be verified by means of birefringence.

In addition to the aforementioned technique, there is another approach to verify the existence of anisotropy of the medium, which is by means of birefringence, using two crossed polarizers. This behavior is observed in dye-loaded molecular sieve crystals with some ordering of the molecules and is characterized for having two different indices of refraction due to the dependence of the refractive index to the polarization. These optically anisotropic materials are said to be birefringent and the crystals present artificial colors owing to the interference of the ordinary and the extraordinary light waves, which pass the crystal with different phase velocities.[56]

In summary, visual microscopic investigations such as fluorescence polarization and birefringence are simple methods that could be used for various purposes:

The main purposes of using polarized microscopy.

- Find the correlation between the orientation of the pores on the microporous host and the crystal shape.
- Verify the preferential alignment of the guest molecules within the molecular sieve pores.

3.4 NONLINEAR (NLO) PROCESSES

The field of nonlinear optics (NLO) has received considerable interest in recent years due to the wide variety of applications it offers in various fields such as photonics, nanophotonics, and optoelectronics.[59–61] Consequently, the design of new NLO materials is becoming more and more important these days. This phenomenon is described as a particular interaction of electromagnetic fields in various media, resulting in new electromagnetic fields, which are

altered in phase, frequency, amplitude, or other propagation characteristics compared to the incident field.[62] Therefore, in nonlinear optics, light induces different optical properties in the medium, and these nonlinear interactions between light and matter are analyzed.

Definition of linear optical behaviour of a medium.

Generally, light waves do not interact with each other and the medium usually exhibits linear optical behavior. Mathematically this would be described as follows, where the relationship between the polarization P of the medium and the electric field strength E remains linear:[56]

$$P = \chi^{(1)}E \tag{3.19}$$

where $X^{(1)}$ is the first-order susceptibility of the medium. This statement is only valid at low light intensities. At higher intensities, deviations in this behavior arise leading to a nonlinear response of the medium. To define these processes, additional terms related to higher-order nonlinear optical effects must be added to the formula already described.[56]

At higher intensities, nonlinear response of the medium arise.

$$P = \chi^{(1)}E + \chi^{(2)}EE + \chi^{(3)}EEE \tag{3.20}$$

Here the coefficients $X^{(2)}$ and $X^{(3)}$ are the higher-order susceptibilities, in particular, the second and third-order effects, considered as the most important since they produce the strongest nonlinear effects in a system. For this reason, second-harmonic generation (SHG) and two-photon absorption (TPA), which are related to the second ($X^{(2)}$) and third-order ($X^{(3)}$) susceptibilities respectively, are of great importance for applications.

Traditional NLO systems.

So far, traditional NLO systems have been based on inorganic crystals such as barium borate (BBO) or monopotassium phosphate (KDP). However, in this work, the aim has been to design other organo-inorganic hybrid systems as an alternative that could be suitable for SHG applications (for a more detailed history of SHG traditional crystals and the evolution towards novel organic materials see the introduction of Section 7.2 of Part III).

For this purpose, it is very crucial to design systems with a non-centrosymmetric arrangement with high values of first-order hyperpolarizability (β). The hyperpolarizability value is specifically known as the second-order response of an organic molecule and, in this sense, the nonlinear response of a material can be improved by increasing this β value in organic molecules, such as by increasing their electronic asymmetry (with stronger donor or acceptor substituent groups) or by increasing the conjugation length between D-A substituents.[63] Therefore, in this thesis, attempts have been made to encapsulate organic molecules with π-conjugated systems that exhibit strong electron donor and acceptor groups (high hyperpolarizability values) into channeled non-centrosymmetric aluminophosphate hosts of small pore size.

Non-centrosymmetric systems with high hyperpolarizability values are crucial for SHG.

3.4.1 *Second-harmonic Generation (SHG)*

Second-harmonic generation or frequency doubling occurs when a laser beam (ultraviolet, visible, or infrared radiation) with a coherent radiation of frequency ν passes through a suitable optical medium with nonlinear polarizability and produces coherent radiation of double the frequency 2ν. This phenomenon is illustrated in Figure 3.14, where two photons of the same wavelength are paired in-phase and the energy is converted into photons with double energy of the incoming beam's frequency (2ν or λ/2). This tendency to cause SHG is characterized by the second-order nonlinear susceptibility of the medium and the interaction does not involve energy absorption from the medium, being just limited to matter (nonlinear coherent scattering).

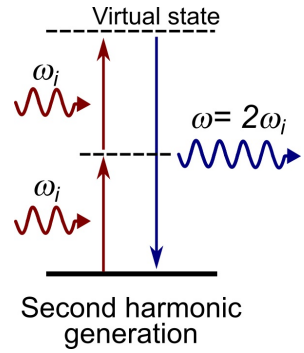

Figure 3.14: Illustration for the second-harmonic generation process.

This effect was first observed by Franken et al. in 1961 in a quartz crystal[64] and today this phenomenon is widely used in laser industry to produce 532 nm green lasers from a 1064 nm laser source, usually Nd:YAG. These lasers are obtained when the initial laser light is passed through a bulk KDP crystal and a portion of the incoming light is converted to 532 nm wavelength. Pulsed lasers are the

most common second-harmonic generators because they produce a high electric field density in the crystal and thus enhance the efficiency of the process.

There is a growing interest for the generation of UV lasers.

Given the great potential of this phenomenon, there is a growing interest in the realization of nonlinear optical waveguides for the generation of laser light in deep UV. Continuous-wave ultraviolet lasers operating in the 200-350 nm wavelength range are very attractive for various spectroscopic and biomedical applications but are extremely difficult to produce. Fortunately, the frequency conversion technique allows the production of these lasers, becoming an extremely valuable technique.[65]

3.5 MICROLASER ACTION

Light amplification by stimulated emission of radiation, *i.e.* laser, has become an important tool for a wide variety of applications, ranging from spectroscopy to material science or communication technology.[56] Indeed, lasers are employed as excitation sources of spectroscopic techniques to analyze many of the processes described above. In a laser, the electric and magnetic fields of the waves oscillate in phase with each other, resulting in a higher intensity of light, producing staggered light waves.

To achieve laser emission, there are three essential requirements:

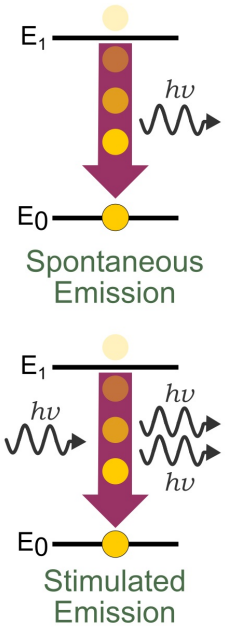

Figure 3.15: Spontaneous *vs* stimulated emission.

i) *High probability of stimulated emission.* Photon emission occurs by spontaneous emission when no additional light source is added. This process is considered a random event. However, if an additional light source is added with the same frequency as the current transition, an excited state can be stimulated to emit a photon. The oscillating electric field of appropriate frequency (incident photon) interacts with an excited atom (depicted in Figure 3.15), and induces emission of a second-photon with the same properties as those of the incident photon. In order to obtain laser action,

the probability of stimulated emission must be greater than that of spontaneous emission.

ii) *Population inversion*: more atoms or molecules must be in higher energy states compared to lower energy states. As a result, the stimulated emission can initiate a cascade (an intense burst of light) of laser emission back to the ground state.

iii) *A resonant cavity.* It provides multiple reflections of fluorescent light back and forth through the active medium and amplifies the coherence of the emitted light causing stimulated emission. Therefore, the pumping cavity not only provides a good coupling between the source and the active absorber material, but is also responsible for the pumping density distribution in the laser element, which is key to achieving uniformity and avoiding optical distortions of the output beam.

Essential requirements to achieve laser emission.

In laser physics, to increase the optical power (gain or amplification), one must maximize the lifetime of the upper state and minimize all competing non-radiative processes. For this purpose, dyes with a long-lived singlet first excited state must be chosen so that population inversion ($N_{S_1} > N_{S_0}$) is feasible. Besides, this inversion can only be achieved with schemes of at least three levels, because with only two levels involved it is not enough for the process to take place. The most popular four-level solid-state laser is the Nd:YAG (neodymium-doped yttrium aluminum garnet). Its mechanism is represented in Figure 3.16, and in this particular case, the transition takes lace into the upper metastable excited laser level, preventing transition to occur back into the ground state.

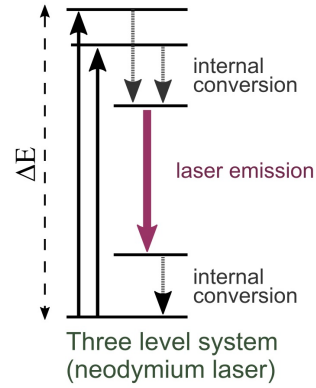

Figure 3.16: Four level energy level diagram of Nd:YAG laser.

In addition, solid-state lasers, and in particular microlasers, are of great interest in device technology because the reduction of laser dimensions leads to even more interesting properties. In microlasers, the stimulated emission process takes place in microcavity nanostructures, being able to generate an intense coherent light at a micro/nanoscale.

Requirements to achieve a microlaser.

For that purpose, the microlaser requires an active medium, a pump to excite the active medium and produce population inversion, and a resonant electromagnetic cavity that contains the active medium to amplify the emitted light. The medium is responsible for amplifying light by stimulated emission and when incorporating it into a resonator, results in a laser with highly monochromatic and coherent output.[66]

Organic molecules are ideal as active media for lasers.

Organic materials are ideal to be used as active media for the fabrication of such compact lasers.[67] For good laser performance, the organic molecules should meet the following requirements: strong absorption and fluorescence bands, low probability of non-radiative deactivation, low tendency to aggregate, a high Stokes shift, and excellent chemical, thermal and photostability. All this accomplished, the light emitted by a good laser dye should show several discrete optical frequencies separated from each other by frequency differences (a typical experimental spectrum of a microlaser is shown in Section 6.8, Figure 6.12), which can be associated with different modes of the optical resonator. There are currently a wide range of organic molecules that can be used as active media for dye lasers.

This thesis's approach to achieve a microlaser based on zeolitic host/guest systems.

In this work, several attempts have been made to develop microlasers based on zeolitic host/guest systems. Laser-active organic media (styryl dyes, described in Section 3.6.1) and crystalline inorganic microresonators have been combined in a micron-sized laser material to see if they could be of interest for photonic applications (explained in more detail in Part III, Chapter 7). Hence, the microcavity (AlPO crystal) could provide the selective feedback of light within the gain medium to enhance the stimulated emission of specific wavelengths, where the outer surfaces of the crystal itself will act as a resonant cavity resembling the Fabry-Perot type cavity.[67] Thus, the formation of sufficiently large aluminophosphate crystals with naturally defined geometric shapes and doped with a high concentration of laser dye, would offer a simple approach to achieve such a microlaser.

3.6 PHOTOPHYSICAL FEATURES OF GUEST DYES

The principal aim is to improve the photophysical properties of the dyes.

In the search for guest dyes suitable for encapsulation into zeotypes that act as molecular containers (nanocavities), the aim is to obtain an improvement of the resulting photophysical characteristics for possible optical applications. Therefore, in this section special emphasis will be placed on the selection of the dyes and their photophysical features.

There are a wide range of organic dyes from different families.

Overall, there is a wide variety of dyes covering the entire UV/Vis spectrum that could be used for optical applications. In general, they are grouped into families, including coumarins, acridines, xanthenes, oxazines, pyromethenes, nitro/azo dyes, cyanines, and styryl dyes. Figure 3.17 shows the absorption and fluorescence spectra of some of these large families of dyes, together with the molecular structure of the specific dye belonging to the spectrum.

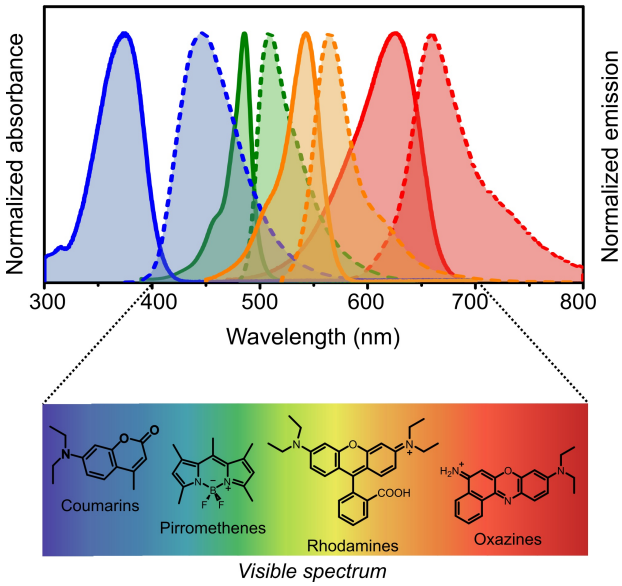

Figure 3.17: Absorption and fluorescence bands of several families of dyes. The molecular structures are shown below in the same order as they appear in the electromagnetic spectrum: coumarins, pyrromethenes, rhodamines, and oxazines.

The dyes that have been selected for this work.

Among all the families mentioned, this work will deal, on the one hand, with styryls and, on the other hand, with families of three fused aromatic rings (acridines, xanthenes, and oxazines). All of them are ideal candidates for the incorporation into aluminophosphates. All fluorophores are aromatic organic compounds that are commonly employed as laser dyes. In addition, they are cationic dyes, so will be strongly absorbed on the negatively charged nanochannels through electrostatic forces. Since their fluorescent characteristics are highly dependent on their nature and chemical structure,[1] the main photophysical characteristics of each family are presented below (for more specific photophysical properties refer to the results part, Part III).

3.6.1 *Styryl dyes*

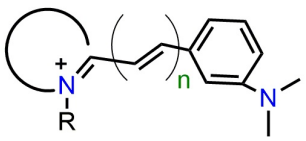

Styryls

Figure 3.18: General structure of styryls.

Styryl dyes consist of an electron donor (D) and electron acceptor (A) building block linked together through a π-conjugated system, forming D-π-A architectures as depicted in Figure 3.18.[68] In general, they present high absorption capacity from the blue to yellow region of the visible spectrum and strongly red shifted fluorescent emission, exhibiting rather large Stokes shifts. These displacements are very important to minimize inner-filter effects (reabsorption and reemission, mentioned in Section 6.2) and are typical of push-pull π-conjugated systems with high hyperpolarizabilities (explained in Section 3.4), which are usually very interesting for NLO applications.

Very flexible molecules with low fluorescence quantum yields.

The two structure partners, D and A, are integrated into a molecule that usually adopts a geometry close to planar.[69] However, the molecule is fully flexible (it can even give cis-trans isomerizations), and upon excitation, its flexibility gives rise to rotational motions around the different bonds drastically increasing internal conversion processes (see Section 3.1.2) responsible for the non-radiative deactivation. Therefore they usually exhibit very low fluorescence quantum yields ($\phi_{fl} < 0.1$).[70,71]

As a consequence of their push-pull character (amine and iminium moieties), their emission comes from an ICT state, a different state of lower energy than the locally excited (LE) (see intraCT process in Section 3.2.2.2) rendering the aforementioned large Stokes shift. Indeed, a photoinduced intra charge transfer process is energetically feasible and leads to an instantaneous change of the dipole moment. The wave functions of the ground state and the excited state differ from each other due to different electron density distributions.

In particular, in most styryls, the specific charge transfer process that takes place is the non-fluorescent twisted intramolecular charge transfer (TICT).[72,73] TICT is a charge transfer process that occurs after photoexcitation in molecules with intramolecular torsion between the donor and acceptor parts (see Figure 3.19). In other words, a fraction of the molecule rotates and twists giving rise to the TICT state. This is also the reason for its low quantum yield because the rotation (non-radiative deactivation) leads to the decoupling of the donor and acceptor orbitals, which makes the emission to the ground state forbidden by the electric dipole.[74]

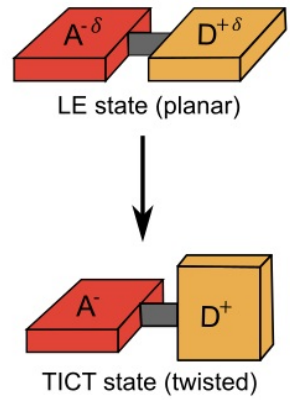

Figure 3.19: Two different states upon excitation: the planar locally excited (LE, partial charge transfer) and twisted intramolecular charge transfer (TICT, full charge transfer).[1]

This charge transfer state is stabilized in polar solvents because polarity favors total charge separation between donor and acceptor molecules.[72] In a non-polar solvent, on the contrary, charge transfer is not favored and they may show poor emission but from their locally excited state (LE, S_1 state, also described in Section 3.2.2.2 and shown in Figure 3.9).

In conclusion, styryl dyes will usually show a reminiscent red shift fluorescence as a consequence of the formation of TICT state upon excitation.[52] In some cases, solvent polarity may not be enough to tip the balance towards one state or the other, and dual fluorescence might be observed instead (LE + TICT).[1]

They show a red shift fluorescence due to TICT state.

In practice, multiple factors affect the emission of these fluorophores. The quantum yield will change as a function of the conformational change of the molecule and the non-radiative decay rate (k_{nr}). It must be taken into account that

pH also has a strong effect on these dyes due to the different acidic or basic species that can be formed, as for example the protonation of the amine group, that could hinder the formation of ICT states, thus expecting very different photophysical characteristics.

By the tight confinement of styryls internal conversion can be reduced.

In this sense, a tight confinement of these molecules in molecular sieves could restrict their molecular motions, reducing internal conversion. Thus, by obtaining a rigid planar D-π-A molecule, efficient ICT would occur without the involvement of large amplitude motions, yielding high fluorescence or even laser efficiency.[71] Besides, a preferred orientation within 1D-nanochannels would lead to a non-centrosymmetric arrangement that is crucial for nonlinear optical applications.[74]

Table 3.2: Summary table of all the styryl chromophores employed with their general donor-linker-acceptor molecular structure.

	ACCEPTOR	LINKER	DONOR
LDS 730 *2-[4-[4-(dimethylamino)phenyl]-1,3-butadienyl]-1,3,3- trimethyl-3Hindolium perchlorate*	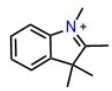		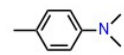
LDS 722 *4-[4-[4-(dimethylamino)phenyl]-1,3-butadienyl]-1-ethyl-pyridinium perchlorate*	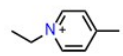		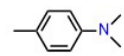
DMASBT *trans-2-[4-[(Dimethylamino)styryl]benzothiazole*	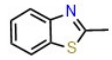		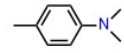
4-DASPI *trans-4-[4-(dimethylamino)-styryl]-1-methylpyridinium iodide*	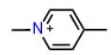		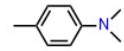
LDS751 *2-[4-[4-(dimethylamino)phenyl]-1,3-butadienyl]-3-ethylbenzothiazolium perchlorate*	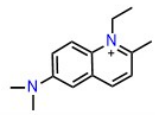		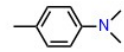

The styryls selected in this thesis.

Table 3.2 shows the particular styryl structures selected for the inclusion into aluminophosphates, including LDS 722, LDS 730, DMASBT, and 4-DASPI; and an addi-

tional structure LDS 751, which has been considered of interest for the near future. In it, the structural differences in terms of donor and acceptor moieties and their π-linkers are illustrated.

3.6.2 *Three Fused aromatic ring dyes*

By connecting the diphenylmethane structure of styryls (Figure 3.18) with an oxygen or nitrogen atom, compounds with fused aromatic rings are obtained (Figure 3.20). This replacement of the alkyl chain by a ring drastically reduces the possibilities of internal rotation and, consequently, these fused aromatic compounds, such as xanthenes, thionines, pyronines, and oxazines show much higher fluorescence quantum yields.

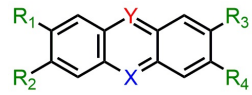

Fused aromatic rings

Figure 3.20: General structure of fused aromatic ring molecules used during this work.

Generally, a large amount of chromophore is needed for optical applications and unfortunately, these molecules are very planar and have a strong tendency to aggregate.[75] The aggregates usually formed in solution are not (or barely) emissive and are efficient deactivators of the emission of the monomers (H-aggregation) leading to a strong loss of fluorescent emission (Section 3.2.1). In these compounds, these changes are visible at relatively low concentrations, and with increasing concentration, strong changes in the absorption spectra are observed. In general, the emission lifetimes of aggregates are shorter compared to that of monomers, due to efficient deactivation processes that are generated by molecular packing between monomers. It should be noted that this tendency to aggregate also depends to a large extent on the hydrophobicity of the environment, affecting not only the degree of aggregation, but also the type of aggregates formed.

They have strong tendency to aggregate.

To minimize molecular aggregation phenomena and activate new photophysical processes, dye molecules have been encapsulated within the pores/cavities of the aluminophosphates of similar size. Depending on the molecular structure of the host and, in particular, on the type of pores (unidirectional channels or cavities), aggregate formation

can be modulated or inhibited.[76] For this purpose, several dyes from three main families have been chosen: acridines, xanthenes, and oxazines.

3.6.2.1 *Acridines*

Acridines are compounds containing one or more nitrogen atoms, also referred to as azarenes. The photophysical properties of these compounds show a significant dependence on the pH and polarity of the medium.[70] In protic solvents, such as alcohols, the fluorescence quantum yields are much higher than in apolar solvents due to hydrogen bonds that are formed which result in a reversal of the n-π* and π-π* states of minimum level. Besides, in the ground state, hydrogen bonds are better stabilized than in the excited state. Therefore, a red shift of the spectra is observed when switching from nonpolar solvents to solvents that can donate hydrogen protons.[1] In some heterocyclic compounds such as acridine it can be difficult to distinguish the n-π* absorption band from the much more intense π-π* absorption bands.

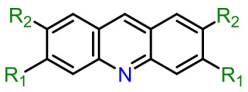

Acridine dyes

	R_1	R_2
Acridine ***(AC)***	H	H
Acridine Orange ***(ACO)***	$N(CH_3)_2$	H
Acridine Yellow ***(ACY)***	NH_2	CH_3

Figure 3.21: The general structure of acridine dyes and a table of the acridine derivatives employed.

The most well-known acridine dyes

In this work, mainly acridine (AC) has been employed (Figure 3.21). Acridine consists of three fused aromatic rings with nitrogen as heteroatom in the central ring and no additional pendant groups. It is structurally related to anthracene with one of the central -CH- groups replaced by nitrogen and it is mildly basic. Among the acridine derivatives, however, there are others that are widely used, such as acridine orange (ACO)[1] or acridine yellow (ACY, also included in Figure 3.21). Acridine orange is based on the acridine heterocyclic skeleton but with two dimethylamino pendant substituents in the R_1 positions; whereas the. acridine yellow, possesses amine and methyl groups in R_1 and R_2 positions. These two have the peculiarity of having high probability of intersystem crossing, being susceptible to phosphorescence Section 3.1.4.1 or delayed fluorescence Section 3.1.4.2 in rigid matrices (briefly discussed in Chapter 10).

All of them are fluorescent and the position of their spectral bands depends on their substituents.

3.6.2.2 *Xanthenes*

Xanthene derivatives also constitute an important class of heterocyclic compounds, consisting of three cyclic rings with oxygen incorporation. The presence of different substituents at position 9 (R_2 position in Figure 3.22) has a strong influence on their physical and chemical properties, as well as their applications. Figure 3.22 illustrates the general structure of these compounds and a table with the derivates employed in this work: rhodamine 123 (R123) and pyronin Y (PY).

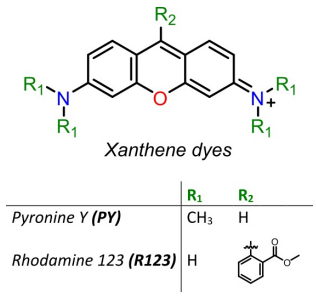

Figure 3.22: General structure of xanthene dyes. A table of the xanthene dyes used for the incorporation into zeotypes is shown below the structure.

Pyronin Y (PY) has a similar molecular structure to the ACO but with oxygen instead of nitrogen as heteroatom. It presents a characteristic pinkish color and bright green fluorescence, which reaches reasonable fluorescence efficiencies.

The replacement of the group in positions R_1 and R_2 by hydrogen and carboxyphenil yields Rhodamine 123. Rhodamines usually exhibit strong absorption and fluorescence bands with small Stokes shifts in the green/red region (500-600 nm) of the visible spectrum, quantum yields of practically 1, and lifetimes around 4 ns.[1,70] The bands are due to transitions from the S_0 and S_1 electronic states.[1] The chromophore responsible for these transitions is the xanthene group consisting of three hexagonal rings. The carboxyphenyl group does not intervene in the conjugation of the aromatic system since it is arranged almost perpendicular to the xanthene ring for steric reasons.[75] Therefore, the band positions do not differ much from pyronin Y to R123, since the substitution at the R_2 position does not have a great impact on it. In fact, R123 exhibits a slight blue shift and a Stokes shift similar with respect to the Pyronin Y.[1]

Photophysical characteristics of Rhodamine 123.

3.6.2.3 *Oxazines*

Oxazines are heterocyclic compounds containing an oxygen and a nitrogen atom in a doubly unsaturated six-membered ring. From this family, the most popular fluorescent dye, Nile Blue, is included. This compound, illustrated in Figure 3.23, is based on the aromatic benzophenoxazine, a fused aromatic compound formed by 4 aromatic rings with a dimethylamino electron donor substitution at the 9-position.

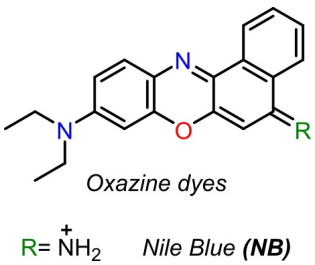

Figure 3.23: The general structure of oxazine dyes and below, the substituent to build up the Nile Blue dye.

Nile Blue has a charge-transfer character in the excited state, giving rise to solvatochromic behaviors.[77] In media of high polarity, the emission is red shifted and usually, the observed quantum yields are lower than in apolar environments.[70]

3.6.3 *BODIPYs*

The extraordinary properties of BODIPY dyes.

As new alternative laser dyes, in recent years, the most outstanding family has been the pyrromethene family; and, in particular, dipyrromethene boron difluorides (BODIPYs), thanks to their extraordinary chemical versatility and photophysical tunability. BODIPY (short for 4,4-difluoro-4-difluoro-4-bora-3a,4a-diaza-s-indacene) compounds have a structure similar to indacene (see structure in Figure 3.17) and offer many advantages: high fluorescence quantum yields owing to the rigidity of the structure, large molar absorption coefficients (40,000-10,000 L $mol^{-1}cm^{-1}$), and good solubility and stability (either photo- or thermal-).

All publications related to BDP dyes during the thesis.

Consequently, they are suitable for many applications due to their robustness and excellent photophysical properties. For example, these dyes are commonly used to label amino acids, nucleotides, and other low molecular weight ligands.[1] In the laboratory, in addition to the synthesis of hybrid materials, the design and analysis for new BDP dyes is noteworthy, which has led to several publications with new structures (8-aryl BODIPY derivatives,[78] symmetric bridged bisBODIPYs,[79,80] BINOL-based O-BODIPYs,[81] and BODIPY-carbohydrate derivatives[82]), although these dyes

will not be used in the present thesis due to their zwitterionic nature. This is because experimentally, the neutral character of the molecule was found to hinder its incorporation into zeotypes due to the lack of electrostatic interactions with the host. However, further experiments are planned in the near future.

BIBLIOGRAPHY

(1) Valeur, B.; Berberan-Santos, M. N., *Molecular fluorescence: principles and applications*; John Wiley & Sons: 2012.

(2) Lakowicz, J. R., *Principles of fluorescence spectroscopy*; Springer: 2006.

(3) Perkampus, H.-H., *UV-VIS Spectroscopy and its Applications*; Springer Laboratory: 1992.

(4) Andrews, D. L.; Lipson, R. H., *Molecular photophysics and spectroscopy*; Morgan & Claypool: 2014.

(5) Cronstedt, A. F. Observation and description of an unknown kind of rock to be named zeolites: Kongl. *Vetenskaps. Acad. Handl. Stockh* **1756**, *17*, 120–123.

(6) Von Ballmoos, R; Higgins, J.; Treacy, M., *Proceedings from the Ninth International Zeolite Conference*; Elsevier Butterworth-Heinemann: 2013.

(7) Guozhong, C; Ying, W, *Nanostructures and Nanomaterials: Synthesis, Properties and Applications*; ACS Publications: 2004.

(8) Tielen, M; Geelen, M; Jacobs, P. In *Proc. Int. Symposium on Zeolite Catalysis*, 1985, pp 1–18.

(9) Harris, J. W.; Bates, J. S.; Bukowski, B. C.; Greeley, J.; Gounder, R. Opportunities in catalysis over metal-zeotypes enabled by descriptions of active centers beyond their binding site. *ACS Catalysis,* **2020**, *10*, 9476–9495.

(10) Lowenstein, W Apparatus for Separating Fluorine from Aluminosilicates by Pyrohydrolysis. *Am. Mineral.* **1954**, *39*, 92.

(11) Lok, B. M.; Messina, C. A.; Patton, R. L.; Gajek, R. T.; Cannan, T. R.; Flanigen, E. M. Crystalline silicoaluminophosphates, 1984.

(12) Lok, B. M.; Messina, C. A.; Patton, R. L.; Gajek, R. T.; Cannan, T. R.; Flanigen, E. M. Silicoaluminophosphate molecular sieves: another new class of microporous crystalline inorganic solids. *Journal of the American Chemical Society,* **1984**, *106*, 6092–6093.

(13) Flanigen, E. M.; Lok, B. M.; Patton, R. L.; Wilson, S. T. In *Studies in Surface Science and Catalysis*, Elsevier: 1986; Vol. 28, pp 103–112.

(14) Hartmann, M.; Kevan, L. Transition-metal ions in aluminophosphate and silicoaluminophosphate molecular sieves: location, interaction with adsorbates and catalytic properties. *Chemical reviews,* **1999**, *99*, 635–663.

(15) Martens, J.; Jacobs, P. Crystalline microporous phosphates-A family of versatile catalysts and adsorbents. *Studies in surface science and catalysis,* **1994**, *85*, 653–685.

(16) Gómez-Hortigüela Sainz, L. et al., *Efecto director de estructura de moléculas fluoradas en la síntesis de aluminofosfatos microporosos cristalinos*; Universidad Autónoma de Madrid: 2006.

(17) Husing, N, *Porous hybrid materials*; Kickelbick, G., Ed.; Wiley Online Library: 2006.

(18) Bernardo Maestro, M. B., *Efecto director de estructura de moléculas quirales derivadas de (1R, 2S)-efedrina en la síntesis de aluminofosfatos microporosos*; Universidad Autónoma de Madrid: 2018.

(19) Baerlocher, C.; McCusker, L. B.; Olson, D. H., *Atlas of zeolite framework types*; Elsevier: 2007.

(20) IZA-International Zeolite Association, Database of zeolite structures. http://www.iza-structure.org/databases/.

(21) Davis, M. E. Ordered porous materials for emerging applications. *Nature,* **2002**, *417*, 813–821.

(22) Pan, H.; Chu, H.; Wang, X.; Li, Y.; Zhao, S.; Li, G.; Li, D. Optical nonlinearity of zeolitic imidazolate framework-67 in the near-infrared region. *Materials Chemistry Frontiers,* **2020**, *4*, 2081–2088.

(23) Jacobs, P.; Flanigen, E.; Jansen, J.; van Bekkum, H., *Introduction to Zeolite Science and Practice*; Elsevier: 2001.

(24) Sola Llano, R., *Synergism between organic and inorganic moieties: in the search of new hybrid materials for optics and biomedicine*; University of the Basque Country UPV-EHU: 2017.

(25) PetteráLillerud, K.; Szostak, R.; Long, A. Two members of the ABC-D6R family of zeolites: zeolite phi and linde D. *Journal of the Chemical Society, Faraday Transactions,* **1994**, *90*, 1547–1551.

(26) Turrina, A.; Garcia, R.; Watts, A. E.; Greer, H. F.; Bradley, J.; Zhou, W.; Cox, P. A.; Shannon, M. D.; Mayoral, A.; Casci, J. L.; A. Wright, P. STA-20: an ABC-6 zeotype structure prepared by co-templating and solved via a hypothetical structure database and STEM-ADF imaging. *Chemistry of Materials,* **2017**, *29*, 2180–2190.

(27) Wilson, S. T.; Broach, R. W.; Blackwell, C. S.; Bateman, C. A.; McGuire, N. K.; Kirchner, R. M. Synthesis, characterization and structure of SAPO-56, a member of the ABC double-six-ring family of materials with stacking sequence AABBCCBB. *Microporous and mesoporous materials,* **1999**, *28*, 125–137.

(28) Dent, L.; Smith, J. Crystal structure of chabazite, a molecular sieve. *Nature,* **1958**, *181*, 1794–1796.

(29) Saxton, C. G.; Kruth, A.; Castro, M.; Wright, P. A.; Howe, R. F. Xenon adsorption in synthetic chabazite zeolites. *Microporous and mesoporous materials,* **2010**, *129*, 68–73.

(30) Martínez-Franco, R.; Sun, J.; Sastre, G.; Yun, Y.; Zou, X.; Moliner, M.; Corma, A. Supra-molecular assembly of aromatic proton sponges to direct the crystallization of extra-large-pore zeotypes. *Proceedings of the Royal Society A: Mathematical, Physical and Engineering Sciences,* **2014**, *470*, 20140107.

(31) Jablonski, A. Efficiency of anti-Stokes fluorescence in dyes. *Nature,* **1933**, *131*, 839–840.

(32) Kubelka, P The Kubelka-Munk theory of reflectance. *Zeitschrift für Physik,* **1931**, *12*, 539.

(33) Mirabella, F. M., *Modern techniques in applied molecular spectroscopy*; John Wiley & Sons: 1998; Vol. 14.

(34) Lichtman, J. W.; Conchello, J. A. Fluorescence microscopy. *Nature methods,* **2005**, *2*, 910–919.

(35) Kasha, M. Characterization of electronic transitions in complex molecules. *Discussions of the Faraday society,* **1950**, *9*, 14–19.

(36) McNaught, A. D.; Wilkinson, A., *Compendium of chemical terminology*; Blackwell Science: 1997; Vol. 1669.

(37) Suggett, D. J.; Prášil, O.; Borowitzka, M. A., *Chlorophyll a fluorescence in aquatic sciences: methods and applications*; Springer: 2010; Vol. 4.

(38) Salla, C. A.; Farias, G.; Rouzières, M.; Dechambenoit, P.; Durola, F.; Bock, H.; de Souza, B.; Bechtold, I. H. Persistent Solid-State Phosphorescence and Delayed Fluorescence at Room Temperature by a Twisted Hydrocarbon. *Angewandte Chemie International Edition,* **2019**, *58*, 6982–6986.

(39) Braslavsky, S. E. Glossary of terms used in photochemistry, (IUPAC Recommendations 2006). *Pure and Applied Chemistry,* **2007**, *79*, 293–465.

(40) Perrin, F Law of decrease in the fluorescent power according to concentration. *Comptes Rendus de l'Académie des Sciences,* **1924**, *178*, 1978–1980.

(41) Kasha, M.; Rawls, H. R.; El-Bayoumi, M. A. The exciton model in molecular spectroscopy. *Pure and applied Chemistry,* **1965**, *11*, 371–392.

(42) Kasha, M. Energy transfer mechanisms and the molecular exciton model for molecular aggregates. *Radiation research,* **1963**, *20*, 55–70.

(43) Förster, T. 10th Spiers Memorial Lecture. Transfer mechanisms of electronic excitation. *Discussions of the Faraday Society,* **1959**, *27*, 7–17.

(44) Arbeloa, F. L.; Martínez, V. M.; Arbeloa, T.; Arbeloa, I. L. Photoresponse and anisotropy of rhodamine dye intercalated in ordered clay layered films. *Journal of Photochemistry and Photobiology C: Photochemistry Reviews,* **2007**, *8*, 85–108.

(45) Lopez, S. G., *Fotofísica de colorantes en medios heterogéneos*; Universidad de Buenos Aires: 2010.

(46) Born, M.; Oppenheimer, J. R. On the quantum theory of molecules. *Annalen der physik,* **1927**, *389*, 457–484.

(47) Tomasini, E. P., *Caracterización espectroscópica y fotofísica del estado triplete de colorantes en sistemas heterogéneos*; Universidad de Buenos Aires. Facultad de Ciencias Exactas y Naturales: 2010.

(48) Demchenko, A. P. The concept of λ-ratiometry in fluorescence sensing and imaging. *Journal of fluorescence,* **2010**, *20*, 1099–1128.

(49) Montero, R. P., *Novel systems for bioimaging and photodynamic therapy: bodipy dyes and silica-based nanocarriers*; University of the Basque Country UPV-EHU: 2020.

(50) Eisenthal, K. B. Intermolecular and intramolecular excited state charge transfer. *Laser Chemistry,* **1983**, *3*, 145–162.

(51) Hoang, H. M.; Pham, T. B. V.; Grampp, G.; Kattnig, D. R. Exciplexes versus loose ion pairs: How does the driving force impact the initial product ratio of photoinduced charge separation reactions? *The journal of physical chemistry letters,* **2014**, *5*, 3188–3194.

(52) López Arbeloa, F; Bañuelos, J; Martínez, V; Arbeloa, T; López Arbeloa, I. Structural, photophysical and lasing properties of pyrromethene dyes. *International Reviews in Physical Chemistry,* **2005**, *24*, 339–374.

(53) Grabowski, Z. R.; Rotkiewicz, K.; Rettig, W. Structural changes accompanying intramolecular electron transfer: focus on twisted intramolecular charge-transfer states and structures. *Chemical reviews,* **2003**, *103*, 3899–4032.

(54) Lee, H. L.; Jang, H. J.; Lee, J. Y. Single molecule white emission by intra-and inter-molecular charge transfer. *Journal of Materials Chemistry C,* **2020**, *8*, 10302–10308.

(55) Dos Remedios, C. G.; Moens, P. D. Fluorescence resonance energy transfer spectroscopy is a reliable" ruler" for measuring structural changes in proteins: dispelling the problem of the unknown orientation factor. *Journal of structural biology,* **1995**, *115*, 175–185.

(56) Hoffmann, K.; Marlow, F., Molecular sieve-based materials for photonic applications In *Handbook of Zeolite Science and Technology*; CRC Press: 2003, pp 1177–1212.

(57) Gozhyk, I.; Clavier, G.; Méallet-Renault, R.; Dvorko, M; Pansu, R.; Audibert, J.-F.; Brosseau, A.; Lafargue, C; Tsvirkun, V; Lozenko, S.; Forget, S.; Chénais, S.; Ulysse, C.; Zyss, J.; M., L. Polarization properties of solid-state organic lasers. *Physical Review A,* **2012**, *86*, 043817.

(58) Gozhyk, I; Boudreau, M; Haghighi, H. R.; Djellali, N; Forget, S; Chénais, S; Ulysse, C; Brosseau, A; Pansu, R; Audibert, J.-F.; Gauvin, S.; Zyss, J.; Lebental, M. Gain properties of dye-doped polymer thin films. *Physical Review B,* **2015**, *92*, 214202.

(59) Suresh, S; Ramanand, A; Jayaraman, D; Mani, P Review on theoretical aspect of nonlinear optics. *Reviews on Advanced Materials Science,* **2012**, *30*, 175–183.

(60) Liu, J.; Gao, W.; Kityk, I.; Liu, X.; Zhen, Z. Optimization of polycyclic electron-donors based on julolidinyl structure in push–pull chromophores for second order NLO effects. *Dyes and Pigments,* **2015**, *122*, 74–84.

(61) Wang, Y.; Pan, S. Recent development of metal borate halides: Crystal chemistry and application in second-order NLO materials. *Coordination Chemistry Reviews,* **2016**, *323*, 15–35.

(62) Williams, D. J. Organic polymeric and non-polymeric materials with large optical nonlinearities. *Angewandte Chemie International Edition in English,* **1984**, *23*, 690–703.

(63) Kanis, D. R.; Ratner, M. A.; Marks, T. J. Design and construction of molecular assemblies with large second-order optical nonlinearities. Quantum chemical aspects. *Chemical Reviews,* **1994**, *94*, 195–242.

(64) Franken, e. P.; Hill, A. E.; Peters, C.; Weinreich, G. Generation of optical harmonics. *Physical Review Letters,* **1961**, *7*, 118–119.

(65) Degl'Innocenti, R.; Guarino, A; Poberaj, G; Günter, P. Second harmonic generation of continuous wave ultraviolet light and production of β-BaB_2O_4 optical waveguides. *Applied physics letters,* **2006**, *89*, 041103.

(66) Gierschner, J.; Varghese, S.; Park, S. Y. Organic single crystal lasers: A materials view. *Advanced Optical Materials,* **2016**, *4*, 348–364.

(67) Zhang, W.; Yao, J.; Zhao, Y. S. Organic micro/nanoscale lasers. *Accounts of chemical research,* **2016**, *49*, 1691–1700.

(68) Wuskell, J. P.; Boudreau, D.; Jin, L.; Engl, R.; Chebolu, R.; Bullen, A.; Hoffacker, K. D.; Kerimo, J.; Cohen, L. B.; Zochowski, M. R. et al. Synthesis, spectra, delivery and potentiometric responses of new styryl dyes with extended spectral ranges. *Journal of neuroscience methods,* **2006**, *151*, 200–215.

(69) Safir Filho, M.; Fiorucci, S.; Martin, A. R.; Benhida, R. Design, synthesis and photophysical studies of styryl-based push–pull fluorophores with remarkable solvatofluorochromism. *New Journal of Chemistry,* **2017**, *41*, 13760–13772.

(70) Dsouza, R. N.; Pischel, U.; Nau, W. M. Fluorescent dyes and their supramolecular host/guest complexes with macrocycles in aqueous solution. *Chemical reviews,* **2011**, *111*, 7941–7980.

(71) Zhang, Z.; Zhang, G.; Wang, J.; Sun, S.; Zhang, Z. The mechanisms of Large Stokes Shift and Fluorescence Quantum Yields in anilino substituted Rhodamine analogue: TICT and PICT. *Computational and Theoretical Chemistry,* **2016**, *1095*, 44–53.

(72) Kim, J.; Lee, M.; Yang, J.-H.; Choy, J.-H. Photophysical Properties of Hemicyanine Dyes Intercalated in Na- Fluorine Mica. *The Journal of Physical Chemistry A,* **2000**, *104*, 1388–1392.

(73) Lee, Y.; Lee, M. Volume Increment Effect on the Photoisomerization of Hemicyanine Dyes in Oligo(ethylene glycol)s. *The Journal of Physical Chemistry A,* **2013**, *117*, 12878–12883.

(74) Epelde Elezcano, N. et al., *Photoactive nanostructured hybrid materials for optical and biomedical applications*; University of the Basque Country UPV-EHU: 2016.

(75) Martínez, V. M., *Intercalación de rodamina 6G en películas ordenadas de arcilla*; Universidad del País Vasco: 2005.

(76) Alarcos, N.; Cohen, B.; Ziółek, M.; Douhal, A. Photochemistry and photophysics in silica-based materials: ultrafast and single molecule spectroscopy observation. *Chemical reviews,* **2017**, *117*, 13639–13720.

(77) Jose, J.; Burgess, K. Benzophenoxazine-based fluorescent dyes for labeling biomolecules. *Tetrahedron,* **2006**, *62*, 11021–11037.

(78) Del Río, M.; Lobo, F.; López, J. C.; Oliden, A.; Bañuelos, J.; López-Arbeloa, I. i.; García-Moreno, I.; Gómez, A. M. One-pot synthesis of rotationally restricted, conjugatable, BODIPY derivatives from phthalides. *The Journal of organic chemistry,* **2017**, *82*, 1240–1247.

(79) López, J. C.; Del Rio, M.; Oliden, A.; Bañuelos, J.; López-Arbeloa, I.; García-Moreno, I.; Gómez, A. M. Solvent-sensitive emitting urea-bridged bis-BODIPYs: ready access to one-pot tandem Staudinger/aza-wittig reaction. *Chemistry- A European Journal* **2017**, *23*, 17511–17520.

(80) Oliden-Sánchez, A.; Sola-Llano, R.; Bañuelos, J.; García-Moreno, I.; Uriel, C.; López, J. C.; Gómez, A. M. Tuning the photonic behavior of symmetrical bis-BODIPY architectures: the key role of the spacer moiety. *Frontiers in chemistry,* **2019**, *7*, 801.

(81) Jiménez, J.; Prieto-Montero, R.; Maroto, B. L.; Moreno, F.; Ortiz, M. J.; Oliden-Sánchez, A.; López-Arbeloa, I.; Martínez-Martínez, V.; de la Moya, S. Manipulating Charge-Transfer States in BODIPYs: A Model Strategy to Rapidly Develop Photodynamic Theragnostic Agents. *Chemistry–A European Journal,* **2020**, *26*, 601–605.

(82) Gómez, A. M.; Uriel, C.; Oliden-Sánchez, A.; Bañuelos, J.; Garcia-Moreno, I.; López, J. C. A Concise Route to Water-Soluble 2, 6-Disubstituted BODIPY-Carbohydrate Fluorophores by Direct Ferrier-Type C-Glycosylation. *The Journal of Organic Chemistry* **2021**, *86*, 9181–9188.

Part II

EXPERIMENTAL DETAILS

This part contains detailed information on the preparation and characterization of the host-guest hybrid materials to help the reader better understand the discussion in Part III.

Inorganic chemical synthesis, one of the pillars of this research project, has allowed the preparation of several hybrid materials based on dye-loaded zeotypes with new potential optical properties. Therefore, in the first place, Chapter 4 explains the basis on the general synthesis procedure employed in this work for the preparation of the aluminophosphates, as well as a step-by-step explanation for each type of zeotypic material (with or without dye).

After crystalline growth of the materials, it is important to analyze and verify the final phase of the resultant systems. In this experimental part of the book, Chapter 5 deals briefly with various structural characterization techniques that are most widely used for aluminophosphates. These include X-Ray diffraction (XRD) for the identification of the final phases and scanning electron microscopy (SEM) to study the morphology of the crystals.

Thereafter, Chapter 6 shows the photophysical techniques employed for the determination of the optical properties of our organic dyes and, above all, of our hybrid materials, which constitute the backbone of this project, including absorption, emission and time-correlated spectroscopy, fluorescence microscopy and other optical techniques.

This thesis is the result of a work between the *Molecular Sieves* group from the *Institute of Catalysis and Petroleochemistry* of CSIC (Madrid), specialized in the synthesis of zeolites and aid-assisted theoretical calculations, and our group, responsible for the selection of suitable dyes and the optical characterization of the resultant hybrid systems. Besides that, sophisticated optical techniques to analyze the second-harmonic generation response and the solid-state microlaser action were carried out in collaboration with the *LuMIn (Light, Material, and Interfaces)* group at the *University of Paris-Saclay (ENS)*.

4

SYNTHESIS OF DYE-LOADED ALUMINOPHOSPHATES

The use of structure directing agents (SDA) transformed the history of zeolite synthesis.

Originally, zeolitic materials were synthesized by using suitable inorganic sources in the synthesis gels; however, in 1961, the range of reagents was extended to include the use of so-called structure-directing agents, SDA, which are usually organic amines or quaternary ammonium cations.[1] The use of these cations completely transformed the synthesis of zeolites and provided a great impetus in the discovery of new families of zeotypes.

Most of the zeolitic materials (zeolites and zeotypes) known today are obtained by hydrothermal synthesis in the laboratory. In fact, the first crystalline microporous aluminophosphates (AlPO) were discovered using this method by Wilson and co-workers in 1982.[2]

Zeolites are prepared by hydrothermal synthesis.

The hydrothermal synthesis of aluminophosphates consists of preparing a homogeneous synthesis gel consisting of an aqueous solution with different metal sources and then subjecting this mixture to crystallization temperatures between 50 and 200 °C under autogenous pressure into autoclaves. These conditions favour the solvation and solubility of the different chemical species present in the reaction medium, promoting the formation of the material.[3–5]

In other words, the synthesis of zeolitic materials involves a first stage of synthesis gel preparation and then the crystalline solid formation. In the following paragraphs, the general process of preparation of the synthesis gels for the family of zeolitic materials studied in this PhD thesis will be explained, followed by a thorough explanation for

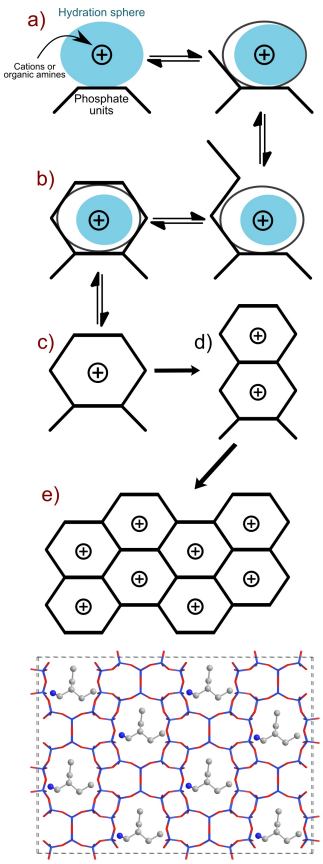

Figure 4.1: The basic mechanism of zeolite assembly driven by structure-directing agents.[6]

each particular inorganic framework (from Section 4.1 to Section 4.7).

In general, to prepare the synthesis gels, the aluminum and phosphorus sources are mixed in water together with the structure directing agent. Since this work focuses on zeotypes and in particular on magnesium or silicon aluminophosphates (see Chapter 2), a third metallic source has to be added to the mixture; thus, while Mg is added in its salt form, Si is added in silica form.

In this initial step, the role played by the structure-directing agent on the formation of the final structure is fundamental, because it governs the synthesis of zeolites. This effect was initially described as the "template effect",[7] in which the organic species organize the tetrahedral units (T-O-T, explained in Chapter 2) around themselves, defining a particular geometry. In this process of "ordering" the amorphous phase of the gel, the T-O-T bonds are progressively formed and broken. The organic amines present in the systems attract the oxide species in their coordination sphere and generate certain preferred geometries with the most energetically favourable orientation.[8] The assembly of the structural elements takes place as represented schematically in Figure 4.1. As a result, the organic molecule drives the synthesis of a given structure and it establishes intermolecular interactions with the zeolitic network, both Van der Waals and electrostatic. The step-by-step mechanism is the following:

- The water molecules create a hydration sphere around the cations, which are progressively replaced by silicate/phosphate[1] units.
- Silicate/phosphate units condense into a chain around the cation until all the water molecules have been completely replaced.

1 Silicate units in aluminosilicates and phosphate units in aluminophosphates

- A preferential topology is established by the maximum interaction between the phosphate chain and the structuring cation.
- Finally, an stable unit is generated, capable of assembling with another similar unit, promoting a certain order and periodicity.

The dye is encapsulated by the crystallization inclusion method.

This work, in addition to obtaining the aluminophosphates, aims to encapsulate dyes into the channels or cavities of the frameworks. For that purpose, the dye incorporation is accomplished by *crystallization inclusion* method.[9] It consists on the direct addition of the fluorophore to the synthesis gel and is occluded "in situ" inside the pores while the inorganic framework is being formed, following the same mechanism that is depicted above for the template in Figure 4.1.

This incorporation method requires guest molecules to be soluble in the synthesis gel, mainly aqueous, and to have molecular structures not very different from those of the SDAs in order not to disrupt the final phase of the system.[10] Another factor that decisively influences the success of the synthesis is their size, being important a good fit between the geometry and size of the molecule and that of the lattice to maximize the interactions between them.

It is the same mechanism as for SDA, so the fluorophores must be similar.

For all these reasons, almost all the fluorescent dyes incorporated here are cationic or have amine or ammonium groups in their structure in order to simulate the same mechanism of the template and help the inorganic framework crystallize around the molecules (there is one exception that will be covered in Section 7.3). A further description of the dyes selected (molecular structure and photophysical properties) is detailed in Section 3.6. This approach, also denominated as "one-pot synthesis"[11] is chosen over post-synthetic diffusional processes due to the advantages it offers:

- There are no traffic jams at the entrances of the pores, reaching a more homogeneous filling of large particles.

- Dye guests with molecular sizes even larger than the entrance of the pore openings can be encapsulated, which is impossible otherwise. There are cases where even though the molecules fit in the cage, they cannot necessarily pass through the windows (due to different dimensions) by diffusion, which drastically limits the possibilities.[12]

Advantages of the crystallization inclusion method over diffusion processes.

- A very tight fit between the pores and the dimensions of the molecular dye is achieved, preventing the leakage of the encapsulated molecules. This factor is key to achieving new or improved optical properties in the final dye-guest system.

- The sample preparation time is shorter as the synthesis is carried out in a unique step.

Once the preparation of the gel is complete, the mixture in the vessel is covered with film and is kept under stirring (between 30 min and 2 h depending on each particular case) and the pH of the gel is measured. Then, the mixture is transferred to a Teflon liner, leaving a space of about one-third of the total volume of the container to ensure optimal pressure (Figure 4.2).

Synthesis procedure by conventional and microwave heating after gel preparation.

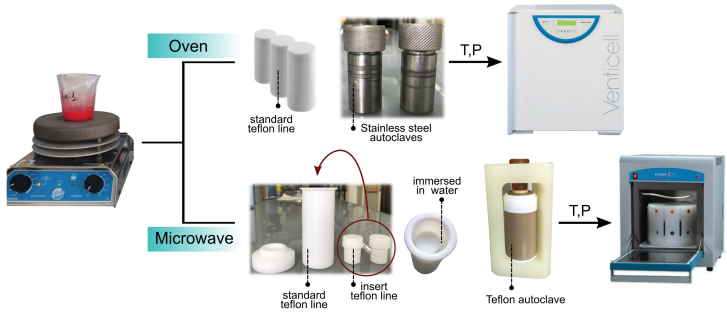

Figure 4.2: The synthesis procedure for the aluminophosphates by conventional (top) and microwave heating (bottom).

Depending on the heating, conventional (CH, *Venticell*) or microwave heating (MW, ETHOS, *Advanced Microwave*

Digestion system), the aqueous mixture is transferred to different Teflon liners and autoclaves (see Figure 4.2). In the case of the oven, standard Teflon lines were used. For the microwave, there are two different types of Teflon lines available: standard and smaller ones called inserts, which are useful for reducing the amount of reagents. In our case, small Teflon lines were used, inserting two of them simultaneously inside the standard Teflon line one on top of the other (represented in Figure 4.2). After, it is filled with water to obtain homogeneous heating. While for the oven approximately 7.8 g are needed, for the microwave the amount is reduced to just 2.8 g. Finally, these liners are placed inside autoclaves, stainless steel autoclave in the former and Teflon autoclave in the latter, and are heated statically or dynamically (continuously rotating) under autogenous pressure, and for reaction times varying from hours to days.

Different Teflon lines and autoclaves employed by CH and MW techniques and the final steps of the synthesis process.

To check if there are any losses, the autoclave is weighed before and after the reaction process. When the reaction is finished, the autoclave is cooled abruptly in water to stop crystal growth. Finally, the resulting material is recovered by filtration, exhaustively washed with distilled water and ethanol, and dried overnight.

In the next sections, the particular syntheses for each framework will be described, as well as the synthesis conditions and reactant proportions, which may change for each case. It is also worth stressing that the crystallization process and the subsequent crystalline structure and physicochemical properties of the materials depend on many factors. The main variables that determine the final structure are the temperature, the composition of the synthesis gel and reaction time:[13–15]

Main variables affecting the resulting system.

- The initial *gel composition* and the *order of reactant addition* influences the crystallization process and therefore the structure and composition of the final phase. Minor changes in the reactant amounts or even in the order of addition can have a strong effect in the initial

solid and liquid phases of the mixture leading sometimes to completely different products.

- *Temperature* of the process. The rate of crystallization is directly proportional to temperature. Hence, at higher temperatures, crystal growth is promoted and generally, denser phases are formed.

- *Reaction time*. Zeolitic materials are metastable phases, exhibiting a system with various equilibrium states in the reaction medium. Consequently, the thermodynamically most stable phase will be formed as the reaction time increases, while those favoured kinetically will be generated at shorter times. This usually results in denser phases at longer times, commonly referred to as Ostwald's rule.[16]

Other variables that should be taken into account.

However, many other parameters can affect the products of reaction, such as reagent type, the degree of mixing, the pH of the medium, the seeding, the presence of cations acting as structure-directing agents, tumbling of autoclaves...[17] All these variables make the process of synthesis very difficult to understand, although attempts will be made to provide some guidelines in the next part of the book (Part III).

4.1 DYE/MAPO-5 (AFI) MATERIALS

Reactants for MgAPO-5 and SAPO-5 synthesis.

The Mg or Si-doped microporous AlPO-5 were prepared using phosphoric acid (H_3PO_4, *Aldrich*, 85 wt%), magnesium acetate tetrahydrate ($Mg(acet)_2{\cdot}4\,H_2O$, *Aldrich*, 99%) for magnesium aluminophosphates (MgAPO) or tetraethyl orthosilicate (TEOS, *Aldrich*, 99%) for silicoaluminophosphates (SAPO), aluminium hydroxide ($Al(OH)_3$, *Aldrich*), triethylamine (TEA, *Aldrich*, 99.5%) as the structure-directing agent and the next chromophores were chosen as dyes of interest: LDS 730 (Styryl 6, 2-[4-[4-(dimethylamino)phenyl]-1,3-butadienyl]-1,3,3- trimethyl-3H-indolium perchlorate, *Exciton*, laser grade) and

DMASBT (trans-2-[4-(dimethylamino)styryl]benzothiazole, *Aldrich*).

The general procedure carried out for the gel preparation is depicted in Figure 4.3.[18] The steps are explained below:

i) Phosphoric acid was mixed with Milli-Q water in a polypropylene vessel and it was kept under vigorous stirring for 2 minutes.

ii) Next, depending on the zeotype to be obtained, the magnesium or silicon source was added to the reactive mixture; being magnesium acetate tetrahydrate for MgAPO-5 and TEOS for SAPO-5.

iii) Aluminium hydroxide was then gently added as the aluminium source and the resulting mixture was left under stirring for another 5-10 minutes.

iv) The structure-directing agent, triethylamine, was added to the reaction gel together with the dye (only in some cases) and was kept stirring for an hour.

v) The pH values of the different gels were then measured. In this case, values between 3 and 6 were registered.

vi) The aqueous mixture was then heated statically at a certain temperature (160 °C or 180 °C) in an autoclave between 2 and 3.5 hours at 500 W in the microwave and for 24 hours in case of conventional heating in the oven.

vii) The solid products were recovered by filtration, exhaustively washed with ethanol and water, and dried at room temperature overnight.

Steps v-vii are repeated continuously for each aluminophosphate material (MgAPO or SAPO) but changing the heating conditions.

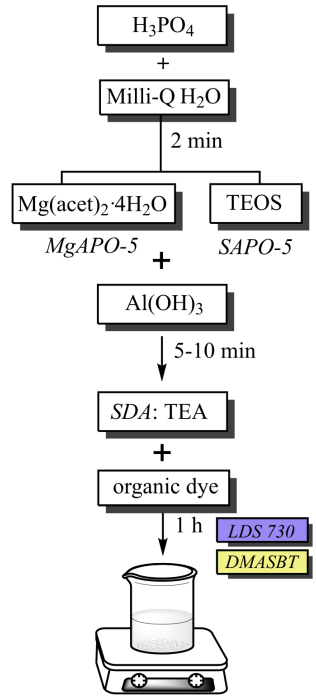

Figure 4.3: General procedure for the gel preparation of MAPO-5.

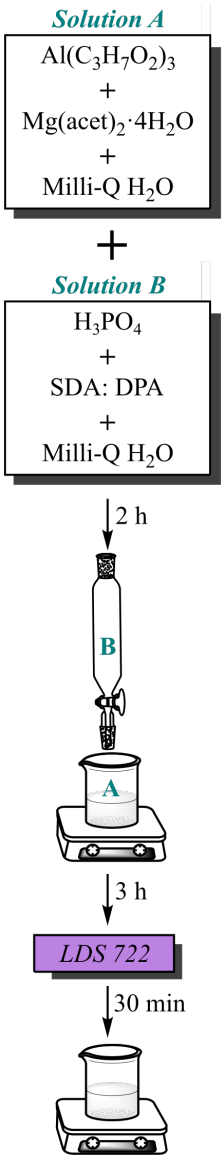

Figure 4.4: Illustrative scheme of the synthesis approach to produce large crystals of MgAPO-11 with LDS 722 dye.

With all these reagents presented herein, gels with the next general molar composition were prepared:

0.2 SiO_2 or x MgO : 1P_2O_5 : (1 − x/2) Al_2O_3 : y TEA : z Dye : w H_2O,

where x is equal to 0.1 or 0.2, y varies from 0.75 to 1.5, z varies from 0.008 to 0.024 and w varies from 300 to 500.

The dyes used in the synthesis of AFI structure were LDS 730 and DMASBT. It is worth noting that highly diluted gels were prepared to ensure the solubility of the dye in the aqueous gel. This type of structure will be expoited in Chapter 7 (Section 7.1 and Section 7.3).

4.2 DYE/MgAPO-11 (AEL) MATERIALS

The synthesis of the MgAPO-11 crystals was carried out in two different ways. The first was used specifically to obtain large crystals and was based on a synthesis by Cheng et. al. with slight modifications.[19]

In this case, aluminum triisopropoxide (Al(O-i-Pr)$_3$, *Aldrich*, 98 wt%), magnesium acetate tetrahydrate (Mg(acet)$_2$·4 H_2O, *Aldrich*, 99 wt%) and orthophosphoric acid (H_3PO_4, *Aldrich*, 85 wt%) were used as sources of aluminium, magnesium and phosphorus, respectively. The structure-directing agent used was dipropylamine (DPA, *Aldrich*, 99%) and all gels were prepared with the next composition:

1.00 Al_2O_3 : 1.04 P_2O_5 : 0.28 MgO : 1.9 DPA : 500 H_2O.

The procedure is illustrated in Figure 4.4 and was followed as described below:

i) Two solutions were prepared and stirred vigorously for 2 hours: in solution A, aluminium triisopropoxide and magnesium acetate tetrahydrate were dissolved in Milli-Q water; and in solution B, ortophosphoric acid and DPA were dissolved in Milli-Q water.

ii) Solution B was added dropwise to solution A under vigorous stirring for another 3 h.

iii) Only in cases where the hybrid system was desired, the dye LDS 722 (Pyridine 2, 4-[4-[4-(dimethylamino)phenyl]-1,3-butadienyl]-1-ethyl-pyridinium perchlorate, *Exciton*) dye was added to the synthesis gel and left in agitation for another half hour.

The prepared gel solution was sealed in a stainless steel autoclave and heated at 180 °C under autogenous pressure for 45-135 h.

The second approach to produce hybrid materials based on the MgAPO-11 structure was prepared with practically the same reagents as in the previous case for magnesium-doped AFI structures (Section 4.1), but varying the SDA to drive the growth of this particular structure. On this occasion, several templates were tested for the synthesis: N-ethylbutylamine (EBA, *Aldrich*, 98%) and dipropylamine (DPA, *Aldrich*, 99%). These syntheses were based on the same gel molar composition described above for the AFI structure (Section 4.1) but further modifications had to be done in the gel preparation process to achieve a pure AEL phase. Figure 4.5 shows the AEL phase synthesis procedure in which the order of addition of the reagents and the stirring time at each step are indicated.[20,21]

The dyes occluded in this framework by this method were LDS 722 (Pyridine 2, 4-[4-[4-(dimethylamino)phenyl]-1,3-butadienyl]-1-ethyl-pyridinium perchlorate, *Exciton*), DMASBT (trans-2-[4-[(Dimethylamino) styryl]benzothiazole, *Exciton*), 4-DASPI (trans-4-[4-(dimethylamino)styryl]-1-methyl-pyridinium iodide, *Aldrich*, 98%), pyronin Y (PY, 3,6-nis(dimethylamino)xanthylium chloride, *Acros Organics*) and acridine (AC, 9-azaanthracene, *Aldrich*, 97%).

The gels were statically heated in the conventional oven at a given temperature (160 °C, 180 °C or 195 °C) for times from 24 hours up to 6 days (larger periods were applied to obtain bigger crystals). Note here that specifically for the LDS 722/AEL system, a certain amount of alcohol (2-propanol, *Scharlab*) was added in the final step to repro-

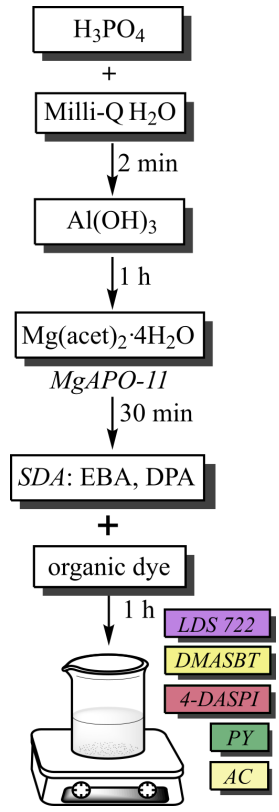

Figure 4.5: General procedure for gel preparation in the synthesis of MgAPO-11.

duce somewhat the conditions necessary for large crystal growth (synthesis described at the beginning of this section), since the Al source added in the previous synthesis (*i.e.* aluminium isopropoxide) was known to generate isopropanol in the synthesis gel. This type of structure will be exploited in Chapter 7 (Section 7.2, 7.3 and 7.4) and Chapter 8 (Section 8.2).

4.3 DYE/MgAPO -36 (ATS) MATERIALS

The reagents, gel molar composition and synthetic procedure for the dye-loaded microporous MgAPO-36 materials was the same as for the MgAPO-5 material (Section 4.1), except for the structure-directing agent, where tripropylamine (TPA, *Aldrich* , 98%) was used.[22–24] In this particular case, the DMASBT dye was the only chromophore occluded in the framework. The gels were statically heated in the conventional oven at 180 °C for 24 h.

4.4 DYE/MgAPO-34 (CHA) MATERIALS

Synthesis gels were prepared with the next molar composition:

0.80 Al_2O_3 : 1 P_2O_5 : 0.47 MgO : 3.3 TEA : 47 H_2O : 0.024 Dye

Orthophosphoric acid (H_3PO_4, *Aldrich*, 85%), pseudobohemite (Al_2O_3, *Sasol*, 75%), magnesium acetate tetrahydrate ($Mg(acet)_2{\cdot}4\,H_2O$, *Aldrich*, 99%) and triethylamine (*Aldrich*, 99.5% TEA) as an SDA were employed as reagents. For the encapsulation 4-DASPI (trans-4-[4-(dimethylamino)styryl]-1-methyl-pyridinium iodide, *Aldrich*, 98%) was selected.

The general synthesis procedure is depicted in Figure 4.6. Pseudoboehmite was added to a solution of orthophosphoric acid in water and left stirring for 15 min. Next, TEA was added to the solution and stirred for 10 min, followed by the addition of magnesium salt and left for an-

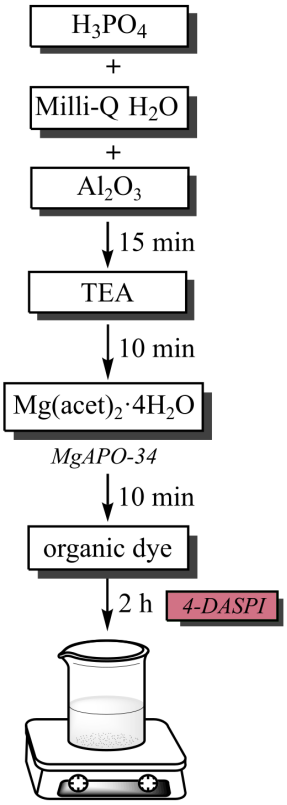

Figure 4.6: Synthesis procedure for dye doped MgAPO-34.

other 10 min of stirring. Then, the organic dye was added and kept stirring for 2 h.[25] The pH was measured and the gel was introduced into autoclaves to be heated statically in the conventional oven at 150 ° C for 48 h. The gel from the autoclaves was filtered, washed with ethanol and water and dried overnight. This type of structure will be exploited in Chapter 7 (Section 7.4).

4.5 DYE/MAPO-56 (AFX) MATERIALS

Synthesis procedure for SAPO-56 or Si-doped AFX.

H_3PO_4 (*Aldrich*, 85%) and pseudobohemite (Al_2O_3, *Sasol*, 75%) were used, together with pyrogenic silica (SiO_2, *Aerosil*, 98%) and N,N,N′,N′-tetramethyl-1,6-hexanediamine (TMHD, *Aldrich*, 99%) as metal source and SDA for Si-doped AFX syntheses, while magnesium acetate tetrahydrate ($Mg(acet)_2{\cdot}4\,H_2O$, *Aldrich*, 99%) and 1,5-bis-(methylpyrrolidinium dihydroxide)-pentane ($MPP(OH)_2$, synthesized in the laboratory and explained in Section 4.5.1) were used instead for Mg-doped AFX gel preparation.

Synthesis gels of the following chemical composition were prepared in the case of Si-doped AFX materials:

$$0.8\ Al_2O_3 : 1\ P_2O_5 : 0.6\ SiO_2 : 2\ TMHD : 40\ H_2O : 0.008\ Dye$$

Following the procedure described in literature,[26,27] all the reagents were added in a specific order (H_2O, H_3PO_4, Al_2O_3, SiO_2, TMHD and organic dye if needed) and stirred for 1.5 h. After that, the pH was measured (≈ 9-10) and left in the oven at 200 °C for 96 h.

Synthesis procedure for MgAPO-56 or Mg-doped AFX.

In case of Mg doped AFX materials the synthesis were prepared with the next general gel molar composition:

$$0.8\ Al_2O_3 : 1\ P_2O_5 : 0.4\ MgO : 1.2\ MPP(OH)_2 : 150\ H_2O : 0.024\ Dye$$

Although the procedure is similar, it is based on a different source.[27] In this regard, all the reagents were added following the next order (H_2O, H_3PO_4, Al_2O_3, $Mg(acet)_4$, $MPP(OH)_2$) and was kept stirring for 1 h. After, the organic

dye was added to the synthesis gel and it was stirred for another additional 30 minutes. Next, the pH was measured and left in the conventional oven at 170 °C or 190 °C for 45 h.

After the heating, the powder was filtered, washed and dried as described in the previous cases. Acridine orange (ACO, N,N,N′,N′-tetramethylacridine-3,6-diamine, *Aldrich*, 99%) and acridine yellow (ACY, 3,6-Diamino-2,7-dimethylacridine monohydrochloride, *Aldrich*, 90%) were occluded inside the cavities of this structure. This structure is cited in the outlook chapter (Chapter 10). It has not been included in the results chapter because it is still under optimization.

4.5.1 *Synthesis of MPP(OH)$_2$*

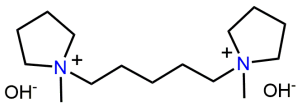

Figure 4.7: Molecular structure of MPP(OH)$_2$

First, 1,5-bis-(methylpyrrolidinium)-pentane dibromide (MPP^{+2} Br^{2-}, Figure 4.7) was prepared by an S_N2 reaction between N-methylpyrrolidine (*Aldrich*, 97%) and 1,5-dibromopentane (*Aldrich*, 97%).[28] N-methylpyrrolidine (25.5 g, 300 mmol) was dissolved in 350 ml of acetone, and 23.0 g (100 mmol) of 1,5-dibromophentane was added dropwise while vigorous stirring. The mixture was stirred under reflux for 48 h, and the organic salt product was collected by filtration, thoroughly washed with acetone and diethyl ether, and dried in vacuum at room temperature.

The resulting bromide salt was finally converted into the hydroxide form through ion-exchange with an anionic resin (*Amberlite IRN-78*, exchange capacity, 4 meq/g; *Supelco*). The resulting basic solution was titrated with HCl (0.1 N, *Panreac*) using phenolphthalein as an indicator, and concentrated by roto-evaporation at 40 °C up to concentrations of 25-30 wt% of (1S,2S)-N,N-ethyl-methyl-pseudoephedrinium hydroxide.

This synthesis was carried out by Luis Gómez Hortigüela at the *Catalysis and Petrochemistry Institute* (CSIC).

4.6 DYE/STA-20 (SWY) MATERIALS

The syntheses were carried out using the gel molar composition indicated below and based on the procedure carried out by Turrina et al.[29,30]

1 $Al(OH)_3$: 0.9 H_3PO_4 : 0.1 SiO_2: 0.42 TrMA : 0.1 (diDABCO)-C6Br_2 : 0.08 TBAOH : 40 H_2O: z Dye

With 2.0 wt% of SAPO-56 (AFX) and where z varies from 0.005 to 0.024.

General procedure for STA-20 synthesis.

In a general procedure for the preparation of STA-20, the reagents were added in the following order and kept stirring: H_3PO_4 (*Aldrich*, 85%), H_2O, fumed silica (*Carbosil*), $Al(OH)_3$ (*Alfa Aesar*), diDABCO-C6 (1,6-(1,4-diazabicyclo[2.2.2]octane)hexyl dibromide, 98%, synthesized in the laboratory and explained in the next Section 4.6.1), trimethylamine TrMA (45 wt% in H_2O, *Aldrich*), TBAOH (tetrabutylammonium hydroxide, 40 wt% in H_2O, *Fluka*) and finally 2% of SAPO-56 seeds (percentage in weight respect to the sum of Al_2O_3, P_2O_5 and SiO_2 and prepared according to the synthesis described above, Section 4.5).

This mixture was kept stirring for 1 h. In the cases where dye-loaded STA-20 materials were prepared, the fluorophore was added in the last step For this framework, LDS 751[2] (6-(Dimethylamino)-2-[4-[4-(dimethylamino)phenyl]-1,3-butadienyl]-1-ethyl-quinolinium Perchlorate, *Exciton*) was chosen.

The role of TBAOH is to adjust the pH to 7 in the synthesis gel.

TBAOH was used to adjust the gel pH to 7, which is necessary for the formation of SWY phase. Therefore, in this step, the pH was continuously measured and TBAOH was added dropwise to fulfil this requirement. Interestingly, for this framework, two templates are needed to direct the formation of two different cavities within the structure: diDABCO-C6 for the bigger cavity (STA-20 cages) and TrMA for the smaller one.

2 This organic dye is no longer commercially available and is often confused with Styril 8.

In order to optimize the synthesis and obtain pure phases systematic variations were carried out. For that reason, different regimes (static and dynamic), temperatures (165 °C and 180 °C) and times (24h and 48 h) were tested. This structure is cited in the outlook chapter (Chapter 10). It has not been included in the results chapter because it is still under optimization.

4.6.1 *Synthesis of diDABCO-C6*

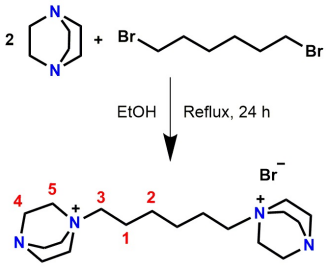

Figure 4.8: Synthesis procedure for diDABCO-C6 molecule.

The organic synthesis of the structure-directing agent diDABCO-C6 (Figure 4.8) for the STA-20 framework was taken from literature.[31] Briefly, the procedure was as follows: 13.0 g (0.05 mol) of 1,6-dibromohexane was dissolved in 50 mL ethanol and added dropwise to a solution of 32.0 g (0.29 mol) 1,4-diazabicyclo[2.2.2]octane (DABCO) dissolved in 100 mL ethanol under stirring at 50 °C. The mixture was refluxed for 24 hours and once cool down, the excess of ethanol was removed by rotary evaporator leaving a white solid. The resulting solid was washed with cold diethyl ether, acetonitrile and acetone, and dried at 50 °C overnight. The reaction yielded 24.11 g (yield 98%) of product.

4.7 DYE/MgITQ-51 (IFO) MATERIALS

The syntheses were carried out using the next general gel molar composition:

0.95 Al_2O_3 : 1 P_2O_5 : x MgO : 1.2 DMAN: y H_2O : 0.008 Dye where x is 0.1 or 0.2 and y is 40 or 100.

First of all, the DMAN (1,8-bis(dimethylamino) naphthalene, 99 wt%, proton sponge, *Aldrich*), Milli-Q H_2O and H_3PO_4 (85%, *Aldrich*) were mixed and the mixture was stirred for 2 hours. Then, a 20 wt% aqueous solution of magnesium chloride hexahydrate ($MgCl_2 \cdot 6\,H_2O$, *Aldrich*) was added to the solution and stirred for 20 min. Finally, the alumina (Al_2O_3, 75%, *Condea*) was added to the gel and left for 30 min.[32,33]

The dyes, Rhodamine 123 (R123; 3,6-Diamino-9-(2-(methoxycarbonyl)phenyl) xanthylium chloride, *Kodak*, laser grade) and/or Nile Blue (NB; 5-aminobenzo[a]phenoxazin-9-ylidene)-diethylazanium, *Exciton*) were incorporated into the gel in this step (if needed) and left for another hour stirring (Figure 4.9). The pH was measured, the gels were transferred to autoclaves and heated in the oven at 150 °C under static conditions for 1 to 5 days. To obtain the microporous aluminophosphate without dye the last step was omitted. This structure will be exploted in the last chapter (Chapter 8, Section 8.1).

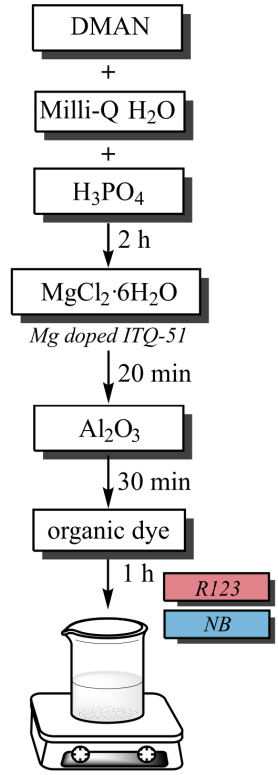

Figure 4.9: General procedure for the gel preparation in the synthesis of Mg-doped ITQ-51.

5

STRUCTURAL CHARACTERIZATION

All the techniques applied for the structural and chemical characterization of our materials are described here.

5.1 X-RAY POWDER DIFFRACTION (PXRD)

PXRD was used for the identification of the crystalline structures.

In order to identify the crystalline structures of solids X-ray powder diffraction (PXRD) was used. The diffraction patterns were collected by using a *Philips X'pert PRO* automatic diffractometer operating at 40 kV and 40 mA, secondary monochromator with Cu-K radiation (λ = 1.5418 Å) and a PIXcel solid-state detector (active length in 2θ = 3.347°). Data were collected from 5 to 80, 2θ (step size 0.026 and time per step 60 s) at RT. A fixed divergence and anti-scattering slit were used giving a constant volume of sample illumination. These measurements were carried out at the *University of the Basque Country (UPV-EHU)*, in *SGIker* advanced research facilities.

5.2 SCANNING ELECTRON MICROSCOPY (SEM)

SEM was used to determine size and morphology of the resultant materials.

The size and morphology of the AlPO materials were characterized by Scanning Electron Microscopy (SEM) in a JEOL JSM-6400 (tungsten filament) and a JEOL JSM-7000F (Field Emission Gun) operating at 20 kV and 10^{-11} A. These measurements were carried out at the *University of the Basque Country (UPV-EHU)*, in *SGIker* advanced research facilities.

6

PHOTOPHYSICAL PROPERTIES

Optical spectroscopy is used to analyze the photophysical behaviour of both organic dyes in solution and hybrid materials, all in an attempt to gain insight into the main properties of these systems. The current section presents detailed information on the experimental techniques employed for the photophysical characterization of our systems. These optical techniques include absorption (UV-Vis spectrophotometry) and emission spectroscopy (steady-state and time-correlated spectrofluorimetry and fluorescence microscopy).

General procedure to measure the photophysical properties of liquid and solid samples.

In general, organic dyes were measured in dilute solutions (2-5 $\cdot$ 10^{-6} M) and in quartz cuvettes of 1 cm. However, when studying the effect of concentration in such systems, cuvettes with different optical paths were used to avoid non-desirable effects such as the inner filter effect (Section 6.2). Regarding this matter, for solutions ranging from 10^{-6} M to 10^{-5} M cuvettes of 1 cm were used, from 10^{-5} M to 10^{-4} M 1 mm cuvettes and when the concentration is higher than 10^{-4} M 0.1 mm optical path cuvettes were used, instead. The hybrid dye/MAPO powder samples were measured in an integrating sphere (explained below in Section 6.1).

Other specific techniques and methods are also explained below, such as NLO measurements, microlaser measurements and computational simulations.

6.1 ABSORPTION SPECTROSCOPY

Figure 6.1: Double beam UV-Vis spectrophotometer (Cary 7000).

Absorption spectra were recorded in a double beam *Agilent Cary 7ooye was not fully soluble in wao* universal measurement spectrophotometer (UMS, Figure 6.1). The UV-Vis spectrometer contains two light sources: a tungsten halogen lamp for the visible region and a deuterium arc lamp for the UV region. It contains a double out-of-plane Littrow monochromator, a ruled line diffraction grating of 1200 lines/nm with a resolution of ± 0.048 nm and a *Hamamatsu R928* photomultiplier as a detector.

Absorption measurements in liquid samples were done in transmittance.

Both liquid and solid samples were measured using this instrumental technique but in different ways. For solutions (organic dyes, standards and dye-loading quantification), the measurements were carried out in transmittance from 200 to 800 nm, with a scan rate of 600 nm/min, an average time of 0.1 s and a data interval of 0.5 nm. All measurements were corrected by baseline correction, recorded with the solvent of each solution as reference. In the specific case of the dye-loaded quantifications, the inorganic framework itself without the dye, dissolved in the same conditions as the sample under study (see more details in Section 6.6), was used as a reference.

Figure 6.2: The internal DRA accessory.

To record the absorption data in bulk powder, an integrating sphere (*Internal DRA 900*, Figure 6.2) was employed to detect the reflected light (see the optical scheme in Figure 6.3). The Internal Diffuse Reflectance accessory (DRA) consists of a 110 mm diameter-integrating sphere in which the reflectance measurement of a sample is made relative to the reference material (either $BaSO_4$ plate or the AlPO without dye). After, the absorption spectra were derived form diffuse reflectance measurements after applying the Kubelka Mulk equation (F(R), Equation 3.6) as described in Section 3.1.1.

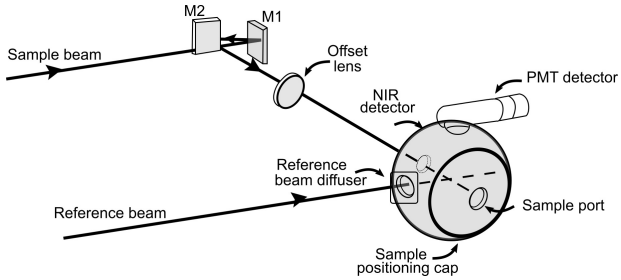

Figure 6.3: The optical design of the DRA.

6.2 FLUORESCENCE SPECTROSCOPY

Figure 6.4: Edinburgh Instruments Spectrofluorimeter, FLSP920 model.

Steady-state measurements were carried out in an *Edinburgh Instruments Spectrofluorimeter* (*FLSP920* model, Figure 6.4), with a 450W continuous xenon arc lamp as the excitation source (*Xe900* model) and a photomultichannel tube (PMT, *Hamamatsu R2658P*) as a detector for the UV-Vis range and a photodiode InGaAs (*Hamamatsu G8605-23*) for the near infrared. The different wavelength response of the optical components was corrected by an emission correction factor applied to the measured spectra.

To obtain fluorescence quantum yields relative method was used for solutions and absolute method for solid samples.

Fluorescence quantum yields were determined using different techniques depending on the state of the sample: a relative method for solutions and an absolute method for solid-state samples. The relative method consists of calculating experimentally the fluorescence quantum yield in solution by comparing the emission of the sample with a reference compound of established fluorescence quantum yield that is independent of the excitation wavelength. Among other requirements, these compounds can be used as a reference as long as they exhibit similar absorption intensity in the same excitation range as the unknown sample and emission in the same range.

When measuring experimentally, the absorbance of the sample and the reference were adjusted until they were almost equal and, once the absorption and emission spectra were recorded, the emission spectra of both solutions measured in the same conditions were compared, calculating the

areas behind each fluorescence band curve and using the following equation.

$$\phi_{fl} = \phi_{fl,R} \frac{I}{I_R} \frac{1 - 10^{-A_R}}{1 - 10^{-A}} \frac{n^2}{n_R^2} \tag{6.1}$$

where I is the intensity area behind the emission band curve, A is the absorbance at the excitation wavelength and n is the refractive index of the medium where each compound is dissolved. Note that the subscript R refers to the values of the reference fluorophore. In this work, several commercial references were used as fluorescence standards, which are mentioned in Part III for each specific case.

However, for measuring fluorescence quantum yields in solid samples, such as powder samples (most of the samples to be studied), this procedure is not feasible. Therefore, for accurate values, absolute fluorescence quantum yields were calculated using the same spectrofluorimeter through an integrating sphere and with a blanking plug made of polytetrafluoroethylene, PTFE. This accessory is 120 mm in diameter and has an inner surface coated with BenFlect to enable efficient scattering of light (nearly 100% diffuse reflectance) over a wide wavelength range (Figure 6.5a).

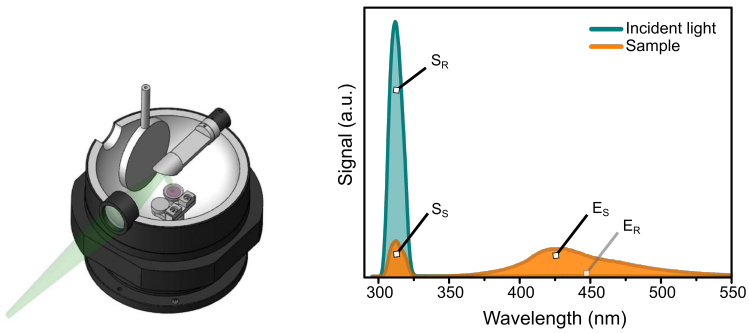

Figure 6.5: **(a)** Integrating sphere accessory. **(b)** Example of a spectrum recorded from a solid sample for the determination of absolute fluorescence quantum yield.

The measurements were performed by direct excitation. The reference scatter and the sample were recorded under the same configuration and conditions on the integrating sphere as shown in Figure 6.6. The emission region of the lamp scatter was also registered for both cases (an example is shown in Figure 6.5b) and both spectra were compared according to Equation 6.2.

$$\phi_{fl,D} = \frac{E_S - E_R}{S_R - S_S} \tag{6.2}$$

where E refers to the area under the curve (integral) of the emission band, S to the reflections or scatter and the subscripts S and R denote the sample and reference, respectively.

Occasionally, in an emission experiment, there may be a significant loss on the fluorescence quantum yield of the dye due to the strong absorption of excitation light.[34] This effect is known as inner filter and consequently makes it difficult to record the fluorescent properties of concentrated solutions, as band shapes often appear distorted as a result of reabsorption of emitted radiation (especially severe for emitters with a small Stokes shift, as it is highly dependent on the spectral overlap).[35] Although these effects can be minimized by controlling the fluorescence signal in a front face configuration, (*i.e.*, in reflection and measuring on the same excitation face) they are always present.

An alternative method to determine and quantify the true fluorescence efficiency is by means of mathematical methods. Therefore, in order to determine the true fluorescence quantum yields, the next steps were followed. First of all, the observed spectra measured with the integrated sphere were compared with a very dilute sample measured in a normal configuration mode. As depicted in Figure 6.7, then, the emission spectra were scaled against each other accurately by tail fitting. From the difference between them, the fraction reduced by reabsorption effect was calculated:

$$a = \frac{\text{Integral}\left(F^{true}\right) - \text{Integral}\left(F^{obs}\right)}{\text{Integral}\left(F^{true}\right)} \tag{6.3}$$

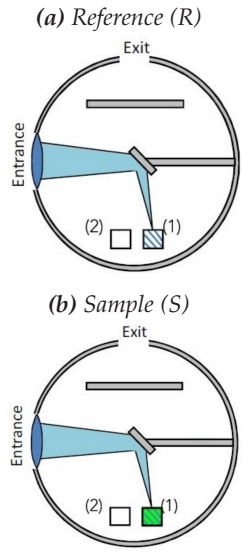

Figure 6.6: Configuration set-up for the direct excitation measurements in the integrating sphere. **(a)** Reference sample (PTFE) in position 1. **(b)** Test sample in position 1. Position 2 remains empty for both measurements. Figure provided by Edinburgh Instruments.

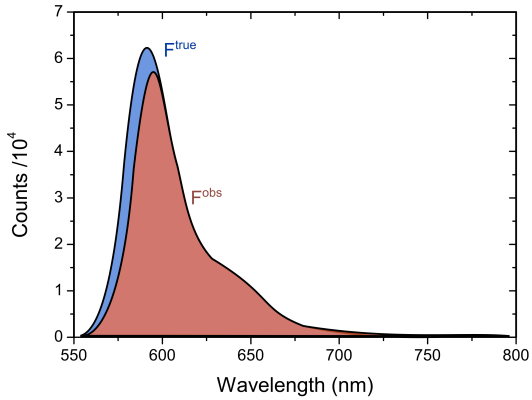

Figure 6.7: True emission spectrum (F^{true}) compared with the fluorescence emission spectrum (F^{obs}) measured in the integrated sphere.

Determination of the true fluorescence quantum yield and supressing the inner filter effects.

Finally, using the following formula the true fluorescence quantum yield was obtained:

$$QY^{true} = \frac{QY^{obs}}{(1-a) + (a \cdot QY^{obs}/100)} \tag{6.4}$$

6.3 TIME-CORRELATED SPECTROSCOPY

Fluorescence decay curves were recorded in the above-cited Edinburgh Instruments Spectroflurimeter (Figure 6.4) by the time-correlated single photon counting (TCSPC) technique and using a microchannel plate photomultiplier (MCP PMT, *Hamamatsu R38090-50*) as a detector.[36,37]

Fluorescence decay curves were registered exciting the samples by a FIANIUM supercontinuum white light laser with 150 ps FWHM (Full Width at Half Maximum) pulses.

The scatter of the laser was avoided in the detection channel by filtering the excitation light with the corresponding cut-off filter (*Lambda Research Optics, Inc.*) placed between the sample and the detector. In general, a power of 0.5 mW, with time windows ranging from 50 to 100 ns and a repetition rate of 10 MHz were employed.

Fluorescence lifetimes (τ) were obtained by the deconvolution method (Figure 6.8), in which the signal of the instrumental response was filtered from the recorded decay curves. To check the quality of the adjustments, the chi-square (χ^2) statistical parameter and the residuals analysis were also monitored.

Fluorescence lifetimes were obtained by deconvolution method.

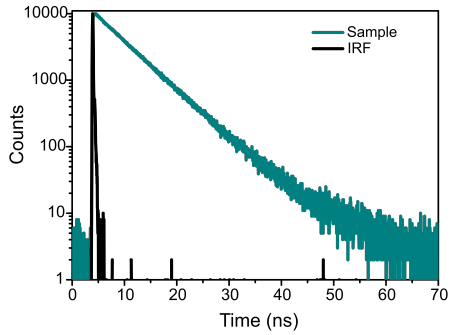

Figure 6.8: Example of a fluorescence decay curve of a sample and the instrument response function (both are used for deconvolution).

Usually, in solid samples, due to the higher heterogeneity in comparison to the solution, a multiexponential behaviour is observed.[38,39] Thereupon, the decay curves are normally adjusted to a sum of exponential decays using Equation 6.5.

In solid samples there is usually multiexponential behaviour, thus the sum of the exponential decays is determined.

$$I_{fl}(t) = \sum_i A_i e^{(-t/\tau_i)} \tag{6.5}$$

where A_i is the pre-exponential term, and τ_i is the fluorescence lifetime. Occasionally, it is difficult to give a physical interpretation of the multi-exponential curves and for this reason, an average lifetime τ is considered according to Equation 6.6:

$$\langle\tau\rangle_{ia} = \frac{\sum A^i \tau_i^2}{\sum A^i \tau_i} \tag{6.6}$$

Long luminescence decay curves were measured similarly, in the same spectrofluorimeter, exciting the sample with a microsecond flash-lamp ($\mu F900$ model, *Edinburgh*

Instruments), recording emission at the maximum fluorescence wavelength and collecting 10000 to 200000 counts at the maximum channel. Fluorescence lifetimes were determined applying an iterative method by the FAST software (*Fluorescence Analysis Software Technology*).

6.4 LASER FLASH-PHOTOLYSIS

Laser Flash Photolysis (LP980, *Edinburgh Instruments*, Figure 6.9) was used to record emission spectra at different delay times after the laser pulse. The spectra were collected with an ICCD detector (*Andor iStar)*. Samples were excited at different wavelengths with a computer-controlled Nd:YAG laser (LS-2134UT-UV3, 1 Hz) coupled to OPO system from LOTIS TII (LT-2215-PC).

Figure 6.9: LP980 Spectrometer of *Edinburgh Instruments*.

6.5 FLUORESCENCE MICROSCOPY

The simplest method for examining the dye-loaded zeotipic compounds is to visually examine the crystals by microscopy. The crystal color is a sensitive indicator of guest species incorporation and crystal imperfections can often be detected as a function of color inhomogeneities. Typically, zeolite crystals loaded with chromophores show almost the same color as the starting solid dye, although sometimes drastic color changes can also be observed, indicating an

influence of the host on the dye or a change in the dye nature during the synthesis process.

Hence, the transmission and fluorescence images of the host-guest systems were recorded with an optical upright widefield microscope with epi configuration (*Olympus BX51*, Figure 6.10a) equipped with a colour CCD camera (DP72). The emission was collected in the same direction of excitation. Indeed, the light emitted from the lamp (120 W short arc lamp, *X-Cite R Series 120Q*, EXFO) positioned in the episcopic lamphouse passed unfiltered (white light) before entering the first interference filter (excitation filter, EX) in the cube set. This light was then directed by a dichroic mirror (DM) that reflects shorter wavelengths to the sample. The fluorescence, emitted by the sample, traveled back freely through the dichroic mirror (letting the longer wavelengths pass through) and finally, was filtered with the emission filters (EM) before arriving at the camera system (Figure 6.10b). Depending on the photophysics of the fluorophore studied, different cube sets were selected: D350/50x (380DCLP dichroic and E400LPv2 cut-off emission) excitation band pass for the UV, D470/70 (495DCLP dichroic and E515LPv2 cut-off emission) for the blue and HQ530/30m (Q660LP dichroic and E580lp cut-off emission) for the red region.

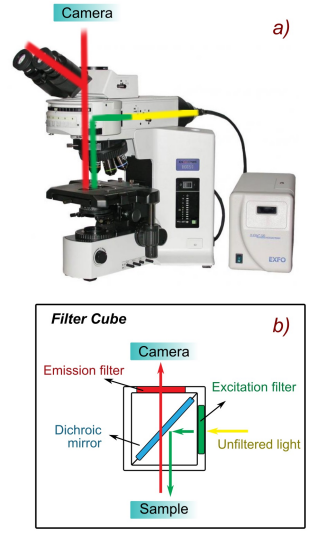

Figure 6.10: **(a)** *Olympus BX51* microscope. **(b)** Scheme of the filter cube.

Linear polarized emission measurements with the optical microscope.

For linear polarized emission experiments, a polarizer (*U-AN-3603*) was incorporated before the registration of the image in the CCD camera. In the present work, these experiments were focused on the fluorescence emission of the ordered systems. In this regard, it is important to note that the fluorescence emission will be maximum if the polarizer placed before detection is collinear to the transition dipole moment of the molecules, and minimum if the polarizer is placed perpendicular (see Fundamentals in Section 3.3).

6.6 PHOTOMETRIC QUANTIFICATION OF THE DYE

An amount of EtOH was added to facilitate dye solubility.

The final dye uptake incorporated in the aluminophosphate frameworks was quantified spectrometrically after dissolv-

ing a certain amount (10 mg) of the sample powder in hydrochloric acid (5 M). However, in some cases where the dye was not fully soluble in water, 80:20 or 50:50 H_2O:EtOH solutions were prepared to help the solubilization of the organic dye in the media.

The quantifications are determined by a calibration method.

The absorption spectra of the samples were compared with the absorptions of the prepared dye standard (known concentrations) solutions, making a calibration curve at analogous conditions. The absorption spectra were recorded with a UV-Vis spectrophotometer (*Cary 7000*), described above in detail (Section 6.1). Dye content values are given throughout this work as mmol dye per 100 g sample powder and in percentage with respect to the initial amount added in the synthesis gel.

6.7 SECOND-HARMONIC GENERATION (SHG) RESPONSE

Single crystal non-linear opical measurements were carried out at École Normale Supérieure (ENS, Paris-Saclay) in the *Laboratory of Light, Matter and Interfaces* (LuMIn).

Set-up for second-harmonic generation measurements.

The SHG response was measured in single crystals of MAPO samples following the steps illustrated in Figure 6.11. With this purpose, an ultrafast Ti: sapphire laser (*Maitai-SP, SpectraPhysics*) was used to generate the NIR (700 nm to 1100 nm) pulses, 120 fs pulse duration (repetition rate 80 MHz) and the polarization of the pulses was controlled by a half-wave plate. The beam was reflected by two short wave pass dichroic beamsplitters (*FF700-SDi01-25x36, Semrock*) in order to compensate s and p polarisation phase delays, and then was focused on the samples using an objective (*PlanApo N.A. 1.4*, x100, *Nikon*).

With this configuration, a wide range of photon flux was available at the sample position. The availability of such a wide range is important for laser power-dependent experiments and key in the investigation of nonlinear processes.

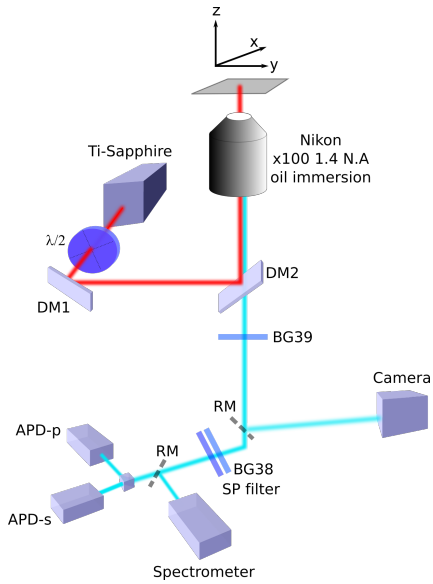

Figure 6.11: Schematic illustration of the SHG measuring set-up.

The sample was mounted on a 3-axis stage (xyz) which allowed scanning and image construction, and SHG was collected by back scatter using the same objective. The generated optical signal was transmitted through the dichroic beamsplitter and through a blue coloured glass filter and a short-pass filter (ET750SP-2P, Chroma) to remove the excitation light. The emitted light was then separated into two polarisation s and p and focused on two avalanche photodiodes for intensity measurement.

6.8 SOLID-STATE LASER ACTION

Set-up for microlaser measurements.

Single crystal solid-state laser measurements were carried out at the *Laboratory of Light, Matter and Interfaces* (LuMIn) in École Normale Supérieure (ENS, Paris-Saclay). An illustrative scheme of the set-up can be seen in Figure 6.12.

The cavity was pumped with a pulsed linearly polarized frequency-doubled Nd:YAG laser (532 nm, 500 ps, 10 Hz). The emission was collected in the substrate plane and injected via a fiber to a spectrometer connected to a cooled

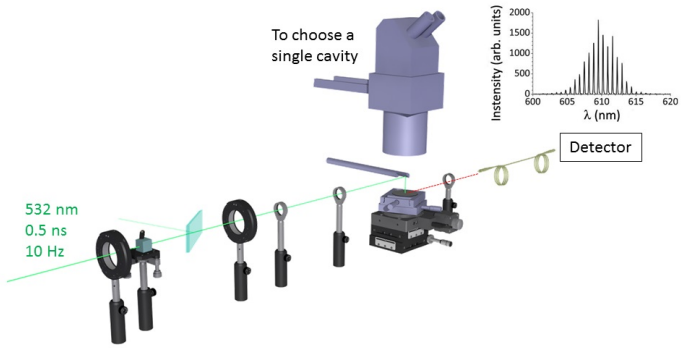

Figure 6.12: Experimental configuration for microlaser action measurements.

CCD camera, with an overall resolution of 0.03 nm. The experiments were performed at room temperature.

6.9 COMPUTATIONAL DETAILS

Determination of ground state optimized geometries.

Ground state (S_0) geometries were optimized by the Density Functional Theory (DFT) using the B3LYP hybrid functional and the triple valence basis set with one polarization function (6-311g*).[40,41] However, in certain cases, the wB97XDA functional was employed when the long-range interactions had to be taken into account.[42] The geometries were checked by the frequency analysis to know whether it corresponded to the true energy minimum and this was confirmed when the analysis did not give any negative value.

Determination of HOMO and LUMO orbitals.

From the optimized geometries, the molecular dipole moments of the organic dyes and the molecular orbitals HOMO (*Highest Occupied Molecular Orbital*) and LUMO (*Lowest Unoccupied Molecular Orbital*) were determined. All the simulations were conducted under the Gaussian 16 software in the computational cluster *ARINA* of the University of the Basque Country (UPV-EHU).

Calculations on the location of dyes embedded within nanoporous MAPO materials (Part III) were carried out by Dr Luis Gómez-Hortigüela from the *Catalysis and Petrochem-*

istry Institute (CSIC). They were based on molecular mechanics simulations as implemented in Forcite module, in Materials Studio 2019 Software.[43]

BIBLIOGRAPHY

(1) Barrer, R.; Denny, P. 201. Hydrothermal chemistry of the silicates. Part IX. Nitrogenous aluminosilicates. *Journal of the Chemical Society (Resumed),* **1961**, 971–982.

(2) Wilson, S. T.; Lok, B. M.; Messina, C. A.; Cannan, T. R.; Flanigen, E. M. Aluminophosphate molecular sieves: a new class of microporous crystalline inorganic solids. *Journal of the American Chemical Society,* **1982**, *104*, 1146–1147.

(3) Cundy, C. S.; Cox, P. A. The hydrothermal synthesis of zeolites: Precursors, intermediates and reaction mechanism. *Microporous and mesoporous materials,* **2005**, *82*, 1–78.

(4) Hamilton, K. E.; Coker, E. N.; Sacco Jr, A.; Dixon, A. G.; Thompson, R. W. The effects of the silica source on the crystallization of zeolite NaX. *Zeolites,* **1993**, *13*, 645–653.

(5) Twomey, T.; Mackay, M; Kuipers, H.; Thompson, R. In situ observation of silicalite nucleation and growth: A light-scattering study. *Zeolites,* **1994**, *14*, 162–168.

(6) Burkett, S. L.; Davis, M. E. Mechanism of structure direction in the synthesis of Si-ZSM-5: an investigation by intermolecular 1H-29Si CP MAS NMR. *The Journal of Physical Chemistry,* **1994**, *98*, 4647–4653.

(7) Lok, B.; Cannan, T.; Messina, C. The role of organic molecules in molecular sieve synthesis. *Zeolites,* **1983**, *3*, 282–291.

(8) Mullin, J. W., *Crystallization*; Elsevier: 2001.

(9) García Salas, R.; Pérez Pariente, J.; Gómez-Hortigüela Sainz, L.; Martínez, V.; López-Arbeloa, Í. Hybrid photoactive material, method for obtaining same and use of the material pat., 2014.

(10) Wöhrle, D; Schulz-Ekloff, G; Bräuchle, C; Laeri, F In *Macromolecular symposia*, 2008; Vol. 270, pp 123–134.

(11) García, R.; Martínez-Martínez, V.; Gómez-Hortigüela, L.; Arbeloa, Í. L.; Pérez-Pariente, J. Anisotropic fluorescence materials: Effect of the synthesis conditions over the incorporation, alignment and aggregation of Pyronine Y within MgAPO-5. *Microporous and mesoporous materials,* **2013**, *172*, 190–199.

(12) Husing, N, *Porous hybrid materials*; Kickelbick, G., Ed.; Wiley Online Library: 2006.

(13) Petrov, I.; Michalev, T. Synthesis of zeolite A: a review. *Scientific works of the University of Ruse,* **2012**, *51*, 30–35.

(14) Davis, M., *Mesoporous zeolites: preparation, characterization and applications*; John Wiley & Sons: 2015.

(15) Barrer, R. M. Zeolites and their synthesis. *Zeolites,* **1981**, *1*, 130–140.

(16) Van Santen, R. A. The Ostwald step rule. *The Journal of Physical Chemistry,* **1984**, *88*, 5768–5769.

(17) Guozhong, C; Ying, W, *Nanostructures and Nanomaterials: Synthesis, Properties and Applications*; ACS Publications: 2004.

(18) Oliden-Sánchez, A.; Sola-Llano, R.; López-Arbeloa, I.; Martínez-Martínez, V. Enhancement of NIR emission by a tight confinement of a hemicyanine dye within zeolitic MgAPO-5 nanochannels. *Photochemical & Photobiological Sciences,* **2018**, *17*, 917–922.

(19) Chen, Y.; Zhai, J.; Xu, X.; Li, I.; Ruan, S.; Tang, Z. Synthesis of large MgAPO-11 single crystals in a F- free system. *CrystEngComm,* **2014**, *16*, 2984–2989.

(20) Sola-Llano, R.; Martínez-Martínez, V.; Fujita, Y.; Gómez-Hortigüela, L.; Alfayate, A.; Uji-i, H.; Fron, E.; Pérez-Pariente, J.; López-Arbeloa, I. Formation of a nonlinear optical host–guest hybrid material by tight confinement of LDS 722 into aluminophosphate 1D nanochannels. *Chemistry–A European Journal,* **2016**, *22*, 15700–15711.

(21) Sola-Llano, R.; Oliden-Sánchez, A.; Alfayate, A.; Gómez-Hortigüela, L.; Pérez-Pariente, J.; Arbeloa, T.; Hofkens, J.; Fron, E.; Martínez-Martínez, V. White Light Emission by Simultaneous One Pot Encapsulation of Dyes into One-Dimensional Channelled Aluminophosphate. *Nanomaterials,* **2020**, *10*, 1173.

(22) Sola-Llano, R.; Gartzia-Rivero, L.; Oliden-S´nchez, A.; Bañuelos, J.; Arbeloa, I. L.; Martínez-Martínez, V., Dye encapsulation into one-dimensional zeolitic materials for optical applications In *Chemistry of Silica and Zeolite-Based Materials*; Elsevier: 2019, pp 229–248.

(23) Sola-Llano, R.; Fujita, Y.; Goímez-Hortiguela, L.; Alfayate, A.; Uji-i, H.; Fron, E.; Toyouchi, S.; Peírez-Pariente, J.; Loípez-Arbeloa, I.; Martínez-Martínez, V. One-directional antenna systems: Energy transfer from monomers to J-Aggregates within 1D nanoporous aluminophosphates. *ACS photonics,* **2017**, *5*, 151–157.

(24) García, R.; Martínez-Martínez, V.; Sola Llano, R.; Loípez-Arbeloa, I.; Peírez-Pariente, J. One-dimensional antenna systems by crystallization inclusion of dyes (one-pot synthesis) within zeolitic MgAPO-36 nanochannels. *The Journal of Physical Chemistry C,* **2013**, *117*, 24063–24070.

(25) Concepción, P; Nieto, J. L.; Mifsud, A; Pérez-Pariente, J Preparation and characterization of Mg-containing AFI and chabazite-type materials. *Zeolites,* **1996**, *16*, 56–64.

(26) Pinilla Herrero, I., *Diseño de materiales SAPO de poro pequeño para su ensayo como catalizadores en el proceso MTO*; Universidad Autónoma de Madrid: 2016.

(27) Maple, M. J.; Williams, C. D. Synthesis and characterisation of aluminophosphate-based zeotype materials prepared with α, ω-bis (N-methylpyrrolidinium) alkane cations as structure-directing agents. *Dalton Transactions,* **2007**, 4175–4181.

(28) Kasneryk, V.; Shamzhy, M.; Zhou, J.; Yue, Q.; Mazur, M.; Mayoral, A.; Luo, Z.; Morris, R. E.; Čejka, J.; Opanasenko, M. Vapour-phase-transport rearrangement technique for the synthesis of new zeolites. *Nature communications,* **2019**, *10*, 1–8.

(29) Casci, J.; Turrina, A.; Garcia Salas, R.; Wright, P. Methods of producing SAPO-56, an AFX-containing molecular sieve pat., 2018.

(30) Turrina, A.; Garcia, R.; Watts, A. E.; Greer, H. F.; Bradley, J.; Zhou, W.; Cox, P. A.; Shannon, M. D.; Mayoral, A.; Casci, J. L. et al. STA-20: an ABC-6 zeotype structure prepared by co-templating and solved via a hypothetical structure database and STEM-ADF imaging. *Chemistry of Materials,* **2017**, *29*, 2180–2190.

(31) Turrina, A.; Garcia, R.; Cox, P. A.; Casci, J. L.; Wright, P. A. Retrosynthetic co-templating method for the preparation of silicoaluminophosphate molecular sieves. *Chemistry of Materials,* **2016**, *28*, 4998–5012.

(32) Martínez-Franco, R.; Moliner, M.; Yun, Y.; Sun, J.; Wan, W.; Zou, X.; Corma, A. Synthesis of an extra-large molecular sieve using proton sponges as organic structure-directing agents. *Proceedings of the National Academy of Sciences,* **2013**, *110*, 3749–3754.

(33) Martínez-Franco, R.; Paris, C.; Moliner, M.; Corma, A. Synthesis of highly stable metal-containing extra-large-pore molecular sieves. *Philosophical Transactions of the Royal Society A: Mathematical, Physical and Engineering Sciences,* **2016**, *374*, 20150075.

(34) Braslavsky, S. E. Glossary of terms used in photochemistry, (IUPAC Recommendations 2006). *Pure and Applied Chemistry,* **2007**, *79*, 293–465.

(35) Lakowicz, J. R., *Principles of fluorescence spectroscopy*; Springer: 2006.

(36) Demas, J. N., *Excited State Lifetime Measurements Academic*; Academic Press: 1983.

(37) O'Connor, D.; Phillips, D, *Time-Correlated Single-Photon Counting*; Academic press: 1984.

(38) Rurack, K.; Hoffmann, K.; Al-Soufi, W.; Resch-Genger, U. 2, 2 '-Bipyridyl-3, 3 '-diol Incorporated into $AlPO_4$-5 Crystals and Its Spectroscopic Properties as Related to Aqueous Liquid Media. *The Journal of Physical Chemistry B*, **2002**, *106*, 9744–9752.

(39) Wiederrecht, G. P.; Sandi, G.; Carrado, K. A.; Seifert, S. Intermolecular dimerization within pillared, layered clay templates. *Chemistry of Materials*, **2001**, *13*, 4233–4238.

(40) Krishnan, R.; Binkley, J. S.; Seeger, R.; Pople, J. A. Self-consistent molecular orbital methods. XX. A basis set for correlated wave functions. *The Journal of Chemical Physics*, **1980**, *72*, 650–654.

(41) Frisch, M. J.; Pople, J. A.; Binkley, J. S. Self-consistent molecular orbital methods 25. Supplementary functions for Gaussian basis sets. *The Journal of Chemical Physics*, **1984**, *80*, 3265–3269.

(42) Chai, J.-D.; Head-Gordon, M. Long-range corrected hybrid density functionals with damped atom–atom dispersion corrections. *Physical Chemistry Chemical Physics*, **2008**, *10*, 6615–6620.

(43) Module, F. Material Studio. *Accelrys Software Inc.* **2013**.

(44) Gándara, F.; López-Arbeloa, F.; Ruiz-Hitzky, E.; Camblor, M. A. "Bottle-around-a-ship" confinement of high loadings of Acridine Orange in new aluminophosphate crystalline materials. *Journal of Materials Chemistry*, **2006**, *16*, 1765–1771.

Part III

RESULTS AND DISCUSSION: DYE-DOPED ZEOTYPES

This part of the book aims to respond to the growing demand for new advanced materials with multiple functionalities to be used in diverse applications such as in the field of photonics. For this purpose, new solid-state hybrid materials with improved optical properties have been developed, based on the combination of photoactive organic molecules with mesoporous aluminophosphate systems of different pore sizes and shapes.

All these tested combinations between chromophores and zeotypes will be covered here, providing a thorough analysis of the results obtained by synergistic effects for each particular dye-doped zeotype system. The new and/or improved properties obtained will be highlighted throughout the chapters, giving special emphasis to the enhancements in the photophysical properties of the dyes, including their fluorescent capacities and the appearance of interesting optical features such as nonlinear optical properties (SHG), microlaser action, or white light emission.

7

STYRYL DYES INTO MAPOs

Systems capable of capturing and emitting light in different regions of the electromagnetic spectrum are of great interest when designing materials for optical applications. In recent years, special interest has been given to the development of materials with spectroscopic bands in the red and near-infrared (NIR) region due to their importance in the field of biomedical imaging for diagnostic and therapeutic applications.[1–3] In these fields, in particular, materials emitting in the range of 700 and 1000 nm are very attractive, as background interference from organisms and tissues is minimized and penetration depth enhanced, allowing the acquisition of highly sensitive fluorescence images in a non-invasive manner. However, fluorophores that can emit from this low-energy region have a small energy gap between the excited state S_1 and the ground state S_0 and the fluorescence can be easily quenched by other non-radiative deactivation pathways (*e.g.* internal conversion), which intensifies the search for suitable dyes.[4–6]

Materials emitting in the NIR region are very interesting for biomedical applications.

In this chapter, dyes from the styryl family have been selected for the encapsulation into the pores of metal-doped AlPO frameworks due to their suitable fluorescence spectroscopic bands at the red edge of the visible spectrum. In particular, four dyes, LDS 730, LDS 722, DMASBT, and 4-DASPI (Section 3.6.1) that emit at low frequencies of the visible spectrum[7–9] will be covered in order to achieve systems with diverse photophysical properties.

Styryl dyes will be encapsulated into MAPOs.

These dyes possess extended π-conjugated systems with donor-acceptor (D-A) building blocks and are chro-

They are push-pull molecules composed of D-A building blocks that emit from an ICT state.

mophoric systems with emission bands highly red shifted with respect to the absorption peak, since their emission does not come from the directly excited state but an intramolecular charge transfer (ICT) state (general photophysical properties of styryls are discussed in Section 3.6.1 and CT states in Section 3.2.2.2).[10,11] This strong push-pull character makes them very promising organic molecules for advanced functional materials and various applications, including nonlinear optics (SHG), organic light-emitting diodes (OLEDs), and bioimaging.[9,12–15] However, as very flexible molecules, their rotational motions cause the intramolecular charge transfer usually to be non-fluorescent. In particular, they undergo a torsion that results in a twisted intramolecular charge transfer state (TICT, Section 3.6.1), characterized by poor fluorescence quantum yields in solution.[16–18]

They are very flexible and do not have fluorescence.

To limit the non-radiative deactivation pathways they will be encapsulated.

Interestingly, this ultrafast (picoseconds) twisting process characteristic of these dyes can be hindered by increasing the viscosity of the medium.[17,19,20] Therefore, in this study, in an attempt to limit the probability of non-radiative deactivation pathways of the excited states by slowing down the internal motions of styryl molecules, the dyes have been encapsulated into channeled MAPOs of small pore size by the *crystallization inclusion* method (Chapter 4). In this way, the fluorescent efficiency of materials emitting in the red or NIR window is expected increase.

1D-channeled AlPOs are used for highly ordered systems and 3D-cages for comparison.

To date, the group's research has focused on the study of solid matrices of nanostructured inorganic materials, especially AlPO with one dimensional channeled structures, with the aim of obtaining highly ordered and fluorescent solid systems for the design of new devices.[21–27] With the same intention, this chapter will deal especially with this type of unidirectional porous systems, specifically, those with AFI, ATS, and AEL structures that have a suitable size to accommodate dyes of different molecular dimensions and geometry; and will conclude with a structure called CHA with pocket-like cavities instead of 1D-channels, allowing to make a comparison with the aforementioned

channeled systems (all structures explained in Section 2.4 and complete data sheets in the Appendix A).

Nonlinear properties such as SHG can be promoted by the synergism of both components.

The confinement provided by the channeled pores allows to achieve various zeolite-based host/guest materials with excellent optical properties, such as emission in the red-NIR region, which could lead, for example, to possible applications in microlasers or nanoscale lasers, since the combination between the pores and the hosted molecules can influence the photophysical properties of the latter. Moreover, with the non-centrosymmetric arrangement obtained in the system due to the unidirectional channels of the structure, nonlinear optical properties such as second-harmonic generation (SHG) can be obtained.

This materials have been prepared by CH and MW heating techniques.

These materials have been synthesized by two heating techniques, using both conventional oven and microwave heating; and the trends in crystallization behavior for each specific system as well as the resulting photophysical properties are analyzed, in order to determine the advantages and disadvantages of each and make a comparison.

Throughout this chapter, the four push-pull styryl dyes used for the encapsulation into unidirectional nanochannel structures have been organized mainly according to their absorption region in solution, as they exhibit emissions in almost the same region of the visible spectrum (yellow-red region) due to the photoinduced formation of intramolecular charge-transfer in the excited state. Thus, the following sections are ordered starting from those with absorptions placed at lower frequencies to those with absorptions at higher frequencies, that is, from the red to the blue region of the visible light spectrum, following this order: LDS 730 > LDS 722 > DMASBT > 4-DASPI (see Table 3.2 in Section 3.6.1).

The following sections are ordered by the absorption characteristics of the dyes from the red to the blue region.

Among the systems to be discussed in this chapter, two publications related to the LDS 730/AFI system (Section 7.1) should be highlighted.

7.1 LDS 730 DYE WITHIN SEVERAL MAPO-5 HOSTS

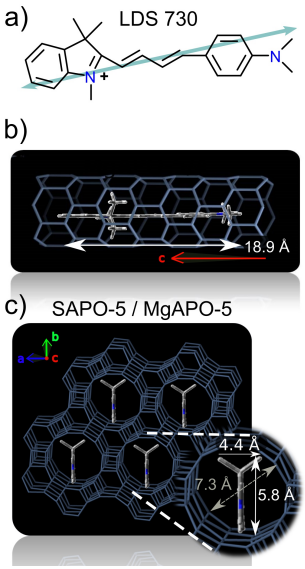

Figure 7.1: **(a)** Molecular structure of LDS 730 with its dipolar moment (blue arrow). **(b)** Illustrative representation of its encapsulation into AlPO-5 (AFI phase) structure[28] along the c-axis of the channel and **(c)** c-axis perpendicular to the plane. The molecular dimensions of the guest and the size of the host channels are also displayed.

Among the selected fluorophores, in the first section, we deal with the most reddish absorbing dye, LDS 730, a very good candidate to develop a new hybrid solid material with interesting optical characteristics in the NIR region. For its occlusion, the inorganic zeolitic structure aluminophosphate five (AlPO-5) with AFI-type structure is used as a host (see Figure 7.1). So far, it is one of the most widely used structures for the incorporation of fluorescent dyes;[29] in fact, MgAPO-5 was the first Mg-doped AlPO synthesized by our group for the development of new hybrid materials.[30] Briefly, the framework (shown in Figure 7.1) has non-interconnected cylindrical channels running along the c-axis of the structure (unidirectional channels). It is classified as a large pore structure formed by 12 MR windows (Section 2.3), resulting in circular channels of 7.3 Å in diameter (Section 2.4 and Section A.1), a dimension that fits very well with the molecular size of many photoactive molecules as demonstrated so far.[24,30,31]

Given that this structure is thermodynamically very stable and easy to crystallize, in this section, Si and Mg heteroatoms have been employed as dopants to generate the SAPO-5 and MgAPO-5 structures respectively (refer to Section 2.2 for the substitution mechanism) in order to analyze the effect of the dopant on the photophysical properties of the resulting hybrid system. Taking advantage of the ease to obtain this phase, in addition to microwave heating, the conventional heating method has also been tested in the synthesis for the Mg-doped framework. In this way, it is possible to determine the benefits of each heating method and establish clear conclusions that can serve as a reference for the rest of the systems, applying the best choice according to the main objective pursued.

As mentioned before, the hemicyanine LDS 730 chromophore (also known as Styryl 6) with a molecular size of 4.4 Å x 5.8 Å x 17.8 Å, matches perfectly with the pore opening of the AFI zeolitic material (Figure 7.1). Therefore, the final hybrid system LDS 730/AFI, is synthesized with the

goal of developing an outstanding material that emits electromagnetic radiation in the near-infrared region. In the following lines, the results of several publications,[32,33] as well as other findings, will be described in detail.

7.1.1 *Photophysics of LDS 730 in solution*

To study the subsequent photophysical characteristics of the hybrid materials, the first step was to study the photophysics of the guest dye in solution. For this purpose, the LDS 730 dye was analyzed in aqueous media, H_2O and H_2O : EtOH (80:20) mixture, to mimic the conditions of the hybrid system and resemble the synthesis gel environment. The slight change in the polarity of the medium by the addition of a small amount of alcohol allows us to better solubilize the dye and analyze its photophysics under different conditions.

In aqueous neutral solution, the dye shows a high absorption capacity in the visible range, with a band centered at 573.0 nm with an absorption coefficient of ε_{max} = 2.2 $\cdot 10^4$ M^{-1} cm^{-1}; together with a reminiscent emission placed at 700.0 nm with very low fluorescence quantum yield (lower than 0.1%). It displays a very large Stokes shift (3166 cm^{-1}, Figure 7.2), a consequence of the formation of an intramolecular charge transfer state upon excitation (ICT, Figure 7.3).

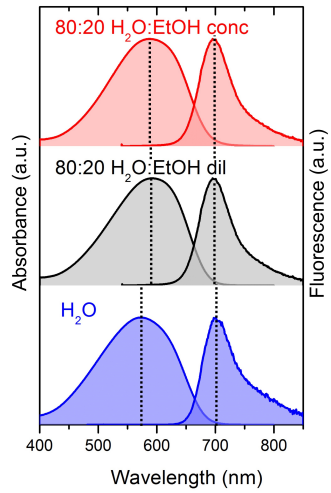

Figure 7.2: Height normalized absorption and emission spectra upon excitation at 530 nm recorded for LDS 730 (aq) at pH = 7 (blue), in 20% EtOH diluted (black) and in 20% EtOH concentrated (red) solutions.

As commented above, this behavior is related to the nature and structure of styryl dyes,[34] since they contain an electron donor group conjugated to an electron-withdrawing group, being amino ($-NMe_2$) and methyl pyrrole (heterocycle) groups respectively, for this particular case (structure given in Figure 7.1a). Excitation of this fluorophore induces the promotion of an electron from the highest occupied orbital (HOMO) to the lowest unoccupied orbital (LUMO) with a characteristic change in the electronic distribution of the molecule, as demonstrated by the theoretical computational calculations depicted in Figure 7.3. According to these calculations, the electron densit-

ies in the initial and final orbitals are distributed differently: in the HOMO state, the electron density is mainly concentrated in the amino group while in the LUMO it is located in the methyl pyrrole, indicating that a charge transfer is taking place.[35]

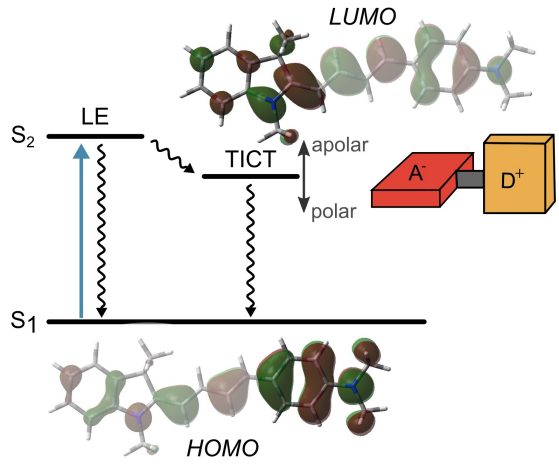

Figure 7.3: Illustration of the intramolecular charge transfer (ICT) mechanism involved upon photoexcitation. The change in electronic distribution between the HOMO and LUMO states in the hemicyanine LDS 730 dye is shown schematically, representing a partial electron transfer from the donor ($-NMe_2$) to the acceptor site (methyl pyrrole) of the molecule. An illustrative figure of the rotation that occurs between the donor (orange) and acceptor (red) of the molecule to a more relaxed, non-fluorescent TICT state is also added. The main photophysical phenomena involved are represented schematically in the Jablonsky diagram (radiative and non-radiative transitions are depicted by solid and curved lines, respectively).

Consequently, in the pure aqueous polar medium, the excited state reached upon excitation (LE state) quickly reverts to the ICT state, because during its lifetime the solvent molecules rotate to reach a more relaxed final state (Section 3.2.2.2).[36] Such a solvent relaxation explains the increase in the red shift of the fluorescence spectrum observed experimentally as the polarity of the solvent was increased (photophysical data given in Table 7.1). In fact,

Table 7.1: Photophysical parameters - absorption (λ_{abs}) and fluorescence maxima (λ_{fl}), molar absorption coefficient (ε_{max}), fluorescence quantum yield (ϕ_{fl}) and fluorescence lifetimes (τ) - of different LDS 730 (aq) dye solutions at several concentrations.

Solvent	λ_{abs} (nm)	λ_{fl} (nm)	$\varepsilon_{max} \cdot 10^{-4}$ ($M^{-1}cm^{-1}$)	ϕ_{fl}	τ (ns)
H_2O					
$6 \cdot 10^{-6}$ M	573.0	700.0	2.2	< 0.01	< 0.1
H_2O:EtOH 80:20					
$6 \cdot 10^{-6}$ M	591.0	695.0	6.8	< 0.01	< 0.1
$6 \cdot 10^{-4}$ M	590.5	695.0	-	-	-

with a slight change in the polarity of the medium (the dielectric constants of water and ethanol are ε_{H_2O} = 80.1 Fm^{-1} and ε_{EtOH} = 25.3 Fm^{-1}) variations in the emission maxima are already observed between pure water solution (λ_{fl} = 700.0 nm,) and a mixture with 20% EtOH (λ_{fl} = 695.0 nm), and observing a 5 nm bathochromic shift due to a higher stabilization of the CT state in excitation.

The photophysical results show that when ethanol is added to water solution in a 20%, the absorption band shifts 18 nm to higher wavelengths (from λ_{abs} = 573 nm in pure H_2O to λ_{abs} = 591 nm in 20% EtOH, Table 7.1 and Figure 7.2), along with an increase of absorbance capacity (from $\varepsilon_{max} = 2.2 \cdot 10^4$ M^{-1} cm^{-1} to $6.8 \cdot 10^4$ M^{-1} cm^{-1}). In general, this effect is attributed to the fact that very polar and protic solvents (*e.g.* water) have specific interactions with the donor amine group ($-NMe_2$), thus reducing its electron-giving character and hence the delocalization of its free electron pair and conjugation of the aromatic system.[36]

However, it should be noted that generally the ground state is more stabilized by hydrogen bonding than the excited state. Indeed, the calculated HOMO-LUMO orbitals display a reduction of the electron density on the donor nitrogen atom after excitation, lowering its ability to form hydrogen bonds in the excited state. Therefore, delocalization and conjugation are feasible in the excited state in a

more polar environment, resulting in a slightly higher red shift of the fluorescence maxima, due to a greater stabilization of the ICT (from λ_{abs} = 695 nm in 20% EtOH to λ_{abs} = 700 nm in H_2O).

In order to analyze the aggregation effect, a more concentrated sample ($6 \cdot 10^{-4}$ M) was prepared in 20% EtOH aqueous solution since this percentage of ethanol greatly enhances the solubility of the dye in comparison to that in water. At high dye concentration, the positions and shapes of the absorption and emission bands are practically the same, meaning that there is no tendency to form aggregates in the studied range (see Figure 7.2).

Regarding its fluorescence properties, since the molecule undergoes internal rotations via different pathways around different single and double bonds, it demonstrates poor fluorescence quantum yields and very short lifetimes in solution ($\phi_{fl} < 0.01$ and $\tau < 0.1$ ns, see Table 7.1). In fact, neither the quantum yield nor the lifetime could be properly registered because they lay under the detection limit of the spectrofluorimeter (*i.e.* the decay curve obtained was similar to the IRF "instrument response function").[16,33]

In this regard, the tight confinement of the LDS 730 dye into a 1D-nanoporous host is crucial to limit its flexibility. The reduced channel spacing is expected to prevent free rotation of the molecule moieties and thus reduce the non-radiative probability, as well as an aligned arrangement of the dye along the channels. Moreover, the inorganic framework may induce a more planar configuration of the dye (with the donor and acceptor molecules almost in the same plane) and promote an emission from a more planar intramolecular charge transfer (denoted as PICT) state, thus hindering any twist of the amine group ($-NMe_2$), that could lead to the formation of twisted intramolecular charge transfer (denoted as TICT state) characterized by a poor or null emission (see more details in Section 3.6.1).

7.1.2 *Dye-SAPO-5 by microwave heating*

Previous experiments performed in the group to obtain dye-zeotype hybrid systems by conventional hydrothermal synthesis have given rise to very promising results.[24,25,27] However, the incorporation of the dye along the channel in some situations was inhomogeneous and generated other minority phases.[25] Furthermore, conventional heating demands large periods of time (from 12 hours to a few days). Fortunately, microwave (MW) irradiation is a good alternative to synthesize hybrid systems in shorter times and with smaller amounts of gel. This technique offers homogeneous heating and avoids the undesired temperature gradients that usually occur during conventional heating.[33]

Thus, to benefit from the advantages described above, the syntheses of Si-doped AFI systems (SAPO-5) were performed by microwave (MW) irradiation making use of the smaller Teflon inserts instead of the typical large ones (synthesis procedure explained in Chapter 4), using a smaller amount of synthesis gel than that normally used. The synthesis employed was originally based on a previous work reported by Dang et al.[37] with slight changes in the gel composition, that is, the addition of a larger amount of water to obtain a dilute gel and aid subsequent solubilization of the LDS 730 dye in the crystallization process (Section 4.1).

The SAPO-5 materials were prepared from gels with the following molar composition and using TEA as a template:

$$0.2\ SiO_2 : 0.9\ P_2O_5 : 1\ Al_2O_3 : y\ TEA : z\ LDS730 : 300\ H_2O$$

varying the amount of SDA (TEA) from y = 0.75 to y = 1.50, and performing the syntheses without dye (z = 0) in cases where the main purpose was to optimize the synthesis of the inorganic framework as a host, or adding z = 0.024 dye when the formation of the dye-zeotypic hybrid system was desired. It is worth mentioning that for all the syntheses that will be presented below, TEOS was used as a source of Si with a 0.2 amount in the gel composition. However, other Si sources such as MAOPTMS

(3-(trimethoxysilyl) propyl methacrylate) and VTES (triethoxyvinylsilane) were also tested, as well as different amounts of SiO_2 (0.1 SiO_2), although these will not be explained here because they did not favor the host formation.

It should be pointed out that according to the thermogravimetric analysis, LDS 730 dye degrades at 260 °C, a temperature determined by the derivative of the registered curve (see Figure C.1 in the Part V). As a consequence, LDS 730 dye cannot withstand very high temperatures under the harsher conditions of hydrothermal synthesis, Since the thermogravimetric analysis (Figure C.1) was performed under atmospheric pressure conditions without taking into account the autogenous pressure generated inside the autoclave. Fortunately, as stated before, AFI structure is a thermodynamically favored structure and generally, it does not require a very high temperature in the synthesis to reach a pure phase. Therefore, the gels were introduced in two identical inserts and heated in the microwave for 5 minutes until a temperature of 160 °C was reached, and then it was kept for different heating times at 500 W in order to optimize conditions. A temperature well below the experimental degradation value obtained in the TGA was always kept, since a higher degradation is expected in the harsher conditions inside the autoclaves (evaluated for other dyes).[38]

All the variations and the different attempts carried out are shown in Table 7.2. A list of all syntheses performed during this thesis categorized by the type of hybrid system (with or without dye) and with their exact real compositions can also be found in Part V of the book (Appendix B). The nomenclature used in this work has always followed the same criterion. In all of them, first, the synthesized structure and the heteroatom used as dopant is specified. Then, several criteria is applied to differentiate the samples with and without dye and those made under different conditions, as will be explained below.

As an example, in the syntheses of this section, the samples without dye have been denoted as SiAFI-X, which stands for AFI structure doped with the silicon heteroatom (SAPO-5), together with a number as a suffix (X) corres-

ponding to the differences in the gel composition and synthesis time. In the case of the syntheses performed with dye, a prefix has been added to the sample names, labeling the samples as S1/SiAFI-X, where S1 refers to the first dye of the styryl family employed during this work, LDS 730. Besides, the letter H added next to the synthesis number refers to a high dye addition in the synthesis gel, which is 0.024 for all of them.

Table 7.2: Synthesis composition of the gel (in terms of SDA and dye added) and synthesis time for SAPO-5 materials. The gels were heated by microwave at 160 °C (500 W) over different heating times.

Sample	y : TEA	z : LDS 730	Time (h)
SiAFI-X			
1	0.75	-	2.0
2	1.00	-	2.0
3	1.50	-	2.0
4	1.50	-	2.5
5	1.50	-	3.0
6	1.50	-	3.5
S1/SiAFI-X			
3H	1.50	0.024	2.0
4H	1.50	0.024	2.5
5H	1.50	0.024	3.0
6H	1.50	0.024	3.5

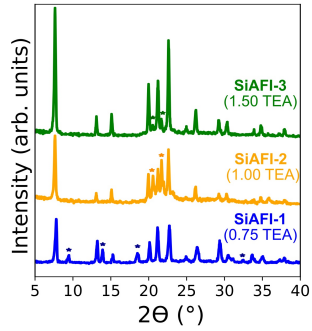

Figure 7.4: PXRD patterns of samples SiAFI-1 to SiAFI-3. Asterisks denote impurity peaks (other phases different from AFI.

According to the synthesis conditions and starting gel composition mentioned above, first of all, the amount of template was varied, maintaining the microwave heating for 2 hours (from sample SiAFI-1 to SiAFI-3 in Table 7.2). The powder X-ray diffractions (PXRD) of these attempts (Figure 7.4 show the AFI phase in all of them, with its characteristic peak at 7.63°. However, impurities are appreciable in the three, although a higher amount of template seems to favor the crystallinity of the main AFI phase. When the TEA content is 0.75 (sample SiAFI-1), phases other than the

main AFI are formed as impurities (marked with asterisks in Figure 7.4), but as the template content increases (1 and 1.5 TEA (SiAFI-2 and SiAFI-3) these impurities seem to disappear and the intensities of the SAPO-5 lattice peaks increase considerably. In fact, there is a gradual increase, obtaining a peak at 7.63° three times higher in intensity for the SiAFI-3 sample compared to SiAFI-1. This reflects that the structure-directing agent aids lattice formation, resulting in greater crystallinity (symmetry and periodicity) with higher amounts.

To further improve its crystallinity and the formation of pure SAPO-5 structure, the TEA was kept with the highest amount and different heating times were applied (SiAFI-3 to SiAFI-6). Likewise, additional attempts with the same experimental conditions were applied but adding 0.024 of dye to the synthesis gel (S1/SiAFI-3H to S1/SiAFI-6H).

Looking closely at X-Ray diffractograms (Figure 7.5a), time affects favorably the crystallinity and purity of the samples until reaching a heating time of 2.5 h, where the peak intensities reach their maximum (sample SiAFI-4). However, at larger heating times (3 and 3.5 h), there is a decrease in the intensities of the peaks. Concerning the dye-containing samples, interestingly, an improvement in the crystals synthesis was observed, as pure phases were obtained in all of them (Figure 7.5b). This is probably due to the fact that the dye itself acts as a structure-directing agent and facilitates the formation of the AFI phase.

In all cases, hexagonal disc shape crystals of 10-30 μm were obtained (see Figure 7.6). According to dye-loaded particles, very whitish powder samples were obtained, suggesting that the dye loading was very low. In fact, the uptake was only 0.01 and 0.02 per 100 g of sample powder in S1/SiAFI-3H and S1/SiAFI-5H samples, respectively (data added later in Table 7.3 and calibration curve shown in Figure C.2 and quantification described in Section 6.6). This may be related to the isomorphic substitution of silicon into the network of the aluminophosphate. It seems that the substitution of two silicon atoms by phosphorous and aluminum is the favored mechanism, forming what is known

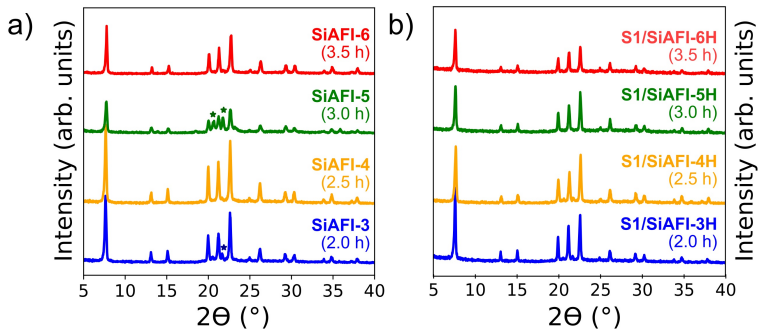

Figure 7.5: **(a)** PXRD patterns of SiAFi (SAPO-5) inorganic structures (from SiAFI-3 to SiAFI-6) and **(b)** S1/SiAFI (dye-loaded SAPO-5) hybrid systems (from S1/SiAFI-3H to S1/SiAFI-6H). Asterisks denote impurity peaks and other phases other than AFI.

as silicon islands and generating a neutral lattice (Section 2.2). Therefore, due to a lack of Brønsted acid sites in the framework, the occlusion of the cationic chromophore is somewhat hindered, and the rendered dye-loadings are very low. Comparing two samples with the same amount of dye added to the gel but different heating times, there is a slight decrease when longer crystallization times were applied, probably assigned to partial dye degradation.

Taking a closer look by fluorescence microscopy, the particles present a bright yellow fluorescence, suggesting the presence of the dye in the structure (Figure 7.6b). To properly confirm the incorporation of the dye molecules into the AFI channels, linearly polarized light experiments (Figure 7.6d-e) were carried out at a single-particle level by incorporating a polarizer before registering the image (experiments explained in Section 6.5).

The fluorescence images collected with the microscope at different polarization orientations show that when the polarizer is set on 50°, only the main fluorescence of one of the crystals is seen (Figure 7.6d), the one with the light polarized parallel to the crystal channel direction (E$\parallel$c). With the increase of the polarization angle to 110° the previous crystal turns off (E$\perp$c, light perpendicular to the channel

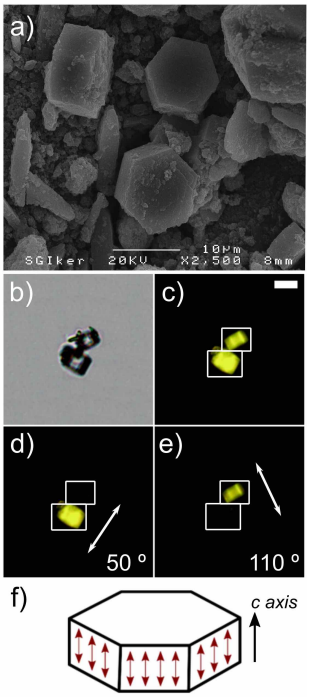

Figure 7.6: S1/SiAFI-3H particle images. **(a)** SEM. **(b)** Transmission and **(c)** fluorescence images under blue light excitation. **(d,e)** Polarized fluorescence images from different orientations (50° and 110°). Scale is of 20 μm (upper white bar). **(f)** Representation of channel and dye orientation in a SAPO-5 particle.

direction) and the other next to it turns on (Figure 7.6e), verifying that the LDS 730 molecules are preferentially oriented along the nanochannels.

This anisotropic response to the polarized light reveals that the dye molecules are oriented perpendicular to the plane of the hexagonal face (Figure 7.6f) of the crystal, along the c-direction of the crystal (see Figure 7.1b) where the nanochannels are located. As a result, crystals deposited on their hexagonal faces did not respond to linearly polarized light. In conclusion, the polarization-dependent response showed that the chromophore molecules are inside the SAPO-5 channels and not adsorbed on the outer surface, as expected after the exhaustive washing which samples are subjected after synthesis.

After certifying the incorporation of the dye within SiAFI structure, the photophysical characterization of the most representative samples (S1/SiAFI-3H and -5H, Table 7.3) in bulk powder was performed.

Table 7.3: Dye-loading and photophysical parameters - dye uptake (mmol/100g), absorption (λ_{abs}), and fluorescence (λ_{fl}) maximum wavelengths, lifetime (τ), and fluorescence quantum yield (ϕ_{fl}) at λ_{exc} = 520 nm - of the bulk powder S1/SiAFI-3H and -5H samples. The same parameters for LDS 730 (aq) are also included for comparison.

System	Dye uptake (mmol/100g)	λ_{abs} (nm)	λ_{fl} (nm)	τ_{fl} (ns)	ϕ_{fl}
LDS 730 (aq)	-	573.0	700.0	< 0.1	< 0.01
S1/SiAFI-3H	0.02	547.0	576.0	1.59	0.03
S1/SiAFI-5H	0.01	547.0	565.0	1.84	0.05

Figure 7.7a shows the main absorption band for S1/SiAFI-3H with vibronic structure hypsochromically shifted with respect to the broad and structureless band recorded for the dye in solution. This fact is typically found in dyes occluded in constrained space.[24,30] In addition, this band shows a large tail with the appearance of a shoulder at longer wavelengths. The first absorption band placed at 547.0 nm is ascribed to the S_0-S_1 locally excited (LE) trans-

ition and the less intense red shifted shoulder placed at around 652.0 nm to a ICT state in the ground state. Interestingly, the fact that the latter is detected only in the hybrid system is a result of the stabilization of the ICT state even in the ground state due to the rigid environment imposed by the host matrix.[25,33]

Regarding the fluorescence emission (Figure 7.7b), the hybrid samples show a huge hypsochromically shifted band in comparison to that in aqueous solution, and is ascribed to the LE band rather than to the ICT typically observed in solution. This change in the excited state behavior is believed to be due to a change in the polarity of the medium, which has become non-polar in the channel environment of the Si-doped AFI structure. As stated before, the substitution of Si in the $AlPO_4$-5 (SAPO-5) network, instead of generating a negatively charged network with Brønsted acid sites as expected, has led instead to the formation of silicon islands, by the replacement of two silicon atoms by phosphorus and aluminum atoms, leading to a neutral network that disfavors the relaxation towards the charge transfer state (ICT, Section 3.2.2.2) and stabilizes the locally excited state (LE).

Interestingly, this LE band displays a modest emission ($\phi_{fl} \geqslant 0.03$) but higher to the fluorescence efficiency registered for the ICT of the dye in solution ($\phi_{fl} \leqslant 0.01$). Regarding the lifetimes, since the dye-loaded hybrid systems (S1/SiAFI-X samples) gave multiexponential fluorescence decay curves, a physical interpretation of every lifetime was very difficult to make and an average lifetime (Equation 6.6, Section 6.3) was considered instead (Table 7.3). These measured lifetimes, along with the fluorescence quantum yields, were also much higher in the hybrid environments (τ = 1.5-1.9 ns), showing improved photophysical properties of the LDS 730 within the solid host.

All these results (higher emission efficiency and longer fluorescence lifetimes) are a direct consequence of the space constraint in the restricted channels of the AFI host, where rotations and vibrations of the dye molecules are to some extent reduced. In addition, the distinct environment cre-

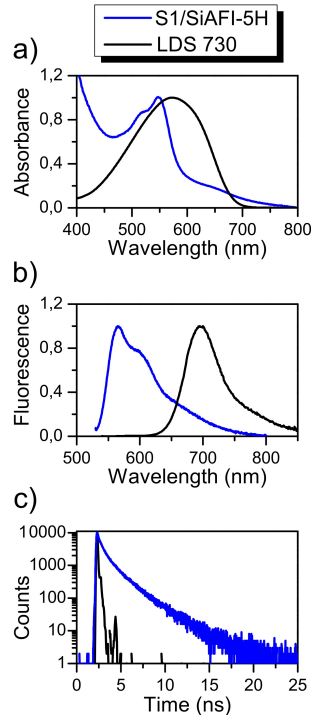

Figure 7.7: Height normalized **(a)** absorption and **(b)** emission spectra, and **(c)** decay curves for the bulk sample S1/SiAFI-5H (blue) and LDS 730 (aq) (black) for comparison. The fluorescence spectrum and the decay curve have been registered upon λ = 520 nm excitation.

ated in the hybrid system has caused the emission of LDS 730 to come from the LE state, rather than the ICT state as in the aqueous solution.

7.1.3 *Dye-MgAPO-5 by microwave heating*

The previous system doped with Si has resulted in scarce incorporation of dye inside the channels of the AFI structure due to the framework's charge neutrality. Therefore, in this section, in order to favor the encapsulation of LDS 730 molecules, avoiding the generation of neutral zones in the structure and promoting net negative charges through the formation of catalytic Brønsted acid sites in the channel walls (isomorphic substitution described in Section 2.2), the divalent Mg cation has been selected as a dopant to replace the Al^{+3} cations. In this way, a negatively charged $AlPO_4$-5 (MgAPO-5) network is generated, that will help the incorporation of a higher amont of LDS 730 and also stabilize its ICT, shifting the fluorescence towards the red region of the visible spectrum.

To synthesize the Mg-substituted LDS 730/AFI composites, hydrothermal synthesis by microwave heating was employed. In all of them, the following reaction system was followed.[33]

x MgO : 1 P_2O_5 : (1-x/2) Al_2O_3 : y TEA : z LDS730 : 305 H_2O

TEA was employed as SDA to direct the crystallization of the AFI phase (same template used for SAPO-5, Section 7.1.2). The gels were heated at 160 °C for 2 hours (more details given in Section 4.1) and x, y, and z parameters (magnesium, template, and dye amount) were systematically varied (Table 7.4). The procedure followed for the nomenclature of the samples is the same used in the previous section (Section 7.1.2).

Thus, syntheses prepared without dye have been labeled as MgAFI-X (where MgAFI refers to the MgAPO-5 framework and X refers to the synthesis number) while those dye-doped have the nomenclature S1/MgAFI-X with

the prefixed term S1 added earlier to aid identification, indicative of the presence of LDS 730 as first styryl dye encapsulated. Note here that some of them have a letter added next to the synthesis number (L, M, H) at the end of the name, which refers to the amount of dye added to the synthesis gel which can be low (L = 0.008), medium (M = 0.016) or high (H = 0.024), respectively. In the syntheses with or without dye, the number at the end indicates certain synthesis conditions related to the amount of MgO and SDA added to the synthesis gel. All the specific gel molar compositions are given in Appendix B.

Table 7.4: Synthesis gel composition, initial pH (before introducing the gel into the MW), and the final dye uptake obtained in the MgAFI (MgAPO-5) materials prepared by MW.

Sample	x MgO	y TEA	z LDS 730	Initial pH	Dye uptake (mmol dye /100g)
MgAFI-X					
1	0.2	1.00	-	3.27	-
2	0.2	0.75	-	3.16	-
3	0.1	0.75	-	4.18	
4	0.1	1.00	-	4.70	
S1/MgAFI-X					
1L	0.2	1.00	0.008	4.13	0.03
1H	0.2	1.00	0.024	5.47	0.04
2L	0.2	0.75	0.008	3.41	0.23
2H	0.2	0.75	0.024	4.45	0.41
3L	0.1	0.75	0.008	4.41	0.06
3H	0.1	0.75	0.024	4.76	0.33
4L	0.1	1.00	0.008	4.76	0.06
4M	0.1	1.00	0.016	5.16	0.17
4H	0.1	1.00	0.024	4.78	0.41

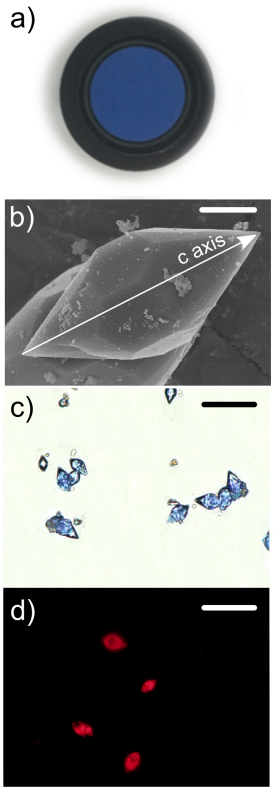

Figure 7.8: **(a)** S1/MgAFI-3H sample powder under ambient light. **(b-d)** Images of the S1/MgAFI particles. **(b)** Scanning electron microscopy photograph taken at 10 kV. Scale = 2.5 μm. Crystal size of 13 μ m. **(c)** Transmission and **(d)** emission images. Scale = 20 μm.

Powder X-ray diffraction (PXRD) patterns (Figure C.3 in Part V) indicate that practically in all the syntheses pure AFI phase has been obtained, showing the characteristic peak of this structure located at 7.58°.[39] Interestingly, in those compositions where some impurities are observed (MgAFI-2 and MgAFI-3, Figure C.3b-c), the addition of the LDS 730 dye to the gel has acted favorably, suppressing non-desired phases and showing the same template effect in the MgAPO-5 structure as that observed for the SAPO-5.

The obtained powders are of an intense blue color (Figure 7.8a), the characteristic of the LDS 730 dye. The analysis of these samples by scanning electron microscopy (SEM) informs about crystal size and morphology in the range of 10-20 μm, with hexagonal prism shape at the center and hexagonal pyramids at the edges (Figure 7.8b), implying that variation of the synthesis conditions (amount of magnesium, SDA and dye) does not modify the phase nor the shape and size of the crystals. Transmission images from the optimal microscope confirm the size and shape of the blue crystals (Figure 7.8c), which show a reddish emission after excitation (Figure 7.8d).

To verify that the dye is encapsulated inside the channels and not adsorbed on the surface, studies with linearly polarized light were performed by fluorescence microscopy. Similar to LDS 730 in SAPO-5 crystals, the anisotropic response again reveals a preferential orientation of the dye molecules. The highest fluorescence signal was achieved when the light was polarized parallel to the long axis of the crystal (also parallel to the channels, E$\parallel$c), indicating the preferential orientation of the transition dipole moments of the dye molecules in this direction (molecular major axis). In contrast, it was practically zero when the light was polarized perpendicular to it (E$\perp$c, data not shown).

Therefore, the anisotropic response to polarized light reveals that the LDS 730 molecules are preferentially oriented along the nanochannels in the c-direction of both SAPO-5 and MgAPO-5 hosts. In fact, the difference between the MgAPO-5 and SAPO-5 particles lies only in the crystal growth in the c-direction of the AFI frame (com-

pare Figure 7.6a and Figure 7.8b), but with the LDS 730 molecules occluded in the same preferred crystal orientation.

The LDS 730 dye uptake into MgAPO-5 was determined and lead to a higher loading than that obtained for the analogous SAPO-5 (Table 7.4 vs Table 7.3). The amount of magnesium and SDA content seem to play a crucial role in the dye occlusion. For instance, in the syntheses denoted as S1/MgAFI-1 (1L and 1H) with 0.2 MgO and 1.00 SDA, very low dye occlusion was achieved within the AFI pores, being always below < 0.05 mmol/100 g sample powder, regardless of the amount of dye added to the gels.

Interestingly, when the amount of Mg is kept at 0.2 and the amount of SDA is reduced to 0.75 (samples 2L and 2H), much higher dye incorporation is achieved even for the synthesis with a low dye content added in the gel (z = 0.008, sample S1/MgAFI-2L). In fact, these samples have given the highest dye uptakes among all the syntheses performed. This effect is attributed to the initial pH of the synthesis, which is more acidic as the amount of template (basic species) decreases and, therefore, further stabilizes the cationic species of the dye. As the substitution of Mg in the structure generates a net negative charge in the channels and there is a major proportion of the dye in cationic form, its incorporation is more favoured (isomorphic substitution explained in Section 2.2 and dye occlusion mechanism in Chapter 4).

Furthermore, the reduction of Mg from x = 0.2 to 0.1 in samples 3 and 4 (Table 7.4) also favors dye uptake, but only in those syntheses with a higher dye content in the initial gel (z = 0.016 and 0.024, samples 3H, 4M, and 4H), where an occlusion between 0.17 and 0.41 mmol/100g sample powder is reached. All in all, comparing these results with the SAPO-5 system mentioned above, the improvement in dye uptake is remarkable, obtaining a 20 times higher dye incorporation in the best of the cases (Table 7.3 vs Table 7.4)

In order to understand how the host and the higher dye uptakes may affect the photophysical properties of the final material, a thorough photophysical characterization of the samples was carried out. Figure 7.9 shows the absorp-

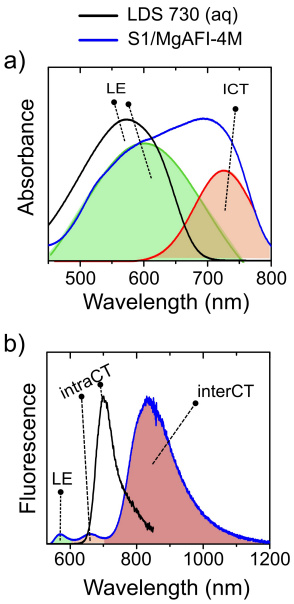

Figure 7.9: Height normalized **(a)** absorption and **(b)** fluorescence spectra upon excitation at 520 nm for the dye LDS 730 (aq) (black) and S1/MgAFI-4M sample (blue) measured in bulk powder. The deconvolution of the absorption band into two gaussian curves is included.

tion and emission spectra collected for the LDS 730 dye in solution (black) and the S1/MgAFI-4M (blue) as representative sample for comparison. The absorption band (Figure 7.9a) of S1/MgAFI-4M sample shows its main band located around 695 nm together with an important shoulder at shorter wavelengths, at around 600 nm. The band is strongly red shifted with respect to that of the dye in aqueous solution (λ_{abs} = 573 nm, black curve in Figure 7.9a). In fact, after deconvolution of the absorption band into two Gaussians, the band centered at 604 nm (green filling), has a relative area under the curve 3 times higher than the band centered at 723 nm (red filling). These bands are assigned to the S_0-S_1 transition and S_0-ICT state, respectively. The stabilization of the CT state in the ground state is a direct consequence of the encapsulation of the dye into the inorganic aluminophosphate-based host, giving rise to a new bathochromically shifted band in the absorption spectrum, unlike what is observed in solution,

Regarding the fluorescence spectrum, the bulk powder shows two weak emission bands around 573 nm and 666 nm (Figure 7.9b, blue spectrum), attributed to emission from the LE (S_1) and ICT states. Apart from those weak signals, the main fluorescence band is registered at 814 nm, highly red shifted and placed in the NIR region. It is believed that, as previously reported in other materials,[12,40] this hybrid system exhibits both intra- and intermolecular CT coupling (so far only intraCT has been seen; the two processes are explained in the fundamentals, Section 3.2.2.2). The donor-acceptor backbone structure can eventually generate a CT complex between two adjacent molecules as depicted in Figure 7.10. Thus, the originating interCT occurs mainly from the donor moiety of one molecule to the acceptor unit of another. The emission is bathochromically shifted with respect to intraCT, and thus also with respect LDS 730 emission in solution.

Intermolecular CT relies primarily on the distance between two molecules.[41] It is favored whenever the distance between donor and acceptor moieties of different molecules is smaller than the distance between the donor and

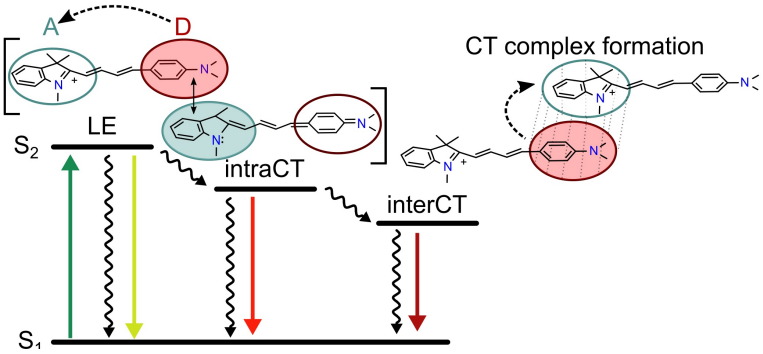

Figure 7.10: Diagram of the emission mechanism for the LDS 730 dye within the nanochannels of the MgAPO-5 structure, showing the experimentally-observed radiative relaxation pathways.

acceptor groups within the same molecule. Consequently, the greater the dye loading, the closer the molecules will be to each other and the more likely the generation of interCT complexes. Indeed, this is verified by photophysical characterization of samples with different dye-loadings (Table 7.5).

When the system contains 0.03 mmol dye per 100 g sample powder (sample 1L), due to a very low loading, no interCT complex is formed and only the band at 676 nm assigned to intraCT emission is registered in this sample (yellow curve in Figure 7.11). The intermolecular charge transfer band emerges when the dye loading reaches 0.06 mmol dye/100 g powder sample and coexists with the intraCT (sample 4L). As the concentration of LDS 730 obtained inside the solid structure increases, we observe a higher contribution of the interCT band in detriment of the intraCT and a clear red shift of its fluorescence maximum (from 775.5 nm in sample 4L to 812.0 nm in 4H, purple curve in Figure 7.11). However, it should be noted that this red shift in the interCT band can be also a consequence of the inner filter effect due to the high optical density reached on the crystals (Section 6.2).

Fluorescence lifetimes were also recorded in the bulk powders, obtaining much longer lifetimes than that in solution($\tau \geqslant 1.5$ ns over < 0.1 ns in solution, Table 7.5), in-

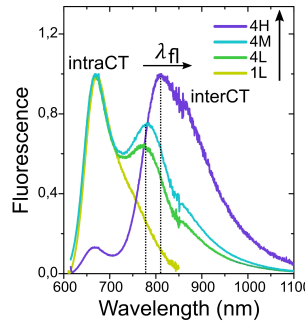

Figure 7.11: Bulk height normalized fluorescence spectra (λ_{exc} = 600 nm) of S1/MgAFI at different dye-loadings. The fluorescence maxima are represented with dashed lines and the arrows in the legend indicate the increase in the dye uptake.

Table 7.5: Dye-loading and fluorescence properties - fluorescence maxima (λ_{fl}), lifetimes (τ), and fluorescence quantum yields (ϕ_{fl}) upon excitation at 600 nm - for S1/MgAFI samples in bulk powder. The same parameters for LDS 730 (aq) are also shown for comparison.

System	Dye uptake (mmol/100g)	λ_{fl} (nm)	τ (ns)	ϕ_{fl}
LDS 730 (aq)	-	700.0	< 0.1	< 0.01
S1/MgAFI-X				
1L	0.03	676.0	2.11	0.08
4L	0.06	668.0/775.5	1.47	0.03
4M	0.17	668.0/785.0	1.51	0.02
4H	0.41	667.0/812.0	1.27	0.02

dicating a decrease in the probability of non-radiative relaxation pathways by the restriction of the molecular motions. This is also reflected in the quantum yields, but especially in sample S1/MgAFI-1L that yielded the best fluorescence quantum yield, near 10% (ϕ_{fl} = 0.08, Table 7.5). This high value is attributed to the low dye uptake of the hybrid system (0.03 mmol/100 g powder sample), with its fluorescence coming only from an intraCT and where the inner filter effects are minimized.

In contrast, in cases where the uptake is higher and the contribution of the interCT state becomes more important, the fluorescence quantum yields drop to values of ϕ_{fl} = 0.02-0.03 (Table 7.5). The emission of interCT is usually less efficient compared to that of the intraCT state due to a higher probability to relax by non-radiative pathways (*i.e.* internal conversion), since it is a lower energy state that is closer to the ground state. This is well reflected in the lifetime values, which decrease as the presence of the latter becomes more important (from 2.11 ns to 1.27 ns from sample 1L to 4H). Besides, as previously mentioned, the contribution of possible inner filters can also induce a quenching in the fluorescence properties.

All in all, the photophysical properties found in these materials are a direct consequence of a more restricted environment for the LDS 730 dye molecules in the narrow nanochannels of the Mg-doped AFI host. This environment imposes rigidity on the organic guest dyes and minimizes rotational and vibrational motions of the molecules, thus reducing the non-radiative pathways responsible for the poor fluorescence of the LDS 730 dye in solution (Section 3.6.1).

In conclusion, the fluorescence ability of LDS 730 has clearly increased once encapsulated into the AFI structure. The problem of scarce dye incorporation found in SAPO-5 has been solved changing the structure dopant from Si to Mg, which has successfully induced Brønsted acid sites on MgAPO-5 nanochannel walls. As a result, a 20 times higher dye uptake has been reached in MgAPO-5 with respect to SAPO-5.

Moreover, it has also been proven that intermolecular interactions are triggered at high dye loadings within channels. In this way, the photophysical properties of the dye can be modulated by favoring the contribution of one of the charge transfer states (intraCT or interCT) over the other. This can be done by playing with the amount of dye incorporated in the AFI framework, and obtaining an emission from the green to the NIR region of the electromagnetic spectrum, a very interesting region for biomedical applications.

7.1.4 *Dye-MgAPO-5 in conventional oven*

Up until now, all the systems studied have been prepared by the microwave regime. This type of heating reduces the synthesis time by an order of magnitude, allows rapid heating of the synthesis gel, produces very homogeneous products, and usually leads to smaller crystal sizes. However, for optical applications, it is more interesting to obtain large crystals (hundreds of microns) to work in single-crystal mode.

In this section, bigger particle materials will be synthesized by conventional heating in order to optimize conditions for optical applications. For this purpose, the compositions that have rendered the highest dye concentrations by microwave (samples 2H and 4H with 0.41 mmol/100 g dye uptakes, Table 7.4) were heated for 24 hours instead of for 2 hours (1 hour in the microwave is scalable to 12 hours in the oven) in large stainless steel autoclaves in a conventional oven. Thus, the gel molar composition used is the same as in the previous section, including the structure-directing agent (TEA). Following the general formula:

x MgO : 1 P_2O_5 : (1-x/2) Al_2O_3 : y TEA : z LDS730 : 305 H_2O

the temperature was set at 160 °C for 24 hours. More information concerning the syntheses can be found in the experimental part, in Section 4.1.

The most representative attempts carried out are shown in Table 7.6. For the nomenclature of the samples, the same criteria have been followed. Since these samples have the same gel compositions as others synthesized by MW, the same names have been used but adding the character prima at the end to denote that they have been heated by conventional furnace.

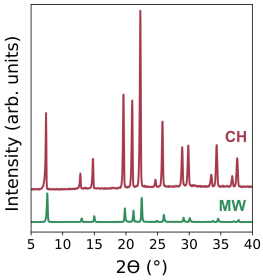

Figure 7.12: PXRD pattern comparison between S1/MgAFI (4H and 4H′) hybrid material synthesized by microwave (MW) and conventional heating (CH).

Table 7.6: Synthesis conditions (composition of the gel), initial pH of the gel, and the final dye uptake obtained in LDS 730/MgAPO-5 composites prepared by CH.

Sample	x	y	z	Initial	Dye uptake
	Gel composition			pH	(mmol dye /100 g)
S1/MgAFI-X					
2H′	0.2	0.75	0.024	5.0	1.21
4H′	0.1	1	0.024	4.4	1.12

X-ray diffraction patterns of the hybrid materials obtained show that pure AFI phase has been obtained for both cases, showing the characteristic peak at 7.58° (Figure C.4

in Part V).[39] The oven diffractograms show very high crystallinities as indicated by the higher intensities of the peaks represented in Figure 7.12, which are almost three times higher than those synthesized by microwave. This is because the crystals rendered by this type of heating are bigger and the quality in terms of crystallinity is higher.

The images taken by scanning electron microscope (Figure 7.13a) and optical microscope (Figure 7.13b-c) show hexagonal prismatic crystals, with an elongated growth along the c-axis of the framework, direction parallel to the channels. As can be clearly observed, these particles are very different both in shape and size from those hexagonal prisms with hexagonal pyramid edges rendered by the microwave (Figure 7.8).

This is also reflected in the X-ray diffractograms. While for MgAPO-5 synthesized by microwave the most intense peak so far has always been the first one in the diffractogram, the one appearing at 7.58° (Figure 7.12, hkl = 100); in the furnace, in contrast, it is at 22.52°, belonging to hkl = 102 (Figure 7.12), indicative of much greater growth in the c-direction with respect to the a-direction. It should also be remembered that in the SAPO-5 structure, hexagonal disks were obtained that grew less in the c-direction of the particle because their most intense peak also corresponded to the first one (7.58°; Figure 7.4 and Figure 7.5).

Besides, the intensity signals in the X-ray diffraction patterns are also in agreement with that studied under the microscope. That is, the lower crystallinity assigned to sample 4H obtained by microwave is directly related to the size of the crystals. The bigger the crystal size, the bigger is also the intensity of the X-ray signals. This is due to the fact that the long synthesis times in the furnace causes the nuclei to form more slowly, resulting in a slower and more symmetric growth and giving more crystalline structures.

Interestingly, between the two samples synthesized by CH with different gel compositions, noticeable changes in crystal shape are also observed. When there is a higher amount of magnesium x = 0.2 (sample 2H'), the peak at 21.01° in XRD (Figure C.4) is more pronounced, indicating

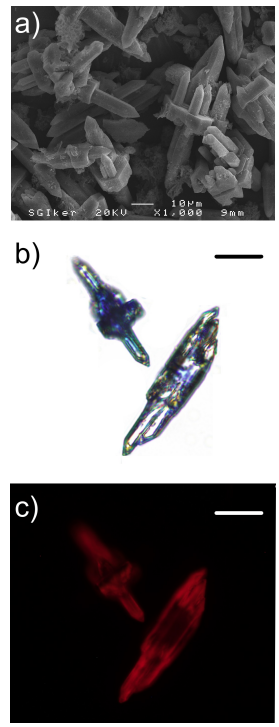

Figure 7.13: **(a)** Scanning electron microscope image together with **(b)** transmission and **(c)** emission images of S1/MgAFI-4H' crystals. Scale = 20 μm.

Figure 7.14: Color difference in the powder samples of the LDS 730/AFI structures obtained: **(a)** SAPO-5 (MW), **(b)** MgAPO-5 (MW) and **(c)** MgAPO-5 (CH).

a higher growth of the crystal in its c-direction, as it has been checked by SEM, rendering needle-shaped crystals of 100 μm in comparison with the 50 μm obtained for x = 0.1 MgO (see SEM images in Figure C.5). Indeed, the presence of Mg it is known to have a great effect on the crystallinity and crystal size, producing much bigger crystals in MgAPO materials in comparison to aluminophosphates, even being up to an order of magnitude larger.[42] All in all, both syntheses rendered crystals much larger than those obtained by microwave (5-20 μm crystals in MW).

The dye uptake in the oven-synthesized samples is higher than 1 mmol dye per 100 g sample powder, being around three times higher than the best uptake obtained by microwave (1.21 mmol dye/ 100 g sample powder in CH versus the 0.41 mmol dye/100 g sample powder achieved by MW; compare the results of Table 7.4 and Table 7.6); showing that 24 hours in the oven facilitate the incorporation of the dye, against the 2 h of microwave heating (see the gradual increase in the color of the powder samples in Figure 7.14). In addition, an increase in the amount of magnesium slightly increases the dye charge within the structure (Table 7.6), probably because more Brønsted acid sites are generated in the pore walls that favor dye incorporation through electrostatic interactions.

To compare the photophysical properties of the dye within the MgAPO-5 system by CH and MW, the 2H' sample has been selected as the most representative. The absorption and fluorescence spectroscopic bands of these two materials with the same composition are shown in Figure 7.15. Sample S1/MgAFI-2H' exhibits the same bands as previously observed by MW, with the main absorption band located at around 695 nm (λ_{abs} = 698.5 nm) and a prominent shoulder at shorter wavelengths at around 600 nm, ascribed to the ICT and LE bands, respectively. Regarding the fluorescence spectrum, the bulk powder shows two fluorescence bands under the excitation at 600 nm, a weaker band at 676.0 nm attributed to the intraCT state and another more intense and broader band at 849.0 nm ascribed to the interCT band, centered in the NIR region (photophysical

data given in Table 7.7), again exhibiting radiative deactivation from the two charge transfer states.

Again, the effect of dye loading on the inter CT complex formation is demonstrated. The higher amount of dye occluded inside the AFI structure by CH has further enhanced the formation of the complex, showing an even larger shift of the fluorescence band, being placed at 849 nm vs 804 nm for the sample synthesized by MW. It is worth mentioning again that this shift could be also partly due to the inner filter effect, affected by the high dye loading within this structure. However, it is clear that the contribution of the interCT complex emission is higher by CH, as a consequence of a higher dye loading (Figure 7.15).

Table 7.7: Dye loading and photophysical parameters - fluorescence maxima (λ_{fl}), fluorescence lifetime (τ), and fluorescence quantum yield (ϕ_{fl}) upon excitation at 600 nm- for CH synthesized S1/MgAFI samples in bulk powder. The same parameters for LDS 730 (aq) are also shown for comparison.

System	Dye uptake (mmol/100g)	λ_{fl} (nm)	ϕ_{fl}
LDS 730 (aq)	-	700.0	< 0.01
S1/MgAFI-2H'	1.21	676.0/849.0	0.01
S1/MgAFI-4H'	1.12	675.5/825.5	0.02

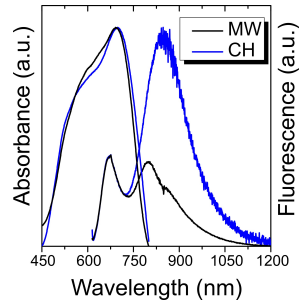

Figure 7.15: Height normalized absorption and fluorescence spectra normalized to the first emission band (λ_{exc} = 600 nm) for the bulk powder samples S1/MgAFI-2H (black) and -2H' (blue) synthesized by MW and CH, respectively.

Overall, the fluorescent quantum yields and lifetimes indicate an improvement over the dye in solution (Table 7.7), suggesting a decrease in non-radiative pathways; nevertheless, a decrease is observed with respect to the best sample obtained by MW (ϕ_{fl} = 0.08 in the S1/MgAFI-1L sample, Table 7.7). This effect probably comes from the increase in the dye concentration that induces a higher formation of CT complex as well as a higher contribution of inner filters.

In any case, we have improved the photophysical properties with respect to the dye in solution for the reasons already described and, in addition, larger and more crystalline particles have been obtained which are much more

interesting for optical applications as will be discussed in subsequent chapters.

7.1.5 *Conclusion*

The strategy presented herein provides a gateway to tightly confine LDS 730 dye into a 1D-nanoporous host limiting its flexibility and guiding its conformation into a planar configuration, reducing the probability of non-radiative deactivation pathways, and also inducing an aligned arrangement of the dyes along the channels, resulting in the appearance of new and improved photophysical properties.

The choice of the metal added as a dopant to the inorganic structure in the synthesis has been of great importance since it has allowed a change in the polarity of the environment and net negative charge generated. Consequently, it has been possible to modulate the resulting photophysical properties of the system, by controlling the polarity of the medium and the extension of the negative charge of the framework. In this way, emission of the LDS 730 dye coming from different excited states has been achieved, from the LE to the intra and interCT states, being able to modulate its emission in the hybrid system. In particular, emissions ranging from 550 nm for the Si-doped structure with less dye loading and neutral environment to 850 nm in the AFI structure doped with Mg with the highest dye loading in and more polar environment were obtained.

Therefore, the photophysical characteristics have been enhanced with great success using both conventional and microwave ovens. On the one hand, while the microwave provides the versatility to rapidly (2 h) achieve the dye-loaded aluminophosphates of interest; on the other hand, the conventional oven offers the advantage of producing very large crystals with high dye uptake. Furthermore, the S1/MgAFI hybrid systems yielded materials with fluorescence bands placed in the NIR region which are of great interest in biomedicine, materials science, and related areas.

7.2 LARGE CRYSTALS OF LDS 722/MgAPO-11

Solid-state lasers and nonlinear optics are closely linked to one another.

Since the discovery of the laser in 1960,[43] laser technology has been widely used in industry, communication, imaging, storage, medicine, and many other fields.[44–48] Today, its further expansion requires the output power and conversion efficiency of the laser to be constantly higher, and the wavelength range to be broader and broader, even tunable. Both characteristics are closely linked to one another, and while the former leads to the development of the solid-state laser, the latter drives us to the discovery of nonlinear optics, since nonlinear optical frequency conversion is necessary to attain such tunability in lasers.[49]

In fact, advances in nonlinear optics and solid-state laser sources were developed in parallel and brought impressive breakthroughs during the first forty years of their development, leading to important applications in optical information processing, integrated optics, or telecommunications.[50–52] As a result, many of today's photonic devices are based on these phenomena, such as optical amplifiers, optical modulators, ultrafast optical switches, or solid-state lasers.[53–56]

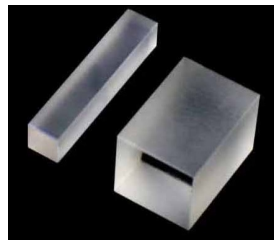

Figure 7.16: Real image of a typical BBO crystal employed as frequency doubler in optical systems.

Most of these optical devices are usually photonic crystals and their capabilities for NLO are greatly enhanced when they feature non-centrosymmetric systems; these possibilities include ultrafast optical switching for communication and even optical computing.[50,57]

Traditional NLO systems are based in inorganic crystals but the fabrication is expensive and time-consuming.

Regarding traditional NLO (refer to Section 3.4 for theoretical background) systems, they are mainly based on inorganic crystals with high chemical and mechanical stability, such as α-quartz, barium borate (BBO, Figure 7.16), monopotassium phosphate (also called potassium dihydrogen phosphate, KDP), potassium titanyl phosphate (KTP) or lithium niobiate ($LiNbO_3$); and also semiconductors like GaSe.[58–61] The time-consuming and costly fabrication processes of these crystals, however, have turned attention to organic-natured systems as an alternative, as these materials offer higher NLO efficiencies, faster responses, lower

Organic systems are a good alternative.

costs, and are easier to process and integrate into optical devices.[62,63]

In general, most of the promising organic compounds are π-conjugated molecules with strong electron donor and acceptor groups at the ends, such as the aforementioned dyes of the styryl family (described previously in Section 3.6.1). Their push-pull nature and high first-order hyperpolarizability values make them especially attractive for this purpose. However, the major drawbacks when trying to achieve an organic system based on such molecules for NLO applications is that they usually crystallize in centrosymmetric mode and suffer from poor physical and chemical stability as well as weak mechanical properties.[64,65]

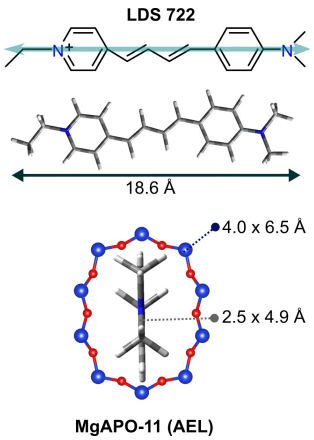

Figure 7.17: Drawing of the LDS 722 dye structure and its encapsulation inside MgAPO-11 cavities (AEL type, 4.0 Å x 6.5 Å). Regarding the dye, its optimized geometry, dipole moment (Mulliken, blue arrow) and dimensions estimated by theoretical calculations are shown.

Fortunately, this problem has recently been overcome by the encapsulation of these organic chromophores into rigid 1D and 2D environments, such as AlPO, which exhibit complementary nonlinear optical activities with respect to inorganic materials.[66,67] For example, previous studies in our group showed that the inclusion of the LDS 722 dye within the inorganic microporous 1D-channeled MgAPO-11 matrix (AEL type structure, see details in Section A.3) system synthesized by CH, successfully produced a hybrid material with very interesting optical applications such as second-harmonic generation.[25]

The inorganic-organic hybrid system was prepared with the aim of improving the emission capacity of the very flexible LDS 722 dye and promoting a preferential orientation of the molecules along the channels. Indeed, the dimensions of the elliptical voids of AEL (4 Å x 6.5 Å) imposed a strong restriction to the chromophore molecules with a molecular size of 2.5 Å x 4.9 Å x 18.6 Å (see Figure 7.17). The key to success lies in the synergy obtained by the confinement effect of the organic dye hosted in a rigid inorganic molecular sieve with good intrinsic physical properties (mechanical, thermal, photo, and chemical stability) and optical transparency in the Vis/NIR region. Thus, a new functional material with high emissive efficiency and frequency conversion properties emerged based on the pref-

erential alignment of the push-pull dye in the zeolitic matrix with 1D channels of molecular dimensions.

LDS 722/AEL system was proved to very good for NLO and is believed to be promising also for microlaser.

Inspired by our previous successful studies, but especially by the high emission efficiency (ϕ_{fl} = 40%) obtained by the encapsulation of this styryl in the magnesium-doped AEL structure, it is also believed to be a promising system to produce the so-called "microlaser action" or laser gain in a microcrystal. In particular, this dye is a good candidate for laser signal because it has so far been demonstrated in solution to have a laser efficiency as high as 43% in the near-infrared of the spectral region, although the fluorescence quantum yields are very low (< 0.01).[35] Therefore, it is believed that this laser signal could be further improved by incorporating this fluorophore within a solid system such as the AlPO framework proposed in this work.

To accomplish the laser action phenomenon (explained in Section 3.5), it is essential to have a resonant cavity suitable for optical feedback. In this section, the outer surface of the crystal itself is expected to act as a resonant cavity, resembling the Fabry-Perot cavity.[68,69] Therefore, the interest of this work is to obtain a solid-state microlaser by increasing the host crystal size.[68]

The main goal is to achieve large crystals as resonant cavity to resemble the Fabry-Perot cavity.

Despite the difficulty in synthesizing highly oriented and defect-free molecular sieve frameworks, the formation of suitable large-sized (around hundreds of microns) aluminophosphate crystals with naturally defined geometrical shapes has been attempted in order to provide a simple approach to achieve microlasers without the need for cutting, polishing, and coating. It is worth noting that conventional heating in the oven is preferred for this purpose since this technique provides relatively large crystals compared to microwave heating (see Section 7.1).

7.2.1 *Photophysics of LDS 722 in solution*

The photophysical properties of LDS 722 dye were analyzed in aqueous solution (Figure 7.18). Similarly to the LDS 730 dye studied in Section 7.1, this hemicyanine dye

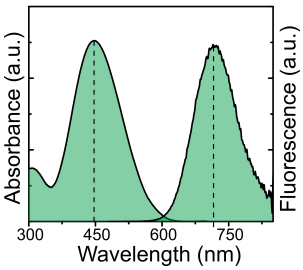

Figure 7.18: Height normalized absorption and emission spectra (λ_{exc} = 470 nm) of LDS 722 dye in water.

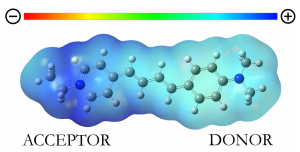

Figure 7.19: Molecular electrostatic potential (MEP) map of the LDS 722 chromophore.

also has a high absorption capacity, but in this case in the blue region of the visible spectrum (λ_{abs} = 446.0 nm) and shows a highly red shifted fluorescence band (λ_{fl} = 715.0 nm) with a relatively large Stokes shift ($\Delta\nu_{st}$ = 8436 cm^{-1}), again originated from an intramolecular charge transfer state favored upon photoexcitation (see spectra in Figure 7.18). This Stokes shift is even more than two times higher than in LDS 730 ($\Delta\nu_{st}$ = 3166 cm^{-1}; Section 7.1.1) because the π-conjugated system is smaller in the hemicyanine LDS 722 dye, shifting its absorption maximum to lower wavelengths. This is similar to what happens with cyanines and carbocyanines (*e.g.* between cyanines Cy3 and Cy5) where noticeable shifts are visible as a function of the chain length.[70] In addition, the difference between the two fluorophores lies in the acceptor moiety, with LDS 722 being more prone to accept electrons and further favoring the charge transfer between both ends of the molecule.

Regarding its fluorescence quantum yield, it shows the same trend as most hemicyanines. The flexibility of the molecule gives rise to non-radiative deactivation pathways, making the fluorescence quantum yield in solution very low ($\phi_{fl} \leqslant 0.01$ and lifetimes very short (τ = 0.08 ns). Typically, in these types of push-pull molecules, the lack of emission is usually caused by a twisted intramolecular charge transfer (TICT, Section 3.6.1). Considering this particular case, the aromatic compound contains a strong electron-donating group (amino group, $-NMe_2$) in one end of the molecular backbone and a strong electron-withdrawing group (alkyl pyridinium heterocycle) in the opposite end, both connected through a flexible alkyl chain (Figure 7.17). The charge density difference between the two ends revealed by the molecular electrostatic potential map calculated by theoretical simulations (Figure 7.19) verifies the presence of donor and acceptor moieties within the molecule.

As a result, upon excitation, a charge transfer occurs in the molecule that leads to a change in the dipole moment of the molecule, making the value of the first hyperpolarizability (β) high, which is as mentioned a very interest-

ing nonlinear optical property to achieve a second-order response (SHG) in optical materials (Section 3.4.1). This, together with its high stokes shift, which is an advantageous feature to minimize the inner filter effect, makes it particularly interesting for laser applications. Nevertheless, the crystallization of π-conjugated organic molecules usually involves a centrosymmetric growth of the crystals and in a non-parallel stacking, a hindrance to yield NLO properties. Therefore, the AlPO-11 (AEL) structure with narrow channels was selected with the intention of restricting the molecule's movements, increasing its fluorescent intensity and promoting the non-centrosymmetric arrangement of molecules by preferential alignment.

Figure 7.20: Photograph of the bulk LDS 722/AEL powder under ambient and UV light.

7.2.2 *Photophysics of LDS 722/AEL system*

In previous work, the confinement of LDS 722 in 1D AEL host led to very interesting features.[25] Since this study will be based on that particular system, the most representative sample obtained at that time will be analyzed first and its most important characteristics highlighted.

The LDS 722/AEL hybrid system prepared by conventional heating showed a deep purple color (Figure 7.20) and an intense reddish emission under UV light, displaying clearly that the amount of dye absorbed by the inorganic structure was relatively high. Indeed, an uptake of 2.20 mmol per 100g of material was obtained, representing 44% of the total dye added to the gel, and resulting in a material with high optical density, a prerequisite to be used in optical applications. Furthermore, the dye molecules showed a high degree of orientation within the channels, with dichroic values of D = 55 (ratio of intensities, Section 3.3),[25] observing a preferential arrangement by polarized fluorescence, that is, with the molecular longitudinal axis located in the same direction as the framework channels.

Looking closely at the photophysics of the bulk powder in Figure 7.21a, the absorption spectra showed the typical band of the LDS 722 dye at around 400 nm, ascribed to

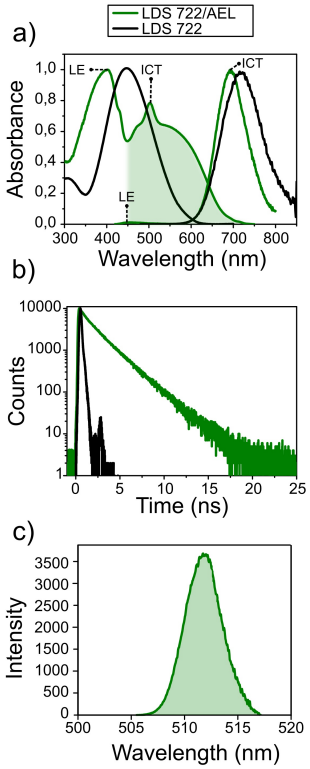

Figure 7.21: (a) Height normalized absorption and emission spectra, and **(b)** fluorescence decay curves recorded for the LDS 722 (aq) (black) and for LDS 722/AEL powder sample (green). **(c)** SHG fluorescence spectrum of LDS 722/AEL powder sample.

the S_0-S_1 "locally excited" (LE) transition, hypsochromically shifted with respect to that recorded for the dye in solution. In addition, another less intense and red shifted band appears at ≈ 500 nm attributed to the ICT state in the ground state. The fact that this ICT band is detected only in the hybrid system and not in solution is a consequence of the stabilization of the ICT state due to a planar configuration adopted in the molecule and imposed by the rigid environment of the host matrix.

Regarding its fluorescence, it comes mainly from the ICT state rather than the LE, because when exciting the sample upon UV-blue light (λ_{exc} = 410 nm), a reminiscent emission band at around 450 nm ascribed to the radiative deactivation of LE is recorded together with the more intense and very red ICT emission band (≈ 680 nm, both are indicated in Figure 7.21a), which indicates an efficient relaxation from the LE state to the final emissive ICT state.

In fact, the hybrid sample showed much higher fluorescence efficiencies than that obtained for the dye in aqueous solution (ϕ_{fl} = 0.41 in powder with respect to ϕ_{fl} ≈ 0.01 in solution), Note here that even higher quantum yields are reached when the ICT band is directly populated (λ_{exc} = 530 nm, exciting the aforementioned stabilized ICT in the ground state). Thus, a dramatic enhancement of the fluorescence capacity of the hemicyanine was achieved through encapsulation into the AEL matrix, recording fluorescence quantum yields up to forty times higher than those of the aqueous solution. In addition, the longer lifetimes (τ = 2.57 ns over τ = 0.08 ns in water, Figure 7.21b) also verify the decrease of non-radiative pathways in the rigid medium due to an emission coming from a planar intramolecular charge transfer (PICT) as mentioned before.

Finally, the viability of the material for NLO applications was proven, yielding a hybrid system with second-order nonlinear optical properties, such as SHG.[25] With a NIR light source of 1024 nm focalized in a single particle and maintaining the polarization direction parallel to the dipolar moment of the molecule (long axis of the molecule, Figure 7.17), or in other words, parallel to the AEL struc-

ture nanochannels; a sharp peak with twice the energy at 512 nm was observed ascribed to second-harmonic generation (Figure 7.21c).

After these successful results, we wish to go one step further and demonstrate that besides the NLO properties, this system could be a good candidate to obtain a solid-state microlaser in a single, fast, cheap and efficient step, avoiding the high cost of inorganic materials.

7.2.3 *Synthesis optimization for microlaser response*

To take advantage of the enhanced laser properties that can be promoted by the highly emissive photoactive molecules in this system, and thus obtain dual applicability in the same optical device (solid-state laser plus NLO properties), the particle size needs to be relatively large, ranging from tens to hundreds of microns.[71] In this way, the well-defined edges of the AEL crystals are expected to act as a resonant cavity for the generation of the laser signal.

To obtain large crystals, one of the most commonly employed techniques is seed growth. For this purpose, suspensions of molecular sieve particles are used to prepare precursor layers, followed by secondary growth on the seeds. So far, the results obtained have not been very successful due to limitations to assemble the seed crystals in order and adjust the growth of the crystal planes.[72]

Another technique is in situ growth by hydrothermal synthesis, which is one of the most widely used methods, although it is by no means the simplest. Due to the lack of understanding of the nucleation and growth mechanism under hydrothermal conditions, it is very difficult to control the heterogeneous nucleation that takes place by this approach, a process to be avoided if crystals of big size are pursued. By this method, there can be many nucleation sites and some crystals may grow smaller and/or with imperfections or even agglomerate and form twins. However, the extensive previous experience in these syntheses and the ease and simplicity by which the final products are ob-

tained have tipped the balance towards hydrothermal synthesis.

Therefore, in this section, the synthesis of large crystals by hydrothermal synthesis is reported using conventional heating and varying multiple synthetic parameters until the optimal conditions for such an objective are found. As a starting point, the attempts carried out by Cheng et. al. for the preparation of large AEL crystals were used but with slight modifications. These authors found that the optimal parameters for the synthesis of large AEL single crystals (without dye) of approximately 250 μm resided in a temperature of 180 °C, a much longer crystallization time than hitherto employed (24 h for the particles of Section 7.2.2), and the following gel composition: 1 Al_2O_3 : 1.04 P_2O_5 : 0.28 MgO : 1.9 DPA : 500 H_2O.[73]

In our case, attempts with and without LDS 722 dye were performed using the same gel composition and temperature at various crystallization times. Thus, the molar composition of the gel was as follows:

1 Al_2O_3 : 1.04 P_2O_5 : 0.28 MgO : 1.9 DPA : x LDS722 : 500 H_2O

It should be noted that the source of Al was different, being aluminum isopropoxide instead of aluminum hydroxide (employed in previous syntheses); and water-rich synthesis gels were prepared to ensure fewer nucleation centers and therefore the growth of larger crystals.[74,75] A crystallization temperature of 180 °C was applied and several crystallization durations (variation from 45 to 138 h) were tested.

All the syntheses were performed according to the procedure explained in Section 4.2, doped with Mg to help the incorporation of the dye (proven in Section 7.1), and stirred with a magnet. The time periods were progressively modified to analyze the effect of time on the crystallization of the AEL phase (each new synthesis doubles the time of the former one, even the first synthesis being already twice as long as the 24 h normally used, Section 7.2.2).

All the attempts are shown in Table 7.8. The nomenclature for the samples has followed the same criteria as explained in Section 7.1, expressing the addition of the dye with the prefix S2, which stands for the second styryl employed in this work. In this case, the number added as a suffix to the end of the name indicates the gel molar composition employed in the synthesis, and A, B, C letters denote different crystallization times. Besides, no letter has been added to indicate the amount of dye added to the gel, since the dye loading was kept constant (0.008).

Table 7.8: Experimental crystallization heating times used for samples without (MgAEL-X) and with (S2/MgAEL-X) dye, and the amount of LDS 722 added to the synthesis gel for the S2/MgAEL-X samples.

Sample	x LDS 722	Time (h)
MgAEL-X		
1A	-	45
1B	-	70
1C	-	138
S2/MgAEL-X		
1A	0.008	45
1B	0.008	70

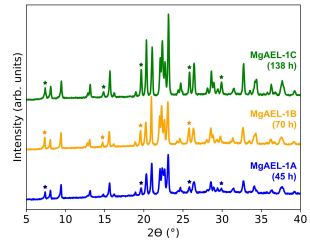

Figure 7.22: X-ray diffractograms of AEL large crystals (MgAEL-X) without LDS 722 dye at several synthesis times. A = 45 h, B = 70 h and C = 138 h.

Hence, the influence of crystallization time on the crystal formation of MgAPO-11 (samples named as MgAEL-X) was examined. The XRD patterns of the synthesized products under different crystallization times (Figure 7.22) correspond well with the standard AEL crystals (the first two peaks of MgAPO-11 are $2\theta = 8.09°$ and $9.56°$), albeit with the existence of amorphous phases and another crystalline AFI phase, indicated by background interferences and by the peak at $7.39°$ found in the diffractograms.

Finding this MgAPO-5 (AFI) phase at long synthesis times is very common, as it is a thermodynamically very stable phase. However, the intensities of the characteristic peaks of this phase are relatively much lower than those

related to the AEL phase (Figure 7.22), indicating that MgAPO-11 is the main phase of the resultant powder.

When comparing the three patterns, the first one synthesized at 45 h shows a considerable background (MgAEL), implying that this time range is not yet sufficient for good crystalline growth. At longer times, an improvement of the signals is observed in terms of peak intensities, indicating a higher crystallinity and a noticeable decrease of interferences from amorphous compounds.

All of the above is likewise reflected by scanning electron microscopy. Figure 7.23 shows the SEM images of three synthesized products in which the formation of large crystalline particles, bigger than 100 μm, can be observed surrounded by smaller impurities phases. These undesired phases may be related to the dilution of the synthesis mixture which, on the one hand, favors the growth of large crystals but, on the other hand, increases the content of by-products.[74,75]

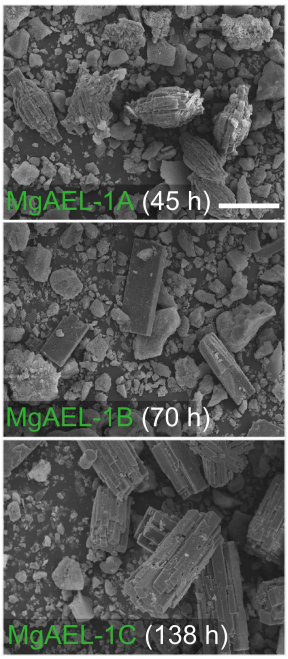

Figure 7.23: Scanning electron microscopy images of MgAEL-X samples at different crysallization times. The scale bar is 100 μm.

At 45 h crystallization time (Figure 7.23), crystals of very irregular morphology and agglomerates appear. After reaching 70 h, the crystal quality and purity improve yielding rectangular prism-shaped AEL crystals of ≈ 150 x 50 x 8 μm^3 (abc directions in the crystal, see Figure 7.24). However, after 138 h, it is more difficult to find single AEL crystals by SEM, because the crystals appear to be tightly bound to one another due to an intergrowth between them.

Therefore, the crystallization time enhances the formation of AEL crystals up to 70 h. After this point, considered as the optimum time, a further increase in time is detrimental. Thus, the conditions applied for the MgAEL-2 sample effectively resulted in very symmetric and well-formed particles. For this reason, in the next attempts, just the first two synthesis times were selected to know whether LDS 722/AEL hybrid large particles could also be achieved by this approach (Table 7.8).

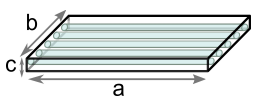

Figure 7.24: Representative sketch of a crystal of AEL framework with its a, b, c orientations.

The final products obtained are mainly white with a few red large crystalline particles visible to the naked eye, indicating the presence of limited but large S2/MgAEL crystals. X-ray diffractograms verify the formation of the

MgAPO-11 structure (see Figure C.6) but again with the presence of amorphous phases and AFI phase. The intensities of the peaks have decreased in comparison to the MgAEL-X samples, indicating a lower crystallinity as a consequence of the addition of the dye (compare Figure 7.22 and Figure C.6). Once again, at the particular reaction time of 70 h, the sample is slightly more crystalline.

Therefore, the single crystals of sample S2/MgAEL-1B were considered the best from this batch of synthesis for further analysis. The crystals were inspected by microscopy (electron and optical) and well-formed crystals of AEL and AFI structures were found. The scanning electron microscopy Figure 7.25a clearly shows an intergrowth between the two phases, with hexagonal crystals of AFI intersected with the rectangular plates of AEL (indicated by white arrows). Interestingly, very large crystals of up to ≈ 250 x 50 x 15 μm^3 size were obtained, even larger than those without dye (Figure 7.23).

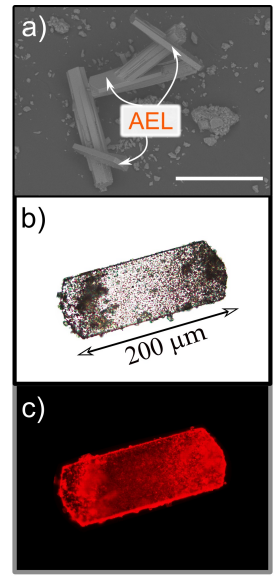

Figure 7.25: **(a)** Scanning electron microscopy images of S2/MgAEL-1B sample. The scale bar is 300 µm. **(b)** Transmission and **(c)** fluorescence images taken with the optical microscope.

Figure 7.25b shows the transmission image of a crystal of 200 µm, a rectangular-like particle with well-defined edges and an apparently small roughness on the crystal surface, probably due to amorphous impurities. Although they look poorly colored in transmission, the sample exhibits an intense red fluorescence under green illumination (with HQ530/30m band-pass filter), characteristic of the emission from the ICT state of the chromophore, as demonstrated in the smaller particles of the previous sample (Section 7.2.2).

As tested below by measurements with linearly polarized light, the optical properties of the chromophore-embedded molecular sieve are highly dependent on the orientation in the nanometer channel structure.[72] Figure 7.26 shows the polarization experiments performed in sample S2/MgAEL-1B. When the polarized light is parallel to the nanochannels of the structure (a-direction, E||c, see Figure 7.24) and thus, to the transition dipole moment of the chromophore molecules (checked by theoretical calculations and shown in Figure 7.17), the maximum emission intensity is recorded onthe crystal (Figure 7.26a).

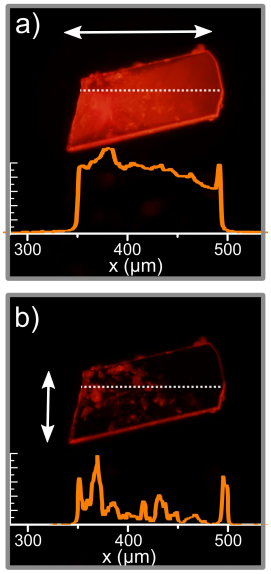

Figure 7.26: Optical microscope fluorescence images of a particle from sample S2/MgAEL-1B with the polarized light (polarizer set prior to detection) **(a)** parallel (E∥c) and **(b)** perpendicular (E⊥c) to the longitudinal axis of the particle (indicated by white arows). The intensity profiles (orange) of the longitudinal distance of the particle are also included, indicated by dashed white lines.

This is also demonstrated by the intensity profiles recorded from the longitudinal crystalline zone of the particle (orange graph in Figure 7.26a), where homogeneous fluorescence intensity is registered along the particle. However, this emission intensity becomes almost null (Figure 7.26b) when polarized light is perpendicular to the channels (b-direction, E⊥c, Figure 7.24), and only a reminiscent fluorescence signal is obtained at the crystal edges (Figure 7.26b). The dichroic ratios determined (D = 50) were as high as those obtained for previously synthesized LDS 722/AEL crystals by the conventional approach (Section 7.2.2).

In conclusion, the highly anisotropic response indicates that LDS 722 was successfully incorporated along the nanochannels of the framework. Regarding optical density, although it was not possible to estimate it due to a large number of inhomogeneities in the material, the incorporation of the dye along the crystal appears to be homogeneous since the emission intensities remain almost constant throughout the particle (Figure 7.26a).

Given the excellent of this host-guest system, it is believed that it could be potentially interesting for microlaser action. In order to test whether the LDS 722/AEL dye-doped zeotype could act as a resonator, laser action measurements were performed in LuMIn (*Light, Material, and Interfaces*) group at the University of Pari-Saclay (ENS). First of all, the optimal settings for the analysis were establish. Samples were prepared on different substrates and conditions, such as mixing the powder in glycerol within a capillary or drop-casting the crystals on a glass or quartz. The cavity was pumped with a pulsed linearly polarized frequency-doubled Nd:YAG laser (λ_{exc} = 532 nm, 500 ps, 10 Hz, experimental setup explained in Section 6.8) at the optimum excitation wavelength for this hybrid system (see Figure 7.21a); and the excited fluorescence light was collected with several microscope objectives (x10 and x50).

In general, the smaller x10 objective led to better results because the excited surface area of the particle was smaller. When using the x50 objective, the light was too focused and the dye bleached too fast, sometimes even seeing the explo-

sion in some of the crystals because the particles did not withstand such high laser intensities. Regarding the different substrates, the quartz was found to be the most suitable among all the materials tested. In the case of the capillary, the glycerol interfered with the crystal preventing resonance from happening and the laser signal was lost before reaching the spectrophotometer. In glass and quartz slides, in contrast, we were able to record the laser signal, being among them the quartz slide more efficient because its lower refractive index allowed a better confinement of the light inside the particle cavity.

Interestingly, by placing the quartz slide upside down, the analyses gave more satisfactory results (more details in next Section 7.3.4.2). Collecting the signal under the holder, the laser emissions were significantly improved, since all interferences that could be generated by direct light-crystal contact were suppressed. Hence, in order to limit to some extent the bleaching of the isolated single crystals and to record stimulated emission signals, an objective of x10 and a quartz slide in an upside-down configuration were employed for all the measurements. All spectra and data were acquired with the best focus and with extreme care to avoid the dropping of crystals.

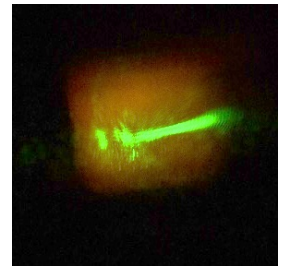

Figure 7.27: Red emission from a single particle of S2/MgAEL-1B sample under Nd:YAG laser (λ_{exc} = 532 nm laser).

However, the analysis for S2/MgAEL-1B sample did not exhibit any laser spike; instead, only red emission from the crystal was recorded as shown in Figure 7.27. This could be ascribed to shape and edges of the crystal itself that do not act as good resonant cavities, and/or to the dye uptake that it may not be high enough to reach the required minimum optical density (could not be estimated due to the high amount of impurities) for such laser application.

Therefore, to improve the quality of LDS 722/AEL crystals and the photophysics of the dye, by avoiding the random and heterogeneous formation of other products[76] and ensuring a high dye loading into the channels, a new synthetic route was tested focused on the control of nucleation and crystal growth.

As a result of the thorough previous study carried out by our group in which many conditions (temperature, time,

and gel composition) were varied, the synthesis of LDS 722/AEL system (Section 7.2.2) resulted in a more pure and homogeneous material. However, the average average" size of the crystals was of a few tens of microns, not big enough for microlaser applications. From that study, we know that the presence of the LDS 722 dye in the synthesis gel, generally acts as a strong structure-directing agent towards the formation of the thermodynamically more stable AFI phase (although its amount with respect to SDA was much lower, 0.008 LDS 722 : 1 SDA). In fact, this phase emerged when comparing with the gel of the same composition but without any LDS 722 dye added.

Thus, for the next stage, previous syntheses of LDS 722/AEL crystals (Section 7.2.2) that have given the best results in terms of phase purity and photophysics were taken as a starting point, to optimize and obtain bigger crystals in the range of hundreds of microns. The most representative sample from that study was prepared with a gel composition of 0.1 MgO : 1 P_2O_5 : 0.95 Al_2O_3 : 1 EBA : 0.008 LDS722: 300 H_2O. The synthesis was set for 24 hours at 195 °C by conventional heating under static regime. Note here that the aluminum source and SDA employed are different with respect to the previous ones used,[73] being now $Al(OH)_3$ and EBA, respectively.

According to the crystallization theory, crystal size is a function of the ratio of nucleation rate and growth rate.[77–79] Thus, in order to obtain large crystals, very low nucleation rates must be achieved. Many parameters govern this condition, such as temperature, time, alkalinity of the gel/medium, aging time in the preparation of the synthesis gel, the concentration of the reactants, and so on. In this sense, a systematic variation of the synthesis conditions was carried out taking into account all the above-mentioned sample-preparation conditions but changing the composition of the

synthesis gel, mainly the H_2O content and addition of 2-propanol, as follows:

0.1 MgO : 1 P_2O_5 : 0.95 Al_2O_3 : 1 EBA : 0.008 LDS722 : x H_2O : y 2−propanol

and varying the crystallization temperature and time. All the experiments carried out are shown in Table 7.9 The guidelines to be followed were the same as those explained in the experimental section (Section 4.2).

Hence, all the experiments were done at two temperatures (180 and 195 °C) and their crystallization time was extended to 70 h. In some syntheses, 2-propanol was added to the synthesis gel to promote crystal growth[73], and/or the amount of water was increased to achieve a dilute environment.

Table 7.9: Temperature (A = 180 °C and B = 195 °C) and variations in the gel composition (LDS 722, water, and 2-propanol) applied for S2/MgAEL-X syntheses. At the end of the table, the average size of the yielded crystals is included.

Sample	Temp (°C)	x	y	AEL Crystal size (μm)
S2/MgAEL-X				
2A	180	300	-	30
2B	195	300	-	20
3A	180	300	6	30
3B	195	300	6	15
4A	180	500	-	30
4B	195	500	-	15
5A	180	500	6	80
5B	195	500	6	30

The X-ray diffractograms shown in Figure C.7 of the do not reveal the existence of AFI phase, being AEL the main phase in all cases. This is confirmed by scanning electron microscopy, in which, moreover, very homogeneous particles in terms of shape and size are observed (see sample 3A in Figure 7.28). Hence, at this point, one

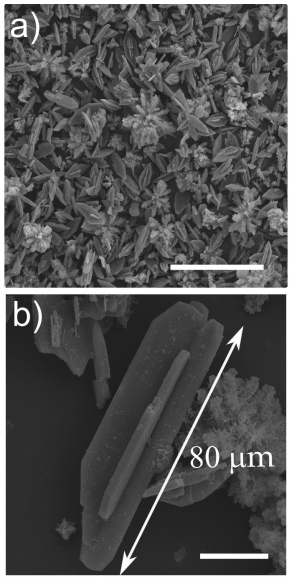

Figure 7.28: Scanning electron microscopy (SEM) image of S2/MgAEL-3A particles. **(a)** Scale is of 100 µm and **(b)** 20 µm

of the main problems mentioned above about the co-crystallization of AFI phase has been solved.

Comparing the syntheses carried out at different temperatures (samples A and B, Table 7.9) and lower amounts of water (300 H_2O, samples 2-3), a smaller growth and size of crystals is observed in those heated at 195 °C (15-20 µm vs 30 µm), as well as a lower crystallinity. The lower temperature seems to promote higher growth of MgAPO-11 crystals. Regarding the addition of isopropanol, no noticeable effect is observed related to the crystal size (compare samples 2A and 3A in Table 7.9).

For the next attempts, a different parameter, the amount of water, was tested (samples 4 and 5, Table 7.9). The concentration in solution greatly affects the degree of saturation of the system and consequently the generation of nucleation points.[80] In dilute gels, growth is favored at the expense of nucleation, leading to the formation of large crystals. Hence, the addition of 500 H_2O aims to considerably reduce the gel concentration and obtain a more dilute gel with the aim of promoting particle growth.

Analyzing the particle sizes of the these attempts with higher amounts of water, the synthesis of sample 5A with a synthesis temperature of 180 °C and propanol in the gel, led to a significant increase of the particle size up to 80 µm. Interestingly, this effect was only observed when isopropanol was added together with high amounts of water. It is hypothesized that this may be related to the OH^- ions, which may increase the solubility of aluminate species, favoring zeolite growth in the dilute gel environment.[80]

All in all, sample 5A has rendered the largest crystal size (80 µm x 20 µm x 3 µm, Figure 7.28b) in this series. The purity of the main phase in the final powder has allowed the estimation of the loaded dye, reaching an uptake of 0.66 mmol per 100 g of powder sample. Furthermore, the emission is in agreement with the photophysics described above (Section 7.2.2), characterized by a main band placed at 674.0 nm and a fluorescence efficiency of 28%. The analysis at the single-particle level (Figure 7.29a) demonstrated homogenous incorporation of the dye along the crystal and

the successful encapsulation into the channels was proved by its high dichroic ratio (D = 40).

Hence, several crystals of sample 5A were tested for laser action, following the same procedure explained above, that is, using a quartz slide in an upside-down configuration and pumping with a pulsed linearly polarized frequency-doubled Nd:YAG laser (λ_{exc} = 532 nm, more details in Section 6.8). These measurements were carried out with the polarization set to the maximum emission (polarized light parallel with respect to the channels' a-axis, E | | c, and thus parallel to the dipole moment of the chromophore molecules).

Figure 7.29b shows the laser spectrum obtained for one of these particles. The broad band registered in the 660-690 nm range is attributed to the fluorescence band of the single microcrystal (with an intensity signal over 50 counts). In addition, there are some well-defined spectral peaks on top of the fluorescence maximum, which are indicative of stimulated emission processes in the LDS 722/AEL system.

However, this trend is not reproducible in many of the crystals, and it was not possible to properly characterize the laser signal. Morphology is likely to have played a role, as the crystals, despite being well formed, appear to be intergrowthed as shown in Figure 7.28b, which may have reduced the quality of the optical cavity and affect to the laser gain. In addition, the dye uptake produced was 3 times lower than that obtained in the first attempts performed in the group, which was probably not high enough to obtain good laser response.

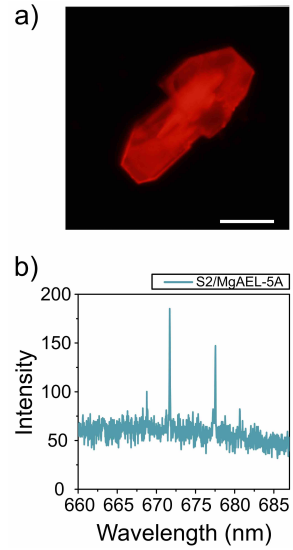

Figure 7.29: **(a)** Emission image upon green excitation light (with HQ530/30m band-pass filter, scale = 20 μm) and **(b)** laser intensity spectrum of sample S2/MgAEL-5A particle under the pump of a Nd:YAG (λ_{exc} = 532 nm) laser.

7.2.4 *Conclusion*

After an exhaustive and methodical variation of the synthesis of MgAPO-11 in a conventional furnace, and combining the observations of two different synthetic procedures,[25,73] a practically pure AEL-phase photoactive hybrid material has been achieved, in which the photophysical properties of the dye have been improved. In addition,

the use of a dilute synthesis gel resulted in rather long and good quality crystals, obtaining crystals up to 250 and 80 μm applying both techniques, making progress in terms of improved crystal growth.

To fully achieve the initially stated objective and to develop a new hybrid material as a solid-state microlaser, further experiments will have to be done. In any case, everything studied so far will serve as a starting point to obtain other photoactive systems different dyes occluded.

7.3 DMASBT DYE INTO VARIOUS MgAPOs: AN IMPROVED MICROLASER ACTION AND SHG RESPONSE.

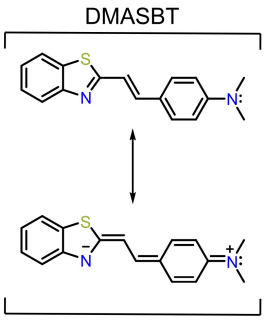

Figure 7.30: Molecular structure of DMASBT and its zwitterionic structure due to charge delocalization between dimethylamino and benzazole.

In light of the interesting results obtained in previous chapters, another dye from the styryl family, DMASBT (trans-2-[4-(dimethylamino)styryl]benzothiazole, Figure 7.30), has been chosen to be encapsulated in the 1D-nanochannel structures of MgAPO-11, MgAPO-5, and MgAPO-36. Following the previous trend, the main goal is to discover new photoactive hybrid materials for the development of systems with nonlinear optical response or solid-state lasers (for more information read the introductions in Chapter 1 and Section 7.2).

A key factor to enhance the properties of the dye and of the hybrid material itself, is to guarantee a good match between the molecular size of the chromophore and the pore dimensions of the system. For this reason, the dye has been incorporated into three different solid matrices with different pore sizes and topology (MgAPO-11, MgAPO-36, and MgAPO-5, Figure 7.31) by the *crystallization inclusion* method. Following the general objectives of this chapter, the main goal is, once again, to obtain a relatively high dye concentration (to reach high optical density) of well-ordered photoactive dye molecules as monomeric species, to boost the photophysical behavior and achieve high fluorescent efficiencies, essential for optical applications.

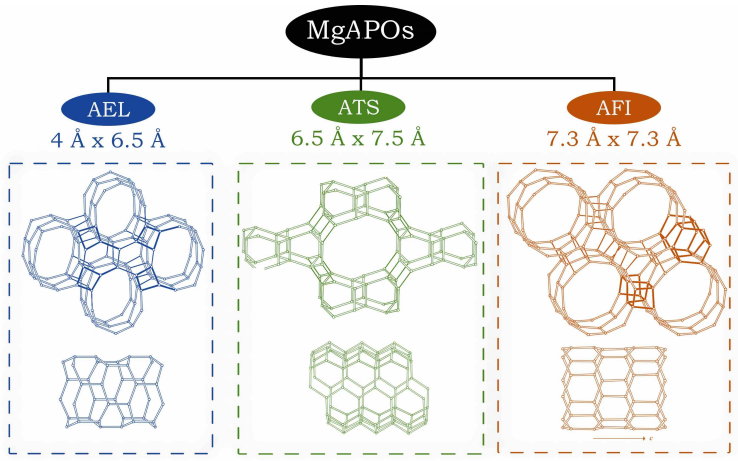

Figure 7.31: Schematic representation of the three aluminophosphate structures selected (MgAPO-11, MgAPO-36, and MgAPO-5) for the incorporation of DMASBT molecule, showing channel topology and pore-dimensions.

Therefore, this work presents the attempts undertaken to obtain a hybrid material that provides, on the one hand, a means to extend the frequency range between the available laser wavelengths by means of SHG; and, on the other hand, the so-called laser gain by resonance generated within the same crystal of large dimensions.

7.3.1 *Photophysical properties of DMASBT in solution*

Before studying the behavior of the resultant hybrid system, it is important to understand the photophysics of the free chromophore in solution. This styryl is very similar in structure to those described above (see Figure 7.30 and for comparison see Table 3.2 in Section 3.6.1), but unlike the previous ones, it is in neutral state in aqueous solution. Consequently, the photophysics are sensitive to the medium, giving rise to the appearance of different (cationic) species depending on the proton concentration (pH) of the environment.

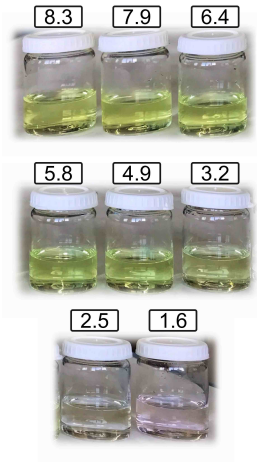

Figure 7.32: DMASBT (aq) in 50% EtOH at different pH values.

In this context, the photophysical behavior of the dye was measured in a 50% EtOH aqueous solution at different proton concentrations. Note here that this dye is not very soluble in water and that its solubility improves with the addition of ethanol. A total of eight solutions were prepared at different pH values, as shown in Figure 7.32, where the color change already indicates the presence of different species. In fact, three different colors were noticed when lowering the pH of the media: yellow from basic pH values to 3.2, colorless between 3 and 2.5; and, finally, slightly pinkish at very low pH $\leqslant$ 1.6.

To gain further insight into the origin of these changes, absorption and fluorescence measurements were performed. All the average wavelengths at the maxima of the recorded spectral bands are listed in Table 7.10 and the spectra are plotted in Figure 7.33.

Table 7.10: Summary of the photophysical properties- absorption (λ_{abs}) and fluorescence (λ_{fl}) wavelength maxima recorded at different excitations (λ_{exc} = 300 nm and 485 nm)- for different species of DMASBT dye ($1.75 \cdot 10^{-5}$M) at different pH conditions in H_2O:EtOH (50:50) solution. The DMABT species are named as neutral for the non-protonated species; monocation I (MC I) for the protonated species with the proton on the dimethylamino; monocation II (MC II) for the protonated species with the proton on the benzothiazole ring; and, dication (DC) for the diprotonated species with protons on both sides (all shown in Figure 7.34).

DMASBT species	pH	λ_{abs} (nm)	λ_{fl} (nm)
Neutral	$\geqslant$ 3.2	396	523 - 527
MC I	1.6 $\leqslant$ pH $\leqslant$ 3.2	301	420-429
MC II	$\leqslant$ 1.6	508	586
DC	$\leqslant$ 1.6	323	413

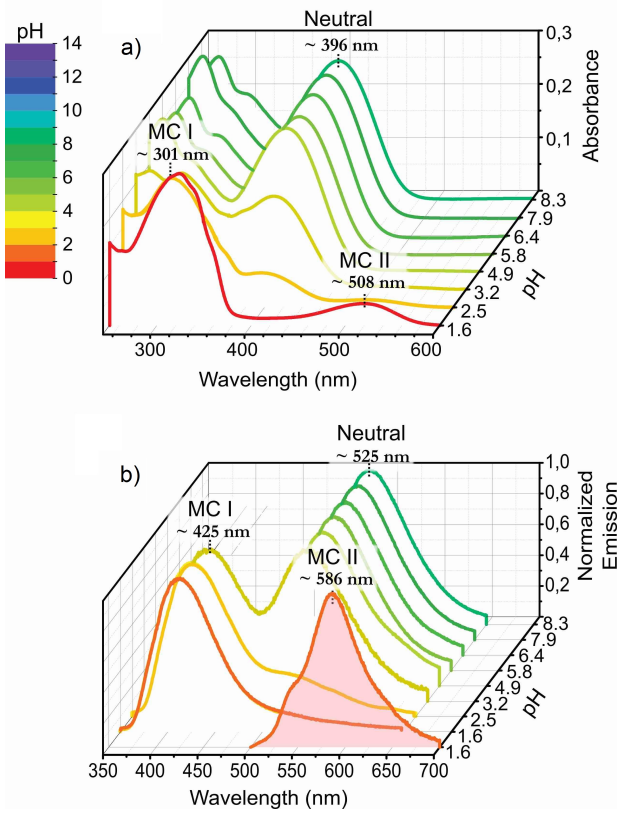

Figure 7.33: **(a)** Absorption and **(b)** normalized fluorescence spectra of DMASBT (aq) in 50% EtOH at different pHs. All the emission spectra were recorded exciting at 300 nm, except for the one filled in red color, which was excited at 485 nm. [DMASBT] = $1.75 \cdot 10^{-5}$ M in all measured solutions.

The absorption spectra (Figure 7.33a) show several bands which were attributed to different species of DMASBT dye (Figure 7.34):

1. *Neutral species (yellow)*: under basic-neutral and not harsh acidic conditions, pH $\geqslant$ 4.9, the absorption spectra show a main band centered at λ_{max} = 396 nm, responsible for the yellow color of the solution (Figure 7.32), together with another band in the UV region, at around 260 nm. This principal band is visible until a pH of around 3, although to a lesser extent (see absorption spectra in the range of pH = 3.2-2.5).

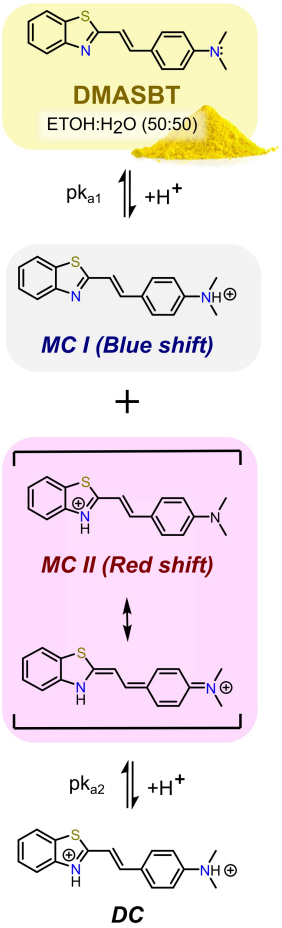

Figure 7.34: pH-dependent behavior of the DMASBT dye. The abbreviation MC refers to the term monocation, indicating the first and second cations found in solution.

As result, a loss of the yellow hue can be appreciated by the naked eye at those pHs (Figure 7.32).

2. *First monocation (MC I, colorless)*: under slightly acidic conditions, pH < pk_a = 4.5,[1] a new absorption band emerges, blue-shifted with respect to that previously assigned, and placed in the UV range at around 301 nm (see the absorption band at pH = 3.2 in Figure 7.33a). This band is related to the protonation of the dimethylamino nitrogen (Monocation I, see its structure in Figure 7.34) and is hypsochromically shifted due to a loss of the conjugation (the lone pair of electrons of the nitrogen atom does not take part in the π-conjugated system). Since this cation absorbs in the UV region, it is characterized by a colorless appearance, as shown in the photograph of the solution prepared at pH = 2.5 (Figure 7.32).

3. *Second monocation (MC II, pink)*: under very acidic conditions, pH < 2, a new weak red shifted band appears at around λ_{max} = 508 nm assigned to Monocation II, in which the benzothiazole ring is protonated (MC II, Figure 7.34), and which is responsible for the pinkish color of the solution (Figure 7.32). Although protonation at this nitrogen is less probable due to its lower basicity with respect to dimethylamino, there is some likelihood of its occurrence under very acidic conditions. Indeed, the relatively large bathochromic shift in the absorption and fluorescence (detailed below) bands is the result of the formation of a stable species with an enlarged π-electronic delocalization.

4. *Dication (colorless)*: at extremely acidic conditions there is a slight red shift of the absorption band of monocation I (from 300 nm to 323 nm, Table 7.10) due to the formation of the dication. Note here that similar to MC I, the diprotonated DMASBT cannot undergo

1 This pk_a is an estimated value calculated from the photophysical data extracted from Figure 7.33 and using the procedure presented in Section C.2.1 of the Appendix. Consistent with data published so far.[81]

any charge-transfer process.[82] Consequently, the two are hardly distinguishable photometrically (in terms of electronic delocalization).

Regarding the emission properties, at pHs > 4.9, the characteristic emission band of the neutral form at around 525 nm is observed (green lines in Figure 7.33b). A further decrease in basicity leads to an equilibrium between the neutral and Monocation I species, registering two fluorescence bands, at 525 nm (neutral) and 425 nm (MC I), respectively. As the pH is further decreased (pH = 1.6), the band of the neutral form of the dye vanishes completely and the emission of MC I and/or diprotonated (DC) is mainly registered at λ_{exc} = 300 nm. More importantly, at this low pH, a new red shifted band, placed at 585 nm ascribed to the MC II, is registered upon λ_{exc} = 485 nm (red-lined spectra in Figure 7.33). Overall, the changes in absorption and emission spectra show the same pattern and agree with the study previously published by Fayed et al.[82]

Regarding the emission efficiency, the fluorescence quantum yields recorded were very low for all the species (ϕ_{fl} < 2%).[2] In the case of the fluorescence spectrum of the DMASBT neutral dye (Figure 7.33b), its large Stokes shift ($\Delta\nu_{stokes} \approx 6200$ cm^{-1}) suggests that the emission comes from a charge transfer state upon excitation. The studies conducted by Saha et al.[81] indicate that it is in fact a TICT due to the rotation around the C-N bond of outer nitrogen (Figure 7.35).[81] The dimethylamino and benzothiazole groups act as donnor and acceptor parts in the structure, where the pyramidal geometry of the nitrogen with sp^3 hybridization allows a twist of 90° and therefore, perpendicular arrangement with respect to the π system of the molecule. This process is generally favored in polar environments resulting in very low fluorescence signals.

For the most stable cationic configurations of the DMASBT dye, studies were carried out in vacuo in the two

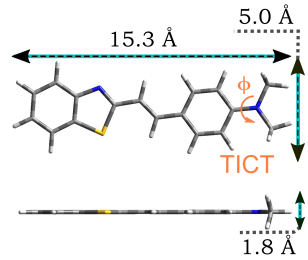

Figure 7.35: DFT optimized geometry of the DMASBT dye structure and its dimensions. Blue and yellow atoms indicate nitrogen and sulfur atoms, respectively.

2 The references used to determine the quantum yields of MC I and neutral species of DMASBT dye are quinine sulfate (0.1M H_2SO_4) and coumarin 152 in ethanol.

possible protonation sites (Figure 7.36). When the proton binds to the external amino group, the nitrogen atom is in sp^3 configuration and is not involved in the aromatic system. As a consequence, in this configuration (MC I), the dimethylamino group can rotate around the C(phenyl)-N single bond to orient the two methyl groups perpendicularly to the adjacent phenyl ring (Figure 7.36a-below), resulting in a slight stabilization of 3.6 kcal/mol. Hence, the flexibility of MC I, mainly rotations and vibrations within the structure (*i.e.* internal conversion), are the main cause of emission deactivation. Note here that the diprotonated form of DMASBT would also be considered to have an sp^3 hybridization due to the structural similarity with respect to MC I; the lack of delocalization in the system makes it unfeasible to generate an sp^2 hybridization in the outer nitrogen.

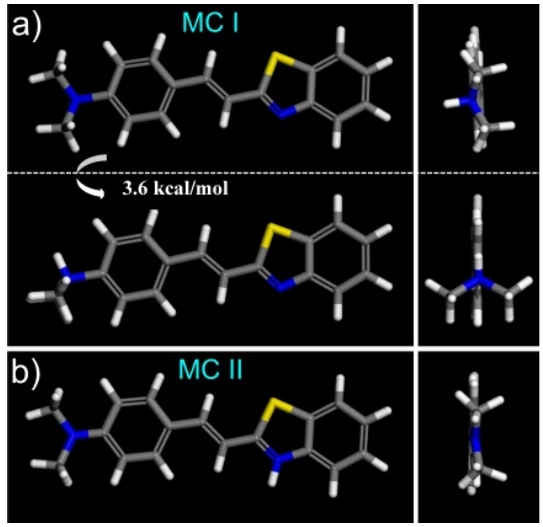

Figure 7.36: DFT geometry-optimized molecular structure of protonated DMASBT on **(a)** the dimethylamino group in two conformations, and **(b)** on the S-N-containing ring.

However, when the proton binds to the N atom in the S-N containing ring (MC II), delocalization occurs in the system (Figure 7.34). This resonant species indeed exhibits sp^2 hybridization on the outer nitrogen demonstrated by optim-

ized DFT geometry simulations, where the outer dimethylamino group does belong to the aromatic system, resulting in a highly planar structure (Figure 7.36b). In this case, the emission does not come from a TICT,[82] since the spin of the $-NMe_2$ moiety is hindered, suggesting the formation of a rigid planar planar D-A (donor-acceptor) conformation with low involvement of molecule motions, leading to a favored planar intramolecular charge transfer (PICT) state even in the ground state Figure 7.33.[83,84]

Although the PICT process usually results in higher fluorescence quantum yields, this is not the present case, once again because, in solution, internal conversion continues to be the main non-radiative deactivation process in the excited state.[84] This suggests that incorporating the molecules of this chromophore into suitable structures by providing a rigid and constrained environment would be an ideal strategy to boost its fluorescence properties.

As mentioned before (Section 7.1), the incorporation of the dye by *crystallization inclusion* method into MgAPOs is favored for cationic molecules (electrostatic force driven). Thus, MC I and/or MC II are expected to be occluded within the MgAPOs channels but not the neutral DMASBT species. Considering the above, in this chapter, the preparation of several hybrid materials composed of Mg-doped aluminophosphates will be carried out, with DMASBT as the photoactive guest species. The resultant photophysical properties and final applicability of the hybrid material will be studied.

7.3.2 *Synthesis of DMAST/MgAPO hybrid materials*

Hereafter, different synthesis attempts are described to facilitate the incorporation of the cationic DMASBT species into the three MgAPO structures. These syntheses were based on the previously described LDS 722/AEL system (Section 7.2) with slight modifications. The three magnesium doped aluminophosphates, with different pore sizes and shapes, are the following: MgAPO-11 (AEL

structure-type with smallest pore dimensions of 4 Å x 6.5 Å), MgAPO-36 (ATS structure-type with elliptical channels of 6.7 Å x 7.5 Å), and MgAPO-5 (AFI structure-type and cylindrical channels of 7.3 Å diameter). All structures are depicted in Figure 7.31; for a more detailed explanation of the hosts, refer to Section 2.4 and to the host systems database in Appendix A.

The gels were prepared with the following general molar composition:

x MgO : 1 P_2O_5: (1 -x/2) Al_2O_3 : y SDA : 0.024 DMASBT : 300 H_2O

in which *x* was varied between 0.1 and 0.2, *y* between 0.75 and 1.5, and the structure-directing agent for each synthesis was chosen depending on the desired final phase: EBA for MgAPO-11, TPA for MgAPO-36, and TEA for MgAPO-5. The amount of dye was always set at 0.024 DMASBT to ensure high dye loading. All these data are collected in Table 7.11, where the samples have been named with the term S3/Structure-X, using the prefix S3 to refer to DMASBT dye (third styryl dye employed throughout the memory), followed by the type of structure (Mg-doped AEL, ATS, or AFI structure types) and finished with a number that indicates the variation in the molar compositions of the gels. All preparations were carried out following the experimental procedure detailed in Section 4.1, 4.2 and 4.3. The gels were heated under static conditions at 180 °C for 24 h in a heating oven (*Heraeus Function Line*).

By applying the *crystallization inclusion* method, our hybrid materials were successfully achieved without major difficulties. X-ray diffraction measurements show that, in general, the final products gave rise to the desired phases, with a few impurities in certain cases (see Figure C.8 and Figure C.9 in the Appendix). SEM images also confirm that the phases were reached (Figure 7.37), showing the distinctive crystal shapes for each particular structure: rectangular-shaped plates for AEL, needle-shaped crystals for the ATS structure, and hexagonal rods for AFI.

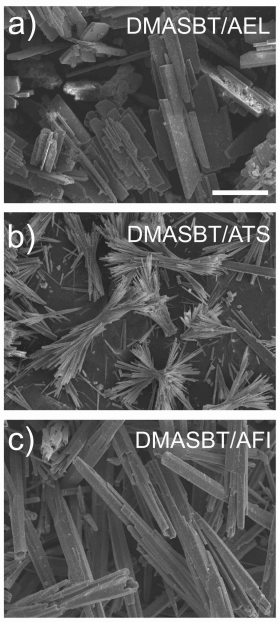

Figure 7.37: SEM images of samples 2 in **(a)** S3/MgAEL **(b)** S3/MgATS, and **(c)** S3/MgAFI. Scale = 100 μm in all photographs.

Table 7.11: Gel molar compositions used for the synthesis of the DMASBT/MgAPO samples, the respective initial (I) and final (F) pH values, the dye uptake expressed as mmol of dye per 100 grams of the solid product, and the average particle size of the resultant hybrid materials.

MgAPO sample	Gel composition		pH		Dye uptake	Cristal size
	x	y	I	F	mmol / 100g	(μm)
S3/MgAEL-X						
1	0.2	0.75	4.2	4.8	0.78	100 - 150
2	0.2	1.00	4.7	5.3	0.59	100 - 200
3	0.2	1.50	6.1	6.0	0.58	70 - 100
4	0.1	0.75	3.9	5.0	0.61	200 - 500
5	0.1	1.00	4.7	6.1	0.55	150 - 200
S3/MgATS-X						
1	0.2	0.75	4.3	4.4	0.59	50 - 200
2	0.2	1.00	4.8	4.5	0.55	100-200
S3/MgAFI-X						
1	0.2	0.75	4.0	4.8	0.88	100 - 350
2	0.2	1.00	4.7	5.2	0.67	250 - 500

In general, regardless of the structure, the cyrstal size is very large. Table 7.11 shows the estimated dimensions for each of the synthesized samples determined by scanning electron microscopy. The crystals formed range between 100 µm-500 µm; high enough for single-crystal measurements and/or applications. Interestingly, there are variations when changing the amount of template (SDA) or Mg content.

For instance, keeping the Mg amount at 0.2 in the synthesis gel, a slight increase in the amount of the structure-directing agent from 0.75 to 1.00 helps the crystal growth (compare samples 1 with samples 2 in Table 7.11), but further increase up to 1.5 (sample 3) produces a decrease in

size, obtaining the smallest crystals (70-100 μm) among all the tested attempts. On the other hand, when fixing the amount of Mg at 0.1 in the synthesis gel, the response is totally opposite. This is verified in the AEL crystals (samples 4 and 5), where the largest dye-doped AEL crystals known so far were obtained using a smaller amount of template (with 0.75 of EBA in the case of sample 4), reaching sizes up to half a millimeter (see Figure 7.38).

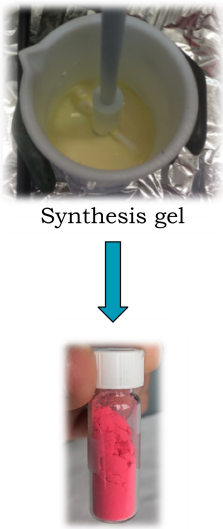

Figure 7.39: Color change from yellow to pink from the synthesis gel to the final solid product upon incorporation of DMASBT dye into MgAPO-11.

Figure 7.38: Photograph of S3/MgAEL-4 particles taken by José Prieto Barranco with extreme macro technology,[85] by stacking 190 images captured at a focus distance of 4 microns from one photograph to the other. A *Mitutoyo M Plan Apo 1X* microscope optic was used on a *Nikon D850* camera, with a focal length of 180 mm. Scale = 400 μm.

The gel molar compositions for each synthesis were selected with the main objective of playing with the acidity of the initial gels so as to favor the presence of the dye in its protonated forms. Indeed, in the synthesis process, a color change was observed from yellow in the initial gel (characteristic of the neutral form), to an intense pink color in some of the resulting powders (Figure 7.39). The pink color of the hybrid powder is indicative of the incorporation of the second cation (MC II) within the channels. However, this variation in the color does not allow to predict at first sight the incorporation of the colorless first cation (MC I), and it is, therefore, necessary to resort to certain analyses to verify it. In any case, this concludes that neutral compounds are not favored for zeolite incorporation,[30] even when the pH of the gel is not very acidic ($4 < pH < 6$, Table 7.11); oth-

erwise, the final color of the product would be yellow or even orange due to the mixture between yellow and pink (sum of the neutral species and MC II).

The quantification of the dye uptake into MgAPOs was carried out by dissolving the matrix in hydrochloric acid and then preparing 50% EtOH aqueous solutions (explained in Section 6.6). The amount of the two monoprotonated species (see calibration curves for each cationic species in Figure C.10 in the Appendix) in acidic environment was taken into account to estimate the total amount of the occluded chromophore. The dye loadings determined for the different samples are shown in the graphical representation in Figure 7.40 and Table 7.11.

Considering the parameters studied, the amount of structure-directing agent added to the gel is the most important factor in terms of the dye loading in the AlPO system. Figure 7.40 indicates that at lower SDA values (0.75 SDA, purple bars), higher dye uptake is obtained for all cases. In fact, this is observed regardless of the amount of magnesium added to the synthesis gel (Figure 7.40a). This can be explained mainly by the basic nature of the SDA.

At lower amounts of SDA, the acidity of the gel increases, and so does the formation of cationic DMASBT species, thus promoting the dye loading. This is well reflected in the initial pH of the gels (shown in Table 7.11), where lower pH values between 3.9 and 4.3 are measured for SDA = 0.75; while with SDA = 1.50 the gel reached a pH = 6.0-6.1. Importantly, the pH-variation in the gel is close to the pk_a value of the dye.

Furthermore, although the magnesium amount does not affect the initial pH of the gels, the dye uptake can also be modulated by this parameter. The presence of magnesium increases the charge imposed in the host structure (see isomorphic substitution mechanism in Section 2.2 of the Fundamentals part) and facilitates the dye incorporation through electrostatic interactions (Figure 7.40a). This is reflected in the S3/MgAEL syntheses in which the SDA is kept constant but the amount of Mg is varied, always ob-

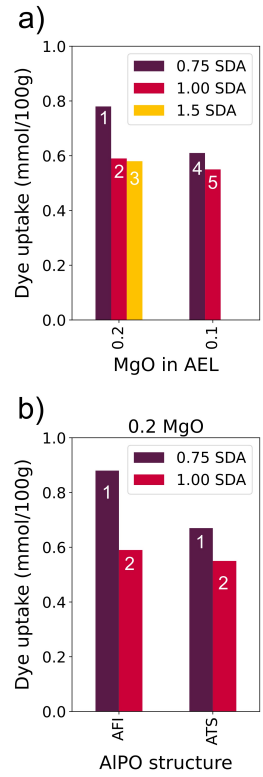

Figure 7.40: Graphical representation of the dye loadings as a function of SDA amount **(a)** in AEL structure (MgAPO-11) at several MgO contents, and **(b)** in AFI (MgAPO-5) and ATS (MgAPO-36) structures with 0.2 MgO.

taining higher dye loadings at higher amounts of Mg (0.2 MgO in Figure 7.40a and Table 7.11).

Therefore, a direct relationship can be established between the dye uptake within zeolitic hosts and the pH-induced in the medium, as well as with the net charge inside the pores due to the magnesium concentration. All these results lead to higher uptakes under more acidic conditions and higher amounts of magnesium in the synthesis gels.

7.3.3 *Photophysical characterization of DMASBT/MgAPO dye-doped zeotypes*

After the successful synthesis of the different MgAPO structures with DMASBT dye, in order to get a better understanding and further evidence of the different dye species occlusion, a comprehensive analysis of all samples was carried out by spectroscopic measurements. The photophysical data is provided in Table 7.12.

The abosrption spectra depicted in Figure 7.41 shows that when the gel composition is fixed at 0.2 MgO and the amount of SDA varies from 1.00 to 0.75, there are important changes in the photophysical behavior. At a template amount of 1.00 (Figure 7.41a), the two bands attributed to the cationic species of the DMASBT dye are only discernible in the AEL structure; whereas in AFI and ATS structures, only the first band related to MC I is clearly detected, the second one (related to MC II species) being barely noticeable.

By reducing the amount of template to 0.75 SDA (Figure 7.41b), the latter band emerges in both AFI and ATS structures revealing higher incorporation of MC II under these specific conditions. However, MC I seems to be the protonated species mainly occluded in AFI and ATS samples regardless of SDA amount, confirmed by the whitish color of the powder samples (see Figure 7.42), whereas MC II is in a much higher extent in the AEL framework (intense pink color in Figure 7.42). This result could be in

line with the hybridization adopted by the nitrogen atom in MC I, which is probably much more impeded than MC II (sp^2 hybridization) in the narrow channel topology of the AEL structure.

Table 7.12: Main photophysical parameters of DMASBT/MgAPO samples: maximum absorption (λ_{abs}) and emission wavelengths (λ_{fl}), fluorescence lifetimes (τ), and fluorescence quantum yields (ϕ_{fl}).

Sample	λ_{abs} (nm)	λ_{fl} (nm)	τ (ns)	ϕ_{fl}[a] (%)	ϕ_{fl}[b] (%)
S3/MgAEL-X					
1	402.5 / 494.0	595.5	3.22	3	56
2	394.5 / 497.5	591.5	3.16	3	63
3	388.5 / 550[c]	577.5	2.66	2	60
4	402.5 / 526[c]	587.0	2.85	3	39[d]
5	392.5 / 509[c]	585.0	2.80	3	62
S3/MgATS-X					
1	375.5 / 493.5	612.0	1.86	1	6
2	373.5 / -	574.5	2.18	1	6
S3/MgAFI-X					
1	371.5 / 490.0	592.5	2.87	1	4
2	372.0 / -	583.0	2.74	2	5

Fluorescence lifetimes (τ) were registered after excitation at 485 nm and given by a sum of exponential decays by means of Equation 6.6. The fluorescence quantum yields (ϕ_{fl}) were measured after excitation at **a)** 380 nm and **b)** 525 nm. **c)** Approximate values (absorption bands are not very well defined). **d)** Under-estimated value due to the presence of some impurities.

The fluorescence of the different samples was studied after the excitation at the two different observed absorption bands (λ_{exc} = 380 nm for MC I and λ_{exc} = 485 nm for MC II). However, the presence of MC I in all structures shows poor emission in all zeolites. The quantum yields obtained exciting at 380 nm were very low for all systems, being less than 3%.

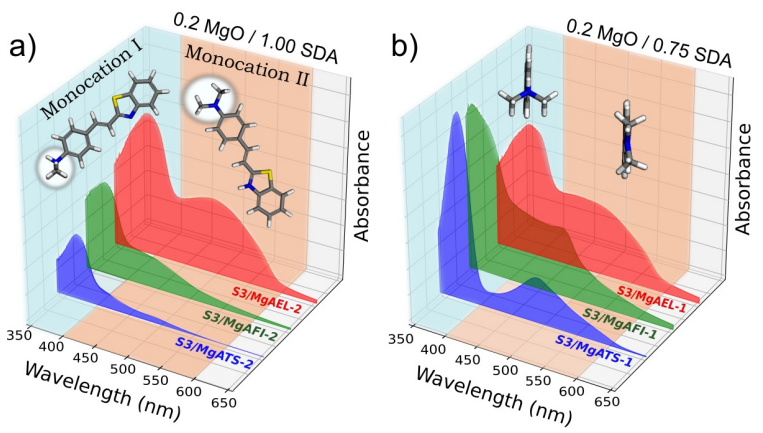

Figure 7.41: Absorption spectra of DMASBT in the different AEL, AFI and ATS structures with a gel molar composition of **(a)** 0.2 MgO / 1.00 SDA (2 samples) and **(b)** 0.2 MgO / 0.75 SDA (1 samples). Optimized geometries of MC I (N with sp^3 hybridization) and MC II (N with sp^2 hybridization) are depicted in blue and red background, respectively, and depicted in front **(a)** and side view **(b).**

Figure 7.42: Color difference between DMASBT/MgAPO powder samples in the three structures (AEL, ATS and AFI).

In contrast, upon excitation to MC II (Figure 7.43), remarkable changes in the emission were obtained depending on the zeolitic structure. Figure 7.43 shows the fluorescence spectra heigh-normalized to the resulting quantum yields of the DMASBT within the three different structures (AEL, AFI, and ATS). The fluorescence maximum was found to be between 575-615 nm (see all the fluorescence maximum values in Table 7.11) and interestingly this band was much more pronounced for the AEL, triggering one order of magnitude its emission compared to the other two structures. That is, DMASBT reached quantum yields up to 63% in AEL with respect to $\approx$ 5% in the case of AFI and ATS aluminophosphates under 525 nm excitation (Table 7.11).

In general, the quantum yield is high for all DMASBT/AEL systems (S3/MgAEL samples), except for sample S3/MgAEL-4. This sample is composed of the largest crystals in this series but with a higher degree of impurities (see PXRD in Figure C.8 and SEM images in Figure C.11 of the Appendix), affecting the quantum yield measurement. This suggests that the fluorescence efficiency may be higher

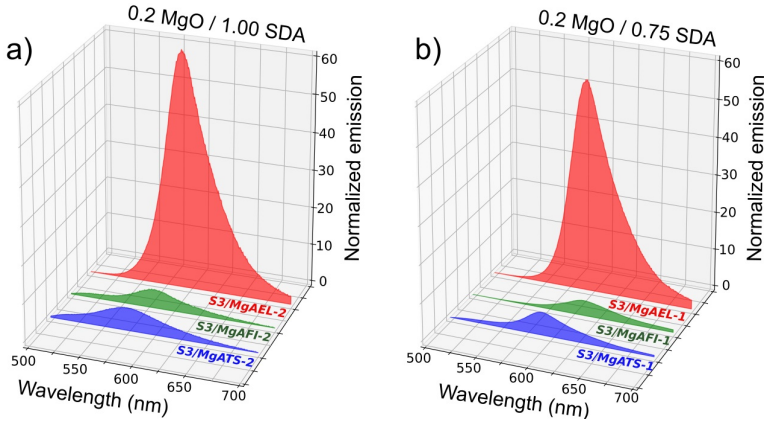

Figure 7.43: Fluorescence spectra of DMASBT within the three different structures AEL, AFI and ATS under 485 nm excitation with a gel molar composition of **(a)** 0.2 MgO / 1.0 SDA and **(b)** 0.2 MgO / 0.75 SDA. The fluorescence bands are height-normalized to their quantum yields.

if the quantum yield could be measured at a particle level (more complete single crystal characterization discussed in the next section, Section 7.3.4).

It is worth recalling that the quantum yield of the dye in solution was lower than 2% (Section 7.3.1). Hence, the confinement of MC II into the different zeolitic frameworks has increased the quantum yield with respect to solution, particularly in the AEL host with the smallest pore size.

The rigidity imposed by the matrix is also noticed by an increase in the lifetimes. The decay curves recorded for the three systems have given lifetimes around 2-3 ns (Table 7.12), indicative of a much greater hindrance of molecular motions with respect to the dye in solution (< 0.1 ns). The increase of the lifetime follows the trend ATS < AFI < AEL (Table 7.12), indicating a better fit of MC II in the host with narrowest nanochannels.

To get further insight into the confinement of protonated dye species within the different zeolite frameworks, theoretical simulations were performed. The interaction energies are reported in Table 7.13, and the dye distribution in the three frameworks is displayed in Figure 7.44

and Figure 7.45. The results clearly show that the interaction energy established between the zeolite framework and the protonated dye is higher for AFI and ATS frameworks, when DMASBT is protonated in the external dimethylamino group (MC I, structure in Figure 7.34). This is naturally a consequence of the protonated dye in this configuration (non-planar structure due to sp^3 hybridization in the external N atom) and the larger cross-section of the 12 MR channels in both inorganic structures, which allow a better fit of MC I, optimizing host-guest interactions.

Table 7.13: The interaction energy of DMASBT as a function of the protonation (MC I, in the dimethylamine, NMe_2; or MC II, in the benzothiazole ring, N_{ring}) confined within the different zeotype frameworks (*i.e.* Zeo··· DMASBT-H^+) and the difference between the interaction energies (ΔE).

MgAPO	*i.e.* Zeo···(DMASBT-H^+) (kcal/mol)		
	MC I	**MC II**	**ΔE (MC II)**
AFI	-217.7	-212.0	+5.7
ATS	-206.5	-198.8	+7.7
AEL	-187.6	-208.3	-20.7

In contrast, the smaller 10 MR channels of the AEL framework imply a worse fit for MC I with non-planar configuration, but much larger host-guest interactions when the dye is protonated on the benzothiazole ring (MC II). As stated before, the molecular structure of MC II remains planar (sp^2 hybridization in the outer N atom) and thus fits better in the elliptical and smaller channels of the AEL framework (Figure 7.45).

These results provide a clear explanation to the experimental observations. Thus, from the studied photophysics and computational calculations, it is possible to conclude that the main species present in the AFI and ATS structures is MC I, while the MC II configuration is more favored in the AEL structure.

Therefore, there is enough evidence to demonstrate that the DMASBT dye comes to fit in such a way into

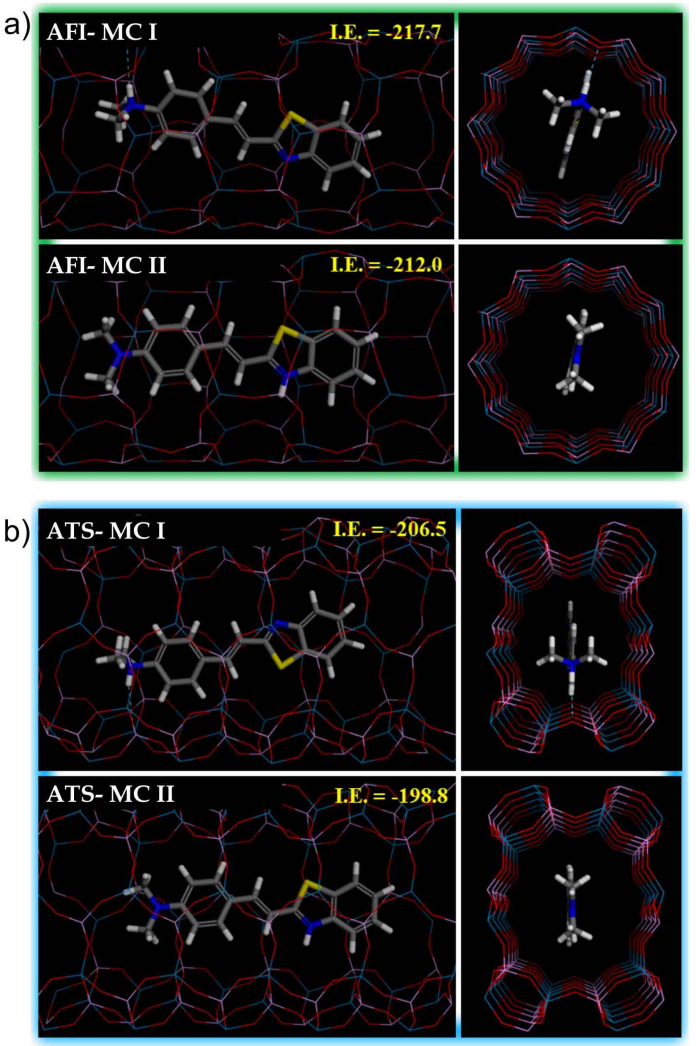

Figure 7.44: DFT optimized geometrical structure of DMASBT in protonated MC I (top) and MC II (bottom) forms confined within the **(a)** cylindrical 12 MR channels of AFI and **(b)** elliptical 12 MR channels of ATS.

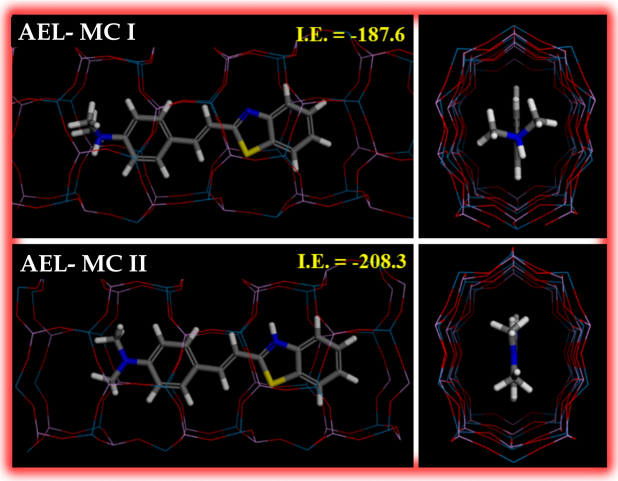

Figure 7.45: DFT optimized geometrical structure of DMASBT in protonated MC I (top) and MC II (bottom) forms confined within elliptical 10 MR AEL channels.

the cylindrical pores of the AEL, where the walls of the nanochannel block all possible rotational and vibrational motions and favor a planar molecular structure. This happens to the extent of obtaining idyllic solid-state photophysics causing an enormous enhancement in fluorescence efficiency and rendering a potentially interesting system for optical applications.

7.3.4 *DMASBT-AEL Single Crystal Characterization: SHG and Laser Action*

The particular encapsulation of Mc II within AEL nanochannels has boosted the optical features by the promotion of a fluorescent planar intramolecular charge transfer in such a rigid environment, which presumably will also force a preferential and ordered arrangement of the dye molecules along the material. Therefore, it could be an ideal candidate for nonlinear optical properties or microlaser action.

In order to test this, a deeper characterization of the DMASBT molecule occluded into the MgAPO-11 nanochan-

nels was carried out by optical microscopy. The diverse experiments performed for the analysis at a single-particle level are shown in Figure 7.46. The experiments were focused on S3/MgAEL-2 sample, the one with highest fluorescence efficiency and with a considerable dye uptake (0.59 mmol/100 g, Table 7.11). Optical microscopy images show crystals of well-defined geometry, large size (150-200 μm) and sharp edges. The particle shows a pale pink color by transmission (Figure 7.46a) and an intense red emission under green excitation light (Figure 7.46b), both characteristic of MC II species.

The feasibility of this hybrid material for NLO applications was proven by polarization experiments. Figure 7.46b shows a particle image with the light polarized parallel to the crystal channel direction (E||c, along the longitudinal axis of the crystal), with its maximum fluorescence intensity. When the polarized light is perpendicular to the channel direction, the fluorescence of the particle switches off (data not shown). Note here that the transition dipole moment of the protonated DMASBT molecule is located parallel to the long molecular axis, as observed for the other styryls analyzed so far.

The recorded fluorescence intensities for mutually perpendicular polarizations yielded a dichroic ratio of D = 100, indicating a very high alignment degree of the photoactive molecules occluded within the MgAPO-11 host. This is the highest anisotropic response achieved in our group so far (being twice than that obtained for the LDS 722/AEL system, see Section 7.2, probably because of the bulkier DMASBT molecule that fits much tighter within the AEL host), evidencing a total alignment within the pores.

The oriented inclusion of DMASBT dye molecules along the unidirectional aluminophosphate type structure also resulted in a strong intrinsic birefringence (Figure 7.47, a phenomenon explained in Section 3.3). When the crossed polarizers were placed parallel to the longitudinal axis of the crystal, an artificial bright pink color (interference colors) was observed by transmission. In contrast, when placing the cross polarizers perpendicular to the crystal length,

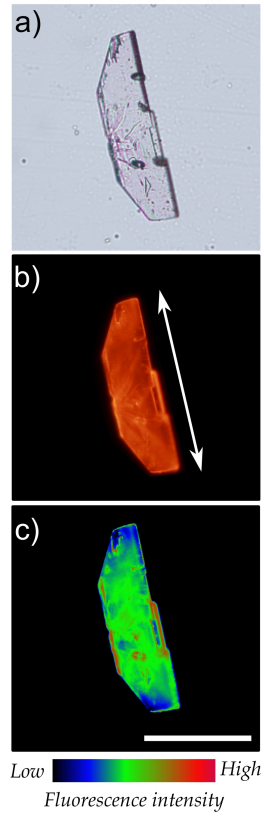

Figure 7.46: Microscope images of DMASBT/AEL particle (sample 2): **(a)** Transmission and **(b)** emission image upon green exitation light (with HQ530/30m band-pass filter) polarized parallel to the white arrow. **(c)** Color map image as a function of the fluorescent intensity. Scale = 100 μm.

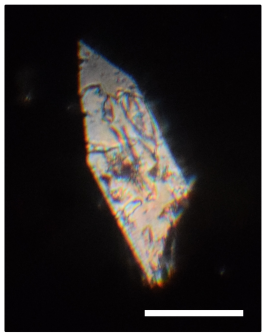

Figure 7.47: Birefringence behavior of S3/MgAEL-5 sample particular. Cross polarizers were set in excitation along the longest axis of the crystal. Scale = 100 μm.

the particle fluorescence is switched off (data not shown). This indicates that the refractive index is different in the two directions, which is a result of the periodic alignment of the molecules.

Besides, the incorporation of the dye is homogeneous in all analyzed single crystals. Figure 7.41c shows the color map of the previos particle as a function of fluorescence intensity, showing uniformity throughout the crystal of about 150 μm, which is a signature of the *crystallization inclusion* method. In fact, the incorporation of dye into such large crystals by diffusional approaches can rarely lead to such homogeneous dye filling. All this confirms that the DMASBT organic dye is homogeneously occluded with its long axis along the longitudinal axis of the crystals (channel direction). The illustration of the dye occlusion into the channels of the AEL structure and the molecules' respective orientation within the crystal are shown in Figure 7.48a and b.

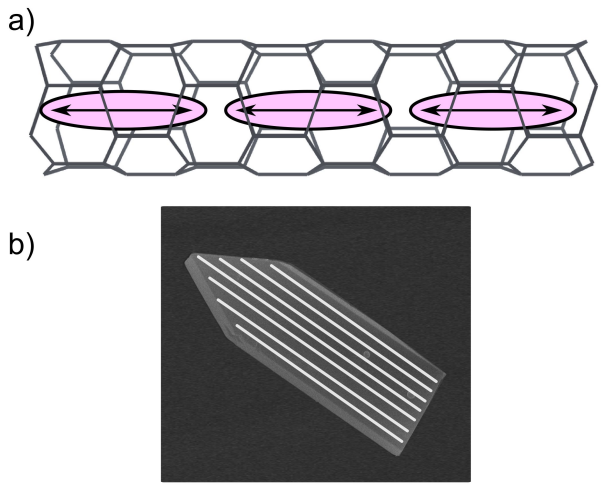

Figure 7.48: **(a)** Illustrative scheme of DMASBT dye occlusion within the nanochannels of the MgAPO-11 host. **(b)** SEM image of sample S2/MgAEL-2 with white lines indicating the orientation of the nanochannels in the AEL framework.

All in all, there is certainty that the alignment and occlusion of the dye molecules within the nanochannels

have been highly satisfactory. Moreover, considering that DMASBT exhibits intrinsic NLO properties due to its push-pull nature and high first-order hyperpolarizability value, makes this hybrid system potentially interesting for non-linear optical applications such as second-harmonic generation (SHG).

7.3.4.1 *Second-Harmonic Generation*

For the study of NLO properties in the DMASBT/AEL system, measurements were also performed at single particle level. A crystal of sample 2 was excited with NIR light at 1020 nm (Figure 7.49a) with the polarization angle of the incident light parallel to the transition dipole moment of the molecule (E||c). The experiment, shown in Figure 7.49b resulted in a sharp peak at 510 nm, attributed to the second-harmonic signal.

The SHG efficiency was studied in the same crystal at different NIR wavelengths (from 800 nm to 1020 nm) in order to identify the most efficient excitation wavelength, with a laser power of 0.2 mW to prevent photobleaching of the dye. According to the results shown in Figure 7.49c, the most efficient excitation wavelength is 1020 nm, and the SHG intensity gradually increases (except in the case of excitation at 975 nm) as the NIR excitation wavelength increases.

The crystal center was then excited at the best excitation wavelength found for the material (1020 nm) at different laser powers (Figure 7.50). The power displayed a quadratic dependence with a slope of ≈ 2 for all curves (Figure 7.50b), which indicates a second-order susceptibility property, verifying that the registered signal is indeed the second-harmonic generation response of the system.

The polarization-dependent properties in the SHG signal were systematically studied in this experiment, revealing that when the light is polarized parallel to y-direction, the signal is practically the total SHG recorded for the system (blue and red, Figure 7.50b). In fact, the signal recorded in the x-direction can be considered negligible, being

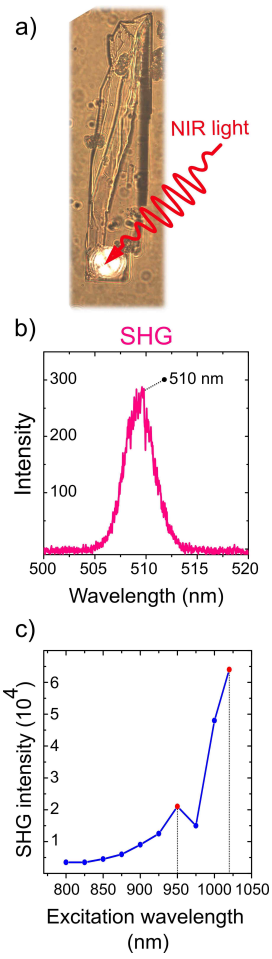

Figure 7.49: **(a)** Analyzed particle of sample S2/MgAEL-2, excited at the bright zone by NIR light (1020 nm) and **(b)** the recorded SHG signal. **(c)** SHG intensity at different excitation wavelengths with 0.2 mW excitation power.

less than 10% of that recorded with the polarization set in the y-direction. The strong polarization effect and the quadratic power dependence confirm that the SHG comes from the dye disposed in a preferred orientation along the AEL nanochannels and not from the crystal itself (proven in previous studies).[25]

This tendency has resulted very similar to that previously studied in our group for LDS 722/AEL crystals.[25] The wavelength tunability for this experiment was performed under similar conditions and also yielded its best excitation wavelength at 1020 nm. This suggests that the NLO response of the styryl/MgAPO is governed mainly by styryl dyes with similar NLO characteristics (high hyperpolarizability and push-pull character between D-A groups within the molecule).

Finally, z-scanning images of the total and polarized-SHG signal at different depths of the crystal were recorded. For this purpose, an area at the center of the crystal was selected (shown in Figure 7.51a).

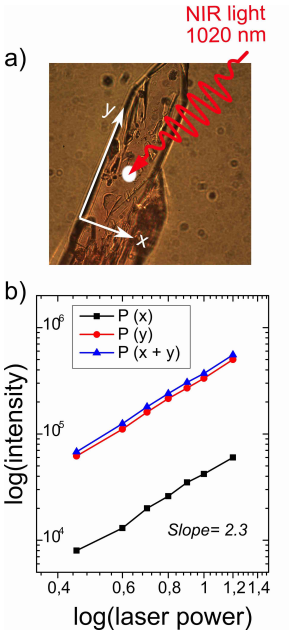

Figure 7.50: **(a)** Analyzed particle of sample S3/MgAEL-2. The white dot indicates the excitation zone for the experiments. **(b)** SHG laser power dependence.

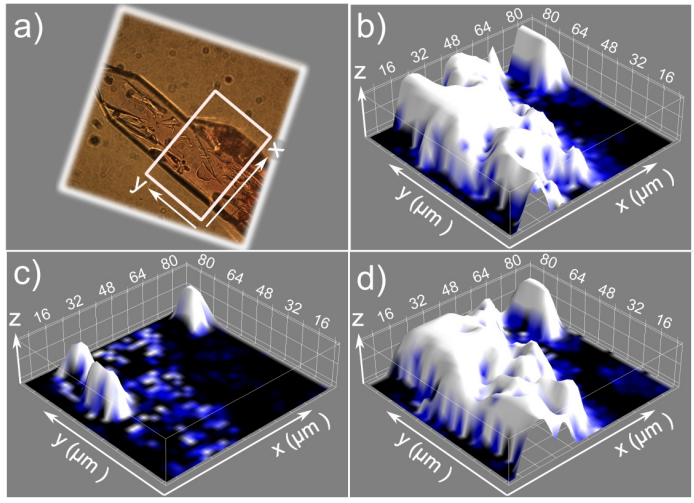

Figure 7.51: SHG measurements in **(a)** S3/MgAEL-2 sample particle and the excited scanning zone indicated with a white square. **(b-d)** Surface map plot of the registered SHG intensity: **(b)** total intensity, **(c)** intensity in x-direction, and **(d)** intensity in y-direction.

By the stacking of all SHG intensity surface images registered at different z-scans, a three-dimensional surface map was obtained (Figure 7.51b-d). In general, the total SHG signal within the particle is homogeneous, except for some areas where defects or cracks in the crystal are visible. The practically null response obtained in the x-direction confirms that the dye is responsible for the SHG.

These experiments conclude that the SHG signal coming from the particle is a consequence of the configuration and distribution adopted by DMASBT dye within the AEL cavities. The host has induced a non-centrosymmetric arrangement, which is critical for the activation of nonlinear optical properties. The intrinsic nonlinear optical properties of the styryl dyes (high values of the first hyperpolarizability achieved by π-conjugated molecules with strong electron donor and acceptor groups) also play a crucial role in the resulting SHG response, since no response was achieved by the encapsulation of other families of dyes into the same framework.[27]

7.3.4.2 *Laser action*

The excellent properties shown by S3/MgAEL samples in terms of fluorescence efficiency may open new perspectives in the investigation of other interesting optical properties. In fact, thys type of dye has already been reported to exhibit laser emission in viscous media.[35,86] In this section, different experiments dedicated to trigger and analyze microlaser action signal on S3/MgAEL single particles are described. The hypothesis is based on the high emission ability and the well-defined edges of large S3/MgAEL particles, which can act as a resonant cavity and consequently induce stimulated emission.

First of all, crystals were prepared on different substrates and mixtures in order to establish the optimal conditions for the analysis, as was done for LDS 722/AEL (Section 7.2). The optimized parameters selected were the same as for the previous LDS 722/AEL crystals. Figure 7.52 shows the laser emission obtained in S3/MgAEL crystal of

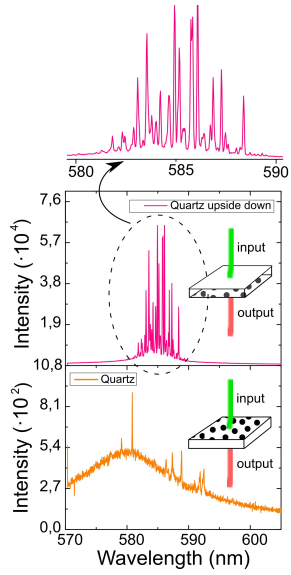

Figure 7.52: Intensity spectra of sample 4 in quartz holder with the quartz slide in up (orange line) and upside down (pink line) configurations, and the laser peaks of the latter magnified. Pumped with a Nd:YAG laser (532 nm, 500 ps, 10 Hz).

sample 4 (Table 7.12) coated on quartz slides. When the particles were placed on the substrate and the slide was faced up to the laser excitation, the recorded spectrum (orange) of the individual microcrystal shows a broad band centered at 580 nm, along with some spectral spikes around the fluorescence band.

Interestingly, by placing the quartz slide upside down, the spikes increase in intensity and number, whereas the broad fluorescence band decreases (pink spectrum, Figure 7.52). Those sharp peaks are assigned to stimulated emission processes occurring in our DMASBT/AEL system triggering laser action on a single crystal. By turning the slide upside-down, and collecting the signal with the spectrophotometer from the bottom, all interferences generated by direct contact are suppressed and the laser signal is significantly enhanced.

To analyze the effect of the size of the crystals on the microlaser action, samples 2 and 4 were selected (Figure 7.53) since both show similar dye uptake but differ in the dimensions of the particles (100-200 μm in sample 2 and up to 500 um in sample 4, Table 7.11). Figure 7.53 shows the spectra registered for single particles under the same conditions (relative pump intensity = 0.75 μJ). On the one hand, sample 2 shows a fluorescence band centered at around 585 nm (close to that registered by fluorescence spectroscopy) albeit no stimulated emission signal. On the other hand, sample 4 demonstrates the opposite, showing a very intense and sharp spectral peaks, indicating stimulated emission.

Therefore, the smaller particles of sample 2, with different shape and a higher presence of defects may prevent the laser from resonating inside the microcavity of the DMASBT/AEL system. However, the well-defined rectangular prism shape of this bigger single-crystal acts as a better resonator activating solid-state microlaser. In fact, the signal is known to be scalable with the propagation length in the cavity.[87] Hence, from an experimental point of view, enlarging the crystal size leads to a higher gain, increasing the action of the microlaser.

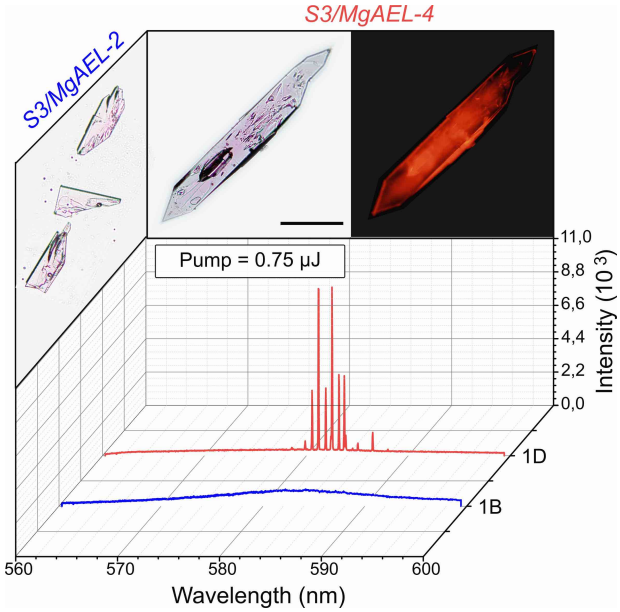

Figure 7.53: Photoluminescence (PL) spectra of sample 2 and 4 (blue and red lines, respectively) by green laser excitation (λ_{exc} = 532 nm, 500 ps, 10 Hz) at a relative pump intensity of 0.75 µJ. Some example transmission images are shown at the top of the spectra for comparison, and in the case of sample 4 its fluorescence image recorded upon excitation with green light is also given (taken from the fluorescence microscope with a band-pass filter HQ530/30m). The scale is 100 µm for the three images.

Now, to determine the pump lasing threshold to activate laser action, S3/MgAEL crystals (sample 4) were excited at different incident pump power intensities (Figure 7.54). Below 0.65 mW, the dye-doped aluminophosphate crystal exhibits a broad peak centered at around 580 nm, characteristic of the spontaneous emission. At an input power of 0.65 mW, we find the laser threshold of the sample, with a few sharp peaks starting to emerge.

As the input power increases above this threshold (0.65 mW), the set of spikes around 590 nm rise sharply in intensity and quantity, suggesting higher optical feedback within the cavity of the structure. In addition, as laser intensity increases, spectral peaks at longer wavelengths gradually

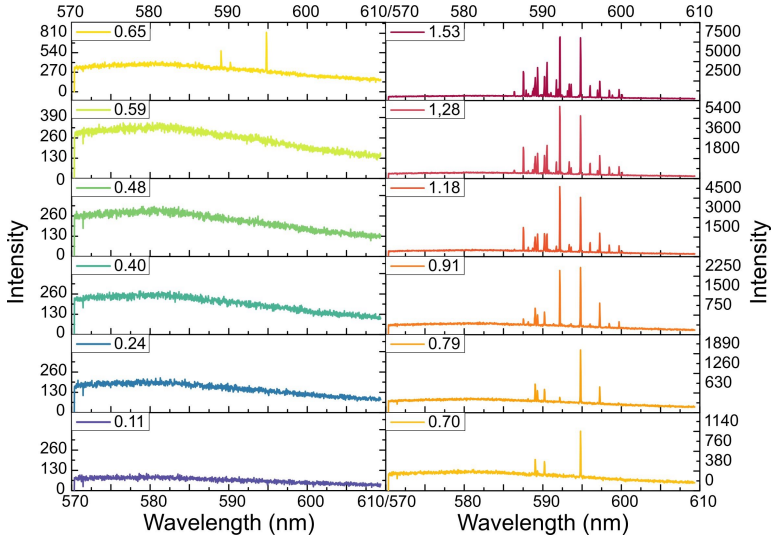

Figure 7.54: Emission intensity spectra of DMAST/AEL hybrid system of sample 4 under several pump power intensities (mW) considered as relative values. Pumped with a Nd:YAG laser (532 nm, 500 ps, 10 Hz).

become more visible due to an increased balance between gain and loss within the crystal.[88]

Further measurements were performed at different incident pumping polarizations using a halfwave plate on excitation to rotate the linear polarization. As illustrated in Figure 7.55, the emission spectra of the particle were measured by tuning the incident polarization from -45° to 45°, at five different positions rotating every 22°. The emission intensities together with the number of peaks change as a function of the incident linear polarized light. The intensity and number of spikes become higher when the polarization direction is fixed at 22°; conversely, the laser signal is lost at -22°.

The total intensities quantified (after subtracting their respective baselines) and plotted as a function of the polarization angle in Figure 7.56 reflect more clearly the polarization dependent behaviour in the particle. In this figure, the corresponding polarization direction with respect to the particle is also depicted, where 22° and -22° correspond to

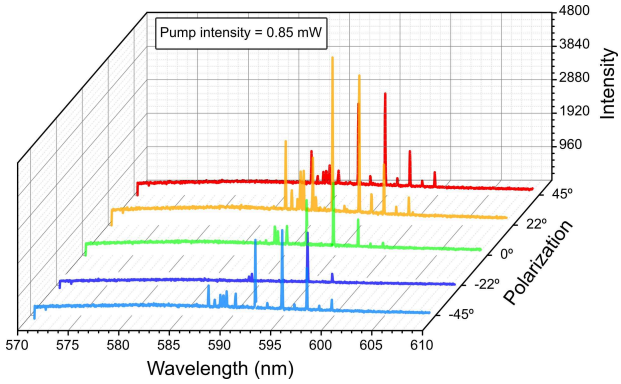

Figure 7.55: Photoluminescence spectra for sample 2 under different incident light polarization at 0.85 mW of pump power intensity (Nd:YAG laser λ_{exc} = 532 nm, 500 ps, 10 Hz). It is important to highlight that the power value given is relative.

an electric vector parallel (E||c) and perpendicular (E⊥c) to the major axis of the DMASBT molecule.

In this graph, the maximum laser intensity signal is recorded at 22°, just when the pump polarization is aligned to the major axis of the crystal and thus along the nanochannels and fluorophore orientation (Figure 7.48). In contrast, when the polarization is changed to a perpendicular orientation, at -22°, the minimum value is obtained. For orientations other than those already mentioned (45°, -45° and 0°), intermediate values are obtained because only a part of the molecules embedded in the channels are excited, resulting in lower stimulated emission.

The proposed the laser generation mechanism in a single crystal is depicted in Figure 7.57. It is believed that light oscillates between the two parallel sidewalls of the crystal and is confined within the crystal. Some pictures taken during the generation of laser action (Figure 7.57a-b) illustrate that the center of the crystal (pumping area) and lateral edges are highly illuminated (illustrative figure also in Figure 7.57c).

Generally, MgAPO-11 particles are characterized by having a defined rectangular prism morphology with an orthorhombic unit cell with *Imma* symmetry (properties given

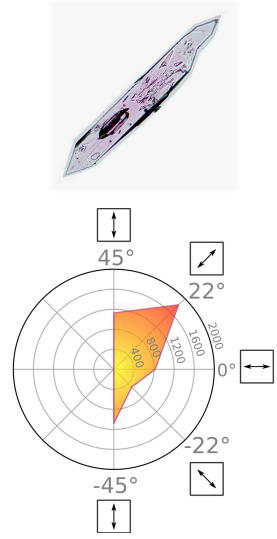

Figure 7.56: Radar chart plot of the total emission intensities registered as a function of the indicent light polarization. The total intensities were determined from the spectra depicted in Figure 7.55.

in the hosts database in Appendix A). Consequently, the prism faces can form mirrors of a ring optical resonator in which the feedback necessary for laser action is successfully reproduced.

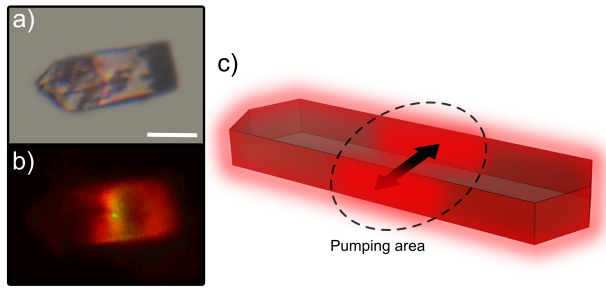

Figure 7.57: **(a)** Transmission and **(b)** fluorescence images of a particle from sample 4. The green dot indicates the green laser excitation and the red emission indicates the fluorescence coming from the particle together with its laser action coming mainly from the edges. Scale = 50 μm. **(c)** Illustrative figure of the laser origin in the DMASBT/AEL system.

So far we have discussed how the pump intensity and polarization have an effect on the lasing properties of the S3/MgAEL particles. In addition, we have generally discussed the direct effect of crystal size and morphology on the laser response. We suspect that the positions of the spectral peaks correspond to different morphology-dependent structure modes, even though this section has not been deeply studied yet. Further experiments are currently underway to determine the resonance modes within different cavities.

In short, this study has served for the recognition of the best crystals for future measurements. Furthermore, we can state that laser emission from a solid microlaser based on dye-doped aluminophosphate has been demonstrated with very good efficiency and very well-defined laser spectra. These systems based on dye-doped zeotypes may be in the spotlight and can play a crucial role in future optical applications.

7.3.5 *Conclusion*

In summary, styryl-type DMASBT dye has been encapsulated into the structures MgAPO-11, MgAPO-36, and MgAPO-5 (AEL, ATS, and AFI, respectively); being the AEL structure with the narrowest channels in this series, the most favorable to enhance the photophysical features of the dye. In particular, this structure has favored the incorporation of monocation II (protonated at the benzothiazole ring), the one characterized by a planar structure and longer π-delocalized system.

The resulting DMASBT/AEL system has proven to be ideal for optical applications due to the rigidity imposed by the matrix. On the one hand, the material exhibits a very high fluorescence quantum yield, 60 times higher than that obtained in aqueous solution and in the red part of the visible spectra. On the other hand, the dye molecules are highly aligned along the nanochannels of the AEL host. Both properties (high fluorescence efficiency and polarization-dependent response), together with the intrinsic nonlinear optical properties of the dye, have resulted in a hybrid material with a NLO response, such as second-harmonic generation.

Moreover, the synthesis of relatively large well-geometrically formed DMASBT/AEL particles (*i.e.* 400 x 75 μm in size) has resulted in a new class of solid microlasers systems, with the crystal itself acting as a resonant cavity, while the dye is the active medium, yielding stimulated emission at a pumping excitation threshold of 0.65 mW.

7.4 4-DASPI STYRYL-DYE INTO 1D-CHANNELED MgAPO-11 (AEL) AND CAGE-LIKE CHABAZITE (CHA)

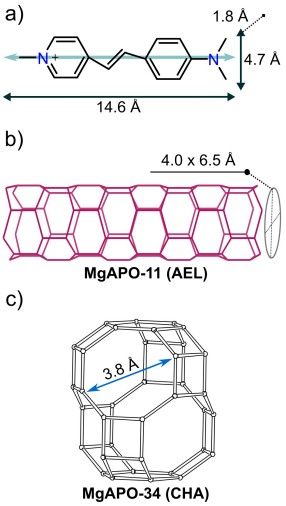

Figure 7.58: **(a)** Structure of 4-DASPI dye. Molecular dimensions and transition dipole moment (blue arrow, Mulliken) estimated by theoretical calculations are depicted. **(b)** 1D channels of MgAPO-11 (AEL) molecular sieve. **(c)** 3D cavity of MgAPO-34 (CHA) framework.

The previous sections were focused on styryl dyes (LDS 730, LDS 722, and DMASBT) occluded in one-dimensional nanochannel MgAPO structures, with the aim of achieving highly fluorescent ordered hybrid materials in the red region of the electromagnetic spectrum. Following the same strategy described in the previous sections, a new hybrid material was synthesized based on the occlusion of the trans-4-[4-(Dimethylamino)styryl]-1-methylpyridinium iodide dye (4-DASPI, Figure 7.58a) as a photoactive guest in the MgAPO-11 inorganic host (Figure 7.58b). Furthermore, with the intention of discovering new structures that confer new optical properties to the chromophores, this same dye was also encapsulated in the Chabacite framework, a structure with 3D cavities (Figure 7.58c) very different from the 1D channels studied so far, but suitable to provide a restricted environment.

7.4.1 *Photophysics of 4-DASPI dye in solution*

To better understand the final photophysical properties of the host-guest systems, studies in aqueous media are a prerequisite. 4-DASPI, the fourth and last styryl dye employed throughout this chapter, was characterized in water solution. This dye is homologous to the previous LDS 722 dye, having dimethylamino as electron donor group and methyl pyridinium as acceptor group but linked by a chain with a single double bond (Figure 7.58a) instead of two double bonds (compare structures in Scheme 3, Chapter 3).

Table 7.14 shows the main photophysical parameters of the 4-DASPI fluorophore in aqueous medium. Similar to LDS 722 (Section 7.2.1), it absorbs in the blue region of the electromagnetic spectrum (λ_{abs} = 449.5 nm) and emits in the red (λ_{fl} = 618.5 nm, Figure 7.59a). The large Stokes shift ($\Delta\nu_{stokes}$ = 6079 cm^{-1}) is due to the push-pull nature

Table 7.14: Photophysical parameters - absorption maximum (λ_{abs}), molar absorption coefficient (ε_{max}), fluorescence maximum (λ_{fl}) and fluorescence quantum yield (ϕ_{fl}) - of the 4-DASPI dye in water solution.

Styryl dye	λ_{abs} (nm)	$\varepsilon_{max} \cdot 10^{-4}$ ($M^{-1}cm^{-1}$)	λ_{fl} (nm)	τ (ns)	ϕ_{fl}
4-DASPI / H_2O	449.5	2.8	492.0 618.5	< 0.1	< 0.01

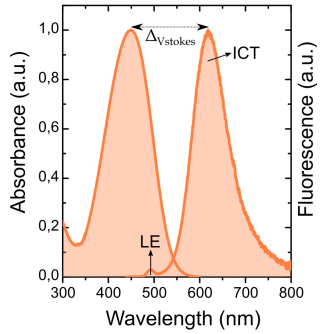

Figure 7.59: Height-normalized absorption and emission spectra (λ_{exc} = 420 nm) recorded for the 4-DASPI dye in solution.

of hemicyanines, as described so far in the photophysics of the previous styryls (Section 3.6.1), where the fluorescence comes from an intramolecular charge transfer between the donor and acceptor moieties favored in the excited state (see the difference in the electronic distribution between HOMO and LUMO orbitals in Figure 7.60a). In fact, in this case, in addition to the main fluorescence band coming from the ICT state, a very weak band appears at higher energies (λ_{fl} = 492.0 nm, Figure 7.59a) ascribed to the LE band. Nevertheless, the dye shows poor fluorescence features in solution (ϕ_{fl} < 0.01 and τ < 0.1), which are barely recordable since they lay under the resolution of the setup.

Hence, the photophysics of this dye follows the same pattern as previous styryl dyes. The main deactivation pathway comes from the flexibility of these molecules, being non-radiative and occurring particularly via molecular motions and internal twisting into the twisted intramolecular charge-transfer state (TICT).[19] Figure 7.60b shows the main rotation of this molecule, which occurs around the single bond between the aniline ring and the pyridylethylene motifs.[20]

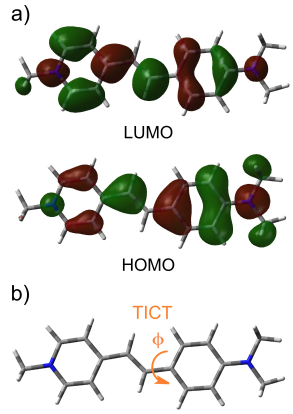

Figure 7.60: **(a)** HOMO and LUMO orbitals, and **(b)** optimized ground state geometry for the 4-DASPI dye with its internal rotation representated.

However, since these photophysical parameters depend on both the polarity and the viscosity/rigidity of the medium,[19] they can be modulated and significantly improved by freezing this dye within a rigid solid matrix with narrow channels. Consequently, the goal is mainly to limit the flexibility of the molecule by slowing down the rotamerism process (TICT) in the excited state.1 In addition to all of the above, the intrinsic NLO properties possessed by this

dye due to its push-pull character make it a very attractive molecule for optical NLO properties.

7.4.2 *Photophysics of 4-DASPI/AEL*

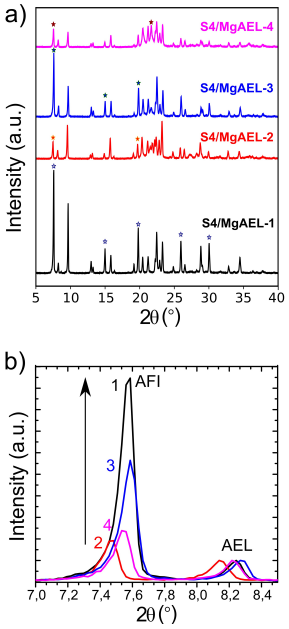

Figure 7.61: **(a)** PXRD patterns of S4/MgAEL-X (4-DASPI/AEL) hybrid systems. Asterisks denote AFI impurity peaks. **(b)** Zoomed difractogram area normalized to the intensity of the first peak belonging to the AEL phase ((≈ 8.2°).

The main results derived from the encapsulation of e 4-DASPI into MgAPO-11 (AEL) and MgAPO-34 (CHA) frameworks (previously described in Section 2.4), both with different topologies and cavities are now detailed. The overall composition of the gel for the synthesis of 4-DASPI/AEL was:

0.95 Al_2O_3 : 1 P_2O_5 : x MgO: y EBA : 0.024 Dye: 300 H_2O

In order to find the most suitable conditions to obtain pure 4-DASPI/AEL systems, systematic variations on x (MgO) and y (EBA) were performed. The water amount was set at 300 and a proportion of 0.024 dye was added, to ensure proper dye-loading in the host. The gels were statically heated in a conventional oven at 180 °C for 24 hours, following the steps explained in the synthesis procedure in Section 4.2. Table 7.15 summarizes the differences in the gel molar compositions employed for the syntheses. For the nomenclature of the samples, the same criterion as before is used. In this case, S4 refers to the fourth dye of the styryl family used during this work, that is 4-DASPI.

The XRD patterns of the samples shown in Figure 7.61a indicate the formation of AEL phase in all of the attempts (the first two peaks of MgAPO-11 appear at 8.2° and 9.6°) but with an important presence of AFI impurities (a more intense peak at 7.5°). Note here that the intensities of the peaks do not indicate that the amount of AFI is greater than that of AEL, because the first peak of AFI appears intense even when there is a slight presence of it.

Interestingly, 4-DASPI, as it has also occurred for LDS 722, acts as a structure-directing agent for AFI phase, even if its amount with respect to the template is very small (0.024 dye vs. 1.00 EBA). In fact, using the same molar composition for many other dyes (*e.g.* AC, MeAC, PY, ACO,

Table 7.15: Variations in gel composition (MgO and EBA), initial pH of the synthesis gel, final dye uptake (expressed as mmol of dye per 100 g of solid product and as percentage of the dye loaded with respect to the initial amount in the gel), and the ratio of the first intense X-ray peaks of the AFI (7.5°) and AEL (8.2°) phases in S4/MgAEL-X (4-DASPI/AEL) materials prepared by conventional heating.

	Gel composition			Dye uptake		X-Ray
Sample	**x (MgO)**	**y (EBA)**	**Initial pH**	**mmol / 100g**	**%**	$I_{AFI/AEL}$
S4/MgAEL-X						
1	0.20	1.00	4.9	8.8	93	9
2	0.20	0.75	4.2	3.1	27	2
3	0.10	1.00	4.8	4.8	41	6
4	0.10	0.75	3.8	3.8	26	2

and ACY) a pure AEL phase has always been obtained without any difficulty.[27,36,89,90]

With the intention of estimating the weight of this secondary phase with respect to the main AEL phase, all the diffractograms were normalized to the intensity of the first peak of AEL phase (Figure 7.61b). Although this is not a quantitative method to determine the real percentage of each phase (for that a pattern matching should be done), it allows an estimation of the presence AFI between the different attempts. Comparing the characteristic peaks of both phases, it is easy to see that the presence of AFI phase is notably higher in samples 1 and 3, in which the synthesis gel was composed of 1.00 EBA and consequently characterized by higher pH values (Table 7.15); whereas in 2 and 4 samples, the contribution of AFI phase is much lower ($I_{AFI/AEL}$ = 2, Table 7.15).

Interestingly a large amount of dye is occluded (quantification procedure detailed in Section 6.6, and calibration curve depicted in Figure C.12 of the Appendix). In fact, the powder shows a very intense dark orange color (Figure 7.62) and important orange emission under UV light. Values from 3 to 9 mmol per 100 g of sample powder

Figure 7.62: Photograph of S4/MgAEL-1 sample in powder under ambient and UV light.

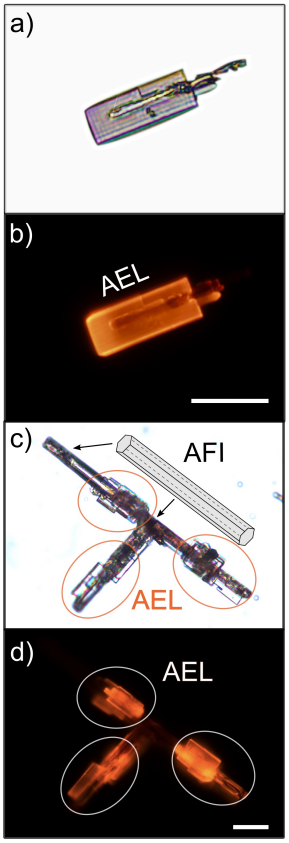

Figure 7.63: Transmission and fluorescence images under green excitation light (HQ530/30m bandpass) of AEL particle **(a, b)**; and for AFI and AEL particles with intergrowth **(c, d)**. The scale (white bar) is 20 µm.

(Table 7.15), which represent a percentage from 25 to almost 95% of dye initially added to the gel, were obtained. Note here that the presence of the MgAPO-5 (AFI) phase affects the determined final dye-uptake values, overestimating the amount occluded in AEL. The higher the presence of this phase is, the higher the loading of the 4-DASPI dye is obtained (Table 7.15). This may be closely related to the dimensions of the channel entrances of the two unidirectional structures formed in the synthesis procedure, where the wider and more cylindrical 7.3 Å cavities of AFI facilitate the incorporation of more 4-DASPI molecules compared to the elliptical channels of AEL (4 Å x 6.5 Å).

To learn more about this incorporation, the particles were analyzed by microscopy. Both AEL and AFI phase crystals have been found within the samples. Figure 7.63a-b show an AEL single particle with well-defined rectangular prism morphology that exhibits a homogeneous and intense orange-red emission under green excitation light (Figure 7.63b) throughout the crystal. Furthermore, the alignment of the dye along the AEL channels was observed by linear polarized fluorescence microscopy, with a D (dichroic ratios) value of 32, resulting in a system with a highly anisotropic response.

However, in some particular cases, these planar crystals have been found intergrown with AFI-like phase particles (Figure 7.63c), which appear as hexagonal and elongated. Importantly, by green excitation light, these crystals do not fluoresce (Figure 7.63d), likely attributed to wider pores of AFI in comparison with AEL, not able to impede molecular torsion and thus cannot boost the photophysical properties of this dye.

The photophysical characterization of the S4/MgAEL system is shown in Table 7.16 and Figure 7.64. As the 4-DASPI/AFI system is not fluorescence, only the fluorescence and excitation spectra of the samples have been recorded to get more precise information on 4-DASPI within the inorganic AEL framework.

S4/MgAEL shows an emission band at 606.0 nm, slightly blue-shifted with respect to solution (618.5 nm, Fig-

ure 7.64a), a typical effect for chromophores encapsulated in very rigid media. The fluorescence band indicates that charge transfer within the 4-DASPI molecule in the excited state is fully efficient, emitting only from the relaxed CT band. In addition, the recorded excitation spectrum displays a broad band placed at 531.5 nm, ensuring that ICT state is responsible for the emission of the system, and not the Locally Excited "LE" band of 4-DASPI (λ_{abs} = 450 nm, Figure 7.64a).

Concerning the quantum yield, the fluorescence efficiency of the dye inside the AEL framework is increased by one order of magnitude, rendering values of 0.10 vs 0.01 in solution (Table 7.16), as a consequence of the rigidity imposed by the zeolitic framework, limiting the flexibility of the dye. Thus, once again, the probability of relaxation by non-radiative pathways has been reduced. It is important to note that these quantum yields do not vary as a function of the gel composition, obtaining generally the same emission efficiency for all presented samples (Table 7.16).

Table 7.16: Fluorescence properties - fluorescence (λ_{fl}) maximum wavelengths, lifetime (τ), and fluorescence quantum yield (ϕ_{fl}) - of the 4-DASPI (aq) and inside MgAEL channels (S4/MgAEL).

System	λ_{fl} (nm)	τ (ns)	ϕ_{fl}
4-DASPI / H_2O	618.5	< 0.1	< 0.01
S4/MgAEL	606.0	0.13 (18%) 3.07 (82%)	0.10

However, compared to the previous systems described with the same inorganic support but different dyes (LDS 722/AEL in Section 7.2 and DMASBT/AEL in Section 7.3), its fluorescent efficiency is relatively low for optical applications. This fact could be attributed to the AFI impurities, since 4-DASPI/AFI can absorb but not emit, leading to underestimated quantum yield values in powder.

Besides, the recorded lifetimes of ≈ 3 ns are much longer than those obtained in solution (< 0.1 ns), in agree-

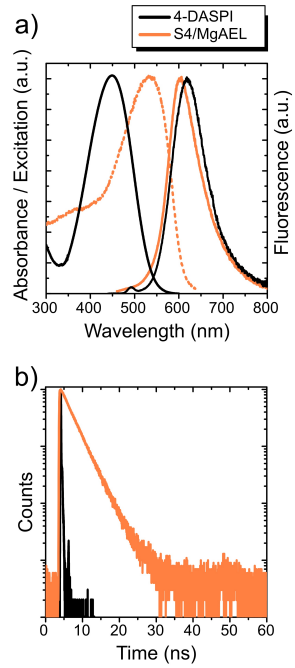

Figure 7.64: (a) Height normalized absorption (continuous line) or excitation (dashed line) and emission (continuous line) spectra; and **(b)** fluorescence decay curves recorded for 4-DASPI (aq) (black) and for S4/MgAEL (4-DASPI/AEL) powder samples (orange).

ment with former results as a result of the confinement of the dye. Note here that the biexponential behavior in the fluorescence decay curves is likely again attributed to the presence of AFI impurities, as a non-emissive system and thus shorter lifetimes values. Hence, the longest lifetime of about 3.07 ns with a weight of 82% is ascribed to the 4-DASPI dye in the AEL structure, while the shortest lifetime of about 0.13 ns with a weight of 18% indicates a less rigid environment, which is likely to be the 4-DASPI within the AFI structure.

In summary, the photophysics of the dye has been improved in AEL with respect to 4-DASPI in solution. However, for use in the applications discussed so far (SHG and microlaser) in single-crystal mode, further experiments would be required in order to achieve particles of suitable size and shape.

7.4.3 *Photophysics of 4-DASPI/CHA*

In an attempt to find other possible alternative structures to the inorganic AEL framework to further improve the photophysics of 4-DASPI, an exhaustive search and study were performed by theoretical simulations focusing mainly on the size and shape of the cavity. After testing several structures, the chabazite structure was selected as potentially interesting. The simulations indicated that the dye can be hosted in a very peculiar configuration (Figure 7.65), *i.e.* between two interconnected three-dimensional chabazite cavities, which open into large 6.7 Å x 10.0 Å ellipsoidal pockets formed by 8-membered rings with a longitudinal distance of 11.7 Å (more details of the structure given in Section X and the Appendix).

The 4-DASPI dye could be incorporated with its bulky head and end groups located in separate CHA cavities, and the central alkenyl chain passing through the smaller 8 MR ring connecting the cavities (Figure 7.65), providing strong-motion restriction and preventing rotations. Consequently, this can be considered a novel hybrid system with a rather

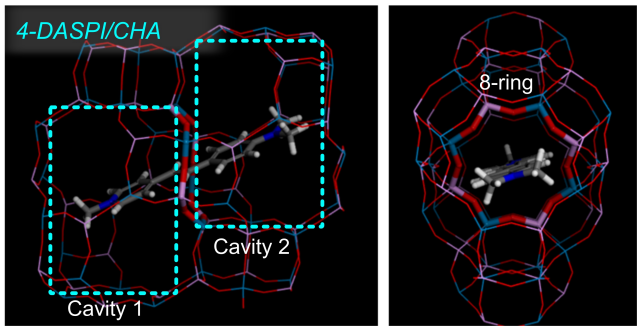

Figure 7.65: The geometry adopted by the 4-DASPI dye between two separate and interconnected CHA cavities. Front (left) and side (right) views of the CHA cavities and the occluded dye molecule.

particular dye arrangement, which could give rise to distinctive photophysical properties.

The Chabazite structure with AlPO-34 topology belongs to the ABC-6 family of zeolites with 3D connected cage systems, and although it has been known for a long time it has been used for the first time in our group. It was one of the first zeolites to be discovered, and its extensive research allows a more straightforward preparation of the structure, giving the possibility to explore its caging effect on photoactive molecules. Therefore, in this section, we will continue to focus on Mg-doped structures, to maximize the incorporation of dye molecules by promoting Brønsted acid sites in the framework (as experimentally demonstrated in Section 7.1).

Thus, for the formation of the inorganic MgAPO-34 host, the following molar composition of the gel was prepared:
3.3 TEA : 0.47 MgO : 0.80 Al_2O_3 : 1 P_2O_5 : 47 H_2O : (0.024 4-DASPI)

The gels were statically heated in the conventional oven at 150 °C for 48 h. The procedure is described in more detail in Section 4.4. The synthesis was set at a low temperature to avoid dye degradation (at 190 °C the dye was observed to degrade) and involved high TEA and Mg contents to avoid

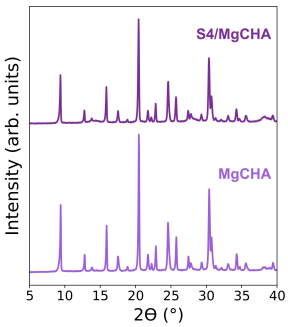

Figure 7.66: X-ray powder diffractions of Chabazite samples synthesized by conventional heating without (MgCHA) and with 4-DASPI dye (S4/MgCHA).

AFI cocrystallization.[91] First, a dye-free synthesis was performed to check that the structure of interest was reached, and then a dye concentration, x was set at 0.024, to obtain the dye-loaded MgAPO-34. The hybrid system will be denoted S4/MgCHA, where S4 refers to the 4-DASPI dye occluded within the Mg-doped CHA structure.

PXRD (Figure 7.66) showed crystallization of pure CHA materials in both cases, with diffraction peaks in good agreement with standard chabazite crystals (first peak at 9.4°).[28] The crystallinity was slightly lower when the material was prepared in the presence of 4-DASPI. The S4/MgCHA solid showed a very light orange colour, indicating a low presence of the dye in the structure. In fact, the amount of estimated dye is around 0.3 mmol per 100 g of powder sample (procedure in Section 6.6). Compared to the dye loading obtained inside the AEL structure (3-9 mmol/100 g, Table 7.15), it was much lower, which could be related to the type of cavities of this structure and to the particular configuration adopted by this fluorophore, confined in-between two cavities of the chabazite.

Figure 7.67a shows small MgAPO-34 crystals, with an average dimension of about 1-3 μm and no appreciable defined morphology. Compared to previous systems, nucleation is much more favored and the crystals obtained have been much smaller (> 20 μm until now). Optical microscopy (Figure 7.67b) shows the same type of crystals but with an intense red fluorescence (Figure 7.67c) when excited with green light.

Polarized fluorescence experiments showed that 4-DASPI molecules in MgAPO-34 crystals do not show a preferential orientation. In the experiments, when the polarization angle (before detection) was tuned from 0° to 90° in several steps, the fluorescence signal of particles did not show any intensity dependence for all the polarization angles.9 This is an indication that 4-DASPI molecules are randomly incorporated inside the cages of the MgAPO-34 due to the three-dimensional cage disposition in the CHA system, contrary to the 1D-channeled 4-DASPI/AEL.

In fact, this lack of alignment of the dye molecules was expected. Due to the symmetry of the zeotype, the molecules are oriented in the *ab* plane, where the channels appear to be interconnected; but within this plane, they can be placed in any orientation within the cavities, and can be arranged in 3 different directions as depicted in Figure 7.68. Although the fluorescence anisotropy technique does not allow us to ensure whether the dye molecules have been introduced into the cavities, it is the most likely since the solid has been thoroughly washed after the synthesis procedure to remove any remaining dye from the surface of the particles.

The photophysical characterization of the S4/MgCHA solid sample (Figure 7.70 and Table 7.17), exhibits two broad absorption bands centered at 343.0 and 437.0 nm (Figure 7.70a). Similarly to DMASBT (Section 7.3), the two bands were assigned to 4-DASPI dye in different protonation forms. In this case, the monocationic (MC) and dicationic (DC) species, respectively, as confirmed by the dye photophysics in solution at different pHs (Figure 7.69). Thus, in a very acidic 4-DASPI aqueous solution (pH = 1) presents an absorption band at 329.0 nm whereas at neutral pH the main band was centered at 450 nm (Figure 7.70a).

Figure 7.70b shows the fluorescence spectra of 4-DASPI in CHA under direct excitation to DC. The less intense peak at lower wavelengths, λ_{fl} = 385.0, is attributed to DC, and the main band, centered at 583.0 nm, is instead attributed to MC, because under direct excitation to this species the same emission band is observed. The high Stokes shift obtained in the hybrid material ($\Delta\nu_{stokes}$ = 5416 cm^{-1} in chabazite and $\Delta\nu_{stokes}$ = 6079 cm^{-1} in solution) and by the bathochromically band registered in the excitation spectrum (maximum at 525 nm, Figure 7.70b, Table 7.17), with respect to its original absorption at 437.0 nm (Figure 7.70a), indicated that the charge transfer state is responsible of the fluorescence emission.

Once again, the main emission band of 4-DASPI in MgAPO-34 cavities is significantly blue-shifted compared to the dye in solution (Figure 7.70b and Table 7.17), at-

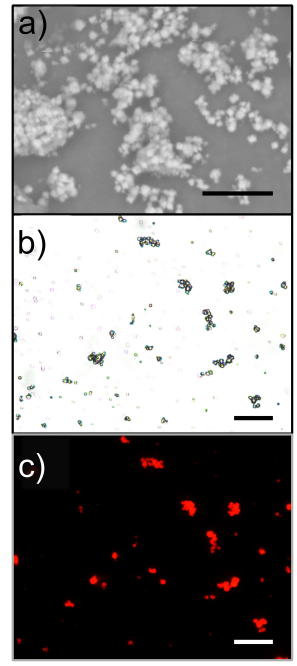

Figure 7.67: Images taken for S4/MgCHA sample by **(a)** scanning-electron microscopy (SEM) and optical microscopy: **(b)** transmission and **(c)** fluorescence taken under green excitation (y el filtro) light. The scale is 20 μm in all of them (black and white bars).

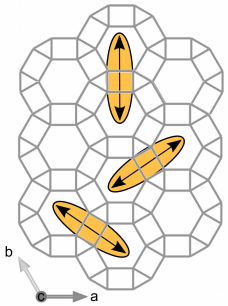

Figure 7.68: The different possible arrangements of the 4-DASPI dye molecules within the ab plane of the CHA inorganic matrix.

tributed to the confinement effect. The physical interactions with the cage walls in the narrow environment of CHA structure is strong, leading to a shift toward higher energies.[92] In fact, the blue-shift in chabazite has resulted higher than that obtained in AEL for 4-DASPI.

Table 7.17: Photophysical parameters - absorption (λ_{abs}) or excitation (λ_{ex}) and fluorescence (λ_{fl}) maximum wavelengths, lifetimes (τ, only the major lifetime contribution is given), and fluorescence quantum yields (ϕ_{fl}) at different excitation wavelengths - of the 4-DASPI fluorophore in different environments (H_2O, MgAEL and MgCHA).

System	λ_{abs} / λ_{ex} (nm)	λ_{fl} (nm)	τ (ns)	ϕ_{fl}
4-DASPI / H_2O	329.0^{D} / 449.5^{M}	492.0 / 618.5	< 0.1	< 0.01
S4/MgCHA	343.0 / 437.0	385.0 / 583.0	2.73^{a}	0.33^{a}
S4/MgAEL	531.5*	602.5	3.12^{a}	0.10^{a}

D) Dicationic species; **M)** Monocationic species
a) Same values at λ_{exc} = 320 nm and λ_{exc} = 450 nm.
* Maximum wavelength taken from the excitation spectra, since the absorption showed a very broad band that was not possible to deconvolute.

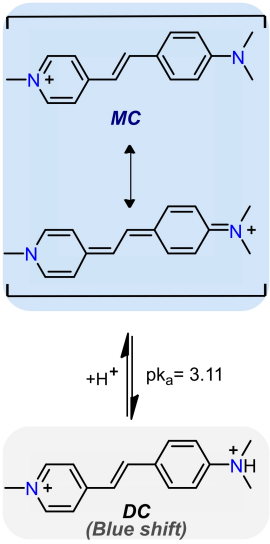

Figure 7.69: Equilibrium between the 4-DASPI (aq) monocation and dication especies

Interestingly, the 4-DASPI loaded CHA material is highly fluorescent independently of the excitation wavelegth, reaching a quantum yield of around 30% (Table 7.17, over 30 times higher than in solution), and very long lifetimes of about 2.7 ns (Table 7.17 and Figure 7.70c). Moreover, these fluorescent quantum yields have been markedly improved in CHA with respect to AEL (≈30% in CHA with respect to ≈ 10% in AEL, Table 7.17), probably because the geometry adopted by the dye inside these cages has lead to a higher restriction of the molecular motions. In any case, it can be concluded that in both structures the motions of the molecule have been satisfactorily hindered and its photophysics is improved.

Considering the good photophysical results obtained for the 4-DASPI/CHA system and the small particles of approximately 1-2 µm, it was thought that they could be interesting to produce random laser in suspension.[93,94] Ran-

dom lasers (RL) are laser devices in which the multiple scattering in disordered media provides optical feedback and leads to laser action.[95–97] In these cases, since the environment contains several scattering centers, the light is scattered many times before escaping from the gain medium, increasing the path length of the light and thus inducing an amplification of the light.[98,99] Since the scattering itself traps the light in the gain medium, there is no need for mirrors.[94,96]

In practice, the small particles (few microns) of S4/MgCHA will provide the disordered medium to generate the scatter necessary to amplify the light. Therefore, a suspension of 4-DASPI/CHA particles in methanol was prepared in rectangular quartz cells of 1 cm optical path length. The suspension was transversely pumped with a wavelength-adjustable optical parametric oscillator (OPO) at 450 nm, 5 mJ power and at a repetition rate of 1 Hz.[100] Excitation pulses were linearly focused into the cell using a combination of positive and negative cylindrical lenses (f = 15 cm and f = -15 cm, respectively) arranged perpendicularly and the fluorescence emission was monitored perpendicular to the excitation beam.

However, no stimulated emission was recorded, probably because the incorporation of the dye was not high enough to activate the laser action, a necessary prerequisite to attain good optical gain (Section 6.8). Therefore, future experiements will be dedicated to promote higher dye incorporation by variations in the synthesis conditions.

7.4.4 *Conclusion*

By employing different types of magnesium-doped aluminophosphates (AEL and CHA) as inorganic supports for 4-DASPI dye molecules in order to provide a rigid environment, fluorescence quantum yields and excited-state lifetimes have been increased significantly, slowing down the torsional motion of the dye. The different inorganic matrices influence and modulate the photophysical proper-

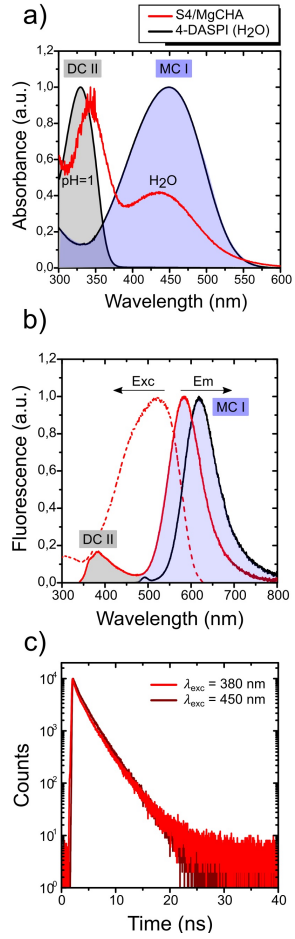

Figure 7.70: Photophysics for the dye 4-DASPI (aq) (black) and S4/MgCHA sample (red) measured in bulk powder: **(a)** height normalized absorption (both MC I and DC II species bands of 4-DASPI in solution are included) **(b)** and fluorescence (λ_{exc} = 420 for the 4-DASPI in water and λ_{exc} = 320 for the solid powder) bands.

ties of this fluorophore offering different functionalities to the resulting hybrid material. Thus, depending on the type of cavities (channels or cages) of the host, either a highly ordered anisotropic material or a very fluorescent system has been obtained.

This last novel system, in which the dye molecules are hosted inside confined cavities, opens up new possibilities to discover other novel structures, which are likely to provide new optical functionalities. These other dye-loaded host systems of the same ABC-6 family (AFX and SWY) will be discussed in the outlook chapter (Chapter 10).

8

NOVEL SYSTEMS FOR ENERGY TRANSFER

The development of artificial systems that mimic the photsynthesis process is very important.

In nature, we find a multitude of processes driven by light energy, such as photosynthesis. In this process, plants and other photoautotrophs absorb solar energy by antenna pigments and efficiently transfer it to photochemical reaction centers where the energy conversion takes place.[101–105] It is a rather complex but very interesting natural process that has attracted many scientists. In fact, one of the most fascinating challenges in photochemistry is the design and development of artificial systems that mimic this natural process. For that purpose, an efficient strategy employed is the energy transfer between different molecules, collecting light through absorption of an organic donor molecule to subsequently transfer the energy to another acceptor component.[106–109]

This can be achieved by promoting FRET processes between different molecules.

A key factor governing the efficiency of this process is the excitation energy transfer (EET) between two chromophores, which is often referred to as Förster Resonance Energy Transfer (FRET, see more details in Section 3.2.2.3).[110,111] A deep knowledge of the most important parameters of this photophysical process, such as the distance between the chromophores and their relative orientations, as well as the exact ratio between donor and acceptor,[112] allows precise control and development of efficient artificial systems to be used in a wide range of applications, *e.g.* photonic antennas, tunable dye-lasers, light modulators, and so on.[113–116]

This chapter will mainly focus on the development of materials based on photoactive molecules subjected to en-

ergy transfer processes aimed for tunable dye lasers and white light emitters. In the first case, the main advantage resides in the possibility to modulate the wavelength of the laser signal over a wide spectral range compared to conventional monochromatic lasers.[117,118] The acceptor molecules are indirectly excited by the transfer of the donor excitation energy, which is usually a robust dye with good photostability that significantly improves the durability of the acceptor. In this way, the laser performance is considerably improved, especially in cases where fluorescence is pursued in the red region of the visible spectrum,[119] an area of particular interest for biomedical applications (explained in Chapter 7).[120]

By this devices it is possible to obtain tunable laser dyes or white light emitters.

In the second case, regarding white light emitters, the emission of the whole region of the visible spectrum is collected by recording the simultaneous emission of the blue, green, and red (RGB colors) regions of the electromagnetic spectrum.[111,120,121] One of the most exploited strategies for the generation of white light is the use of mixed multicomponent systems that emit in different regions and induce a partial energy transfer between donor and acceptor molecules.[122–124] Furthermore, by choosing the appropriate proportions between donors and acceptors it is possible to modulate the resulting emission color.

However, organic dyes tend to aggregate at high concentrations.

When designing systems with organic dyes, one of the prerequisites is that the material must be optically dense for optical applications. However, many of these fluorescent molecules have a relatively high tendency to self-associate under these conditions (in aqueous solution or solid-state). Thus, at high dye contents, overall laser performance is usually negatively affected by aggregation, as they compete with monomers when absorbing the pump irradiation. Since aggregates are generally characterized as non-fluorescent, or much less fluorescent than monomers (except for very specific examples)[31], they drastically decrease the fluorescence capacity and consequently the laser action (Section 3.2.1).

In this context, the aim of this chapter is the search for high dye loadings in hybrid systems avoiding aggreg-

ation, in order to promote FRET processes by the simultaneous encapsulation of several chromophores within zeotypes.[113,125,126] To this aim, two molecular sieves have been selected: the framework IFO, a relatively novel structure characterized for having extra-large one-dimensional pores; and AEL, proven to be an ideal host for a wide variety of dye guests (covered in Section 7.2, 7.3 and 7.4 respectively). Regarding the allocated organic dyes, mainly robust laser dyes with a general molecular structure built up by three fused aromatic rings have been selected (Section 3.6.2). All of them have different fluorescence features and are potentially susceptible to aggregation at high concentrations. Therefore, their incorporation into zeotypes will be used as a strategy to:

To avoid aggregations they will be encapsulated into IFO and AEL structures.

The main objectives pursued by the incorporation of dye molecules.

i) Protect and isolate the molecules to avoid specific interactions with the surrounding media and photodegradation.

ii) Improve the photophysical properties of the enclosed fluorophores by restricting molecular motions and aggregation.

iii) Promote energy transfer mechanisms among the encapsulated dyes to tune the emission light of the final hybrid system.

Hence, along the following lines, we will describe and discuss the designed materials and their final photophysical characteristics, paying special attention to the changes in the properties of isolated molecules once inside the zeolitic structures and the ongoing energy transfer mechanisms.

A published article and another one in preparation.

Among the systems to be discussed in this chapter, a published paper related to white light emission in AEL framework (Section 8.2) should be highlighted.[89] Regarding the IFO structure, there is an article under preparation that includes the most significant results.

8.1 EXTRA-LARGE MgITQ-51 (IFO) MOLECULAR SIEVE

The synthesis of extra-large pore zeotypes is of great importance for the development of new systems susceptible to expand their use as catalysts or molecular sieves. In the past, many attempts were made to discover materials with bigger cavities (classification in Section 2.3) by the use of big molecular size SDAs. However, with this approach, the likelihood of finding suitable template candidates is very small, since it is very difficult for molecules to meet all the requirements, including adequate size, rigidity, thermal stability, and hydrophobicity.[127,128]

In this sense, a new concept that solves the previous problem was introduced by Gómez-Hortigüela et. al.[129–131] and Corma et. al.[132] where the structure guidance of the porous materials was based on the supramolecular self-assembly of the structure-directing agent. For example, LTA[132] and AFI[127,130] zeolites were successfully synthesized by this method, using aromatic molecules that self-aggregate and form stable bulky dimers,[129] which are primarily responsible for driving a particular structure of the microporous network.[133]

The great advantage of this method is that allows the use of relatively simple molecules (bulky and rigid), known as organic structure-directing agents (OSDAs), usually soluble in the synthesis medium and with strong non-bonded interactions with the inorganic host.[128,133] In this way, these organic templates have opened the door to the discovery of many new and more complex extra-large pore zeolites.[134–139] One of them is the ITQ-51 structure (IFO framework type), a one-dimensional 16-ring channel framework with a pore opening of 9.3 Å x 10.6 Å (Figure 8.1a and Section 2.4). It was discovered in 2013,[140] and is synthesized with DMAN (1,8-bis(dimethylamino)naphthalene, Figure 8.1b) as OSDA, that self-assembles and forms dimers able to stabilize the very large pores (see illustrative representation in Figure 8.1a).[133]

Interestingly, this novel structure allows the encapsulation of larger dyes into its extra-large channels. For this

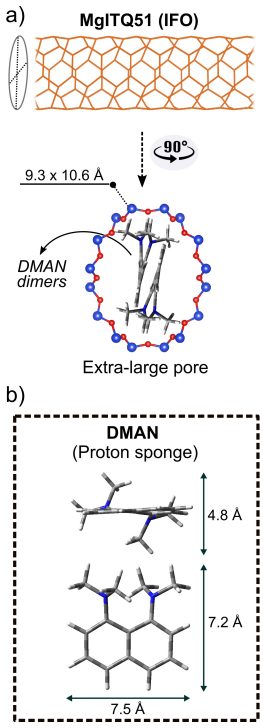

Figure 8.1: **(a)** Illustrative representation of the IFO framework nanochannels and the view of the pore opening by a 90° turn with the allocated DMAN dimers inside. The pore dimensions are also indicated. **(b)** Optimized geometry of the DMAN (up and front view) with its molecular dimensions.

very reason, this structure has been used to incorporate for the first time larger laser dyes such as rhodamine 123 (R123) and Nile Blue (NB). Following the trend of this thesis, to facilitate the incorporation of these fluorophores, the inorganic structure has been doped with magnesium (MgITQ-50) and its synthesis conditions were optimized. In the following lines we will show a complete study of the zeotype including the photophysical characterization of its template, together with a thorough analysis of the achieved dye-loaded host-guest materials.

8.1.1 *Photophysics of DMAN template in solution*

Before explaining the synthesis of the Mg-doped zeotype and dye-doped hybrid systems, a small emphasis will be made on the photophysics of DMAN in solution, since for the first time we employ a bulky aromatic OSDA with interesting photophysical properties by itself.

DMAN (Figure 8.1) is an aromatic diamine that combines strong basicity (pK_a < 12.3)[141,142] with a high affinity for protons, hence it is often referred to as proton sponge. Moreover, it shows a tendency to aggregate and form dimers. To analyze its photophysical behavior, six solutions were prepared in aqueous media, at different pH-s and concentrations: acidic (pH = 2), neutral (pH = 7, similar to the conditions of the synthesis gel, Section 8.1.2), and basic solutions (pH = 12), each of them at two extreme concentrations, diluted (7· 10^{-5} M) and concentrated (7· 10^{-3} M).

The photophysics of DMAN in the protonated state (pH < pk_a) is shown in Figure 8.2a and Table 8.1. Both diluted and concentrated DMAN-H^+ species at acidic (pH = 2) and neutral (pH = 7) conditions present similar characteristics, with the main absorption band at 285 nm and a highly shifted emission at around 462 nm. This is in agreement with published data, and the very large Stokes shift ($\Delta\upsilon_{St} \approx 13500\ cm^{-1}$, Table 8.1) observed for the monoprotonated species is a consequence of the formation of a strongly

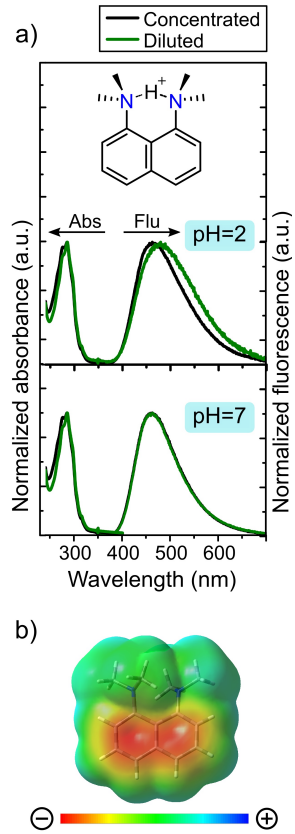

Figure 8.2: **(a)** Height normalized absorption and fluorescence spectra of DMAN at different concentrations (diluted = 7·10^{-5} M and concentrated = 7·10^{-3} M, green and black lines, respectively) and different pH-s. The molecular structure of the protonated species is included. **(b)** Molecular electrostatic potential (MEP) map of DMAN.

relaxed and highly polar intraCT, involving motions of the DMA groups (dimethylamines) in the excited state.[133,141,142]

The electrostatic potential map of DMAN in Figure 8.2b suggests a strong charge-transfer character of the molecule with a highly partitioned electronic distribution between the DMAs and the naphthalene moiety. The ICT shows weak emissive capability, resulting in a fluorescence quantum yield of around $\leqslant$1% (Table 8.1).[141] Lifetimes could not be measured in our setup (laser excitation not available in the UV range), but are known to be very long, in the order of 10-15 nanoseconds.[141]

Table 8.1: Photophysical data - absorption (λ_{abs}) and fluorescence (λ_{fl}) wavelength maxima and Stokes shift ($\Delta\upsilon_{St}$) - of DMAN (aq) at different pH-s and concentrations (diluted = $7{\cdot}10^{-5}$ M and concentrated = $7{\cdot}10^{-3}$ M).

[DMAN]	pH	λ_{abs} (nm)	λ_{fl} (nm)	$\Delta\upsilon_{St}$ (cm^{-1})
Dil.	2	285.0	475.5	14233
Conc.	2	284.5	462.0	13504
Dil.	7	285.0	462.0	13443
Conc.	7	284.5	462.0	13504
Dil.	12	345.5	448.0	6622
Conc.	12	381.5	442.0	3588

The results clearly indicate that self-interactions of DMAN protonated species do not occur in either dilute or concentrated solutions in the measured range. However, a completely different scenario is found in basic media, at pH = 12, approaching the pk_a of the molecule (Figure 8.3 and Table 8.1).

Here we find the main absorption band located at 345 nm in diluted medium, red shifted with respect to the one previously observed. This displacement to longer wavelengths upon basifying the medium indicates the formation of neutral DMAN as a consequence of the electronic coupling between the electron pairs of the amino and aro-

matic rings.[141] This neutral species, even at not very high concentrations, appears to form aggregates, characterized by a long tail up to 700 nm in the absorption spectra (highlighted with purple color in Figure 8.3). Moreover, as the concentration increases, the absorption shifts even more bathochromically (from 345.5 to 381.5 nm, Table 8.1) because the interactions between the molecules become stronger, likely resulting in the formation of J-aggregates in solution. It should be noted that these aggregates are visible even to the naked eye since the solution switches from transparent to a purplish hue as the concentration increases at this pH. Furthermore, the species found in solution at this pH is barely soluble at any of the prepared concentrations, including the diluted one.

Upon excitation to the neutral monomer (λ_{exc} = 350 nm), the fluorescence spectrum shows its maximum around 445 nm regardless of the solution concentration,[132] which resembles that of DMAN-H^+ in water, but slightly blue shifted (Table 8.1). Evidence suggests that this emission is still coming from an intraCT state.[140,142] The reddish emission band found in acidic media may be related to the more polar character of the CT state (hydrogen bonds in DMAN-H^+) and the better solvation by water molecules, thereby stabilizing it and leading it to lower energies. Another possible explanation may be that DMAN is subjected to important geometrical changes in the excited state, which implies a geometrical relaxation and a reorientation of the dimethylamino groups.[142]

Figure 8.4 displays the emission of a concentrated sample of DMAN at pH = 12, recorded at high pumping conditions (80 mW power) and at different delay times after the laser pulse upon excitation at the tail range of the absorption spectra (λ_{exc} = 460 nm, setup described in Section 6.4). For short delay times, a band centered at 515 nm together with a shoulder at around 600 nm is observed. As the delay increases, the band at shorter wavelengths gradually decreases, and the shoulder at higher wavelengths becomes the main emissive band (delays $\geqslant$ 20 ns).

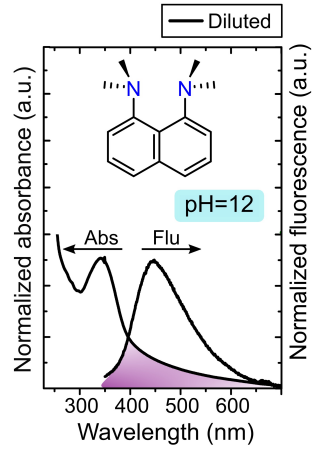

Figure 8.3: Height normalized absorption, and fluorescence spectra of the diluted DMAN (aq) ($7{\cdot}10^{-5}$ M) at pH = 12. The molecular structure of the neutral species is shown above and the purple filling indicates the formation of aggregates.

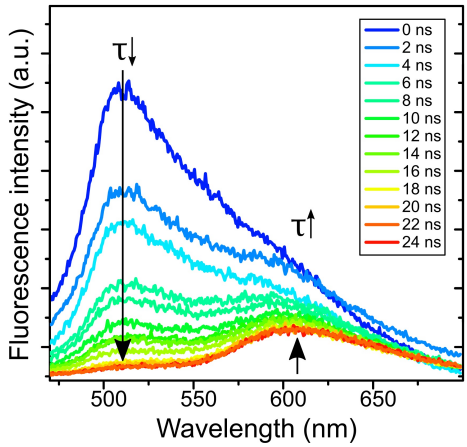

Figure 8.4: Fluorescence emission spectra for DMAN (aq, ph = 12) at different delay times after laser pulse (from 0 to 24 ns, every 2 ns) upon excitation at 460 nm at a laser power of 80 mW.

These two bands may imply the formation of two types of aggregates with different relative geometric dispositions in the ground and/or excited state, *i.e.* the intermolecular charge transfer complex responsible for the red-tail in absorption and the excimers that are only formed in the excited state. Both species are characterized by long lifetimes.[141] The emission characterized by shorter lifetimes could be related to aggregates of intermolecular charge transfer character, while the one with longer lifetimes could be assigned to a π-π stacking of the monomers generating excimers in the excited state (Section 3.2.2.1). A deeper characterization of the nature of the emission of these DMAN species at basic pH and at high concentration is difficult to perform in solution. The presence of these species completely quenches the emission of monomeric DMAN resulting in quantum yields close to zero regardless of their concentration in solution (Table 8.1).[141,142]

In short, the photophysics of the organic structure-directing agent used for the formation of the ITQ-51 structure is quite complex, being highly dependent on the pH of the medium and consequently on the species generated

in each state, having a high tendency to self-associate in its neutral state.

8.1.2 *Synthesis of IFO and photophysics of occluded DMAN*

The Mg-doped IFO zeotype was synthesized with the following gel composition based on previous studies:[140,143]

$$0.95\ Al_2O_3 : 1.00\ P_2O_5 : 0.1\ MgO : 1.2\ DMAN : 40\ H_2O$$

As mentioned above, the protonated aromatic sponge DMAN was used as SDA and the divalent transition metal Mg^{+2} ion was introduced as a substituent to favor Brønsted acid sites. Therefore, the Mg-containing ITQ-51 materials were prepared at 150 °C under static conditions. In previous studies conducted by other scientists, the gels were heated for 5 days. In our case, in order to perform a kinetic study, different heating times were applied, at 1, 2, 3, and 5 days, respectively. Refer to the experimental part for a more detailed explanation of the syntheses (Section 4.7) and the Appendix for the exact gel compositions (Appendix B).

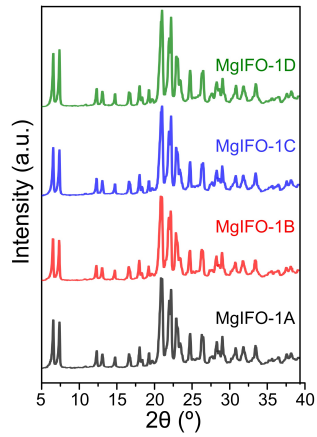

Figure 8.5: PXRD patterns for MgIFO-1 samples at different heating times. A = 1, B = 2, C = 3 and D = 5 days.

The PXRD patterns of the prepared samples confirm the crystallization of pure IFO structure in all the attempts (Figure 8.5), with its characteristic first peak around 6.5° in the diffractogram.[28] Interestingly, there are no apparent differences (similar intensities) between the heating times applied during the preparation of the structure, indicating the successful crystallization of this phase at 1 day of heating, reducing the heating time.

Scanning electron microscopy images (Figure 8.6a) show a homogeneous size distribution of ITQ-51 crystalline particles, with no visible amorphous phases or crystals with different morphologies. The IFO samples show platelike crystalline particles with sizes ranging from 5 to 10 μm, intergrown in an aggregate morphology.

For all samples, the incorporation of DMAN molecules within the crystalline framework of MgIFO has been high, with 34-37% of DMAN occluded with respect to the initial amount added to the gel (quantification procedure described in Section 6.6 and calibration curve shown in Fig-

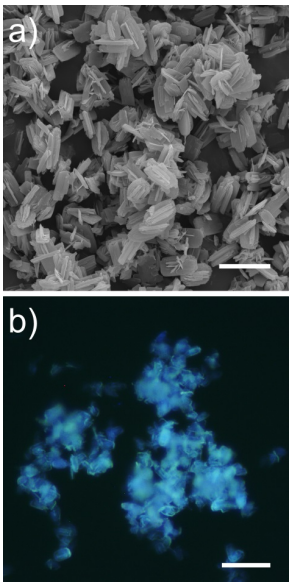

Figure 8.6: MgIFO particle images. **(a)** SEM (scale = 10 μm) and **(b)** fluorescence image under UV excitation (D350/50x band-pass, scale = 20 μm).

ure C.14). Such high template loadings may also explain the excellent structure direction driven by this aromatic molecule resulting in a very pure phase and homogeneous crystallization.

Interestingly, the particles analyzed by optical microscopy (Figure 8.6b) show bright blue fluorescence under UV excitation light. This suggests that the confinement of the DMAN molecules inside the nanochannels of IFO has improved fluorescence properties with respect to solution. To get more information about the distribution of DMAN molecules inside the nanochannels, studies were performed with linearly polarized light. These studies do not reveal any preferred orientation of the DMAN within the channels, probably due to various possible dispositions that the molecules can adopt within the extra-large pores of the structure (Figure 8.1a).

Therefore, an in-depth photophysical characterization of the bulk white powder of the MgIFO zeotypes was performed. UV-Vis absorption spectrum shows (Figure 8.7a) the appearance of the main band at around 300 nm together with a very broad band at higher wavelengths, approximately from 450 to 700 nm.

As studied in the previous section (Section 8.1.1), this protonated aromatic sponge exhibits a photophysical dependence on environmental conditions. However, its high basicity (pk_a = 12.3) almost completely ensures its protonation in the synthesis medium (initial and final pH of the prepared gels are around 2 and 8 approximately), thus allowing the necessary organic-inorganic interactions during the nucleation-crystallization processes.[133]

Hence, the first and most prominent band, at around 315 nm, red shifted with respect to the protonated DMAN-H^+ in solution (285 nm, Table 8.1), and blue-shifted with respect to the neutral molecule (345 nm), is attributed mainly to the protonated DMAN monomer, although a minor contribution of the neutral species cannot be excluded. Upon excitation to this band (λ_{exc} = 315 nm, blue spectrum in Figure 8.7) a well-defined emission band appears with its maximum at 412 nm, which is in agreement with previous

studies of DMAN within IFO.[133] The excitation spectrum shows a band at 288 nm, very similar to that registered for the DMAN-H^+ in aqueous solution (285 nm, Table 8.1) ensuring that protonated DMAN species is responsible for the fluorescence of the system.

Interestingly, the fluorescence efficiency for the trapped monomer DMAN-H^+ is much higher, 24%, compared to 1% in solution (Table 8.1), explaining the intense blue emission observed by optical microscopy (Figure 8.6b). This improvement in the fluorescent quantum yield can be attributed to the confinement effect within the IFO cavities, probably due to the hindrance of dimethylamino motions reducing internal conversion processes.

Moreover, as mentioned above, the UV-Vis absorption spectrum also shows the presence of a red shifted broad band centered around 550 nm (Figure 8.7a). This peak is likely assigned to DMAN complexes, expected in the crystalline environment of the IFO structure. The recorded emission spectra upon excitation to this band (λ_{exc} = 460 nm, Figure 8.7c) confirm the formation of two emissive complexes: one centered at around 540 nm and another red shifted at around 650 nm (515 nm and 600 nm in solution, Section 8.1.1). Like in solution, they are believed to belong to complexes of interCT nature and π-π stacking excimers, respectively, but from the protonated DMAN species. Note here that the emission efficiency of those complexes is much lower in comparison with the isolated DMAN molecules.

The excitation spectrum shows a red shifted characteristic band (Figure 8.7c) similar to that obtained in the absorption spectra (compare with Figure 8.7a), confirming the aforementioned assignation. Indeed, this band appears slightly red shifted and with a more-defined shape than that observed in the absorption spectrum (Figure 8.7a) indicating a higher contribution of these complexes in the excited state. This is a typical feature of interCT complexes. Note here that excimers only exist in the excited electronic state because they dissociate after photon emission.

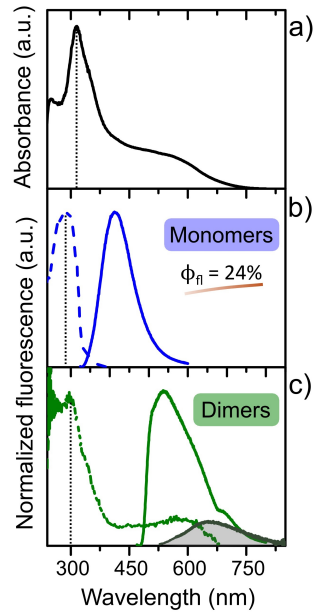

Figure 8.7: Photophysical characterization of MgIFO material in bulk powder: **(a)** absorption (black), **(b)** height normalized excitation (dashed lines) and emission spectra (continuous lines) for the DMAN monomer (blue, λ_{exc} = 315 nm) and **(c)** its aggregates (green, λ_{exc} = 460 and 550 nm).

Therefore, it is concluded that the incorporation of the structure-directing agent DMAN takes place both in its monomeric and associate state, resulting in feasible self-interactions of the DMAN molecules in the synthesis gel and the final ITQ-51 solid prepared.[133] On the other hand, a highly fluorescent material has been obtained as a consequence of the enhanced photophysical properties of the constrained monomer.

Surprisingly, this improvement is affected by the aging time of the system. After a few months of the synthesis, a sharp decrease in the fluorescent emission was detected in all samples. Optical microscopy images (Figure 8.8) show this abrupt change in intensity and color hue over time, where it is possible to discern between particles that have undergone a drastic fluorescent quenching from an intense blue to fainter green color.

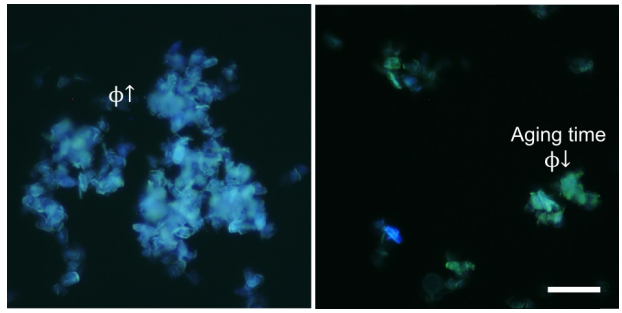

Figure 8.8: Fluorescence images of MgIFO particles under UV excitation (D350/50x band-pass) **(a)** right after synthesis and **(b)** a few months later. Scale = 20 μm.

This strange phenomenon in the material was not to be expected in materials as stable as the zeotypes. Hence, in an attempt to understand the change in the system's behavior, photophysics was again thoroughly characterized. All this data is included in Table 8.2. The most notable change was observed in terms of the fluorescent quantum yield and average lifetimes of the DMAN monomer, registering a very sharp decrease from 24% to 5% (Figure 8.9a) in the fluorescence efficiencies and from 7.03 ns to 5.62 ns in the lifetimes. In addition, the emission spectra recorded for the aggreg-

ates (Figure 8.9b) showed a narrower and bathochromically shifted band (at around 600 nm) with respect to the previous one. One of the hypotheses for this photophysical change is a geometrical redistribution of the DMAN complexes within the ITQ-51 structure with time.

Table 8.2: Photophysical parameters - absorption (λ_{abs}) and fluorescence maximum (λ_{fl}) wavelengths, and lifetimes (τ, average lifetime considered according to Equation 6.6) of DMAN monomers and dimers within the MgIFO structure over time.

Sample	DMAN	λ_{abs} (nm)	λ_{fl} (nm)	τ (ns)	ϕ_{fl}
MgIFO	*Monomers*	316.0	412.0	7.03	0.24
	Dimers	450-700*	536.0	ND	< 0.01
MgIFO (16 months)	*Monomers*	316.0	412.0	5.62	0.05
	Dimers	450-700*	603.0	ND	< 0.01

The lifetimes and fluorescence quantum yields were recorded upon excitation at 315 nm for DMAN monomers and 460 nm for the dimers.
* Tail in the absorption spectra.
ND: not possible to determine because the signal was too low.

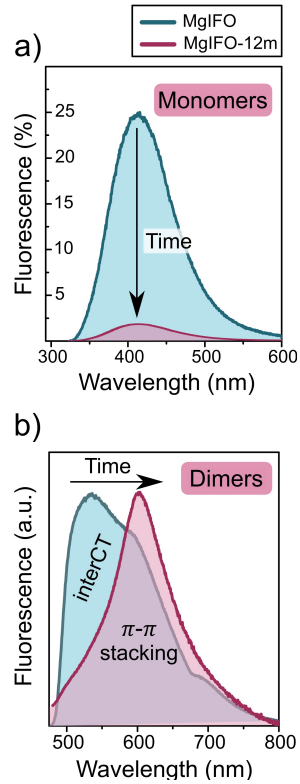

Figure 8.9: Photophysical changes in the MgIFO material after 12 months, from blue to red-colored spectrum: **(a)** fluorescence spectrum of DMAN monomers normalized to its quantum yield (λ_{exc} = 315 nm), and **(b)** height normalized fluorescence spectra of DMAN dimers. (λ_{exc} = 460 nm).

To further elucidate the changes of the DMAN complexes within the IFO structure, a computational study was performed. The optimized geometries of the DMAN dimers in the zeotype structure are shown in Figure 8.10. Calculations reveal that DMAN molecules can be located in two possible thermodynamically stable configurations inside the 16-ring channels.

In the first dimer geometry, the naphthalene unit of one of the monomers is disposed in front of the DMA groups of the second monomer and vice versa, favoring an interCT process between both moieties (Figure 8.10a). In the second, the naphthalene groups are in a face-to-face disposition ensuring π-π type interactions between the aromatic rings and typical conformation of exciplexes (Figure 8.10b). The two arrangements seek to maximize interaction between dimers and the energetic difference between the two is relatively small, both configurations being highly stable.

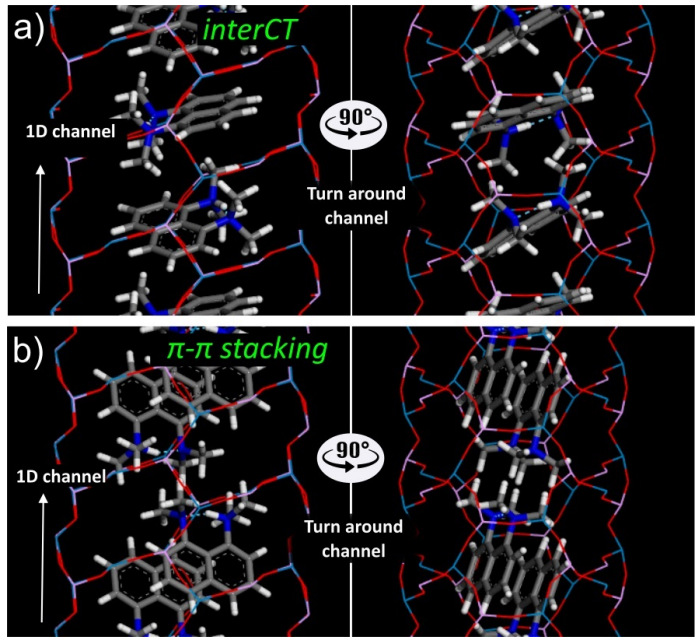

Figure 8.10: Two possible stable configurations for DMAN aggregates within the IFO structure: **(a)** with interCT character, with the DMA and naphthalene groups, face to face, and **(b)** with π-π type interactions, with the aromatic naphthalene groups face to face.

The computational model reveals that the aging time has favored the redistribution of aggregates within the channels, and explains the new emission band at 603 nm (Figure 8.9b and Table 8.2), assigned to dimers with π-π interactions between aromatic rings,[132] which are thermodynamically more stable over time than those with interCT character (maximum at 536 nm, Table 8.2). All this explains the drop in the fluorescent quantum yield of DMAN. Over time, the different ordering of the organic molecules leads to the generation of less fluorescent aggregates and causes an overall fluorescence decrease in the system.

To sum up, the self-assembly role of protonated aromatic sponges is crucial for the resultant photophysical properties of the extra-large pore zeolite ITQ-51. Furthermore, although the fluorescent efficiency of the material has been affected over time, a blue fluorescent zeotypic mater-

ial has been achieved for the first time without the need to incorporate any other dyes into the synthesis gel.

In light of the results, the next stage is focused on the encapsulation of bulky laser dyes with the idea of exploiting these blue fluorescent features of OSDA and thereby promoting an energy transfer to other molecular entities trapped in the channels.

8.1.3 *Coencapsulation of other dyes for energy transfer (FRET)*

In this new section, energy transfer processes between units of different entities are pursued by the encapsulation of other fluorescent dyes into the unidirectional channels together with DMAN. In this sense, knowing that the DMAN-IFO zeotype emits mainly in the blue region (Figure 8.11a), two laser dyes, rhodamine 123 (R123) and Nile Blue (NB), have been selected to create suitable FRET pairs with DMAN and thus tune the final emission of the system.

The first of these, R123, is a well-known laser dye of the xanthene family (Section 3.6.2.2). It absorbs and emits in the green region of the visible electromagnetic spectrum (λ_{abs} = 498 nm and λ_{fl} = 525 nm in H_2O, Figure 8.11b) and exhibits quantum yields of nearly 1.[144] Complementarily, Nile Blue, an oxazine-type dye (Section 3.6.2.3) exhibits absorption and emission in the red-edge of the visible spectra (λ_{abs} = 635 nm and λ_{fl} = 674 nm in H_2O, Figure 8.11c)[145] and high quantum yields in polar environments. Both are very bulky laser dyes (dimensions in Figure 8.11) that cannot be encapsulated in the previous structures presented throughout this thesis (AFI, ATS, AEL, or CHA). However, they show interesting properties to drive new photophysical features inside the unidirectional channels of the IFO structure (9.3 Å x 10.6 Å, Figure 8.1).

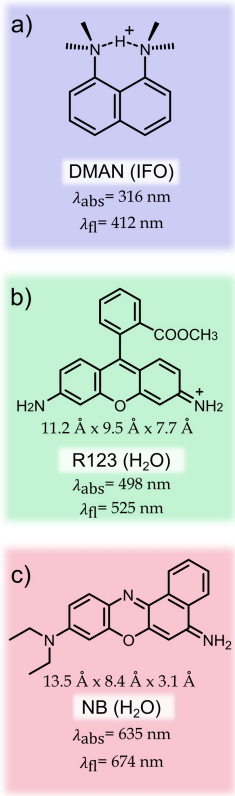

Figure 8.11: Selected molecular structures for energy transfer within MgIFO channels with their molecular dimensions (calculated from optimized geometries) and photophysical properties: **(a)** DMAN (SDA), **(b)** Rhodamine 123 (R123), and **(c)** Nile Blue (NB) with blue, green and red emissions respectively.

Therefore, several attempts were made using the same gel composition previously described for MgIFO, but adding an amount of dye to the synthesis gel.

0.95 Al_2O_3 : 1.00 P_2O_5 : 0.1 MgO : 1.2 DMAN : 40 H_2O : 0.008 Dye (R123 and/or NB)

The most representative samples are shown in Table 8.3. Note here that the total amount of dye added was kept at x = 0.008 so as not to disrupt the IFO phase and that is much lower compared to the amount of DMAN acting as SDA. The gels were heated at 150 °c for 24 h, the optimum time considered in the previous section for particle crystallization (experimental procedure in Section 4.7). Following the same sample labeling criteria, the MgIFO zeotypes were named with the prefixes F1 or F2, indicating the first (R123) or second dye (NB) of the family of three fused aromatic rings encapsulated throughout this thesis.

Table 8.3: Relative ratios of DMAN and each dye added to the synthesis gel (in total x = 0.008) in the dye-doped MgIFO hybrid materials.

Sample	**Dye amount added to the gel**		
	DMAN	*R123*	*NB*
F1/MgIFO	1.2	0.008	-
F2/MgIFO	1.2	-	0.008
F1+F2/MgIFO	1.2	0.004	0.004

The PXRD patterns show that the dyes do not alter the phase formation, obtaining pure crystallization of the IFO structure in all attempts (Figure C.13 in the Appendix). As for the first sample synthesized with R123, the optical microscopy images (Figure 8.12a) show a homogeneous distribution of crystalline particles and a distinctive green emission typical of this dye. Although the incorporation was found to be low (0.03 mmol of dye per 100 g of sample powder), its presence is clearly seen in the absorption spectra by its characteristic band placed at 514 nm together with

the main absorption peak of DMAN at 315 nm (data shown in Table 8.4).

Table 8.4: Photophysical parameters - absorption (λ_{abs}) and fluorescence maximum (λ_{fl}) wavelengths, and lifetimes (τ, average lifetime considered according to Equation 6.6) - of the dye-doped MgIFO samples.

Sample	Dye	λ_{abs} (nm)	λ_{fl} (nm)
F1/MgIFO	*DMAN*	315.0	417.0
	R123	514.0	538.0 - 540.0
F2/MgIFO	*DMAN*	316.0	418.0
	NB	595.0*	628.5
F1+F2/MgIFO	*DMAN*	310.0	418.0
	R123	515.0	529.5
	NB	-	629.5

* Value obtained from the excitation spectrum

Regardless of the excited species, either DMAN (λ_{exc} = 380 nm) or directly R123 (λ_{exc} = 480 nm), the rhodamine emission is observed at 538.0-540.0 nm (Table 8.4), responsible for the green emission of the particles (Figure 8.12a). Hence, an energy transfer is taking places from DMAN acting as donor to R123 acting as acceptor. This energy transfer in not complete since upon direct excitation of DMAN we detect both emission bands (Figure 8.12b). The excitation spectrum (Figure 8.12c) provides further evidence of this transfer showing that the rhodamine emission comes also in part from the DMAN monomers.

It is worth mentioning that other attempts were made with this dye to favor higher loadings. In these cases, the amount of water in the synthesis gel was increased (100 H_2O) to enhance dye solubility in the gel, as well as the amount of Mg (0.2 MgO) to favor Brønsted acid sites. However, these have not been included as they resulted in very similar dye uptakes.

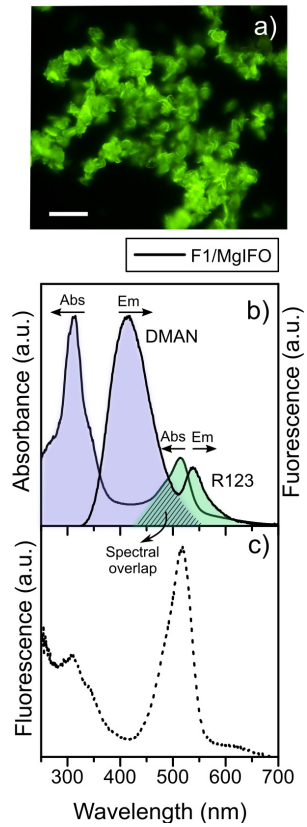

Figure 8.12: Photophysical characterization of sample F1/MgIFO. **(a)** Fluorescence image of the particles under blue excitation light (D470/40 band-pass). Scale = 20 µm. **(b)** Height normalized absorption and emission spectra of the bulk powder, and **(c)** its excitation spectrum.

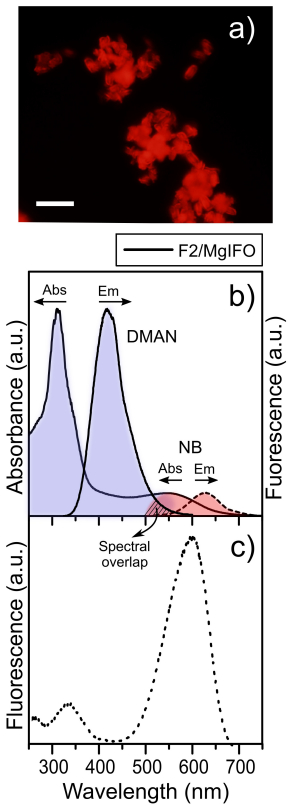

Figure 8.13: Photophysical characterization of sample F2/MgIFO. **(a)** Fluorescence image under green excitation light (HQ530/30m band-pass). Scale = 20 µm. **(b)** Height normalized absorption and emission spectra of the bulk powder recorded upon different excitation wavelengths (λ_{exc} = 315 nm and 500 nm, continuous and dashed lines respectively). **(c)** Excitation spectrum.

The other dye selected for the encapsulation is Nile Blue, which exhibits interesting absoption and emission bands in the red range (Figure 8.11b). Quantifications indicate that NB incorporation has been low compared to DMAN (160 vs 0.06 mmol dye/100g sample powder), although particles of this F2/MgIFO material show red fluorescence, which could be probably due to this oxazine dye (Figure 8.13a).

Analyzing the photophysics of the bulk powder, the absorption spectrum shows a band at around 550 nm (Figure 8.13a). By this band, it is difficult to confirm whether the incorporation of the dye has been successful or not, since it may also be due to the contribution of the DMAN dimers (Table 8.2 or Figure 8.7a). In addition, the emission maximum (dashed spectra in Figure 8.13b) is centered at 628.5 nm, quite close to the π-π aggregates of DMAN, still not being possible to discern between the two.

The excitation spectrum (Figure 8.13c) helps us clarify that this emission belongs to NB, due to the appearance of a well-defined band at 594.5 nm (λ_{abs} = 635 nm in H_2O) indicating that there is Nile Blue absorbed within the MgIFO zeotype. Moreover, it also reveals that, in fact, some energy transfer from the donor DMAN to the acceptor NB occurs, by the appearance of a weak band at 327 nm, assigned to the monomeric DMAN (Figure 8.13c). In contrast, the emission recorded by direct excitation to DMAN monomers does not show the presence of NB and only the band ascribed to DMAN is discernible (Figure 8.13b).

Therefore, the energy transfer has not been as efficient as in the previous system with R123 (sample F1/MgIFO). This may occur due to the lower overlap between the emission spectra of donor DMAN and the absorption band of the acceptor NB as shown in Figures 8.13b and 8.12b (prerequisites for an efficient FRET explained in Section 3.2.2.3).

In the third and last attempt, in order to promote a FRET cascade, the two dyes, R123 and NB, have been incorporated into the synthesis gel (see the relative dye ratios in Table 8.3). In this way, the aim has been to achieve an energy transfer from DMAN to R123, which has so far proved ef-

fective, to then consecutively transfer this energy to NB, taking advantage of the higher spectral overlap between these two dyes, R123 and NB (Figure 8.12b and Figure 8.13b), compared to DMAN and NB.

As in the previous samples, the absorption spectrum (Figure 8.14a) shows well-defined bands for DMAN and R123 at 310.0 and 515.5 respectively, but not in contrast for NB, where only a tail in the red part is discernible. The recorded emissions indicate that the three molecular entities coexist in the same system, with blue (418 nm), green (529.5 nm), and red (629.5 nm) fluorescence peaks attributed to DMAN, R123, and NB, respectively (data shown in Table 8.4), recorded under direct excitation to each species (Figure 8.14a).

The FRET processes among the three dyes is evidenced by the excitation spectra (Figure 8.14b). In fact, the three main bands that correspond to the DMAN, R123, and NB are visible at 321.0 nm, 518.0 nm, and 589.5 nm, when the emission was set at 700 nm. However, the FRET efficiency is not entirely effective probably as consequence of the poor dye uptake of R123 and NB compared to DMAN. The results presented above indicate that the relative dye ratios are highly important to efficiently achieve high FRET probabilities. For this reason, further experiements will be carried out to optimize the dye loadings.

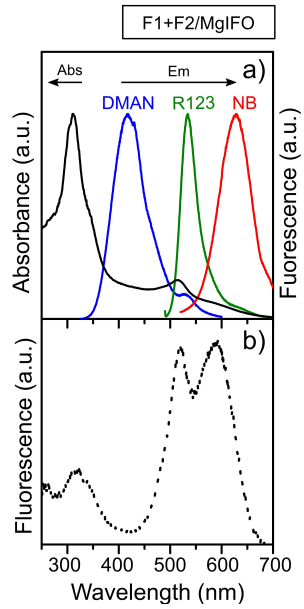

Figure 8.14: Photophysical characterization of the bulk powder F1+F2/MgIFO. **(a)** Height normalized absorption (black) and emission spectra recorded upon different excitation wavelengths (λ_{exc} = 315 nm, 480 nm and 500 nm, blue green and red lines respectively). **(b)** Excitation spectrum.

8.1.4 *Conclusion*

In this section, a zeotype with blue fluorescent properties, a magnesium doped IFO, has been synthesized without the need to incorporate additional dyes into the synthesis gel, due to the intrinsic emissive characteristics of the template guiding the crystallization. In addition, it has been demonstrated that this material shows photophysical changes over time, due to the fact that the structure-directing organic agent (DMAN) employed for its crystallization exhibits a redistribution within the unidirectional IFO channels, favor-

ing the formation towards thermodynamically more stable aggregates.

Based on a starting fluorescent zeotype, the fluorescence range of the material has been broadened by combining suitable dyes with properties in the green and red regions of the visible spectrum, inducing FRET processes between the encapsulated dyes.

8.2 WHITE LIGHT EMISSION IN MgAPO-11 (AEL) FRAMEWORK

White-light emitters composed of organic compounds have attracted attention in lighting devices.

Conventional lighting systems, such as incandescent or fluorescent bulbs, are part of our daily needs. However, they are very inefficient and waste energy or contain toxic substances such as mercury.[146] For this reason, significant advances in solid-state lighting (SSL) technology have been made in recent years,[147] among which white light-emitting organic materials have attracted much attention as key components in display and lighting devices.[148]

Among them, organic light-emitting diode (OLED) based devices are well known and almost necessary in any technological device present in everyday life, since they offer numerous advantages, such as high-energy efficiency, long lifetime, and are environmentally friendly. In addition, they are composed of organic compounds that allow low-cost manufacturing processes.[149,150]

However, purely organic devices age prematurely.

Accordingly, this section aims to develop a material to produce white light emission based on photoactive molecules. To this end, it is necessary to achieve blue/yellow or red/green/blue emission at the same time, which means that the devices require at least two emitting materials, usually organic dyes, in the material structure.[40] However, the main drawback of purely organic devices is their premature aging. In this sense, an effective way to avoid this problem is by protecting them with another structure, preferably a porous inorganic framework that allows the dyes to be encapsulated in nanocavities, thus protecting them from photo, chemical, and thermal degradation. The dye-

doped hybrid materials can be easily and cheaply prepared (Chapter 4) while promoting energy transfer phenomena inside the cavities of the framework.

Therefore, they will be encapsulated into cavities to protect them from degradation and to boost FRET processes.

Therefore, following the same trend as in the previous section, we will describe the simultaneous encapsulation of several chromophores within the inorganic host MgAPO-11, which has proven to be an ideal host for a wide variety of guest dyes (results in Chapter 7). In order to improve light capture and obtain a wider range of emission in the material, the strategy adopted has been the use of a mixed multi-component system with emission in the three regions of the electromagnetic spectrum (blue, green and red) promoted and controlled through partial FRET processes, thus building a multicolor artificial antenna system.

A blue (AC), green (PY) and red (LDS 722) dye will be encapsulated into AEL host.

Taking into account the requirements for effective Förster Resonance Energy Transfer (FRET, Section 3.2.2.3) and the required emission ranges, the selected dyes are acridine (AC), pyronin Y (PY), and hemicyanine LDS 722 (shown in Figure 8.15). On the one hand, AC and PY, are molecular structures with three fused aromatic rings, which have been selected as blue and green-emitting dyes. Structurally they are very similar, however, pyronin Y (Section 3.6.2.2) is slightly bulkier than acridine (Section 3.6.2.1). On the other hand, as already described in this thesis, LDS 722 is a styryl dye (Section 3.6.1) characterized by its emission in the red region of the electromagnetic spectrum (Section 7.2).

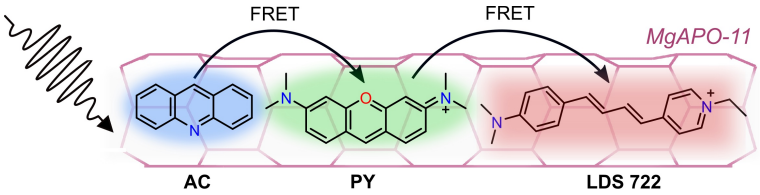

Figure 8.15: Schematic representation of the artificial luminescent antenna prepared by the insertion of three different dyes (AC, PY, and LDS 722) into the AEL zeolite channels.

Among them, the aim has been to control the efficiency of partial energy transfer between donor and acceptor mo-

lecules, being acridine the main energy donor moiety, and LDS 722 constituting the final acceptor dye in the FRET cascade. Therefore, in the following lines, we will briefly discuss the results of a recently published paper in which a solid-state hybrid system with efficient white light emission under UV excitation was successfully achieved.[89]

8.2.1 *AEL hybrid systems loaded with a single dye*

The selection of these dyes was based on their individual photophysics inside the chosen framework. For this purpose, all of them were previously encapsulated in the MgAPO-11 (AEL) framework and analyzed separately. A brief summary of the overall photophysical data is given in Table 8.5 and by the spectra and CIE coordinates plotted in Figure 8.16.

The acridine-loaded MgAPO-11 material (AC/AEL), which absorbs at 414 nm and emits at 481 nm, has been demonstrated to be a good blue cyan emitter with CIE (Commission Internationale de l'Eclairage) coordinates of 0.18, 0.33 (x, y). Under UV excitation it exhibits a relatively high fluorescence quantum yield of 54% and a long fluorescence lifetime of 27 ns attributed to the protonated species of the AC monomers, ACH^+.[27]

The pyronin Y dye (PY, Figure 8.15) encapsulated in MgAPO-11 (PY/AEL) with absorption at 524 nm, revealed the characteristic green emission of PY monomers at 544 nm (CIE under blue excitation light = 0.35, 0.64). Compared to PY in aqueous solution (ϕ_{fl} = 0.21, τ_{fl} = 2 ns) it possesses higher fluorescence quantum yield and longer lifetime (ϕ_{fl} = 0.29, τ_{fl} = 4.2 ns).[24]

Finally, the LDS 722 dye occluded in AEL (LDS 722/AEL) shows a very broad absorption region due to the coexistence of two absorption bands, one at 397 nm in the UV region attributed to LE main transition and the other at 503 nm, a broad band at higher wavelengths assigned to the intramolecular charge transfer (ICT) state. The material has demonstrated red emission properties with its maximum at

670 nm (CIE under green excitation light = 0.69, 0.31) with a much higher quantum yield (ϕ_{fl} = 0.55) than the corresponding one in aqueous solution ($\phi_{fl} \leqslant$ 0.01), due to a large constraint imposed by the AEL nanopores (Section 7.2).[25]

Table 8.5: Photophysical parameters - absorption (λ_{abs}) and fluorescence maxima (λ_{fl}), Commission Internationale de l'Eclairage (CIE) coordinates, fluorescence quantum yield (ϕ_{fl}) and fluorescence lifetimes (τ) - of the single dyes within the AEL inorganic framework.

Dye-doped system	λ_{abs} (nm)	λ_{fl} (nm)	CIE (x, y)	ϕ_{fl}	τ (ns)
AC/AEL	414	481	0.18, 0.33	0.54	2.7
PY/AEL	524	544	0.35, 0.64	0.29	4.2
LDS 722/AEL	397/503	670	0.69, 0.31*	0.55	2.6

*CIE coordinates under green excitation light at λ_{exc} = 530 nm.

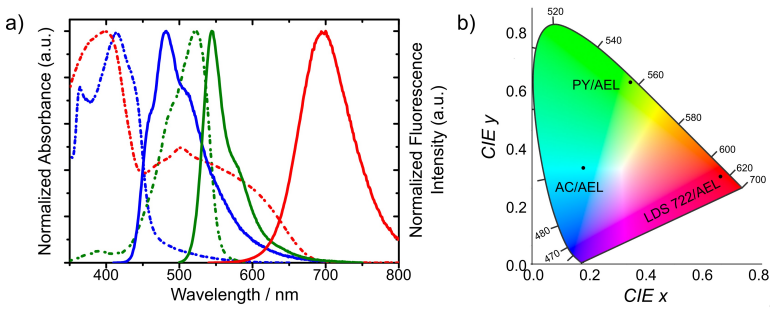

Figure 8.16: **(a)** Height normalized absorption spectra (dashed lines) and fluorescence spectra (solid lines) of MgAPO-11 samples containing a single dye: AC/AEL (blue lines), PY/AEL (green lines), and LDS 722/AEL (red lines). **(b)** CIE 1931 coordinates diagram with the fluorescence emissions of the four samples under UV light.

As already mentioned, the emission of white light in this AEL host containing a mixture of dyes must be assisted by a successive FRET energy transfer process between the fluorophores. Therefore, acridine has been selected as the main energy donor moiety, due to its high fluorescent

quantum yield and its small molecular size, facilitating a high loading rate of the dye into the host, which is preferable to obtain relatively large donor:acceptor ratios (50:1 is recommended) to ensure an efficient FRET process.[27]

As acceptor in the first step, PY dye was selected. It should be noted that the FRET process between AC and PY in MgAPO-11 has been previously demonstrated to be efficient in the AC-PY/AEL system, which was favored by three main reasons: the strong spectral overlap between the emission band of the donor ACH^+ and the absorption band of the acceptor PY (Figure 8.16), the high fluorescence quantum yield and lifetime of the donor and the high probability of finding neighboring acceptor molecules.[27]

This PY moiety will serve also as energy donor to LDS 722 in the last stage. The broad ICT absorption band of LDS 722, in fact, the most efficient absorption band for red emission (Section 7.2), shows indeed a good overlap with the PY/AEL emission band (Figure 8.16). However, it should be noted that this ICT band also overlaps with the AC/AEL fluorescence, which opens the possibility of directly transferring the energy from the AC to the LDS 722 moiety. Moreover, LDS 722 can also be excited under UV light, although as mentioned, this excitation wavelength is not the most efficient for this dye.[25] However, the FRET cascade in the system has to be partial to generate light in the full of the spectrum; hence, in case of loss of efficiency during the process, the reception of light in the red part of the spectrum is ensured.

Therefore, as the resulting emission from the present materials involves simultaneous FRET channels between the three dyes, it is crucial to optimize the relative ratio of the simultaneously encapsulated dyes in the AEL channels.

8.2.2 *Energy transfer between simultaneously encapsulated dyes*

Experimentally, predicting the degree of incorporation of an isolated dye into the inorganic matrix by *crystallization*

inclusion method is not an easy task. Moreover, when dealing with a mixture of dyes in the synthesis gel, as in the present case, optimizing the relative proportions of the occluded dyes becomes even more complicated, having to control the amounts added to the synthesis gel. In addition to typical parameters such as solubility, the dyes may compete with each other and favor/prevent the entry of the others. Hence, there may not be a direct relationship between the amount of dye initially added to the gel and the amount of dye found in the particles after crystallization, so that finding the right proportions of each dye in the synthesis gel is often a matter of trial and error.

In order to find the optimum composition with the three dyes, the following general molar composition was used:

$$0.9\ Al_2O_3 : 1\ P_2O_5 : 0.2\ MgO : 0.75\ EBA : x\ Dyes : 300\ H_2O$$

Systematic variations were made in the synthesis gel, always keeping the total amount of dye constant at x = 0.024 but varying the relative proportions between fluorophores. Gels were heated under autogenous pressure in static regime for 24 h at 160 °C by the procedure explained in Section 4.2 of the experimental part. The pH values of the synthesis gels ranged from 4 to 5.

Table 8.6 shows the most representative samples, which were synthesized in the *Molecular Sieves* group of the *Institute of Catalysis and Petrochemistry* of the CSIC (Madrid). M3/MgAEL represents the Mg-doped AEL matrix with a mixture of three encapsulated dyes. The relative ratio of the dyes in the synthesis gel is indicated in parentheses next to the number of each sample name. For example, the dye ratio of sample 2 is 5:1:1, indicating 5 of AC, 1 of PY, and 1 of LDS 722. Considering that the total amount of the dyes is kept at 0.024, the added ratio for AC, PY, and LDS 722 is 0.018, 0.003, and 0.003, respectively.

Table 8.6: The relative proportion of each dye in the initial synthesis gel (given in parenthesis in the sample names in AC: PY: LDS 722 order), final amount of dye occluded into AEL expressed as mmol dye per 100 g powder, fluorescence quantum yield (ϕ_{fl}, λ_{exc} = 530 nm), Commission Internationale de l'Eclairage (CIE) coordinates, and Correlated Color Temperature (CCT) number of the overall emission for each sample expressed in Kelvin degrees.

Sample (dye ratio)	Dye amount into AEL (mmol/100g)			ϕ_{fl}	CIE (x, y)	CCT (K)
(AC: PY: LDS22)	AC	PY	LDS 722			
M3/MgAEL-X						
1 (1:1:1)	3.19	0.14	0.09	0.08	0.42, 0.41	3350
2 (5:1:1)	7.44	0.02	0.79	0.07	0.31, 0.32	6750
3 (4:2:1)	6.94	0.08	0.45	0.10	0.32, 0.34	6070
4 (3:1:1)	8.26	0.06	0.55	0.17	0.34, 0.34	5170
5 (3:1:2)	9.49	0.06	0.64	0.04	0.35, 0.32	4600

The resulting materials were fully characterized by spectroscopic techniques and the emission color of all samples was determined by chromaticity experiments (CIE coordinates in Table 8.6), in order to check if the emission color was close to the pure white color coordinates (x = 0.33 and y = 0.33) in the 1931 diagram.

The quantification of the uptake for all dyes was not an easy task due to the overlap between the absorption regions of the dyes in solution. Furthermore, the incorporation of each dye into the MgAPO-11 structure does not follow a linear correlation with the initial proportion added to the synthesis gel (Table 8.6). For example, in the first attempt, sample M3/MgAEL-1, where the dyes were added to the synthesis gel in equal proportions (x = 0.008), the estimated final amount of dyes loaded was 3.19 mmol of AC, 0.14 mmol of PY, and 0.09 mmol of LDS 722 per 100 g of sample powder (Table 8.6). All this suggests that there is a strong competition between the dyes to be encapsulated into the nanopores of the AEL host, where the incorpor-

ation of acridine dye is much more favored compared to the other two, presumably due to its smaller dimensions and/or higher affinity with the inner face of the channel walls. Nevertheless, the incorporation of the dyes in any of the proportions does not modify the structure of AEL. In the case of the first prepared material, sample M3/MgAEL-1, a yellowish emission (Figure 8.17a) was observed as confirmed from the CIE chromaticity coordinates (Table 8.6, Figure 8.17b-c), showing a deficit of blue component. According to the color temperature, CCT, determined from the CIE coordinates,[151] a numerical value of 3350 K was achieved (Figure 8.18), which is classified as "warm white", *i.e.* a pleasant orange to yellowish-white color suitable especially for bedrooms, living rooms, and restaurant lightings, to name a few examples.

To achieve a material with an emission closer to pure white light, with nearly the same emission intensity over the entire range of the electromagnetic spectrum, in the following attempt, the amount of blue-emitting AC dye (first donor in the FRET cascade of the three-dye system) in M3/MgAEL-2 was significantly increased with an amount 5 times greater in proportion than PY and LDS 722 (Table 8.6).

Compared to the previous test, the incorporation achieved for AC was more than double (7.44 vs 3.19 mmol dye/100 g sample powder, Table 8.6). Regarding the other components, interestingly, much higher incorporation of LDS 722 with respect to PY and even with respect to sample 1 (Table 8.6) was also observed. This experimental fact can be attributed to the strong competition between PY and LDS 722 dyes to be embedded in the MgAPO structure when the amount of AC is much higher in comparison, with the incorporation of PY being hindered by the presence of LDS 722 in the gel. In fact, the height dimensions of PY (perpendicular to the major molecular axis) are larger than those of AC and LDS 722 (Figure 8.15), resulting in a tighter fit of PY in the AEL nanochannels and leading to more difficult incorporation.

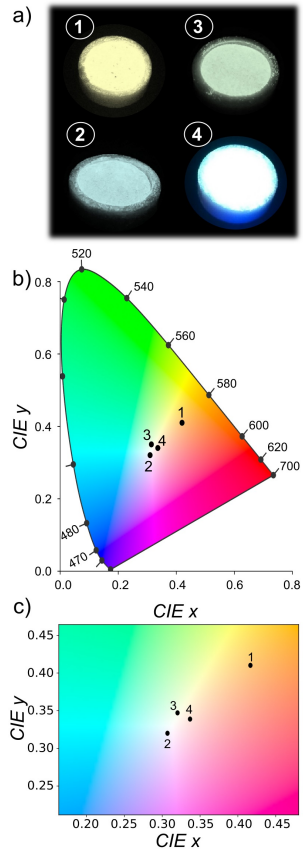

Figure 8.17: (a) Powder samples under UV illumination and the corresponding CIE 1931 diagram for the resultant fluorescent emission in **(b)** standard and **(c)** magnified scale. The color of the samples has turned out to be 1 = warm white, 2 = cool white, 3 = cool white and 4 = neutral white.

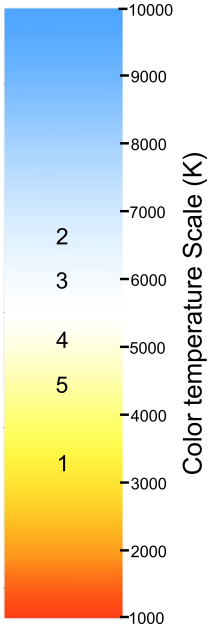

Figure 8.18: Correlated color temperatures (CCT) of the prepared samples.

As a result of higher AC incorporation, the fluorescent emission of M3/MgAEL-2 shows CIE coordinates closer to pure white under UV excitation (Figure 8.17b-c), but still with a slightly bluish hue (Figure 8.17a). Consequently, a relatively high CCT is obtained (6750 K, Table 8.6), falling in the range of the so-called "cool white", which is similar to daylight but with a bluish-white appearance that is often used when higher brightness is required, such as in industrial areas, garages, stores or art studios. However, it does not yet exhibit the necessary high fluorescence quantum yield ($\phi_{fl} \leqslant 0.10$ for samples 1-2) required for optical applications.

As mentioned above, PY presents a dual behavior in the hybrid system, acting both as an acceptor of the energy coming from AC, and as a donor transferring its energy to LDS 722. Hence, to provide a slightly higher contribution of the green emission and improve the energy transfer towards the final red-emitting entity, the relative amount of PY with respect to LDS 722 was increased in the synthesis gel (0.007 PY and 0.003 LDS 722) in the following trial. Sample M3/MgAEL-3 (Table 8.6) was prepared with a ratio of 4AC: 2PY: 1LDS 722, also slightly reducing the amount of AC in the synthesis gel (x = 0.014) with the intention of shifting the emission color of the gel out of the blue region. The fluorescent light of the resulting hybrid material in this case is not far from the desired pure white emission and shows a relatively higher efficiency than the previous samples (ϕ_{fl} = 0.10). Regarding the CCT number obtained, it is of 6070 K. The sample falls within the "cool light" range (Table 8.6, Figure 8.18), indicating an improvement over the previous ones, although it may still show a bluish hue in the white light, albeit very subtle.

Considering the last results, in the next attempt for sample M3/MgAEL-4, slight changes were made in the relative proportions of the dyes. The amount of AC dye was kept constant (x = 0.014), but a slightly lower amount of PY (0.005 PY and 0.005 LDS 722) was used with respect to sample 3, with a ratio of 3 AC:1 PY:1 LDS 722 in the initial gel. In this sample, the final estimated amount of loaded

dyes of 8.26 mmol AC, 0.06 mmol PY, and 0.55 mmol LDS 722 per 100 g of sample powder (Table 8.6), which corresponds to a ratio of 138:1:9, resulted in a pure white light-emitting material under ultraviolet excitation light (see CIE coordinates in Table 8.6 and Figure 8.17). This ratio has turned out to be very favorable mainly due to a much higher ratio of the main donor (AC) to the acceptor (PY). Moreover, it should not be forgotten that acridine could also act as a donor to LDS 722, which has probably guaranteed an efficient FRET process and consequently the generation of white light.[27]

This white emission is the result of the very similar emission intensities achieved in the blue (480 nm), green (540 nm), and red (670 nm) regions of the visible spectrum, which are characteristic of each encapsulated dye (Figure 8.19). Moreover, it has proved to be the sample with the highest fluorescence quantum yield (about 17%) among all the samples described in this work (Table 8.6). According to its corresponding CCT number, it is defined as a neutral white color, characterized by a bright white light, appropriate for illuminating many places such as kitchens, bathrooms, offices, classrooms, or hospitals.

To achieve a slightly warmer light without reaching the yellowness of sample 1, and thus have a battery of adequate samples with different shades of white emission, a new sample was prepared (M3/MgAEL-5) with a higher amount of LDS 722 with respect to sample 4 (3 AC:1 PY:2 LDS 722 in the synthesis gel, Table 8.6).

The sample showed neutral white light emission (CCT = 4600 K), a little warmer than in the previous sample (Figure 8.18), although with a lower fluorescence quantum yield (Table 8.6). This decrease could be attributed to the higher presence of LDS 722 (Table 8.6). Indeed, this dye can also be excited under UV light (Figure 8.16), populating its LE state. However, its emission efficiency is much lower than when its ICT state is directly excited (λ_{exc} = 530 nm; Section 7.2.2), and therefore, it could contribute to decreasing the overall fluorescence quantum yield.

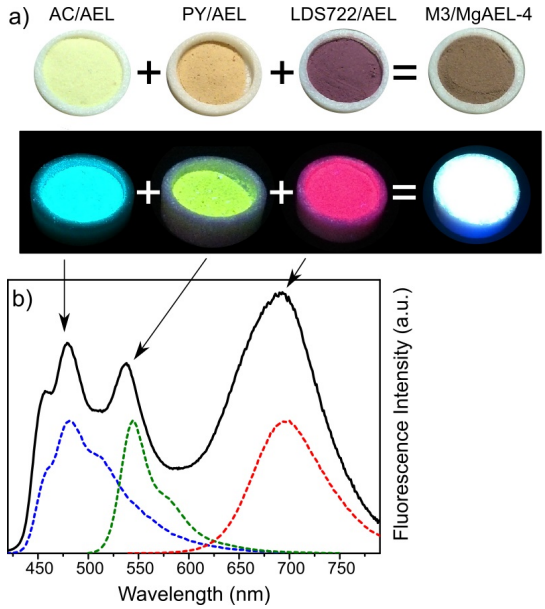

Figure 8.19: **(a)** Real images of the samples with each dye (AC, PY, and LDS 722) separately encapsulated in MgAPO-11, and the sample with the optimized mixture of the three dyes (M3/MgAPO-4) under ambient light (up) and UV illumination (down). **(b)** Emission spectra of sample M3/MgAEL-4 powder recorded upon UV excitation (325-375 nm).

All in all, the best white light-emitting hybrid material under UV illumination was obtained from an initial gel composition of 0.9 Al_2O_3 : 1.0 P_2O_5 : 0.2 MgO : 0.75 EBA : 0.0144 AC : 0.0048 PY : 0.0048 LDS 722 : 300 H_2O, with a relative dye ratio in the initial gel of 3 AC: 1 PY: 1 LDS 722. The results presented above indicate that, although it is very difficult to predict the best synthesis conditions in terms of the ratio of dye added to the initial gel, a solid-state white light-emitting material with relatively high fluorescence capability can be achieved by applying slight changes in the synthesis gel. Thus, by the rational study of the proportions of the different fluorescent agents it has been shown that with subtle changes, one can easily modulate and obtain warm or cool white light by increasing LDS 722 for the former and AC for the latter.

8.2.3 *Conclusion*

By the simultaneous occlusion of rationally chosen dyes, emitting in the blue (AC), green (PY) and red region (LDS 722) of the electromagnetic spectrum, into the one-dimensional channels of a magnesium-aluminophosphate with AEL-zeolitic type structure, MgAPO-11, a solid-state system with efficient white light emission under UV excitation has been achieved. The final color is a consequence of successive partial energy transfer processes between the dyes tightly confined in the restricted pore space of the zeotype. Furthermore, the color emission can be easily adjusted by the relative proportions added to the initial synthesis gel depending on the type of illumination required. Thus, with subtle changes in the proportions of donor and acceptor dyes, one can easily modulate and obtain a warmer or cooler white light.

In conclusion, an easy, not time-consuming, and inexpensive method has been presented to fabricate a hybrid material with white light emission that could be used for future commercial applications, in which organic moieties are more protected from aging and degradation effects due to the protection provided by the inorganic matrix.

BIBLIOGRAPHY

(1) Pansare, V. J.; Hejazi, S.; Faenza, W. J.; Prud'homme, R. K. Review of long-wavelength optical and NIR imaging materials: contrast agents, fluorophores, and multifunctional nano carriers. *Chemistry of materials* **2012**, *24*, 812–827.

(2) Li, L.; Dong, X.; Li, J.; Wei, J. A short review on NIR-II organic small molecule dyes. *Dyes and Pigments* **2020**, *183*, 108756.

(3) Du, Y.; Liu, X.; Zhu, S. Near-infrared-II cyanine/polymethine dyes, current state and perspective. *Frontiers in Chemistry* **2021**, *9*, 718709.

(4) Escobedo, J. O.; Rusin, O.; Lim, S.; Strongin, R. M. NIR dyes for bioimaging applications. *Current opinion in chemical biology* **2010**, *14*, 64–70.

(5) Stoyanov, S., Probes: dyes fluorescing in the NIR region In *Near-infrared applications in biotechnology*; CRC Press: 2020, pp 35–93.

(6) Kim, K. H.; Singha, S.; Jun, Y. W.; Reo, Y. J.; Kim, H. R.; Ryu, H. G.; Bhunia, S.; Ahn, K. H. Far-red/near-infrared emitting, two-photon absorbing, and bio-stable amino-Si-pyronin dyes. *Chemical science* **2019**, *10*, 9028–9037.

(7) Kothavale, S.; Sekar, N. Methoxy supported, deep red emitting mono, bis and tris triphenylamine-isophorone based styryl colorants: synthesis, photophysical properties, ICT, TICT emission and viscosity sensitivity. *Dyes and Pigments* **2017**, *136*, 116–130.

(8) Abeywickrama, C. S.; Wijesinghe, K. J.; Stahelin, R. V.; Pang, Y. Bright red-emitting highly reliable styryl probe with large stokes shift for visualizing mitochondria in live cells under wash-free conditions. *Sensors and Actuators B: Chemical* **2019**, *285*, 76–83.

(9) Zarins, E.; Jubels, J.; Kokars, V. In *Advanced Materials Research*, 2011; Vol. 222, pp 271–274.

(10) Cho, B. R.; Son, K. H.; Lee, S. H.; Song, Y.-S.; Lee, Y.-K.; Jeon, S.-J.; Choi, J. H.; Lee, H.; Cho, M. Two photon absorption properties of 1, 3, 5-tricyano-2, 4, 6-tris (styryl) benzene derivatives. *Journal of the American Chemical Society*, **2001**, *123*, 10039–10045.

(11) Dahal, D.; Ojha, K. R.; Pokhrel, S.; Paruchuri, S.; Konopka, M.; Liu, Q.; Pang, Y. NIR-emitting styryl dyes with large Stokes' shifts for imaging application: From cellular plasma membrane, mitochondria to zebrafish neuromast. *Dyes and Pigments* **2021**, *194*, 109629.

(12) Gao, F.-W.; Zhong, R.-L.; Xu, H.-L.; Su, Z.-M. Intra-and intermolecular charge transfer in a novel dimer: cooperatively enhancing second-order optical nonlinearity. *The Journal of Physical Chemistry C* **2017**, *121*, 25472–25478.

(13) Li, B.; Tong, R.; Zhu, R.; Meng, F.; Tian, H.; Qian, S. The ultrafast dynamics and nonlinear optical properties of tribranched styryl derivatives based on 1, 3, 5-triazine. *The Journal of Physical Chemistry B* **2005**, *109*, 10705–10710.

(14) Huang, J. Y.; Lewis, A.; Loew, L. Nonlinear optical properties of potential sensitive styryl dyes. *Biophysical journal* **1988**, *53*, 665–670.

(15) Millard, A. C.; Jin, L.; Wuskell, J. P.; Lewis, A.; Loew, L. M. Sensitivity of second harmonic generation from styryl dyes to transmembrane potential. *Biophysical journal* **2004**, *86*, 1169–1176.

(16) Mártire, D.; Massad, W.; Montejano, H.; Gonzalez, M.; Caregnato, P.; Villata, L.; García, N. Properties of singlet-and triplet-excited states of hemicyanine dyes. *Chemical Papers* **2014**, *68*, 1137–1140.

(17) Kim, J.; Lee, M.; Yang, J.-H.; Choy, J.-H. Photophysical Properties of Hemicyanine Dyes Intercalated in Na- Fluorine Mica. *The Journal of Physical Chemistry A* **2000**, *104*, 1388–1392.

(18) Lee, Y.; Lee, M. Volume Increment Effect on the Photoisomerization of Hemicyanine Dyes in Oligo (ethylene glycol) s. *The Journal of Physical Chemistry A* **2013**, *117*, 12878–12883.

(19) Jee, A.-Y.; Bae, E.; Lee, M. Internal motion of an electronically excited molecule in viscoelastic media. *The Journal of chemical physics* **2010**, *133*, 014507.

(20) Jee, A.-Y.; Lee, M. Excited-State Dynamics of a Hemicyanine Dye in Polymer Blends. *ChemPhysChem* **2010**, *11*, 793–795.

(21) Takashima, Y.; Martínez, V. M.; Furukawa, S.; Kondo, M.; Shimomura, S.; Uehara, H.; Nakahama, M.; Sugimoto, K.; Kitagawa, S. Molecular decoding using luminescence from an entangled porous framework. *Nature communications* **2011**, *2*, 1–8.

(22) Martínez-Martínez, V.; Corcóstegui, C.; Prieto, J. B.; Gartzia, L.; Salleres, S.; Arbeloa, I. L. Distribution and orientation study of dyes intercalated into single sepiolite fibers. A confocal fluorescence microscopy approach. *Journal of Materials Chemistry* **2011**, *21*, 269–276.

(23) Gartzia-Rivero, L.; Bañuelos-Prieto, J.; Martínez-Martínez, V.; Lopez Arbeloa, I. Versatile photoactive materials based on zeolite L doped with laser dyes. *ChemPlusChem* **2012**, *77*, 61–70.

(24) Martínez-Martínez, V.; García, R.; Gómez-Hortigüela, L.; Pérez-Pariente, J.; López-Arbeloa, I. Modulating Dye Aggregation by Incorporation into 1D-MgAPO Nanochannels. *Chemistry–A European Journal* **2013**, *19*, 9859–9865.

(25) Sola-Llano, R.; Martínez-Martínez, V.; Fujita, Y.; Gómez-Hortigüela, L.; Alfayate, A.; Uji-i, H.; Fron, E.; Pérez-Pariente, J.; López-Arbeloa, I. Formation of a nonlinear optical host–guest hybrid material by tight confinement of LDS 722 into aluminophosphate 1D nanochannels. *Chemistry–A European Journal* **2016**, *22*, 15700–15711.

(26) García, R.; Martínez-Martínez, V.; Sola Llano, R.; López-Arbeloa, I.; Pérez-Pariente, J. One-dimensional antenna systems by crystallization inclusion of dyes (one-pot synthesis) within zeolitic MgAPO-36 nanochannels. *The Journal of Physical Chemistry C* **2013**, *117*, 24063–24070.

(27) Martinez-Martinez, V.; Garcia, R.; Gómez-Hortigüela, L.; Sola Llano, R.; Perez-Pariente, J.; Lopez-Arbeloa, I. Highly luminescent and optically switchable hybrid material by one-pot encapsulation of dyes into MgAPO-11 unidirectional nanopores. *ACS Photonics* **2014**, *1*, 205–211.

(28) Baerlocher, C.; McCusker, L. B.; Olson, D. H., *Atlas of zeolite framework types*; Elsevier: 2007.

(29) Weiß, Ö; Loerke, J; Wüstefeld, U; Marlow, F; Schüth, F Host–Guest Interactions and Laser Activity in $AlPO_4$-5/Laser Dye Composites. *Journal of Solid State Chemistry* **2002**, *167*, 302–309.

(30) García, R.; Martínez-Martínez, V.; Gómez-Hortigüela, L.; Arbeloa, I. L.; Pérez-Pariente, J. Anisotropic fluorescence materials: Effect of the synthesis conditions over the incorporation, alignment and aggregation of Pyronine Y within MgAPO-5. *Microporous and mesoporous materials* **2013**, *172*, 190–199.

(31) Sola-Llano, R.; Fujita, Y.; Gómez-Hortigüela, L.; Alfayate, A.; Uji-i, H.; Fron, E.; Toyouchi, S.; Pérez-Pariente, J.; López-Arbeloa, I.; Martínez-Martínez, V. One-directional antenna systems: Energy transfer from monomers to J-Aggregates within 1D nanoporous aluminophosphates. *Acs Photonics* **2017**, *5*, 151–157.

(32) Sola-Llano, R.; Gartzia-Rivero, L.; Oliden-S´nchez, A.; Bañuelos, J.; Arbeloa, I. L.; Martínez-Martínez, V., Dye encapsulation into one-dimensional zeolitic materials for optical applications In *Chemistry of Silica and Zeolite-Based Materials*; Elsevier: 2019, pp 229–248.

(33) Oliden-Sánchez, A.; Sola-Llano, R.; López-Arbeloa, I.; Martínez-Martínez, V. Enhancement of NIR emission by a tight confinement of a hemicyanine dye within zeolitic MgAPO-5 nanochannels. *Photochemical & Photobiological Sciences* **2018**, *17*, 917–922.

(34) Wang, Z.-S.; Li, F.-Y.; Huang, C.-H.; Wang, L.; Wei, M.; Jin, L.-P.; Li, N.-Q. Photoelectric conversion properties of nanocrystalline TiO2 electrodes sensitized with hemicyanine derivatives. *The Journal of Physical Chemistry B* **2000**, *104*, 9676–9682.

(35) Cerdán, L.; Costela, A.; García-Moreno, I.; Bañuelos, J.; López-Arbeloa, I. Singular laser behavior of hemicyanine dyes: unsurpassed efficiency and finely structured spectrum in the near-IR region. *Laser Physics Letters* **2012**, *9*, 426.

(36) Valeur, B.; Berberan-Santos, M. N., *Molecular fluorescence: principles and applications*; John Wiley & Sons: 2012.

(37) Dang, T. T. H.; Zubowa, H.-L.; Bentrup, U.; Richter, M.; Martin, A. Microwave-assisted synthesis and characterization of Cu-containing $AlPO_4$-5 and SAPO-5. *Microporous and mesoporous materials* **2009**, *123*, 209–220.

(38) Oliden-Sánchez, A., *Microwave synthesis and photophysical characterization of hybrid materials based on the encapsulation of dyes into unidirectional aluminophosphates*; University of the Basque Country (UPV-EHU): 2017.

(39) Bennett, J.; Cohen, J.; Flanigen, E. M.; Pluth, J.; Smith, J., Crystal structure of tetrapropylammonium hydroxide–aluminum phosphate number 5 In *Intrazeolite Chemistry*; ACS Publications: 1983.

(40) Lee, H. L.; Jang, H. J.; Lee, J. Y. Single molecule white emission by intra-and inter-molecular charge transfer. *Journal of Materials Chemistry C* **2020**, *8*, 10302–10308.

(41) Epelde-Elezcano, N.; Duque-Redondo, E.; Martinez-Martinez, V.; Manzano, H.; Lopez-Arbeloa, I. Preparation, photophysical characterization, and modeling of LDS722/Laponite 2D-Ordered hybrid films. *Langmuir* **2014**, *30*, 10112–10117.

(42) Li, J.-J.; Guo, Y.; Li, G.-D.; Chen, J.-S.; Li, C.-J.; Zou, Y.-C. Investigation into the role of MgO in the synthesis of MAPO-11 large single crystals. *Microporous and mesoporous materials* **2005**, *79*, 79–84.

(43) Maiman, T. H., *Stimulated optical radiation in ruby*; University of Chicago Press: 1960.

(44) Waynant, R. W.; Ilev, I. K.; Gannot, I. Mid–infrared laser applications in medicine and biology. *Philosophical Transactions of the Royal Society of London. Series A: Mathematical, Physical and Engineering Sciences* **2001**, *359*, 635–644.

(45) Partovi, A.; Peale, D.; Wuttig, M.; Murray, C. A.; Zydzik, G.; Hopkins, L.; Baldwin, K.; Hobson, W. S.; Wynn, J.; Lopata, J.; Dhar, L.; Chichester, R.; H-J Yeh, J. High-power laser light source for near-field optics and its application to high-density optical data storage. *Applied Physics Letters* **1999**, *75*, 1515–1517.

(46) Wang, X.; Pang, Y.; Ku, G.; Xie, X.; Stoica, G.; Wang, L. V. Noninvasive laser-induced photoacoustic tomography for structural and functional in vivo imaging of the brain. *Nature biotechnology* **2003**, *21*, 803–806.

(47) Vanwiggeren, G. D.; Roy, R. Communication with chaotic lasers. *Science* **1998**, *279*, 1198–1200.

(48) Malinauskas, M.; Žukauskas, A.; Hasegawa, S.; Hayasaki, Y.; Mizeikis, V.; Buividas, R.; Juodkazis, S. Ultrafast laser processing of materials: from science to industry. *Light: Science & Applications* **2016**, *5*, e16133–e16133.

(49) Yao, J.; Wang, Y., *Nonlinear optics and solid-state lasers: advanced concepts, tuning-fundamentals and applications*; Springer Science & Business Media: 2012; Vol. 164.

(50) Suresh, S.; Ramanand, A.; Jayaraman, D.; Mani, P. Review on theoretical aspect of nonlinear optics. *Review on Advanced Materials Science* **2012**, *30*, 175–183.

(51) Schneider, T., *Nonlinear optics in telecommunications*; Springer Science & Business Media: 2004.

(52) Sain, B.; Meier, C.; Zentgraf, T. Nonlinear optics in all-dielectric nanoantennas and metasurfaces: a review. *Advanced Photonics* **2019**, *1*, 024002.

(53) Agrawal, G. P., Nonlinear fiber optics In *Nonlinear Science at the Dawn of the 21st Century*; Springer: 2000, pp 195–211.

(54) Liu, W.; Liu, M.; Liu, X.; Wang, X.; Deng, H.-X.; Lei, M.; Wei, Z.; Wei, Z. Recent advances of 2D materials in nonlinear photonics and fiber lasers. *Advanced Optical Materials* **2020**, *8*, 1901631.

(55) Cassan, E.; Grillet, C.; Neshev, D. N.; Moss, D. J. Nonlinear integrated photonics. *Photonics research* **2018**, *6*, 1–2.

(56) Mohan, S.; Murugesan, P. New materials for diode pumped solid state lasers and its applications to medical photonics. *Asian Journal of Chemistry* **2006**, *18*, 3253.

(57) Soljačić, M.; Ibanescu, M.; Johnson, S. G.; Fink, Y.; Joannopoulos, J. D. Optimal bistable switching in nonlinear photonic crystals. *Physical Review E* **2002**, *66*, 055601.

(58) Nikogosyan, D. N., *Nonlinear optical crystals: a complete survey*; Springer Science & Business Media: 2006.

(59) Mori, Y.; Sasaki, T. Development of new NLO borate crystals. *Bulletin of Materials Science* **1999**, *22*, 399–403.

(60) Rode, M. N.; Mehsram, D. V., *Nonlinear optical crystals for laser*; Empyreal Publishing House: 2019.

(61) Allakhverdiev, K.; Salayev, E. In *XIX International Symposium on High-Power Laser Systems and Applications 2012*, 2013; Vol. 8677, p 867718.

(62) Drost, K. J.; Jen, A. K. Y.; Rao, V. P. Designing organic NLO materials. *Chemtech* **1995**, *25*, 16–25.

(63) Kaino, T.; Tomaru, S. Organic materials for nonlinear optics. *Advanced Materials* **1993**, *5*, 172–178.

(64) He, G. S.; Tan, L. S.; Zheng, Q.; Prasad, P. N. Multiphoton absorbing materials: molecular designs, characterizations, and applications. *Chemical Reviews* **2008**, *108*, 1245–1330.

(65) Lou, A. J.-T.; Marks, T. J. A twist on nonlinear optics: understanding the unique response of π-twisted chromophores. *Accounts of chemical research* **2019**, *52*, 1428–1438.

(66) Yu, J.; Cui, Y.; Wu, C.; Yang, Y.; Wang, Z.; O'Keeffe, M.; Chen, B.; Qian, G. Second-order nonlinear optical activity induced by ordered dipolar chromophores confined in the pores of an anionic metal–organic framework. *Angewandte Chemie* **2012**, *124*, 10694–10697.

(67) Ahmed, S.; Jiang, X.; Wang, C.; Kalsoom, U. e.; Wang, B.; Khan, J.; Muhammad, Y.; Duan, Y.; Zhu, H.; Ren, X.; Zhang, H. An Insightful Picture of Nonlinear Photonics in 2D Materials and their Applications: Recent Advances and Future Prospects. *Advanced Optical Materials* **2021**, *9*, 2001671.

(68) Kotik, J; Newstein, M. Theory of LASER Oscillations in Fabry-Perot Resonators. *Journal of Applied Physics* **1961**, *32*, 178–186.

(69) Lawrence, M.; Willke, B; Husman, M.; Gustafson, E.; Byer, R. Dynamic response of a Fabry–Perot interferometer. *Journal of the Optical Society of America B* **1999**, *16*, 523–532.

(70) Ishchenko, A. The length of the polymethine chain and the spectral-luminescent properties of symmetrical cyanine dyes. *Russian chemical bulletin* **1994**, *43*, 1161–1174.

(71) Manzo, M.; Cavazos, O. Solid state optical microlasers fabrication via microfluidic channels. *Optics* **2020**, *1*, 88–96.

(72) Xu, R.; Zhu, G.; Yin, X.; Wan, X.; Qiu, S. Epitaxial growth of highly-oriented $AlPO_4$-5 molecular sieve films for microlaser systems. *Journal of Materials Chemistry* **2006**, *16*, 2200–2204.

(73) Chen, Y.; Zhai, J.; Xu, X.; Li, I.; Ruan, S.; Tang, Z. Synthesis of large MgAPO-11 single crystals in a F- free system. *Crystal engineering communications* **2014**, *16*, 2984–2989.

(74) Karanikolos, G. N.; Garcia, H.; Corma, A.; Tsapatsis, M. Growth of $AlPO_4$-5 and CoAPO-5 films from amorphous seeds. *Microporous and mesoporous materials* **2008**, *115*, 11–22.

(75) Finger, G; Richter-Mendau, J; Bülow, M; Kornatowski, J On synthesis conditions for tailoring $AlPO_4$-5 crystal dimensions. *Zeolites* **1991**, *11*, 443–448.

(76) Nadimi, S.; Oliver, S.; Kuperman, A.; Lough, A.; Ozin, G. A.; Garcés, J. M.; Olken, M. M.; Rudolf, P., Nonaqueous synthesis of large zeolite and molecular sieve crystals In *Studies in Surface Science and Catalysis*; Elsevier: 1994; Vol. 84, pp 93–100.

(77) Xu, X.; Zhai, J.; Chen, Y.; Li, I.; Chen, H.; Ruan, S.; Tang, Z. Synthesis and characterization of large single crystal of ZAPSO-43. *Microporous and mesoporous materials* **2014**, *196*, 314–320.

(78) Xu, X.; Zhai, J.; Chen, Y.; Li, I.; Chen, H.; Ruan, S.; Tang, Z. Synthesis of large single crystals of AlPO–LTA by using n-Propylamine as structure directing agent. *Journal of crystal growth* **2014**, *407*, 1–5.

(79) Kuperman, A.; Nadimi, S.; Oliver, S.; Ozin, G. A.; Garcés, J. M.; Olken, M. M. Non-aqueous synthesis of giant crystals of zeolites and molecular sieves. *Nature* **1993**, *365*, 239–242.

(80) Vuong, G. T.; Do, T. O. Nanozeolites and nanoporous zeolitic composites: Synthesis and applications. *Mesoporous Zeolites: Preparation, Characterization and Applications* **2015**.

(81) Saha, S. K.; Purkayastha, P.; Das, A. B. Photophysical characterization and effect of pH on the twisted intramolecular charge transfer fluorescence of trans-2-[4-(dimethylamino) styryl] benzothiazole. *Journal of photochemistry and photobiology A: Chemistry* **2008**, *195*, 368–377.

(82) Fayed, T. A.; Ali, S. S. Protonation Dependent Photoinduced Intramolecular Charge Transfer in 2-(p-Dimethylaminostyryl) Benzazoles. *Spectroscopy letters* **2003**, *36*, 375–386.

(83) Chatterjee, S. Photophysical and Photochemical Properties of Some Push-Pull Aromatic Olefins and Photochemistry of a Few Ortho-Substituted Stilbenes, Ph.D. Thesis, 2014.

(84) Zhang, Z.; Zhang, G.; Wang, J.; Sun, S.; Zhang, Z. The mechanisms of Large Stokes Shift and Fluorescence Quantum Yields in anilino substituted Rhodamine analogue: TICT and PICT. *Computational and Theoretical Chemistry* **2016**, *1095*, 44–53.

(85) Barranco, J. P.; Selma, C. G.; Gómez, F. C. Compact equipment for extreme macro photography, US Patent App. 17/044,037, 2021.

(86) Avhad, K. C.; Patil, D. S.; Chitrambalam, S; Sreenath, M.; Joe, I. H.; Sekar, N. Viscosity induced emission of red-emitting NLOphoric coumarin morpholine-thiazole hybrid styryl dyes as FMRs: consolidated experimental and theoretical approach. *Optical Materials* **2018**, *79*, 90–107.

(87) Vietze, U; Krauss, O; Laeri, F; Ihlein, G; Schüth, F; Limburg, B; Abraham, M Zeolite-dye microlasers. *Physical review letters* **1998**, *81*, 4628–4631.

(88) Gozhyk, I; Boudreau, M; Haghighi, H. R.; Djellali, N; Forget, S; Chénais, S; Ulysse, C; Brosseau, A; Pansu, R; Audibert, J.-F. et al. Gain properties of dye-doped polymer thin films. *Physical Review B* **2015**, *92*, 214202.

(89) Sola-Llano, R.; Oliden-Sánchez, A.; Alfayate, A.; Gómez-Hortigüela, L.; Pérez-Pariente, J.; Arbeloa, T.; Hofkens, J.; Fron, E.; Martínez-Martínez, V. White Light Emission by Simultaneous One Pot Encapsulation of Dyes into One-Dimensional Channelled Aluminophosphate. *Nanomaterials* **2020**, *10*, 1173.

(90) Sola Llano, R., *Synergism between organic and inorganic moieties: in the search of new hybrid materials for optics and biomedicine*; University of the Basque Country (UPV-EHU): 2017.

(91) Concepción, P; Nieto, J. L.; Mifsud, A; Pérez-Pariente, J Preparation and characterization of Mg-containing AFI and chabazite-type materials. *Zeolites,* **1996**, *16*, 56–64.

(92) Chen, Y.; Fu, L.; Xu, X.; Li, I. L.; Ruan, S.; Jian, D.; Zhai, J. In *Second International Conference on Photonics and Optical Engineering*, 2017; Vol. 10256, pp 785–792.

(93) Li, R.; Yu, J.; Wang, S.; Shi, Y.; Wang, Z.; Wang, K.; Ni, Z.; Yang, X.; Wei, Z.; Chen, R. Surface modification of all-inorganic halide perovskite nanorods by a microscale hydrophobic zeolite for stable and sensitive laser humidity sensing. *Nanoscale,* **2020**, *12*, 13360–13367.

(94) Leonetti, M; Conti, C; López, C. Random laser tailored by directional stimulated emission. *Physical Review A* **2012**, *85*, 043841.

(95) Albalad, J.; Carné-Sánchez, A.; Grancha, T.; Hernández-López, L.; Maspoch, D. Protection strategies for directionally-controlled synthesis of previously inaccessible metal–organic polyhedra (MOPs): the cases of carboxylate-and amino-functionalised Rh (ii)-MOPs. *Chemical communications* **2019**, *55*, 12785–12788.

(96) Cao, H. Random lasers: development, features and applications. *Optics and photonics news* **2005**, *16*, 24–29.

(97) Caselli, N.; Consoli, A.; Sánchez, Á. M. M.; López, C. Networks of mutually coupled random lasers. *Optica* **2021**, *8*, 193–201.

(98) Redding, B.; Choma, M. A.; Cao, H. Speckle-free laser imaging using random laser illumination. *Nature photonics* **2012**, *6*, 355–359.

(99) Ni, Y.; Wan, H.; Liang, W.; Zhang, S.; Xu, X.; Li, L.; Shao, Y.; Ruan, S.; Zhang, W. Random lasing carbon dot fibers for multi-level anti-counterfeiting. *Nanoscale* **2021**, *13*, 16872–16878.

(100) Whinnery, J. R. Laser measurement of optical absorption in liquids. *Accounts of Chemical Research* **1974**, *7*, 225–231.

(101) Van Grondelle, R.; Dekker, J. P.; Gillbro, T.; Sundstrom, V. Energy transfer and trapping in photosynthesis. *Biochimica et Biophysica Acta (BBA)-Bioenergetics* **1994**, *1187*, 1–65.

(102) Demmig-Adams, B.; Stewart, J. J.; Burch, T. A.; Adams III, W. W. Insights from placing photosynthetic light harvesting into context. *The journal of physical chemistry letters* **2014**, *5*, 2880–2889.

(103) Scholes, G. D.; Fleming, G. R.; Olaya-Castro, A.; Van Grondelle, R. Lessons from nature about solar light harvesting. *Nature chemistry* **2011**, *3*, 763–774.

(104) Scholes, G. D.; Mirkovic, T.; Turner, D. B.; Fassioli, F.; Buchleitner, A. Solar light harvesting by energy transfer: from ecology to coherence. *Energy & Environmental Science* **2012**, *5*, 9374–9393.

(105) Croce, R.; Van Amerongen, H. Natural strategies for photosynthetic light harvesting. *Nature chemical biology* **2014**, *10*, 492–501.

(106) Whang, D. R.; Apaydin, D. H. Artificial photosynthesis: Learning from nature. *ChemPhotoChem* **2018**, *2*, 148–160.

(107) Gust, D.; Moore, T. A.; Moore, A. L. Mimicking photosynthetic solar energy transduction. *Accounts of Chemical Research* **2001**, *34*, 40–48.

(108) El-Khouly, M. E.; El-Mohsnawy, E.; Fukuzumi, S. Solar energy conversion: From natural to artificial photosynthesis. *Journal of photochemistry and photobiology C: Photochemistry Reviews* **2017**, *31*, 36–83.

(109) Chen, L.; Shenai, P.; Zheng, F.; Somoza, A.; Zhao, Y. Optimal energy transfer in light-harvesting systems. *Molecules* **2015**, *20*, 15224–15272.

(110) Şener, M.; Strümpfer, J.; Hsin, J.; Chandler, D.; Scheuring, S.; Hunter, C. N.; Schulten, K. Förster energy transfer theory as reflected in the structures of photosynthetic light-harvesting systems. *ChemPhysChem* **2011**, *12*, 518–531.

(111) Sapsford, K. E.; Berti, L.; Medintz, I. L. Materials for fluorescence resonance energy transfer analysis: beyond traditional donor–acceptor combinations. *Angewandte Chemie International Edition* **2006**, *45*, 4562–4589.

(112) Lakowicz, J. R., *Principles of fluorescence spectroscopy*; Springer: 2006.

(113) Calzaferri, G.; Li, H.; Brühwiler, D. Dye-modified nanochannel materials for photoelectronic and optical devices. *Chemistry–A European Journal* **2008**, *14*, 7442–7449.

(114) Huang, Y.; Qiu, F.; Chen, R.; Yan, D.; Zhu, X. Fluorescence resonance energy transfer-based drug delivery systems for enhanced photodynamic therapy. *Journal of Materials Chemistry B* **2020**, *8*, 3772–3788.

(115) Stanisavljevic, M.; Krizkova, S.; Vaculovicova, M.; Kizek, R.; Adam, V. Quantum dots-fluorescence resonance energy transfer-based nanosensors and their application. *Biosensors and Bioelectronics* **2015**, *74*, 562–574.

(116) Anand, V.; Dhamodharan, R. White light emission from fluorene-EDOT and phenothiazine-hydroquinone based D–π–A conjugated systems in solution, gel and film forms. *New Journal of Chemistry* **2017**, *41*, 9741–9751.

(117) Grivas, C.; Pollnau, M. Organic solid-state integrated amplifiers and lasers. *Laser & photonics reviews* **2012**, *6*, 419–462.

(118) Duarte, F. J., *Tunable laser applications*; CRC press: 2008.

(119) Yuan, L.; Lin, W.; Zheng, K.; Zhu, S. FRET-based small-molecule fluorescent probes: rational design and bioimaging applications. *Accounts of chemical research* **2013**, *46*, 1462–1473.

(120) Wen, Y.; Sheng, T.; Zhu, X.; Zhuo, C.; Su, S.; Li, H.; Hu, S.; Zhu, Q. L.; Wu, X. Introduction of red-green-blue fluorescent dyes into a metal–organic framework for tunable white light emission. *Advanced Materials* **2017**, *29*, 1700778.

(121) Maiti, D. K.; Roy, S.; Baral, A.; Banerjee, A. A fluorescent gold-cluster containing a new three-component system for white light emission through a cascade of energy transfer. *Journal of Materials Chemistry C* **2014**, *2*, 6574–6581.

(122) Vijayakumar, C.; Praveen, V. K.; Ajayaghosh, A. RGB emission through controlled donor self-assembly and modulation of excitation energy transfer: A novel strategy to white-light-emitting organogels. *Advanced materials* **2009**, *21*, 2059–2063.

(123) Denißen, M.; Hannen, R.; Itskalov, D.; Biesen, L.; Nirmalananthan-Budau, N.; Hoffmann, K.; Reiss, G. J.; Resch-Genger, U.; Müller, T. J. One-pot synthesis of a white-light emissive bichromophore operated by aggregation-induced dual emission (AIDE) and partial energy transfer. *Chemical Communications* **2020**, *56*, 7407–7410.

(124) Rao, K. V.; Datta, K.; Eswaramoorthy, M.; George, S. J. Highly Pure Solid-State White-Light Emission from Solution-Processable Soft-Hybrids. *Advanced Materials* **2013**, *25*, 1713–1718.

(125) Hu, D. D.; Lin, J.; Zhang, Q.; Lu, J. N.; Wang, X. Y.; Wang, Y. W.; Bu, F.; Ding, L. F.; Wang, L.; Wu, T. Multi-step host–guest energy transfer between inorganic chalcogenide-based semiconductor zeolite material and organic dye molecules. *Chemistry of Materials* **2015**, *27*, 4099–4104.

(126) Yan, D.; Tang, Y.; Lin, H.; Wang, D. Tunable two-color luminescence and host–guest energy transfer of fluorescent chromophores encapsulated in metal-organic frameworks. *Scientific reports* **2014**, *4*, 1–7.

(127) Gómez-Hortiguela, L.; López-Arbeloa, F.; Cora, F.; Pérez-Pariente, J. Supramolecular chemistry in the structure direction of microporous materials from aromatic structure-directing agents. *Journal of the American Chemical Society* **2008**, *130*, 13274–13284.

(128) Gómez-Hortigüela, L.; López-Arbeloa, F.; Pérez-Pariente, J. Aggregation behavior of (S)-(-)-N-benzylpyrrolidine-2-methanol in the synthesis of the AFI structure in the presence of dopants. *Microporous and mesoporous materials* **2009**, *119*, 299–305.

(129) Gómez-Hortigüela, L.; Pérez-Pariente, J.; Corà, F.; Catlow, C. R. A.; Blasco, T. Structure-directing role of molecules containing benzyl rings in the synthesis of a large-pore aluminophosphate molecular sieve: An experimental and computational study. *The Journal of Physical Chemistry B* **2005**, *109*, 21539–21548.

(130) Gómez-Hortigüela, L.; Corà, F.; Catlow, C. R. A.; Pérez-Pariente, J. Computational study of the structure-directing effect of benzylpyrrolidine and its fluorinated derivatives in the synthesis of the aluminophosphate $AlPO_4$-5. *Journal of the American Chemical Society* **2004**, *126*, 12097–12102.

(131) Gómez-Hortigüela, L.; Corà, F.; Catlow, C. R. A.; Pérez-Pariente, J. Computational study of a chiral supramolecular arrangement of organic structure directing molecules for the AFI structure. *Physical Chemistry Chemical Physics* **2006**, *8*, 486–493.

(132) Corma, A.; Rey, F.; Rius, J.; Sabater, M. J.; Valencia, S. Supramolecular self-assembled molecules as organic directing agent for synthesis of zeolites. *Nature* **2004**, *431*, 287–290.

(133) Martínez-Franco, R.; Sun, J.; Sastre, G.; Yun, Y.; Zou, X.; Moliner, M.; Corma, A. Supra-molecular assembly of aromatic proton sponges to direct the crystallization of extra-large-pore zeotypes. *Proceedings of the Royal Society A: Mathematical, Physical and Engineering Sciences* **2014**, *470*, 20140107.

(134) Boal, B. W.; Zones, S. I.; Davis, M. E. Triptycene structure-directing agents in aluminophosphate synthesis. *Microporous and Mesoporous Materials* **2015**, *208*, 203–211.

(135) Luo, Y.; Smeets, S.; Wang, Z.; Sun, J.; Yang, W. Synthesis and Structure Determination of SCM-15: A 3D Large Pore Zeolite with Interconnected Straight 12× 12× 10-Ring Channels. *Chemistry–A European Journal* **2019**, *25*, 2184–2188.

(136) Kang, J. H.; Xie, D.; Zones, S. I.; Smeets, S.; McCusker, L. B.; Davis, M. E. Synthesis and characterization of CIT-13, a germanosilicate molecular sieve with extra-large pore openings. *Chemistry of Materials* **2016**, *28*, 6250–6259.

(137) Zi, W.-W.; Gao, Z.; Zhang, J.; Lv, J.-H.; Zhao, B.-X.; Jiang, Y.-F.; Du, H.-B.; Chen, F.-J. Designed synthesis of an extra-large pore zeolite with a 14-membered ring channel via supramolecular assembly templating approach. *Microporous and Mesoporous Materials* **2019**, *290*, 109654.

(138) Zhang, C.; Kapaca, E.; Li, J.; Liu, Y.; Yi, X.; Zheng, A.; Zou, X.; Jiang, J.; Yu, J. An Extra-Large-Pore Zeolite with 24× 8× 8-Ring Channels Using a Structure-Directing Agent Derived from Traditional Chinese Medicine. *Angewandte Chemie International Edition* **2018**, *57*, 6486–6490.

(139) Jiang, J.; Xu, Y.; Cheng, P.; Sun, Q.; Yu, J.; Corma, A.; Xu, R. Investigation of extra-large pore zeolite synthesis by a high-throughput approach. *Chemistry of Materials* **2011**, *23*, 4709–4715.

(140) Martínez-Franco, R.; Moliner, M.; Yun, Y.; Sun, J.; Wan, W.; Zou, X.; Corma, A. Synthesis of an extra-large molecular sieve using proton sponges as organic structure-directing agents. *Proceedings of the National Academy of Sciences* **2013**, *110*, 3749–3754.

(141) Szemik-Hojniak, A.; Rettig, W.; Deperasińska, I. The forbidden emission of protonated proton sponge. *Chemical physics letters* **2001**, *343*, 404–412.

(142) Szemik-Hojniak, A.; Balkowski, G.; Wurpel, G. W.; Herbich, J.; van der Waals, J. H.; Buma, W. J. Photophysics of 1, 8-bis (dimethylamino) naphthalene in solution: Internal charge transfer with a twist. *The Journal of Physical Chemistry A* **2004**, *108*, 10623–10631.

(143) Martínez-Franco, R.; Paris, C.; Moliner, M.; Corma, A. Synthesis of highly stable metal-containing extra-large-pore molecular sieves. *Philosophical Transactions of the Royal Society A: Mathematical, Physical and Engineering Sciences* **2016**, *374*, 20150075.

(144) Pal, P.; Zeng, H.; Durocher, G.; Girard, D.; Giasson, R.; Blanchard, L.; Gaboury, L.; Villeneuve, L. Spectroscopic and photophysical properties of some new rhodamine derivatives in

cationic, anionic and neutral micelles. *Journal of Photochemistry and Photobiology A: Chemistry* **1996**, *98*, 65–72.

(145) Jose, J.; Ueno, Y.; Burgess, K. Water-soluble Nile blue derivatives: syntheses and photophysical properties. *Chemistry–A European Journal* **2009**, *15*, 418–423.

(146) Chen, Z.; Ho, C. L.; Wang, L.; Wong, W. Y. Single-molecular white-light emitters and their potential WOLED applications. *Advanced Materials* **2020**, *32*, 1903269.

(147) Tsao, J. Y. Solid-state lighting: lamps, chips, and materials for tomorrow. *IEEE Circuits and Devices Magazine* **2004**, *20*, 28–37.

(148) Mukherjee, S.; Thilagar, P. Organic white-light emitting materials. *Dyes and Pigments* **2014**, *110*, 2–27.

(149) Li, G.; Shinar, J. Combinatorial fabrication and studies of bright white organic light-emitting devices based on emission from rubrene-doped 4, 4-bis (2, 2-diphenylvinyl)-1, 1-biphenyl. *Applied Physics Letters* **2003**, *83*, 5359–5361.

(150) Li, Y.; Rizzo, A.; Cingolani, R.; Gigli, G. Bright White-Light-Emitting Device from Ternary Nanocrystal Composites. *Advanced materials* **2006**, *18*, 2545–2548.

(151) McCamy, C. S. Correlated color temperature as an explicit function of chromaticity coordinates. *Color Research & Application* **1992**, *17*, 142–144.

(152) Girnus, I; Jancke, K; Vetter, R; Richter-Mendau, J; Caro, J Large $AlPO_4$-5 crystals by microwave heating. *Zeolites* **1995**, *15*, 33–39.

(153) Girnus, I.; Hoffmann, K.; Marlow, F.; Caro, J.; Döring, G. Large CoAPO-5 single crystals: microwave synthesis and anisotropic optical absorption. *Microporous Materials* **1994**, *2*, 537–541.

(154) Moss, D., *Biomedical Applications of Synchrotron Infrared Microspectroscopy*; Royal Society of Chemistry: 2011.

(155) Chen, C.; Wang, H., *Biomedical applications and toxicology of carbon nanomaterials*; John Wiley & Sons: 2016.

(156) Ellis, D. I.; Goodacre, R. Metabolic fingerprinting in disease diagnosis: biomedical applications of infrared and Raman spectroscopy. *Analyst* **2006**, *131*, 875–885.

(157) Nasim, H.; Jamil, Y. Diode lasers: From laboratory to industry. *Optics & Laser Technology* **2014**, *56*, 211–222.

(158) Chipem, F. A.; Mishra, A.; Krishnamoorthy, G The role of hydrogen bonding in excited state intramolecular charge transfer. *Physical Chemistry Chemical Physics,* **2012**, *14*, 8775–8790.

(159) Resch-Genger, U.; Grabolle, M.; Cavaliere-Jaricot, S.; Nitschke, R.; Nann, T. Quantum dots versus organic dyes as fluorescent labels. *Nature methods* **2008**, *5*, 763–775.

Part IV

CONCLUSIONS AND FUTURE PERSPECTIVE

This part evaluates the results obtained throughout the thesis and summarizes the most important conclusions reached. In addition, proposals for future research and experiments are mentioned, giving alternative solutions to the limitations found in the study.

9

CONCLUSIONS

The results presented in this thesis demonstrate the feasibility of occluding dyes into restricted nanocavities of zeotypic materials to promote new and/or enhanced photophysical processes in organic fluorophores. In this way, the one-pot incorporation of rationally selected dyes into suitable aluminophosphates by the *crystallization inclusion* method has allowed the straightforward development of fluorescent hybrid materials with outstanding functionalities, such as an important anisotropic response to linearly polarized light, second harmonic generation, laser gain, tunable emission or white light emission.

By the crystallization inclusion fluorescent hybrid materials are directly developed.

The following lines summarize the main conclusions and findings related to the hybrid systems developed throughout this thesis based on the acquired results.

- The design and proper selection of the components that make up the photoactive hybrid systems are crucial to establish the perfect combination and improve the photophysical properties, such as the fluorescence efficiency, which will determine the final emissive properties of the photoactive material and, therefore, its best field of application. The most important factors to consider in the design are the type (channels or cages) and dimensions of the host nanochannels, and the molecular size and intrinsic properties of the guest dyes.

The importance of a good match between guest dyes and the nanochannels of the hosts.

- Dye-loaded hybrid materials can be prepared by both conventional and microwave heating methods. The

The advantages of each heating technique.

use of one method over the other has a major impact on the resulting particle size of the material; that is, while the microwave allows fast and efficient heating and results in smaller crystals, the conventional oven produces large, well-formed crystals suitable for optical applications.

The importance of Brønsted acid sites for cationic dye incorporation.

- The choice of metal dopant for isomorphic substitution in the aluminophosphate material is key to favor cationic dye incorporation. These ionic metals affect the generation degree of Brønsted acid sites in the framework and the polarity of the medium. Consequently, it is possible to control the amount of encapsulated dye and modulate the final properties of the material in cases where there is a strong dependence on the dye concentration and/or the distance between molecules.

By adjusting the synthesis gels, high optical density materials are obtained.

- In this way, by adjusting the initial synthesis gel, materials with high optical density (high loadings of photoactive species) suitable for optical applications can be produced, without observing a detriment in the emissive characteristics of the fluorophores by molecular aggregation, due to the very restricted space provided by the channels of the prepared inorganic structures.

The occlusion provides a constraint environment to the dyes.

- The occlusion provides a constrained environment and drives the geometry of the guest dyes generating interesting optical features. In particular, the occlusion of dyes with high flexibility and internal conversion processes (*e.g.* styryls such as LDS 730, LDS 722, DMASBT, and 4-DASPI) within narrow channeled/-porous structures (*e.g.* AFI, AEL and CHA) favors a highly rigid and planar configuration of these molecules, triggering their fluorescence quantum yields.

- In the search for nonlinear optical properties, dyes with intrinsic NLO properties (push-pull character) and structures with unidirectional channels have

proven to be a perfect match, inducing an aligned arrangement of dye molecules along the channels (demonstrated by the high values of quantified dichroic ratios) and leading to non-centrosymmetric systems. As a consequence, dye-doped crystals with second harmonic generation have been reached. The best SHG system was found in DMASBT/AEL hybrid material, able to double the frequency of light from NIR to visible light.

Dyes with push-pull character combined with 1D-channeled structures are perfect for NLO.

- To obtain solid-state lasers it is a prerequisite to have relatively large and well-formed particles with defined edges acting as resonant cavities, as well as high dye loadings. Dilute synthesis gels specifically promote large particle sizes since they govern nucleation and crystal growth. Microlaser action has been successfully achieved in DMASBT/AEL hybrid material.

In microlasers is essential to have large crystals that act as resonant cavities.

- The presence of a photophysically active aromatic organic structure-directing agent can affect the resulting properties of the final material and thus confer fluorescent properties without the addition of any other dye. This has been the case for the IFO structure, in which the organic molecule DMAN is used as a template, leading to an intense blue emission, which has changed with the aging time, as a consequence of a molecular redistribution and different self-association.

Organic aromatic SDAs can influence the final photophysical properties.

- The synthesis strategy employed in this work also allows the simultaneous occlusion of different active guests whose combination has given rise to artificial antennas. In these systems, the resultant fluorescence color emission is highly dependent on the probability of FRET processes between the simultaneously occluded dyes in the restricted space of the zeotype channels. Likewise, distribution, concentration and relative proportions of the dyes play a key role in im-

In artificial antennas the final fluorescence is highly dependent on FRET processes.

proving FRET efficiency, and consequently influence the final emissive properties of the resultant material:

The two hybrid systems developed by the promotion of FRET processes.

- On the one hand, the bulkier laser dyes, such as R123 (green emission) and NB (red emission), that were occluded together with the template DMAN (blue emission) in the large pores of the IFO framework as FRET pairs, induced different emissive properties (green or red fluorescence) compared to the starting structure, allowing to develop possible efficient lasers in different areas of the spectrum.
- On the other hand, the smaller three-ring dyes such as acridine, pyronin Y, and the styryl dye LDS 722 with blue, green, and red emission, respectively, which were encapsulated into AEL channels in the right proportion, resulted in efficient white light emission upon UV excitation. This color emission can easily be adjusted to warmer or cooler white light depending on the type of illumination required, by playing with the relative proportions added to the initial synthesis gel.

10

FUTURE OUTLOOK

The dye-doped zeotypic materials presented in this work have shown strong potential for future applications in the field of optics and photonics. However, the interest and applicability of these versatile systems is not limited to what has been presented so far, but they still offer a great possibility to exploit and extend the range of applications. In the following lines, some challenges will be addressed to improve the operability of these systems and fulfill some of the initial perspectives pursued in this thesis that have not been achieved to date. Many of the approaches and experiments listed below are currently being undertaken and others will be carried out in the near future:

- One of the most interesting systems obtained is the DMASBT/AEL (Chapter 7, Section 7.3), which has shown great dual applicability, with NLO and microlaser response in single crystal level. Other styryls such as LDS 722 or 4-DASPI have also been tested in the same AEL structure, although the low dye loadings or lack of well-formed large crystals has not allowed the development of solid-state laser materials. However, they are also expected to be good candidates. Indeed, some laser signal (albeit low) has been observed in the case of LDS 722/AEL (Section 7.2.3). Moreover, 4-DASPI/AEL has showed high fluorescence properties and dye loadings, although in small and irregular crystal particles (Section 7.4.2). Therefore, further experiments will be performed and the synthesis conditions will be optimized varying the gel

composition (amount of dye, water, template, addition of isopropanol), heating temperature and time, in order to ensure the formation of big, well-defined crystalline particles with a suitable optical density to trigger microlaser action.

- Regarding the 4-DASPI/CHA system (Chapter 7, Section 7.4), the exceptional incorporation of the dye inside chabazite cavities (lodged within two neighbouring cage units) has rendered a system with high fluorescent quantum yield. However, the low dye/SDA ratio (0.024 4-DASPI / 3.3 TEA) in addition to the complex configuration adopted by the dye molecules between two cavities of CHA framework, has probably influenced the low incorporation reached. Therefore, as a future perspective, we intend to increase the amount of dye in the synthesis gel by 3 to 5 times, in order to simulate the same ratios used for other systems (typically 0.024 dye/1 TEA). In addition, the LDS 722 styryl dye has already been occluded into the cages of this structure, but the photophysical study and its potential applicability as a random laser remains to be tested.

- In the extra-large pore structure of IFO, it has been demonstrated that FRET energy transfer processes can be eventually promoted. However, although the incorporation of DMAN acting as a donor has been high, the amount of R123 and NB has been scarce in comparison, hampering an efficient FRET cascade. In this sense, several attempts are being made to favour a higher dye loading, such as increasing the amount of Mg and water content in the synthesis gel. In fact, a gel composition with 0.2 MgO and 100 H_2O for NB have turned out to be favorable. On the contrary, for R123, these conditions do not favor a higher incorporation, probably due to the large size of the molecule. Therefore, other combinations will be tried, such as the use of other types of dyes, i.e. flavine dyes as sub-

stitutes for R123 and i.e. smaller oxazine dyes as substitutes for NB.

On the other hand, based on the results of the present doctoral work, other promising research lines have been opened in the field of dye-doped zeotypic systems. For example, related to CHA structure, two other structures from the same ABC-6 family, are now being studied: MAPO-56 (AFX) and STA-20 (SWY). Both structures (Figure 10.1) give rise to 3D connected pore systems bounded by 8R walls with 6R aperture windows, leading to very similar entrances to that of CHA (≈ 3.8 Å x 3.8 Å, Section A.4, A.6 and A.7).

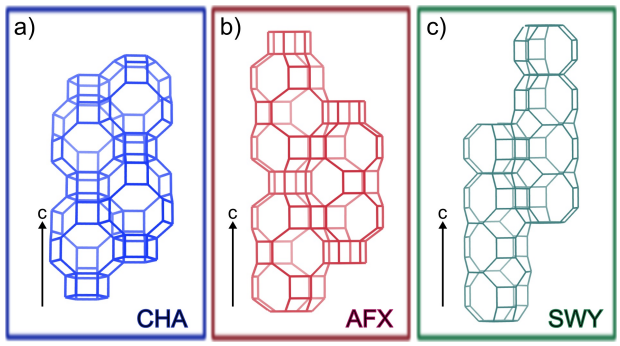

Figure 10.1: Three aluminophosphates of the ABC-6 family with 3D cavities: **(a)** CHA (studied throughout this thesis), **(b)** AFX, and **(c)** SWY.

A brief summary of the results obtained so far are presented below:

- *AFX tridimensional channel network*

  AFX shows more than one type of cage, gmelinite (gme) and AFT respectively.[1] The largest one, AFT (Figure 10.1b), has an open window of 3.4 Å x 3.6 Å and a length of 16.59 Å. Note that the aperture of the windows interconnecting the cavities is smaller compared to the CHA structure and dye molecules cannot be accommodated between two adjacent cavities (Figure 10.1a-b). For this reason, the main idea is

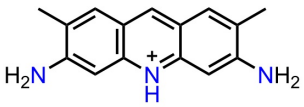

Acridine Yellow (ACY)

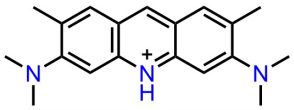

Acridine Orange (ACO)

Figure 10.2: Structure of acridine yellow (ACY) and acridine orange (ACO).

to exploit this structure to host the dye along a single AFT cage. In this regard, smaller dyes have been selected for the incorporation, namely acridine yellow and acridine orange (Figure 10.3).

Acridine derivatives (Section 3.6.2.1) are well known as dyes with a high probability of intersystem crossing processes allowing phosphorescence at low temperature or delayed fluorescence at room temperature (Section 3.1.4.1 and Section 3.1.4.2). The latter phenomenon is a very interesting photophysical process to be used in commercial OLEDs.[2,3] To trigger delayed fluorescence, the inorganic framework should provide a very rigid environment to the dye and avoid molecular self aggregation.

To this end, several syntheses are currently in progress. The AFX network as SAPO-56 and MgAPO-56 have been synthesized using TMHD (N, N, N′, N′-tetramethyl-1,6-hexanediamine) as a template (both procedures and gel compositions are given in Section 4.5). As observed for other structures, only the Mg-doped systems (MgAPO-56) have given satisfactory results in terms of dye loading. Interestingly, an important contribution of a new phase, identified as DFO, has been obtained together with AFX, regardless of the temperature employed for the synthesis (170 °C or 190 °C). DFO is characterized by a perpendicularly cross-linked 10- and 12-membered rings, with two types of unidirectional 12-membered channels of 6.2 Å and 7.3 Å diameters (Figure 10.2a).[4,5]

The two phases are easily distinguished by optical microscopy (Figure 10.4). AFX shows plain crystals with hexagonal morphology and very low color (Figure 10.4a), while the DFO particles are much larger and present an intense yellow (ACY) or orange (ACO) color by transmission (Figure 10.4b), indicating higher dye incorporation (occlusion verified by linear polarized emission measurements). Both particles exhibit fluorescent characteristics, but it is the DFO frame-

work that has promoted delayed fluorescence in acridine dyes. In fact, very long emission lifetimes of about 58 ms and 46 ms, have been registered for the samples synthesized with ACO and ACY, respectively (Figure 10.2b).

In light of these promising results, efforts are being made to further explore the characteristics of these new materials (AFX and DFO) and understand the processes involved. Therefore, new experiments are currently being carried out to obtain acridine-doped pure phase AFX and DFO phases, to boost (delayed) fluorescence in each particular structure.

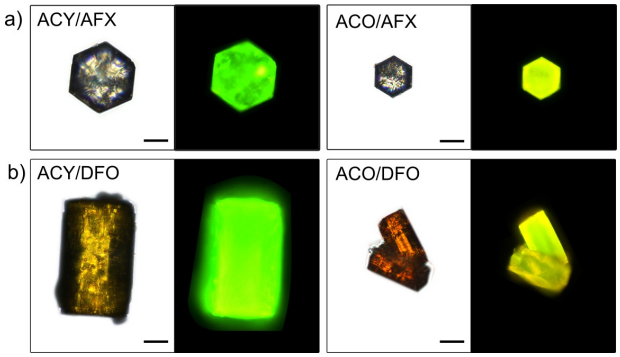

Figure 10.4: Transmission and fluorescence images upon blue excitation light (D470/40 band-pass) of **(a)** AFX and **(b)** DFO particles with ACY (left) and ACO (right) dyes synthesized at 170 °C. Scale = 20 µm.

- *Novel STA-20 (SWY) structure*

  The SWY structure is the most novel structure among all presented in this thesis. It was discovered very recently, in 2017.[6] This network also contains single 6R units and three types of cages: gme, can, and sta-20. It presents the longest three-dimensional cavity (22.7 Å) in an ordered ABC-6 material (Figure 10.1c), enabling the hosting of larger molecules. In fact, an aid-computed study indicates that dyes from the styryl family fit very well within these SWY cavities (Figure 10.5). Therefore, several syntheses are being per-

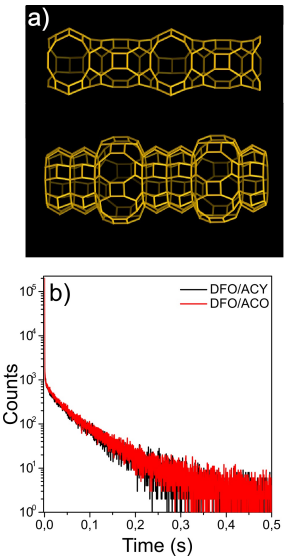

Figure 10.3: **(a)** The two types of 12-ring channel views of the DFO framework. **(b)** Fluorescence decay curve in 0.5 seconds window of MgAFX samples synthesized with ACY (red) and ACO (black) and with a pronounced amount of DFO (170 °C). It is important to say that AFX is also present in this sample but is not the cause of this phenomenon.

formed following the detailed procedure and with the gel composition described in Section 4.6.

Among all the attempts, LDS 751/SWY system (dye structure in Figure 10.6a) has shown interesting preliminar photophysical characteristics. Although the dye loading is low, the hybrid system shows red fluorescence with very long lifetimes of 20 ns, assigned to the confinement effect in the *STA-20* cages.

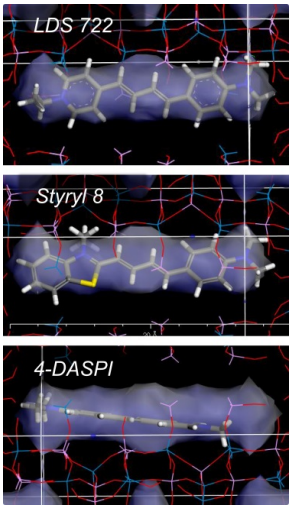

Figure 10.5: Molecular docking of some styryl dyes (LDS 722, Styryl 8 and 4-DASPI) within the 3D cavities of STA-20 framework.

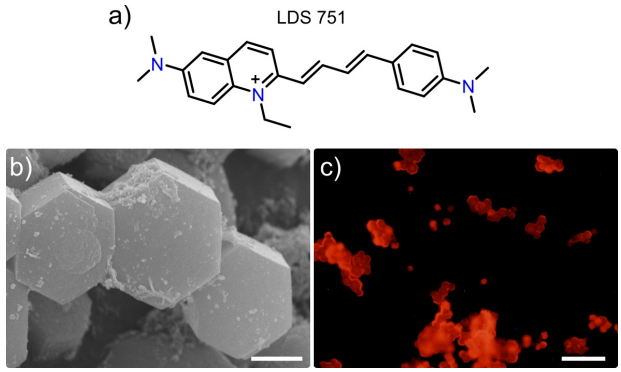

Figure 10.6: **(a)** Molecular structure of LDS 751 dye. **(b)** SEM (scale = 2 μm) and **(c)** fluorescence images upon green excitation light (HQ530/30m band-pass, scale = 20 μm) of LDS 751/SWY hybrid particles.

Therefore, this new structure is considered very promising, and further effort will be done to obtain an Mg-doped framework that will enable higher incorporation of dye molecules that give rise to diverse and brand new photoactive materials. .

All in all, the presented systems offer versatility and a wide range of possibilities, since they allow to rationally choose and adapt an inorganic matrix to the preferences or requirements of the fluorescent dyes or lasers of interest, thus achieving their maximum potential and allowing a broader use for more advanced devices. In this sense, we intend to proceed by exploiting new ideas and performing experiments that will allow us to achieve objectives and new discoveries applicable in the fields of optics and photonics.

BIBLIOGRAPHY

(1) Feng, P.; Bu, X.; Yang, C. S. Synthesis and single crystal structure of an AFX-type magnesium aluminophosphate. *Microporous and mesoporous materials* **2001**, *50*, 145–149.

(2) Méhes, G.; Nomura, H.; Zhang, Q.; Nakagawa, T.; Adachi, C. Enhanced electroluminescence efficiency in a spiro-acridine derivative through thermally activated delayed fluorescence. *Angewandte Chemie International Edition* **2012**, *51*, 11311–11315.

(3) Zeng, W.; Lai, H. Y.; Lee, W. K.; Jiao, M.; Shiu, Y. J.; Zhong, C.; Gong, S.; Zhou, T.; Xie, G.; Sarma, M.; Wong, K. T.; Wu, C.-C.; Yang, C. Achieving Nearly 30% External Quantum Efficiency for Orange–Red Organic Light Emitting Diodes by Employing Thermally Activated Delayed Fluorescence Emitters Composed of 1, 8-Naphthalimide-Acridine Hybrids. *Advanced Materials* **2018**, *30*, 1704961.

(4) Lobo, R. F.; Zones, S. I.; Medrud, R. C. Synthesis and Rietveld refinement of the small-pore zeolite SSZ-16. *Chemistry of materials* **1996**, *8*, 2409–2411.

(5) Baerlocher, C.; McCusker, L. B.; Olson, D. H., *Atlas of zeolite framework types*; Elsevier: 2007.

(6) Turrina, A.; Garcia, R.; Watts, A. E.; Greer, H. F.; Bradley, J.; Zhou, W.; Cox, P. A.; Shannon, M. D.; Mayoral, A.; Casci, J. L.; Wright, P. A. STA-20: an ABC-6 zeotype structure prepared by co-templating and solved via a hypothetical structure database and STEM-ADF imaging. *Chemistry of Materials* **2017**, *29*, 2180–2190.

Part V

APPENDIX

This final part of the thesis includes all the complementary material, such as a database with structural information of all the aluminophosphates employed, tables with the syntheses carried out and the actual compositions for each case, and supporting documentation to verify the results presented.

A

HOST SYSTEMS DATABASE

The following pages provide a database with structural information on all the types of zeotype structures that have been selected in this thesis.

A.1 FRAMEWORK TYPE AFI

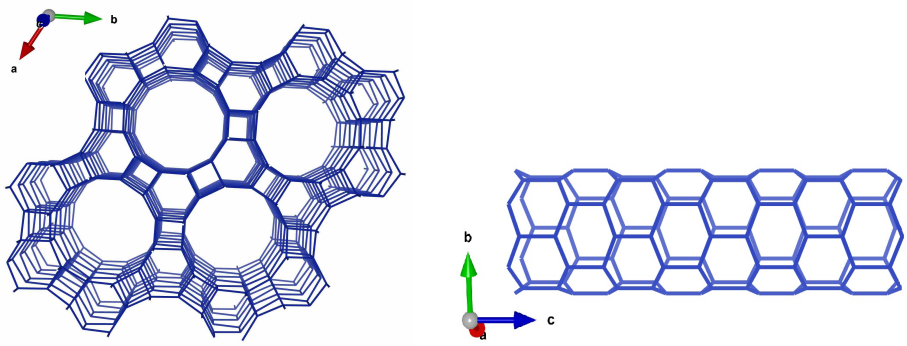

Name and Code derivation:

- Aluminophosphate-five
- $AlPO_4$-5 (five)
- AFI

Year reported: 1987
Idealized cell data: hexagonal, *P6cc*, a = 13.8 Å, c = 8.6 Å
Framework density: 17.3 T/1000 $Å^3$
Channels: 7.3 x 7.3 Å
Biggest ringe size: 12 MR
Dimensionality: 1D

Hybrid materials with this framework type:

- LDS 730 / SAPO-5
- LDS 730 / MgAPO-5
- DMASBT / MgAPO-5

A.2 FRAMEWORK TYPE ATS

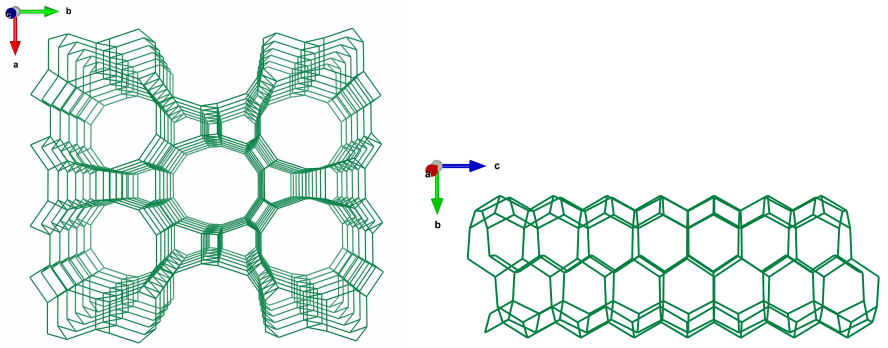

Name and Code derivation:

- MAPO-36 (thirty-six)
- ATS

Year reported: 1992
Idealized cell data: orthorhombic, *Cmcm*, a = 13.2 Å, b = 21.6 Å, c = 5.3 Å
Framework density: 16.4 T/1000 Å^3
Channels: 6.5 x 7.5 Å
Bigger ringe size: 12 MR
Dimensionality: 1D

Hybrid materials with this framework type:

- DMASBT / MgAPO-36

A.3 FRAMEWORK TYPE AEL

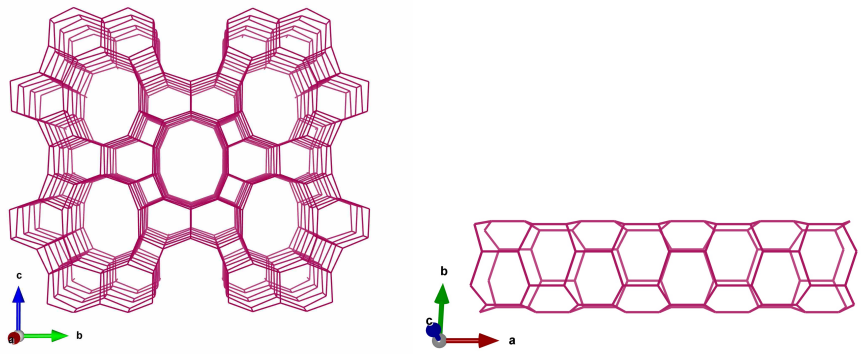

Name and Code derivation:

- Aluminophosphate-eleven
- $AlPO_4$-11 (eleven)
- AEL

Year reported: 1987
Idealized cell data: orthorhombic, *Imma*, a = 8.3 Å, b = 18.7 Å, c = 13.4 Å
Framework density: 19.1 T/1000 $Å^3$
Channels: 4.0 x 6.5 Å
Biggest ringe size: 10 MR
Dimensionality: 1D

Hybrid materials with this framework type:

- LDS 722 / MgAPO-11
- DMASBT / MgAPO-11
- AC + PY + LDS 722 / MgAPO-11

A.4 FRAMEWORK TYPE CHA

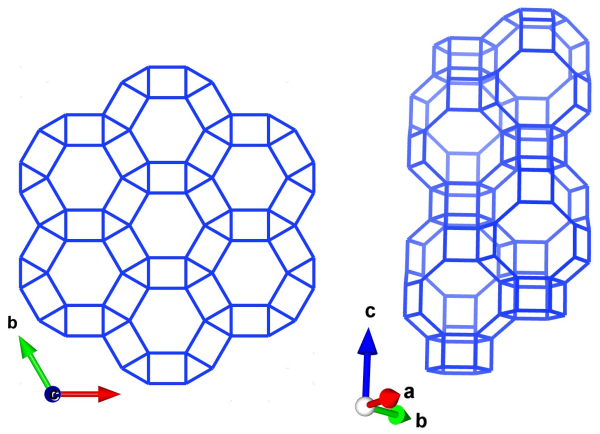

Name and Code derivation:

- Chabazite
- CHA

Year reported: 1978
Idealized cell data: trigonal, $R\bar{3}m$, a = 13.7Å, c = 14.8Å
Framework density: 14.5 T/1000 Å^3
Channels: 3.8 x 3.8 Å (variable due to considerable flexibility)
Bigger ringe size: 8 MR
Dimensionality: 3D

Hybrid materials with this framework type:

- 4-DASPI / MgAPO-34

A.5 FRAMEWORK TYPE IFO

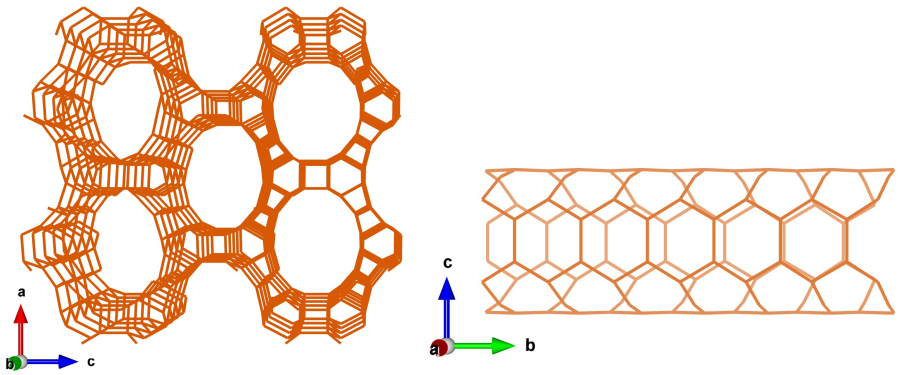

Name and Code derivation:

- Instituto de Tecnologia Quimica Valencia - fifty-one
- ITQ-51 (fifty-one)
- IFO

Year reported: 2013
Idealized cell data: monoclinic, $P12_1/n1$, a = 23.3 Å, b = 16.5 Å, c = 5.0 Å
Framework density: 16.7 T/1000 $Å^3$
Channels: 9.3 x 10.6 Å
Bigger ringe size: 16 MR
Dimensionality: 1D

Hybrid materials with this framework type:

- R123 / MgITQ-51
- NB / MgITQ-51
- R123 + NB / MgITQ-51

A.6 FRAMEWORK TYPE AFX

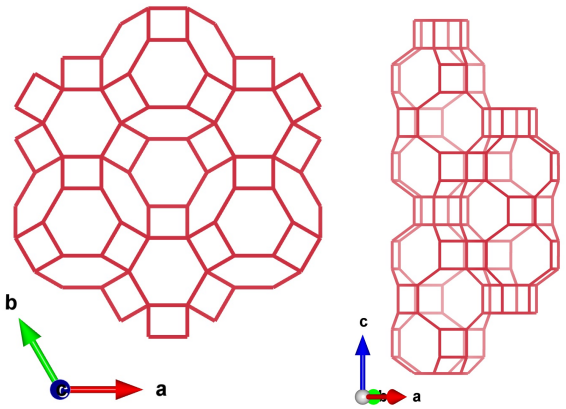

Name and Code derivation:

- Silico-Aluminophosphate-fifty-six
- SAPO-56 (fifty-six)
- AFX

Year reported: 1994
Idealized cell data: hexagonal, $P6_3/mmc$, a = 13.7 Å, c = 19.7 Å
Framework density: 14.7 T/1000 $Å^3$
Channels: 3.4 x 3.6 Å
Bigger ringe size: 8 MR
Dimensionality: 3D

Hybrid materials with this framework type:

- ACY / SAPO-56
- ACO / SAPO-56
- ACY / MgAPO-56
- ACO / MgAPO-56

A.7 FRAMEWORK TYPE SWY

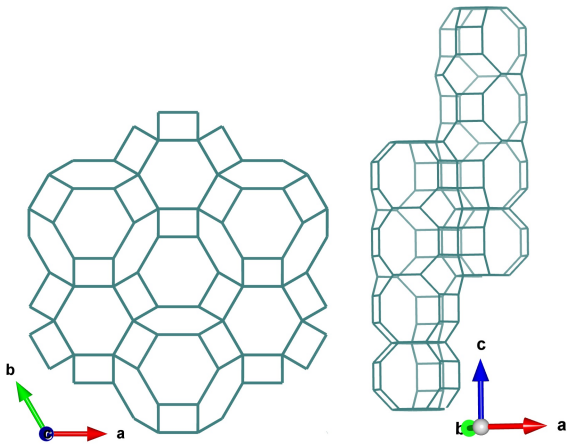

Name and Code derivation:

- University of Saint Andrews - twenty
- STA-20 (twent(y))
- SWY

Year reported: 2017
Idealized cell data: trigonal, *P31c*, a = 13.2 Å, b = 13.2 Å, c = 30.6 Å
Framework density: 15.7 T/1000 $Å^3$
Channels: 4.0 x 3.9 Å
Bigger ringe size: 8 MR
Dimensionality: 3D

Hybrid materials with this framework type:

- LDS 751 / STA-20

B

SPECIFIC GEL MOLAR COMPOSISITIONS FOR EACH SYSTEM

The following tables show the real gel compositions for each (dye-doped) zeotype synthesized by microwave and conventional oven.

- SAPO-5 (MW)

Sample	Al_2O_3	P_2O_5	SiO_2	TEA	H_2O
SiAFI-1	1.01	0.96	0.20	0.75	314.92
SiAFI-2	1.00	0.97	0.20	1.00	310.11
SiAFI-3	1.00	0.97	0.20	1.50	305.13
SiAFI-4	1.02	0.94	0.20	1.49	306.52
SiAFI-5	1.05	0.95	0.20	1.49	304.60
SiAFI-6	1.02	1.07	0.20	1.49	304.76

- LDS 730/ SAPO-5 (MW)

Sample	Al_2O_3	P_2O_5	SiO_2	TEA	LDS 730	H_2O
S1/SiAFI-3H	1.00	0.91	0.20	1.50	0.024	304.95
S1/SiAFI-4H	1.00	0.91	0.20	1.50	0.024	304.95
S1/SiAFI-5H	1.00	0.91	0.20	1.50	0.024	304.95
S1/SiAFI-6H	1.01	0.95	0.20	1.49	0.026	304.66

- MgAPO-5 (MW)

Sample	Al_2O_3	P_2O_5	MgO	TEA	H_2O
MgAFI-1	0.89	1.10	0.22	0.96	306.66
MgAFI-2	0.90	1.03	0.20	0.75	302.53
MgAFI-3	0.97	1.05	0.10	0.75	304.64
MgAFI-4	0.97	1.02	0.11	1.00	310.31

- LDS 730/ MgAPO-5 (MW)

Sample	Al_2O_3	P_2O_5	MgO	TEA	LDS 730	H_2O
S1/MgAFI-1L	0.91	1.11	0.21	1.00	0.009	305.61
S1/MgAFI-1H	0.90	1.03	0.20	1.00	0.024	304.76
S1/MgAFI-2L	0.90	1.08	0.20	0.75	0.010	305.16
S1/MgAFI-2H	0.91	1.05	0.20	0.75	0.024	304.76
S1/MgAFI-3L	0.95	0.97	0.10	0.75	0.008	305.57
S1/MgAFI-3H	0.95	0.98	0.11	0.75	0.024	305.95
S1/MgAFI-4L	0.95	1.03	0.10	1.00	0.009	313.78
S1/MgAFI-4M	0.95	1.00	0.11	1.00	0.016	304.65
S1/MgAFI-4H	0.95	1.09	0.10	1.00	0.024	305.57

- LDS 730/ MgAPO-5 (CH)

Sample	Al_2O_3	P_2O_5	MgO	TEA	LDS 730	H_2O
S1/MgAFI-2H′	0.91	1.00	0.21	0.74	0.024	304.74
S1/MgAFI-4H′	0.95	1.00	0.10	0.99	0.025	304.34

- MgAPO-11 (CH)

Sample	Al_2O_3	P_2O_5	MgO	DPA	H_2O
MgAEL-1	0.97	1.08	0.28	1.86	498.72

- LDS 722/ MgAPO-11 (CH)

Sample	Al_2O_3	P_2O_5	MgO	EBA	LDS 722	H_2O	2-propanol
S2/MgAEL-1	0.97	1.05	0.28	1.94	0.008	501.88	-
S2/MgAEL-2	0.94	1.00	0.10	0.98	0.008	300.63	-
S2/MgAEL-3	0.96	0.98	0.10	0.96	0.008	302.37	6.00
S2/MgAEL-4	0.96	1.00	0.10	0.97	0.008	500.01	-
S2/MgAEL-5	0.96	1.00	0.10	1.11	0.008	504.03	6.14

- DMASBT/MgAPO-11 (CH)

Sample	Al_2O_3	P_2O_5	MgO	SDA	DMASBT	H_2O
S3/MgAEL-1	0.90	1.00	0.20	0.75	0.025	300.11
S3/MgAEL-2	0.90	1.02	0.20	0.97	0.024	300.42
S3/MgAEL-3	0.89	1.00	0.20	1.48	0.024	300.38
S3/MgAEL-4	0.95	1.02	0.10	0.74	0.024	300.10
S3/MgAEL-5	0.95	0.99	0.10	1.00	0.024	300.85
S3/MgATS-1	0.91	0.98	0.20	0.80	0.024	299.59
S3/MgATS-2	0.90	1.01	0.20	0.98	0.024	300.32
S3/MgAFI-1	0.92	0.99	0.21	0.76	0.024	300.57
S3/MgAFI-2	0.90	1.00	0.20	0.98	0.024	200.28

- DMASBT/MgAPO-36 (CH)

Sample	Al_2O_3	P_2O_5	MgO	SDA	DMASBT	H_2O
S3/MgATS-1	0.91	0.98	0.20	0.80	0.024	299.59
S3/MgATS-2	0.90	1.01	0.20	0.98	0.024	300.32

- DMASBT/MgAPO-5 (CH)

Sample	Al_2O_3	P_2O_5	MgO	SDA	DMASBT	H_2O
S3/MgAFI-1	0.92	0.99	0.21	0.76	0.024	300.57
S3/MgAFI-2	0.90	1.00	0.20	0.98	0.024	200.28

- 4-DASPI/MgAPO-11 (CH)

Sample	Al_2O_3	P_2O_5	MgO	EBA	4-DASPI	H_2O
S4/MgAEL-1	0.91	0.99	0.20	1.04	0.026	300.27
S4/MgAEL-2	0.91	1.01	0.20	0.75	0.025	299.64
S4/MgAEL-3	0.96	1.02	0.10	1.04	0.024	299.85
S4/MgAEL-4	0.93	1.02	0.10	0.75	0.024	298.53

- 4-DASPI/MgAPO-34 (CH)

Sample	Al_2O_3	P_2O_5	MgO	TEA	4-DASPI	H_2O
MgCHA	0.77	1.00	0.47	3.30	-	47.00
S4/MgCHA	0.77	1.00	0.47	3.30	0.024	47.00

- Dye/MgITQ-51 (CH)

Sample	Al_2O_3	P_2O_5	MgO	DMAN	H_2O	Dye
MgIFO-1	0.95	1.00	0.10	1.21	39.92	-
F1/MgIFO-1	0.95	1.00	0.10	1.20	40.19	0.008 R123
F2/MgIFO-1	0.94	0.99	0.10	1.22	42.59	0.008 NB
F1+F2/MgIFO-1	0.98	1.02	0.11	1.23	40.24	0.004 R123 + 0.004 NB

C

SUPPORTING INFORMATION

All supporting documentation and information necessary to verify the results and performed calculations is provided here.

C.1 SUPPORTING FIGURES

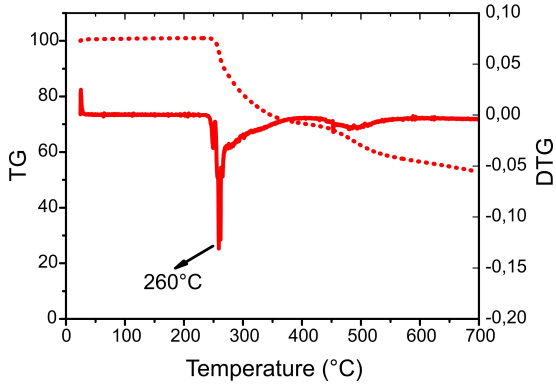

Figure C.1: Overall thermogravimetric decomposition (TG) process of the LDS 730 dye and determination of the decomposition characteristic temperature by the derivative thermogravimetric method (DTG).

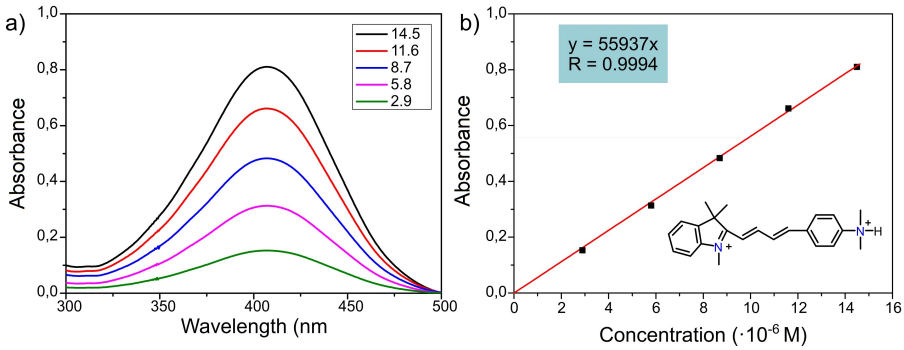

Figure C.2: Calibration **(a)** solutions and **(b)** curve of LDS 730 in a solution of 20% EtOH in acid media (HCl). The concentrations given are in µM ($\cdot 10^{-6}$ M). It should be noted that since the quantification was performed in a very acidic medium to ensure the degradation of the matrix, the species to be quantified was the diprotonated molecule ph < pk_a, which is blue-shifted in comparison to the monocation due to a loss in conjugation.

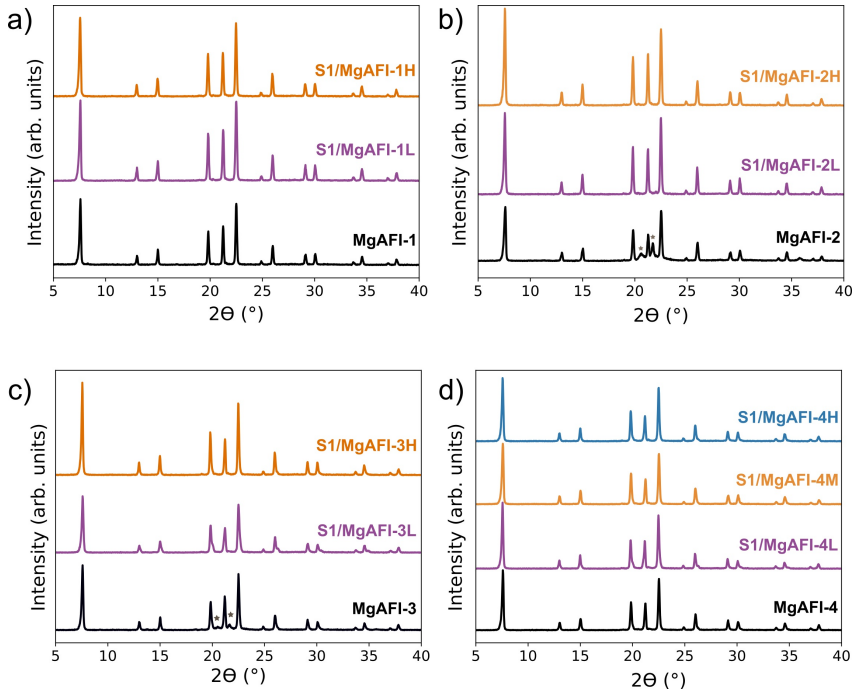

Figure C.3: X-ray powder diffractions of MgAFI samples synthesized by microwave heating: **(a)** 1, **(b)** 2, **(c)** 3, and **(d)** 4.

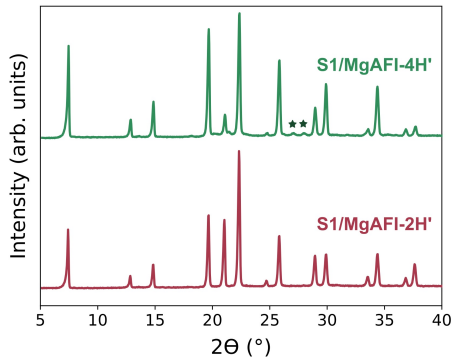

Figure C.4: X-ray powder diffractions of MgAFI samples synthesized by conventional heating.

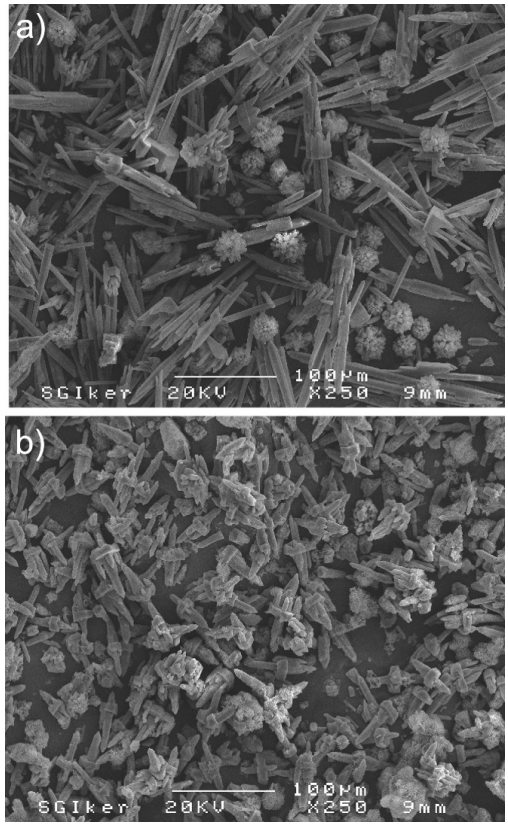

Figure C.5: Scanning electron microscopy images for samples S1/MgAFI-2H′ and S1/MgAFI-4H′ synthesized with different MgO compositions.

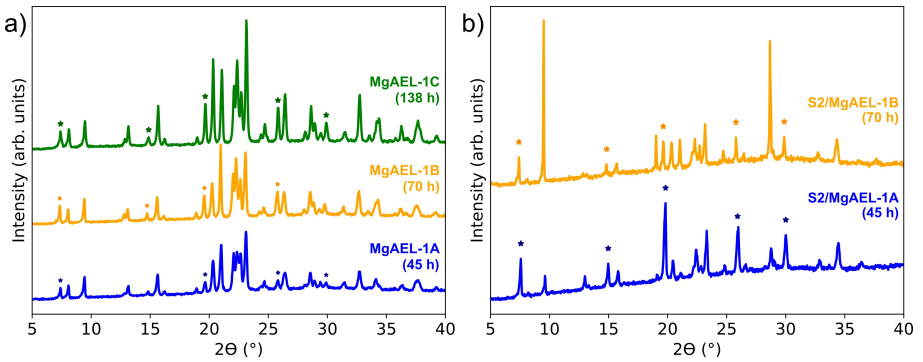

Figure C.6: X-ray diffractions of AEL large crystals **(a)** without (MgAEL-X) and **(b)** with LDS 722 dye (S2/MgAEL-X) at several synthesis times. A = 45 h, B = 70 h and C = 138 h.

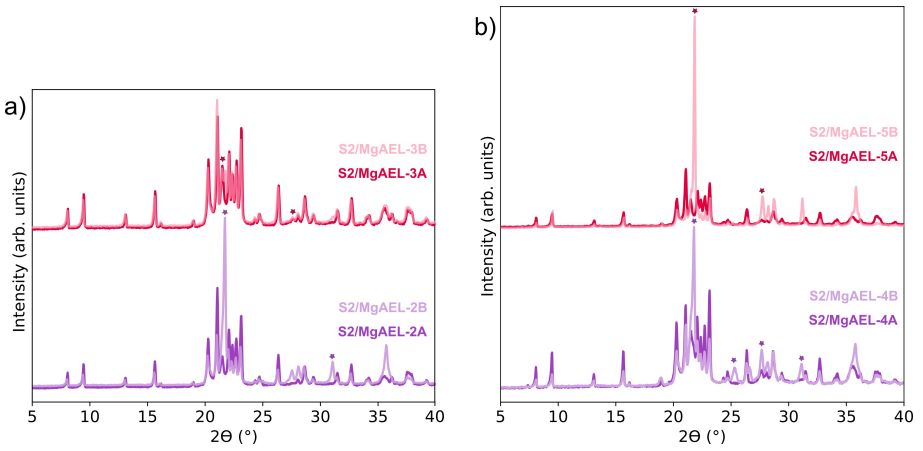

Figure C.7: X-ray diffractions of dye-doped (LDS 722) AEL large crystals with the synthesis made at different gel compositions and at two different temperatures (A = 180 ° C, B = 195 ° C) superposed: **(a)** S2/MgAEL-2 and -3, and **(b)** S2/MgAEL-4 and -5.

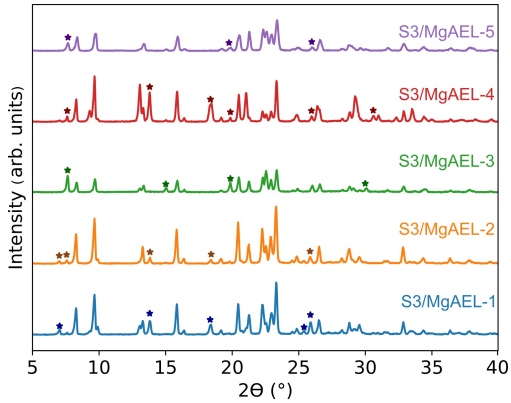

Figure C.8: PXRD patterns of DMASBT/AEL (S3MgAEL-X) samples prepared under different synthesis conditions by CH, which are summarized in Table 7.11 of the manuscript. Asterisks indicate diffractions of phases formed other than the main phase.

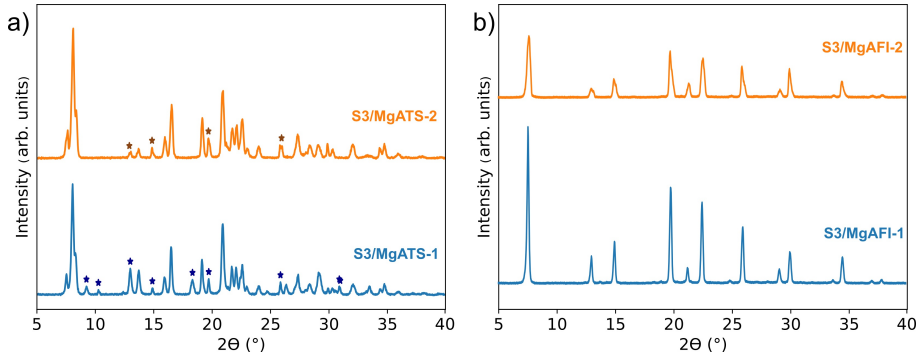

Figure C.9: PXRD patterns of **(a)** DMASBT/ATS (S3/MgATS-X) and **(b)** DMASBT/AFI (S3/MgAFI-X) samples prepared under different synthesis conditions by CH, which are summarized in Table 7.11 of the manuscript. Asterisks indicate diffractions of phases formed other than the main phase.

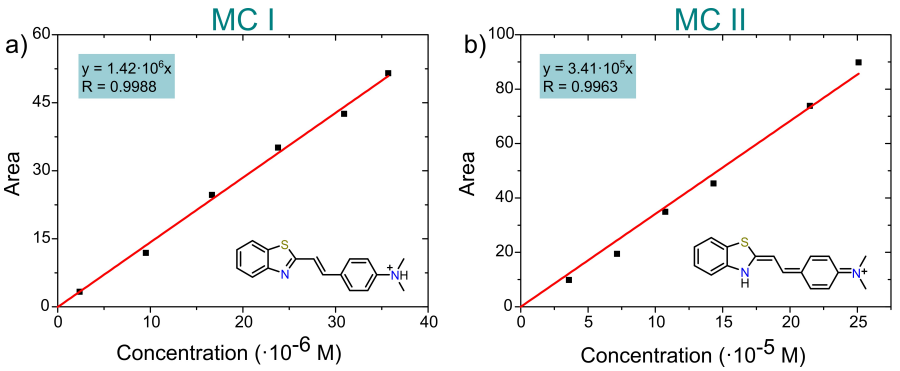

Figure C.10: Calibration curves for the two DMASBT (aq) monocation (MC I and MC II) species in 50% EtOH in acid media (HCl): **(a)** Monocation I and **(b)** monocation II.

Figure C.11: Scanning-electron microscopy image of sample S3/MgAEL-4.

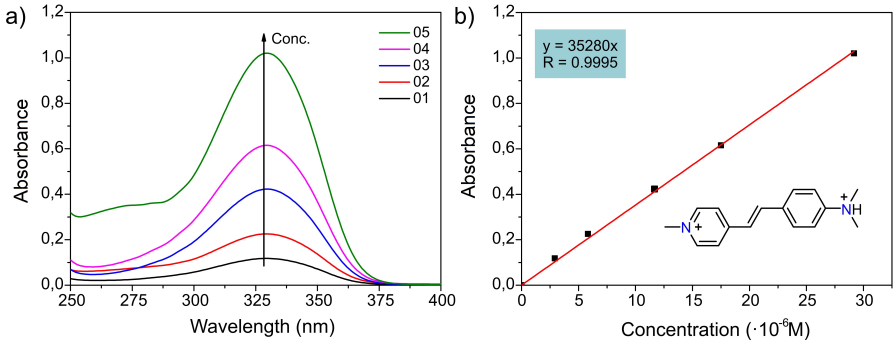

Figure C.12: Calibration of 4-DASPI in deionized water in acid media (HCl). The concentrations given are in µM ($\cdot\ 10^{-6}$ M). It should be noted that since the quantification was performed in a very acidic medium to ensure the degradation of the matrix, the species to be quantified was the diprotonated molecule ph < pK_a, which is blue-shifted in comparison to the monocation due to a loss in conjugation.

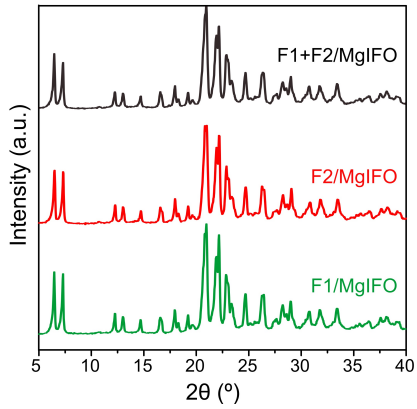

Figure C.13: PXRD patterns of dye-doped MgIFO samples. F1 = R123 and F2 = NB.

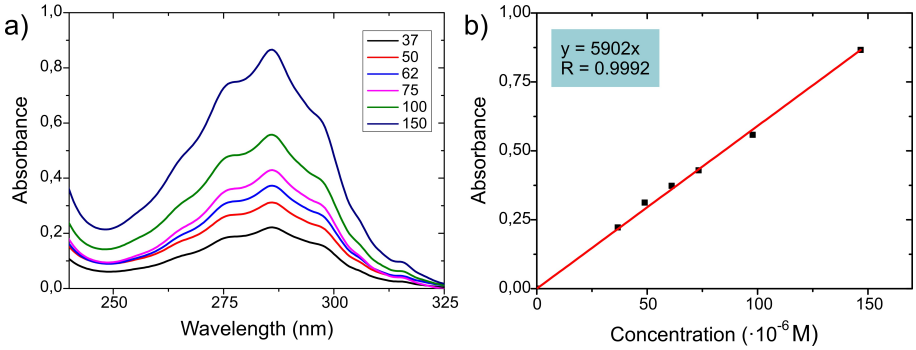

Figure C.14: Calibration **(a)** solutions and **(b)** curve of DMAN in a 50:50 EtOH:H_2O aqueous solution in acid media (HCl). The concentrations given are in µM ($\cdot\ 10^{-6}$ M).

C.2 SUPPORTING EXPLANATIONS

C.2.1 *Determination of* pk_a

The pk_a of DMASBT was determined by using the following equation:[1]

$$pH = pk_a + \log\left(\frac{A_{max}(\lambda_{DMASBT}) - A}{A - A_{max}(\lambda_{DMASBT...H^+})}\right) \tag{C.1}$$

where $A_{max}(\lambda_{DMASBT})$ and $A_{max}(\lambda_{DMASBT...H^+})$ refer to the maximum absorbance values of the DMASBT molecule in neutral and protonated form when only these species are present and A refers to the absorbance of the molecule in the respective buffer solutions.

$$y = 2.020x + 4.504$$

When the acidic and basic species are equal it is known that the pH of the solution will be equal to the value of pk_a. Therefore, the pk_a obtained was:

$$\boxed{pk_a = 4.50}$$

1 Pandey, M.; Jaipal, A; Kumar, A; Malik, R; Charde, S. Determination of pKa of felodipine using UV–Visible spectroscopy. *Spectrochimica Acta Part A: Molecular and Biomolecular Spectroscopy* **2013**, *115*, 887–890